

***Laser spectroscopy of  
small metal-containing  
free radicals***

Thesis submitted for the degree of  
Doctor of Philosophy  
at the University of Leicester

by

**Matthew Simon Beardah BSc (Leicester)**

Department of Chemistry  
University of Leicester

September 1999

UMI Number: U594548

All rights reserved

INFORMATION TO ALL USERS

The quality of this reproduction is dependent upon the quality of the copy submitted.

In the unlikely event that the author did not send a complete manuscript and there are missing pages, these will be noted. Also, if material had to be removed, a note will indicate the deletion.



UMI U594548

Published by ProQuest LLC 2013. Copyright in the Dissertation held by the Author.  
Microform Edition © ProQuest LLC.

All rights reserved. This work is protected against  
unauthorized copying under Title 17, United States Code.



ProQuest LLC  
789 East Eisenhower Parkway  
P.O. Box 1346  
Ann Arbor, MI 48106-1346

**TITLE** Laser spectroscopy of small metal-containing free radicals

**AUTHOR** Matthew Simon Beardah

**ABSTRACT**

The work presented in this thesis is concerned with the preparation of small supersonically-cooled alkaline-earth metal-containing polyatomic molecules by a laser ablation method, with subsequent detection using laser electronic spectroscopy. The results of spectroscopic studies involving three alkaline-earth metal-containing free radicals are presented.

A new electronic transition, the  $\tilde{D}^2\Sigma^+ - \tilde{X}^2\Sigma^+$  system, of the BaOH free radical is reported. The laser-induced fluorescence (LIF) spectrum is relatively straightforward, showing a simple vibrational progression in the Ba-O stretching mode ( $\nu_3$ ). A re-investigation of the  $\tilde{C} - \tilde{X}$  system of BaOH, carried out under supersonic jet conditions for the first time, is also presented. The LIF excitation spectrum is rather more complex than expected and possible explanations for these observations are considered.

Five new electronic transitions of the SrOH free radical are reported for the first time. Three of these, the  $\tilde{D}^2\Sigma^+ - \tilde{X}^2\Sigma^+$ ,  $\tilde{E}^2\Sigma^+ - \tilde{X}^2\Sigma^+$  and  $\tilde{F}^2\Pi - \tilde{X}^2\Sigma^+$  transitions, show simple structure in their vibrationally-resolved LIF excitation spectra. Another new transition, the  $\tilde{C}^2\Pi - \tilde{X}^2\Sigma^+$  transition, is remarkably complex. It is proposed that a combination of Renner-Teller coupling and a 'reverse-polarised'  $\pi$  orbital in the  $\tilde{C}^2\Pi$  electronic state is responsible for the added complexity in the LIF excitation spectrum. The  $\tilde{B}'^2\Sigma^+ - \tilde{X}^2\Sigma^+$  electronic transition of SrOH shows evidence of vibronic interaction with the nearby  $\tilde{C}^2\Pi$  state.

A dispersed fluorescence study of the ground state ( $\tilde{X}^2\Sigma^+$ ) of the MgCCH radical is also presented. The results of this study, in addition to a previous FTIR-matrix isolation study, have now accounted for four out of the five fundamental vibrational frequencies of ground state MgCCH.

Finally, experiments involving a newly constructed REMPI-TOF mass spectrometer are discussed. Initial test experiments involving NO, CaOH, SrOH and SrCCH show that while the mass spectrometer detection aspect of the instrument is working well, supersonic cooling has proved elusive. Possible design aspects of the spectrometer which may be affecting the supersonic cooling are discussed, along with suggestions for future improvements.

## STATEMENT OF ORIGINALITY

The work presented in this thesis was conducted by the author during the period between October 1996 and September 1999 in the Department of Chemistry, University of Leicester and is original unless otherwise acknowledged in the text or references.

The work presented in Chapters 4 and 6 was performed in conjunction with Dr Simon Pooley and Dr Gary Corlett, respectively. The REMPI-TOF mass spectrometer, described in Chapter 7, was originally designed by Dr Andrew Bezant. This aside, none of the work has been submitted for another degree at this or any other university.

Signed Matthew Beardah Date 22/12/99  
Matthew S. Beardah



## ACKNOWLEDGEMENTS

First and foremost, I am indebted to my supervisor, Dr Andrew Ellis, for his guidance in all areas of my scientific development and for furthering my appreciation of experimental and theoretical spectroscopy throughout the duration of my Ph.D. I am especially grateful for his patience, advice and constructive criticism in the preparation of this thesis.

To all members of the laser research group, past and present, I would like to convey my appreciation for providing an extremely good humoured working environment. Special thanks must go to Greg for pointing out the many 'interesting features' of everyday life. To Barry, for all those trips to the cinema and scientific discussions at the curry house - thanks for that! To the forefathers of the group, thanks to Gary for teaching me patience in the art of laser 'tweaking' and to Andy for his friendship, camaraderie and crash course in fire safety!

My thanks also go to the technical staff of the Chemistry department for their unfaltering expertise. To John and Keith, thanks for transforming many a half-hearted sketch into a magnificent piece of spectroscopic equipment. To Gerry and Phil, for teaching me that electronics is as difficult as I always thought it was - thanks for always making things work again!

I would like to thank the Engineering and Physical Sciences Research Council for funding my postgraduate studies. I am also especially indebted to the Society of the Chemical Industry for honouring me with the award of a Messel Scholarship. It has been a real pleasure to present my research to the society in an environment that embraces all areas of science so readily and enthusiastically.

Finally, I would like to thank the most important people in my life for their support, during all of my academic studies. To my wife, Alison, for being my best friend and soulmate throughout the whole of my university career. To my parents, for their unconditional support in all my endeavours and for always being there. Thanks to my brothers, Christian and Julian, for introducing me to the delights of Mr Shings - may it forever rain crispy aromatic duck! My appreciation also goes to Jan and Pete for their unfaltering generosity and for donating their Vauxhall Nova to a good cause - may it rest in peace.

## LIST OF PUBLICATIONS

Some of the work presented in this thesis has also appeared in the following publications,

‘Production and detection of short-lived metal-containing molecules in the gas phase: A review’

M.S. Beardah and A.M. Ellis, *J. Chem. Technol. Biotechnol.*, **74** (1999) 863

‘Observation of several new electronic transitions of the SrOH free radical’

M.S. Beardah and A.M. Ellis, *J. Chem. Phys.*, **110** (1999) 11244

‘Electronic spectroscopy of the  $\tilde{C}^2\Pi - \tilde{X}^2\Sigma^+$  and  $\tilde{D}^2\Sigma^+ - \tilde{X}^2\Sigma^+$  transitions of BaOH’

S.J. Pooley, M.S. Beardah and A.M. Ellis, *J. Elec. Spec. Rel. Phen.*, **97** (1998) 77

‘A dispersed fluorescence investigation of the low frequency vibrations of MgCCH ( $\tilde{X}^2\Sigma^+$ )’

G.K. Corlett, M.S. Beardah and A.M. Ellis, *J. Mol. Spec.*, **185** (1998) 202

## TABLE OF CONTENTS

Abstract	i
Statement of originality	ii
Acknowledgements	iii
List of publications	iv
Table of contents	v
List of figures and tables	ix
 <b>Chapter One:</b> <i>Introduction</i>	 <b>1</b>
1.1    Introduction	1
1.2    Metal-containing free radicals	2
1.2.1    Early studies of metal-containing radicals	4
1.3    Polyatomic metal-containing molecules	6
1.4    Molecular beam and supersonic jet studies	8
1.5    This thesis	10
<i>References</i>	12
 <b>Chapter Two:</b> <i>Experimental</i>	 <b>19</b>
2.1    Introduction	19
2.2    Radical production	19
2.2.1    The LIF chamber	21
2.2.2    Gas delivery	22
2.2.3    Laser ablation/photolysis	24
2.2.4    Supersonic jets and molecular beams	26
2.3    Electronic spectroscopy	33
2.3.1    Laser induced fluorescence (LIF) excitation spectroscopy	33
2.3.2    Dispersed fluorescence (DF) spectroscopy	37
2.4    Overview of the laser systems	37
2.4.1    The Excimer laser	39
2.4.2    The Neodymium-YAG laser	40
2.4.3    The Scanmate tunable dye laser	40
2.5    Experimental synchronisation	43
<i>References</i>	45

<b>Chapter Three:</b>	<i>Monohydroxide derivatives of the alkaline-earth metals</i>	<b>46</b>
3.1	Background	46
3.2	Electronic structure	47
3.3	Previous spectroscopic studies of the alkaline-earth monohydroxides	52
3.3.1	MgOH	52
3.3.2	CaOH	53
3.3.3	BaOH and SrOH	54
3.4	Present work	54
3.5	Angular momentum coupling in linear molecules	55
3.5.1	Spin-orbit coupling	55
3.5.2	The Renner-Teller effect	59
3.5.3	Other angular momentum coupling interactions	61
3.5.3.1	Lambda-type doubling	61
3.5.3.2	Spin-rotation interaction	61
3.6	Fermi resonance	63
	<i>References</i>	64
<b>Chapter Four:</b>	<i>Electronic spectroscopy of the <math>\tilde{C} - \tilde{X}</math> and <math>\tilde{D} - \tilde{X}</math> transitions of BaOH</i>	<b>67</b>
4.1	Introduction	67
4.2	Experimental	67
4.3	Results and discussion	68
4.3.1	The $\tilde{D}^2\Sigma^+ - \tilde{X}^2\Sigma^+$ system	68
4.3.1.1	Vibrational structure	68
4.3.1.2	Electronic state assignment	71
4.3.1.3	Rotational structure	73
4.3.2	The $\tilde{C} - \tilde{X}$ region	73
4.3.2.1	Identifying the BaOH bands	75
4.3.2.2	Vibrational structure	78
4.3.2.3	Rotational analysis	81
4.3.2.4	The BaOH $\tilde{C}$ state: linear or bent?	86
4.4	Conclusions	89
	<i>References</i>	90

<b>Chapter Five:</b>	<i>Observation of several new electronic transitions of the SrOH free radical</i>	<b>92</b>
5.1	Introduction	92
5.2	Experimental	92
5.3	Results and discussion	93
5.3.1	The $\tilde{C}^2\Pi - \tilde{X}^2\Sigma^+$ system	95
5.3.1.1	Overview	95
5.3.1.2	Electronic origin	95
5.3.1.3	Higher vibronic bands	100
5.3.1.4	Complexity of the $\tilde{C} - \tilde{X}$ spectrum: evidence for Renner-Teller coupling	107
5.3.1.5	Bands to the red of the $\tilde{C} - \tilde{X}$ origin	114
5.3.2	The $\tilde{D}^2\Sigma^+ - \tilde{X}^2\Sigma^+$ system	120
5.3.2.1	Emission from the $\tilde{C}^2\Pi$ and $\tilde{D}^2\Sigma^+$ states of SrOH	126
5.3.3	The $\tilde{E}^2\Sigma^+ - \tilde{X}^2\Sigma^+$ system	130
5.3.4	The $\tilde{F}^2\Pi - \tilde{X}^2\Sigma^+$ system	131
5.3.5	Character of excited electronic states of SrOH	134
5.3.6	Comparison with other MOH molecules	138
5.4	Conclusions	138
	<i>References</i>	140
<b>Chapter Six:</b>	<i>A dispersed fluorescence investigation of the low frequency vibrations of MgCCH (<math>\tilde{X}^2\Sigma^+</math>)</i>	<b>142</b>
6.1	Introduction	142
6.2	Experimental	143
6.3	Results and discussion	143
6.4	Conclusions	147
	<i>References</i>	148
<b>Chapter Seven:</b>	<i>Testing of a new REMPI-TOF spectrometer</i>	<b>149</b>
7.1	Introduction	149
7.2	Fundamental aspects of REMPI spectroscopy	150

7.2.1	The REMPI mechanism	150
7.2.2	Multiphoton selection rules	153
7.3	Experimental aspects of REMPI spectroscopy	154
7.3.1	Sample preparation and radical production	154
7.3.2	The REMPI chamber	158
7.3.3	Ion detection: Time-of-flight (TOF) mass spectrometry	159
7.3.3.1	Wiley-McLaren time-of-flight mass spectrometer	159
7.4	Results and discussion	163
7.4.1	REMPI spectroscopy of nitric oxide (NO)	163
7.4.1.1	Sample preparation and operational conditions	163
7.4.1.2	(1+1) REMPI spectrum of the $A^2\Sigma^+ - X^2\Pi$ electronic system of NO	164
7.4.1.3	Determining the source of supersonic jet/molecular beam disruption	167
7.4.1.4	Future modifications to the REMPI-TOF apparatus	171
7.4.2	REMPI spectroscopy of the CaOH and SrOH free radicals	171
7.4.2.1	CaOH	172
7.4.2.2	SrOH	173
7.4.2.3	SrCCH	175
7.5	Conclusions	176
	<i>References</i>	177

## LIST OF FIGURES AND TABLES

### *Figures*

2.1	Schematic diagram of experimental apparatus.	20
2.2	Schematic diagram of gas delivery system.	23
2.3	Laser ablation/photolysis fixture.	25
2.4	Schematic diagram showing the essence of a supersonic jet expansion.	28
2.5	LIF excitation spectra of the $A^2\Sigma^+ - X^2\Pi$ electronic transition of NO.	30
2.6	Structure of a continuous supersonic expansion.	32
2.7	Decay processes which can occur following an absorption transition.	35
2.8	Energy diagram showing the LIF process.	36
2.9	Energy diagram showing the DF process.	38
2.10	Schematic diagram of the Scanmate 2E dye laser.	42
2.11	Timing aspects of experimental synchronisation.	44
3.1	Illustration of low-lying electronic states of $\text{Sr}^+$ , $\text{SrF}$ and $\text{SrOH}$ .	48
3.2	Orbital shapes for the low-lying electronic states of $\text{CaF}$ .	51
3.3	Hund's case (a) and (c) in linear triatomic molecules.	57
3.4	Renner-Teller coupling in linear triatomic molecules.	60
3.5	$\Lambda$ -type doubling in $^2\Pi$ electronic states.	62
4.1	Jet-cooled LIF spectrum of the $\tilde{D}^2\Sigma^+ - \tilde{X}^2\Sigma^+$ transition of $\text{BaOH}$ .	69
4.2	Dispersed fluorescence spectra of the $\tilde{D}^2\Sigma^+ - \tilde{X}^2\Sigma^+ 0_0^0$ and $3_0^1$ bands.	70
4.3	Comparison of the energies of the known electronic states of $\text{BaF}$ and $\text{BaOH}$ .	72
4.4	Rotational contour and simulation of the $\tilde{D}^2\Sigma^+ - \tilde{X}^2\Sigma^+ 0_0^0$ transition.	74
4.5	Survey LIF scan of the $\tilde{C} - \tilde{X}$ region of $\text{BaOH}$ .	76
4.6	Dispersed fluorescence spectrum of the $\tilde{C}'^2\Pi_{1/2} - \tilde{X}^2\Sigma^+ 0_0^0$ transition.	79
4.7	Dispersed fluorescence spectra of the $20967\text{ cm}^{-1}$ transition.	80
4.8	Low-lying $\nu_2$ vibrational levels of ground state $\text{BaOH}$ .	82
4.9	Rotational contour and simulation of the $\tilde{C}'^2\Pi_{1/2} - \tilde{X}^2\Sigma^+ 0_0^0$ transition.	83
4.10	Orientations of the orbitals in the $\tilde{A}^2\Pi$ and $\tilde{C}^2\Pi$ states of $\text{BaOH}$ .	88
5.1	LIF spectrum showing the $\tilde{C}^2\Pi - \tilde{X}^2\Sigma^+$ system of $\text{SrOH}$ .	96
5.2	Comparison of the energies of electronic states of $\text{SrF}$ and $\text{SrOH}$ .	97

5.3	DF spectra of the $\tilde{C}^2\Pi_{1/2} - \tilde{X}^2\Sigma^+$ and $\tilde{C}^2\Pi_{3/2} - \tilde{X}^2\Sigma^+$ $0_0^0$ transitions.	99
5.4	Rotational contours of the bands centred at 27291 and 27315 $\text{cm}^{-1}$ .	101
5.5	Expanded view and simulation of the band centred at 27429 $\text{cm}^{-1}$ .	103
5.6	DF spectra of the bands at 27429 $\text{cm}^{-1}$ , 27522 $\text{cm}^{-1}$ and 27588 $\text{cm}^{-1}$ .	104
5.7	Rotational contours of the bands at 27522 $\text{cm}^{-1}$ and 27588 $\text{cm}^{-1}$ .	106
5.8	Correlation of the vibronic levels of a $^2\Pi$ electronic state.	109
5.9	Observed and predicted bands in the $\tilde{C}^2\Pi - \tilde{X}^2\Sigma^+$ system of SrOH.	112
5.10	LIF spectrum showing the $\tilde{B}'^2\Sigma^+ - \tilde{X}^2\Sigma^+$ system of SrOH.	115
5.11	Expanded view and simulation of the band at 25997 $\text{cm}^{-1}$ .	117
5.12	Dispersed fluorescence spectrum of the $\tilde{B}'^2\Sigma^+ - \tilde{X}^2\Sigma^+$ $3_0^1 2_0^1$ transition.	121
5.13	LIF spectrum of the $\tilde{D}^2\Sigma^+ - \tilde{X}^2\Sigma^+$ and $\tilde{E}^2\Sigma^+ - \tilde{X}^2\Sigma^+$ systems of SrOH.	122
5.14	DF spectra of the bands at 27698 $\text{cm}^{-1}$ , 28317 $\text{cm}^{-1}$ and 28956 $\text{cm}^{-1}$ .	124
5.15	Rotational contour and simulation of the $\tilde{D}^2\Sigma^+ - \tilde{X}^2\Sigma^+$ $0_0^0$ transition.	125
5.16	DF spectrum obtained by laser excitation of the band at 27422 $\text{cm}^{-1}$ .	129
5.17	Rotational contour and simulation of the $\tilde{E}^2\Sigma^+ - \tilde{X}^2\Sigma^+$ $3_0^2$ transition.	132
5.18	LIF spectrum of the $\tilde{F}^2\Pi - \tilde{X}^2\Sigma^+$ transition of SrOH.	133
6.1	Dispersed fluorescence spectrum of the $\tilde{A}^2\Pi_{1/2} - \tilde{X}^2\Sigma^+$ $0_0^0$ transition.	144
6.2	Dispersed fluorescence spectrum of the $\tilde{A}^2\Pi_{1/2} - \tilde{X}^2\Sigma^+$ $3_0^1$ transition.	146
7.1	Schematic diagram showing one colour (1+1) and (2+2) REMPI.	151
7.2	Schematic diagram of the apparatus used in REMPI experiments.	155
7.3	Schematic diagram illustrating the modified REMPI flange.	157
7.4	Schematic diagram illustrating two TOF spectrometer designs.	160
7.5	Illustration of the real-time $\text{NO}^+$ ion signal.	165
7.6	(1+1) REMPI and LIF spectra of the $\tilde{A}^2\Sigma^+ - \tilde{X}^2\Pi$ transition of NO.	166
7.7	Schematic diagram illustrating the deviation of the molecular beam.	169
7.8	Ion peaks due to various alkaline-earth metal-containing species.	174

## Tables

3.1	Spectroscopic constants in low-lying electronic states of CaF and CaOH.	50
3.2	Previously observed electronic states of the alkaline-earth monohydroxides.	52
3.3	Spin-orbit splitting constants in MF and MOH.	58



4.1	Molecular constants of BaOH and BaF.	85
5.1	Major vibronic bands in the 25990-28500 cm <sup>-1</sup> region and their assignments.	94
5.2	Comparison of the Sr-O and Sr-F stretching modes in SrOH and SrF.	98
5.3	Molecular constants for the $\tilde{X}^2\Sigma^+$ state of SrOH.	127
5.4	Comparison of experimental and calculated values of $\nu_2$ .	128
5.5	Comparison of experimental and calculated values of $\nu_3$ .	128
5.6	Summary of spectroscopic constants for the new electronic states of SrOH.	135
6.1	Vibrational frequencies of MgCCH in the ground $\tilde{X}^2\Sigma^+$ state.	147
7.1	Free radicals identified by various REMPI mechanisms.	152
7.2	Time-of-flight mass spectrometer specifications.	162

# *Chapter One*

## *Introduction*

## 1.1 *Introduction*

Very few chemical reactions proceed directly from reactant(s) to product(s). In most cases a reaction occurs via several elementary steps, each involving atomic or molecular chemical intermediates that are produced and consumed very rapidly during each stage of the reaction. Normally, the reaction must be initiated by 'activating' one, or more, of the bonds in the reactant and this may be achieved using heat or light, or by the use of catalysis to lower the activation energy of a key step. Unlike the starting reactant(s) or the end product(s), the chemical intermediates cannot be easily isolated. A clear distinction can be made between chemical intermediates and transition states in the profile of a chemical reaction. Chemical intermediates can be generally thought of as being extremely reactive, but physically stable, i.e. they correspond to energy minima on the potential surface of the reaction pathway. Transition states correspond to energy maxima (or more correctly, saddle points) on the potential surface which are physically unstable and are liable to undergo spontaneous decomposition. Many chemical intermediates contain one or more unpaired electrons and are, therefore, free radicals.

Free radical chemical intermediates play a crucial role in the outcome of many reactions and processes in all areas of chemistry, ranging from biochemical events and catalysis, through to combustion, atmospheric and even interstellar processes. Detection and physical characterisation of intermediates will inevitably lead to a fuller understanding of the intrinsic role they play in many chemical pathways. However, due to the high reactivity of intermediates in the majority of chemical reactions, their absolute concentrations are usually low. Historically, routine laboratory instruments, such as standard IR or UV/VIS spectrometers, have proved too insensitive to detect the low radical concentrations in chemical reactions. In the last two decades, more specialised spectroscopic techniques, often involving laser light sources, have made the study of free radicals much less difficult and are primarily responsible for the increased interest in these species, especially in the gas-phase. Laser-induced fluorescence (LIF) spectroscopy<sup>1</sup> is one of the most widely used methods for detecting radicals, although it does suffer from significant limitations. Other highly sensitive laser-based spectroscopic techniques are also important, examples of which include resonance-enhanced multi-photon ionisation (REMPI),<sup>2</sup> diode laser spectroscopy<sup>3</sup> and, most recently of all, cavity ringdown laser absorption.<sup>4</sup> Additionally, these techniques are often used to observe radicals that have been seeded, at low concentrations, into inert gas supersonic jets.

Supersonic jets<sup>5</sup> provide excellent environments for studying short-lived chemical species. Once introduced into this medium molecules will undergo very few collisions. Those collisions which do take place, which are mainly limited to the early stages of the expansion, occur with inert gas atoms and these have the effect of cooling the internal degrees of freedom of the molecules. The consequence of this is that spectra are considerably simplified in comparison with those recorded at room temperature, since fewer molecular energy levels have significant populations. For larger molecules, which may have very complex rotational and vibrational energy level manifolds, the simplification brought about by supersonic jet cooling is often an invaluable aid in spectroscopic analysis. A more detailed discussion of supersonic jets will be given in Chapter 2.

Laser-based spectroscopy can reveal important information concerning the bonding and structure of the intermediates, in addition to allowing real-time monitoring of their populations during chemical reactions. The latter can be an invaluable aid in elucidating reaction mechanisms of important environmental or industrial processes. Spectroscopic probing of intermediates can also reveal a wealth of information regarding the dynamics and kinetics of specific processes.

## 1.2 *Metal-containing free radicals*

Although the history of free radical studies is significant and interesting, the following discussion will concentrate on the development of techniques for studying and characterising *metal-containing* free radicals, since these are the target in the current work. Additionally, the discussion will concentrate solely on *gas-phase* work. Detailed accounts regarding the spectroscopy of metal-containing intermediates in low temperature matrices can be found in many excellent articles and theses, including references 6-9.

The interaction of metals with organic and inorganic molecules is of fundamental importance in many areas of chemistry, with perhaps the most notable areas being catalysis and synthetic organometallic chemistry. Of all the chemical syntheses that are carried out in the chemical industry, over two-thirds involve the use of a metal catalyst at some stage. Many catalytic processes involve cleavage of a carbon-carbon sigma bond, via insertion of a transition metal directly into the bond. Another extremely important

family of reactants, that are amongst the most versatile in organic chemistry, are Grignard reagents ( $\text{R-Mg-X}$ , where  $\text{R}$  = alkyl and  $\text{X}$  = halide).<sup>10</sup> Very often, the specific mechanisms of magnesium-carbon bond formation in reactions involving Grignard reagents are vague, or ambiguous. Clearly, identifying molecules that are likely to be involved in such mechanisms is important with respect to improving the efficiency of many organic syntheses.

The interaction of metal atoms with organic ligands has important implications for biochemistry. Many key biological functions include the formation and breaking of metal-carbon bonds. Examples include the role of metals, such as iron and magnesium, in haematology, or plant photosynthesis.<sup>11-12</sup> Another major area where metal-ligand interactions are vital is in the semiconductor industry. The optimum growth conditions (such as temperature and partial pressures of the precursors) for preparing semiconductor materials are essential. Gas-phase studies of the decomposition products and mechanisms of various organometallic semiconductor precursors ( $(\text{CH}_3\text{CH}_2)_3\text{Ga}$ ,  $(\text{CH}_3)_6\text{Si}_2$ , etc.) should result in more efficient methods for semiconductor preparation.<sup>13-14</sup> One of the keys to understanding these processes is to determine the nature of the metal-ligand interactions, and in particular to characterise the intermediates formed on decomposition and the manner by which the metal influences the dynamics and kinetics of the decomposition process.

Other areas of chemistry which involve important contributions from metal-containing radicals include combustion, atmospheric and interstellar chemistry. Initially, the combustion chemistry of metals attracted attention because of the intense colours that are observed when metals, or metal salts, are burned in flames. The mechanistic aspects of combustion chemistry involving metals are still relatively unknown since they are thought to involve highly complex radical reactions of metal monoxides and hydroxides.<sup>15</sup> More recent studies of metal combustion have tended towards elucidating the dynamical and kinetic aspects of these processes.<sup>16</sup>

Metal-containing radicals are thought to play significant roles in the complex chemistry of Earth's upper atmosphere.<sup>17</sup> The most important metals in this regard are iron, magnesium and sodium. The upper atmosphere chemistry of sodium is particularly interesting. Sodium, and many of its compounds, are highly reactive and undergo many reactions,

including those that are responsible for the sodium airglow. The basic mechanism for the sodium airglow (caused by emission from electronically excited sodium atoms ( $\text{Na } ^2P\text{-}^2S$  transition)), was first suggested by Chapman, in 1939,<sup>18</sup> as,



Although this may look like a relatively simple process, the specifics of the mechanism are still uncertain. The two lowest electronic states of NaO are very close together and both are energetically accessible in reaction (1.1). It is thought that the specific electronic state of the NaO formed in reaction (1.1) has significant consequences upon the Na formed in reaction (1.2). Laboratory-based studies involving characterisation of the electronic states of NaO should ultimately be useful in identifying the precise role of NaO in the Chapman mechanism.

Alkaline-earth metal-containing radicals are also thought to be involved in both atmospheric and interstellar chemistry. It has been speculated that the ablation of metals from meteors results in the formation of CaOH in the upper atmosphere.<sup>19</sup> Additionally, a number of alkaline-earth molecules should be present in the atmospheres of cool-oxygen rich stars.<sup>20</sup> Other metal-containing molecules, notably MgNC<sup>21-22</sup> and MgCN,<sup>23</sup> have been identified in the circumstellar envelope of the IRC+10216 carbon star. It is probably only a matter of time before many other metal-containing molecules are observed in stellar and interstellar space.

### 1.2.1 *Early studies of metal-containing radicals*

At the beginning of the 1980's, the vast majority of spectroscopic information pertaining to metal-containing species involved diatomic molecules. Indeed, all of the available experimental and theoretical information obtained before 1977 was collected together by Huber and Herzberg and published in their book, entitled 'Molecular spectra and molecular structure IV: Constants of diatomic molecules'.<sup>24</sup> This contains comprehensive data for all diatomics, not only metal-containing, derived from a wide variety of spectroscopic methods. Until 1975 the production of metal-containing diatomic molecules had been carried out via methods such as flash photolysis,<sup>25</sup> shock tubes,<sup>26</sup> exploding

wires,<sup>27</sup> arcs,<sup>28</sup> and in oxygen-hydrocarbon flames seeded with the appropriate metal compounds.<sup>15</sup> Spectra of molecules formed in these sources were often extremely congested due to the high internal rotational temperatures of the molecules.

Examples of spectroscopic probing of *polyatomic* metal-containing radicals were rare in the literature until the early 1980's. The first polyatomic derivatives of the alkaline-earth metals were studied by Herschel as far back as 1823,<sup>29</sup> when the monohydroxides were prepared in a flame environment and studied by emission spectroscopy. Significant flame emission studies were carried out by Charton and Gaydon, amongst others,<sup>15</sup> in the 1950's and 60's. They observed emission due to many metal-containing oxides and hydroxides, including BaOH, SrOH, SnOH, MnOH and Al<sub>2</sub>O<sub>3</sub>.

The introduction of the Broida oven in 1975<sup>30</sup> provided a simple method of preparing metal-containing diatomics, such as BaO, BaF, and FeO, with significantly lower internal temperatures (~500 K) than had been obtainable with previous production methods. Consequently, the quality of spectra were considerably enhanced in many cases using this technique. In a Broida oven, metal atoms are evaporated from a small ceramic crucible which is resistively heated using a tungsten wire basket. The vaporised metal atoms are entrained in a flowing inert carrier gas, such as argon or helium, which passes around the crucible. Molecular products are formed by mixing the metal vapour with an appropriate oxidising agent, a short distance above the crucible.

A key feature of the Broida oven is the large number of product molecules (10<sup>13</sup> molecules cm<sup>-3</sup>) that can be entrained into the carrier gas flow.<sup>31</sup> Also, since a significant number of product molecules are formed in electronically excited states, the method is ideally suited to optical emission spectroscopies. A chemiluminescent flame is often observed above the mixing region. However, although the technique works well for those metals which have a significant vapour pressure at temperatures below ~1000 K, the thermal insulation requirements of the Broida oven limit its use for metals with higher melting points. This is why, although investigations of many metal-containing diatomics were carried out using this method in the late 1970's and early 1980's, they were mainly limited to molecules involving the alkali and alkaline-earth metals.<sup>32-34</sup>

A new method for producing metal-containing diatomics, and simple polyatomics, of refractory metals was introduced by Trkula and Harris in 1982.<sup>35</sup> The technique is based

upon the well established method of hollow-cathode sputtering to produce metal atoms in the gas-phase.<sup>36</sup> However, the apparatus designed by Trkula and Harris, efficiently mixes metal atoms into a flow of inert carrier gas by passing it through the hollow cathode. The metal atoms are carried into a mixing region where an appropriate gas is injected to produce the metal-containing product. In a similar way to the Broida oven, a chemiluminescent flame is usually produced which can be probed via optical emission spectroscopy. The product molecules are produced at ambient rotational temperatures, ranging from 300-400 K. Early examples of molecules produced via this method include CuO, CuH and CuOH.<sup>37-39</sup> Indeed, this method is still used regularly to produce refractory metal-containing molecules, examples of which include AgO, FeH, TiH, and BeH.<sup>40-43</sup>

Another flow-type method for preparing metal-containing diatomics has been employed by several research groups and incorporates a combination of resistive heating and microwave discharge, or electron bombardment. A solid metal-containing salt is resistively heated in a crucible to create gas-phase molecules. The molecules are entrained into a flow of inert carrier gas, which may contain a gaseous precursor/reactant molecule. The gas mixture is then subjected to a microwave discharge, or electron bombardment, resulting in formation of the desired radical (among many other possible products). Again, this method is particularly suited to optical emission spectroscopy since the species are frequently produced in electronically excited states. A large number of, predominantly, diatomic metal-containing molecules have been produced by this method, including TiO, SrF, ScO and CoO.<sup>44-47</sup> For example, TiO was produced via resistive heating of  $\text{Ti}(\text{C}_5\text{H}_5)_2\text{Cl}_2$  in a tantalum furnace prior to microwave discharge in the presence of  $\text{O}_2$  and Ar.<sup>44</sup>

### 1.3 *Polyatomic metal-containing molecules*

One of the most significant moments in the study of *polyatomic* metal-containing radicals came with the discovery, by Harris and co-workers in 1983, that alkaline-earth monohydroxides and monoamides could be easily prepared in a Broida oven with relatively low internal temperatures ( $\sim 500$  K).<sup>48</sup> The molecules were formed by entraining metal atoms, produced via resistive heating of the appropriate alkaline-earth metal, into flowing argon. Water, or hydrazine, was injected into the gas flow several centimetres downstream of the heating source, resulting in a chemiluminescent flame containing MOH

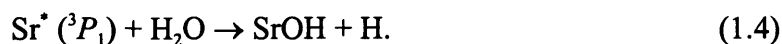


or  $\text{MNH}_2$  radicals. Initial experiments involved optical emission with subsequent studies involving laser-induced fluorescence spectroscopy.

Following the initial work of Harris and co-workers, the possibility of preparing other polyatomic metal-containing molecules in the Broida oven was immediately exploited by several other groups, particularly those of Bernath and, much later, Ziurys. In the period between 1984 and 1992 Bernath observed at least fifteen families of alkaline-earth ( $\text{M} = \text{Ca}, \text{Sr}, \text{Ba}$ ) containing molecules, including small molecules such as the monohydroxides ( $\text{MOH}$ ), monomethyls ( $\text{MCH}_3$ ), monoacetylides ( $\text{MCCH}$ ), monoamides ( $\text{MNH}_2$ ), monoisocyanides ( $\text{MNC}$ ), monoalkoxides ( $\text{MOR}$ ) and monothiolates ( $\text{MSH}$ ), along with larger molecules such as the monocyclopentadienyls ( $\text{MC}_5\text{H}_5$ ) and the monopyrrolates ( $\text{MC}_4\text{H}_4\text{N}$ ).<sup>49-68</sup> Bernath showed that for reactions of the type



laser excitation of the metal vapour to the metastable  $^3P_1$  electronic state, prior to injection of the oxidant, resulted in a significant increase in the concentration of the product molecule, via the accelerated reaction,



This is particularly important in the production of organometallic derivatives, such as  $\text{MC}_5\text{H}_5$ , which cannot be formed via reaction of ground state metal atoms with  $\text{C}_5\text{H}_6$  in the Broida oven.<sup>31</sup>

The majority of Bernath's studies involved LIF spectroscopy via the first and second excited states of most of the above molecules. While vibrationally-resolved spectra could often be obtained, rotationally-resolved spectra were far more difficult to acquire. The primary reason for this is that rotational congestion is generally a severe problem at  $\sim 500$  K. For small molecules, such as the metal monohydroxides, the rotational structure can be significantly simplified by using laser excitation with filtered fluorescence detection. However, for larger molecules, such as the alkaline-earth monocyclopentadienyls and monopyrrolates, rotationally-resolved spectra cannot be obtained by this route because of extensive collisional redistribution of excited state populations. Consequently, while most

of the small alkaline-earth containing molecules that have been prepared in a Broida oven have been subjected to rotational analysis, comparable studies on larger molecules are rare.

In 1994, a modified Broida oven spectrometer was designed in the Ziurys laboratory to enable pure rotational spectra of metal-containing radicals to be obtained in the 65-550 GHz range.<sup>69</sup> In the intervening years, the Ziurys group has provided millimetre/submillimetre rotational spectra for over fifteen metal-containing polyatomic free radicals, including metal monomethylidyne (MCH), metal monoacetylides (MCCH), metal monomethyls (MCH<sub>3</sub>), metal monoisocyanides (MNC) and metal monohydroxides (MOH).<sup>70-98</sup> The principle difficulty in modifying the Broida oven to facilitate pure rotational measurements is pressure broadening, since this dominates linewidths in the millimetre-wave region. To overcome this problem, superior pumping speeds are required in the source chamber of the oven.

#### 1.4 *Molecular beam and supersonic jet studies*

The obvious solution to the problems caused by relatively high temperatures is to prepare molecules in the ultracold environment of a supersonic jet. The use of continuous and pulsed supersonic jet expansions to facilitate rotational and vibrational simplification of gas-phase spectra (see Chapter 2) has been recognised since the late 1970's. Examples of radical production immediately prior to, or during the supersonic expansion, are commonplace in the literature. However, until the early 1980's, most examples involved inorganic, or organic, radicals that were produced by fragmentation of larger parent molecules. The usual methods of producing radical fragments included seeding of a suitable precursor into an inert carrier gas, followed by laser photolysis at the throat of the nozzle,<sup>99</sup> electrical discharge prior to or during the expansion,<sup>100</sup> or pyrolysis before the expansion.<sup>101</sup>

Unfortunately, these methods are rarely appropriate for making *metal-containing* species because of the lack of suitable precursors. A suitable precursor must not only possess a structure such that fragmentation of one, or more, bonds will yield the desired product, but it must also be reasonably volatile in order to obtain gas-phase species. At present, examples of metal-containing polyatomics which have been produced prior to, or during supersonic expansion by laser photolysis, electrical discharge or pyrolysis of a metal-

containing precursor, are quite rare. Notable exceptions include experiments carried out by the Miller and Ellis research groups in the early and mid-1990's, involving the  $\text{ZnCH}_3$ ,  $\text{ZnC}_2\text{H}_5$  and  $\text{CdCH}_3$  free radicals. Supersonically cooled  $\text{ZnCH}_3$ <sup>102-103</sup> and  $\text{ZnC}_2\text{H}_5$ <sup>103</sup> were both successfully prepared by Ellis and co-workers following electrical discharge of the appropriate gas-phase dialkyl-zinc precursor immediately prior to supersonic expansion. In a series of separate studies by Miller and co-workers  $\text{ZnCH}_3$ ,  $\text{CdCH}_3$  and their inert gas complexes, were prepared by laser photolysis of the respective dimethyl-metal precursors just after the supersonic nozzle.<sup>104-105</sup>

In order to produce a wider range of supersonically cooled metal-containing molecules, an alternative production method was required. In 1981, a seminal article by Smalley and co-workers described a new technique for creating small metallic clusters by laser ablation of a metal target prior to supersonic expansion.<sup>106</sup> The Smalley-type design is the basis for the laser ablation nozzle used in this work and is discussed more thoroughly in Chapter 2. Throughout the 1980's a significant number of articles were published by Smalley and co-workers involving the spectroscopy of many neutral, and ionic, small metal clusters, including  $\text{Cu}_2$ ,  $\text{Cr}_2$ ,  $\text{Mo}_2$ ,  $\text{Cu}_3$ ,  $\text{V}_2$ ,  $\text{Ni}_2$ ,  $\text{Si}_n^-$ ,  $\text{Al}_n^-$  and  $\text{GaAs}$ .<sup>107-118</sup> Bondybey and co-workers were also responsible for a wealth of information throughout the 1980's regarding gas-phase and matrix isolation studies of small metallic clusters prepared using the Smalley ablation nozzle.<sup>119-125</sup>

In 1990, the first examples involving the combination of supersonic cooling with laser ablation to produce non-cluster metal-containing polyatomic radicals was reported by Whitham *et al.*<sup>126</sup> These workers obtained LIF spectra of  $\text{CaCCH}$ ,  $\text{CaNC}$  and  $\text{CaNH}_2$  by this route. Whitham *et al.* proposed that calcium-containing molecules were created by insertion/elimination reactions of electronically excited calcium atoms (formed by laser ablation) with small organic and inorganic precursors, entrained into a pulse of helium or argon, 10-15 mm behind a supersonic nozzle. Laser ablation was carried out using the second harmonic of a Nd:YAG laser, operating at 532 nm.

The potential of laser ablation as a source of a diverse range of metal-containing molecules in the gas-phase cannot be understated. All metals, no matter how refractory, can be ablated with intense pulsed lasers. Indeed, since the first example of its use in 1981, a significant number of spectroscopic studies of supersonically-cooled metal-containing

radicals have been carried out using the technique. The Steimle group has produced many diatomic and polyatomic molecules, ranging from alkaline-earth containing species, such as  $\text{CaOCH}_3$  and  $\text{CaNH}_2$ , through to transition metal molecules, such as  $\text{YC}_2$  and  $\text{MoN}$ .<sup>127-130</sup> Other groups have also been successful. The groups of Simard and Hackett, based in Ottawa, regularly publish research articles involving metal-containing radicals prepared via laser ablation/photolysis, such as  $\text{YCCH}$ ,  $\text{LaF}$  and  $\text{NbS}$ .<sup>131-133</sup> The research groups of Bernath, Miller and Ellis have also published a number of articles describing the spectroscopy of supersonically cooled metal-containing molecules prepared by laser ablation/photolysis. Some of these include  $\text{SrOH}$ ,  $\text{LiO}$ ,  $\text{MgCCH}$ ,  $\text{CaC}_3\text{H}_5$ ,  $\text{MgCH}_3$ ,  $\text{Al}_2\text{O}$  and  $\text{CaNH}_2$ .<sup>134-140</sup>

To date, one group of metal-containing molecules that have not received much attention are polyatomic molecules containing d-block metals. Although a number have been mentioned above, e.g.  $\text{YCCH}$ , the list is reasonably short. Several studies, carried out in the research group of Merer, aptly illustrate the difficulties in interpreting the spectra of such molecules as  $\text{TiCH}$ ,  $\text{VCH}$ , and  $\text{WCH}$ .<sup>141-143</sup> Extreme congestion, due to the high density of electronic states, can lead to significant perturbations in the spectra of these molecules. Consequently, full band assignments can be extremely difficult to achieve.

Laser ablation does have drawbacks. Since it is usually combined with various forms of laser spectroscopy, multiple laser systems are required, including the ablation laser and one, or more, probe lasers. Consequently, the initial cost of setting up a laboratory is rather high. Another drawback is that the ablation process does not usually produce a clean source of metal-containing molecules. For example, experiments in the Ellis laboratory<sup>144</sup> have shown that laser ablation of calcium metal in the presence of acetone produces a number of metal-containing radicals including  $\text{CaCCH}$ ,  $\text{CaCH}_3$ ,  $\text{CaH}$ ,  $\text{Ca}_2$  and  $\text{CaOH}$ , in addition to other products such as  $\text{C}_3$ ,  $\text{CH}$  and  $\text{OH}$ . This can be a problem when using probe techniques such as laser-induced fluorescence spectroscopy, since all the above molecules possess strong LIF spectra, some of which overlap.

## 1.5 *This thesis*

The work presented in this thesis describes the results of several studies of small supersonically cooled alkaline-earth metal-containing polyatomic free radicals. These have been prepared by laser ablation and detected via laser-based electronic spectroscopy.

Chapter 2 presents an overall description of the experimental apparatus used to prepare, and subsequently detect, metal-containing species in the gas-phase. An introduction to several of the most important aspects of the experimental procedure are considered. Initially, details of the radical production method (laser ablation) are outlined, along with a discussion of supersonic cooling, followed by a description of two forms of laser-based electronic spectroscopy used to detect the radicals, namely laser-induced fluorescence (LIF) excitation and dispersed fluorescence (DF). Additionally, short descriptions of the specific laser systems are presented.

One of the major themes of this thesis involves the spectroscopic studies of alkaline-earth monohydroxides (MOH). A summary of former studies of these molecules is presented, along with a general discussion of their electronic structures, in Chapter 3.

The work discussed in Chapters 4 and 5 details the results of two studies involving alkaline-earth monohydroxides, namely BaOH and SrOH. Several previously unidentified electronic transitions have been observed for the first time in this work, using LIF spectroscopy. The majority of these new transitions are relatively simple, showing vibrational structure in only the metal-oxygen stretching vibration. However, both molecules have  $\tilde{C} - \tilde{X}$  transitions which show complex and unusual vibrational structure in their respective excitation spectra. Arguments are presented which attempt to account for this unusual structure, based upon the idea of the unpaired electron residing in a ‘reverse polarised’ metal-centred orbital interacting with the OH ligand.

The work discussed in Chapter 6 involves a dispersed fluorescence investigation of the ground ( $^2\Sigma^+$ ) state of MgCCH. The results of this study, along with those of a previous IR matrix isolation study, have now accounted for four out of the five fundamental vibrational frequencies of MgCCH.

Finally, Chapter 7 concludes with a description of several test experiments that have been performed using a newly constructed resonance-enhanced multi-photon ionisation time-of-flight mass spectrometer (REMPI-TOFMS). The introduction of this technique offers the prospect of recording mass-selected electronic spectra of metal-containing radicals, thereby removing any potential ambiguities over the spectral carrier.

## References

- 1 D.L. Andrews and A.A. Demidov (Ed.), *An Introduction to Laser Spectroscopy* (Plenum Press, New York, 1995)
- 2 M.N.R. Ashfold and J.D. Howe, *Ann. Rev. Phys. Chem.*, **45** (1994) 57
- 3 E. Hirota, *Pure Appl. Chem.*, **70** (1998) 1145
- 4 M.D. Wheeler, S.M. Newman, A.J. Orr-Ewing and M.N.R. Ashfold, *J. Chem. Soc. Faraday Trans.*, **94** (1998) 337
- 5 J.M. Hollas, *High Resolution Spectroscopy*, (Wiley, London, 1998)
- 6 A.M. Beardah, *Ph.D Thesis*, University of Leicester, 1999
- 7 B.J. Pollard, *Ph.D Thesis*, University of Leicester, 1999
- 8 R.J.H. Clark and R.E. Hester (Ed.), *Spectroscopy of Matrix-Isolated Species*, (Wiley, Chichester, 1989)
- 9 L. Andrews and M. Moskovits (Ed.), *Chemistry and Physics of Matrix-Isolated Species*, (Elsevier, North-Holland, 1989)
- 10 G.E. Coates, *Organometallic Compounds*, (Methuen, London, 1960)
- 11 A.V. Hoffbrand (Ed.), *Postgraduate Haematology*, (Butterworth/Heinemann, Oxford, 1999)
- 12 D. Grierson, *Plant Molecular Biology*, (Blackie, Glasgow, 1984)
- 13 A.S. Grady, R.E. Linney, R.D. Markwell, G.P. Mills, D.K. Russell, P.J. Williams and A.C. Jones, *J. Mater. Chem.*, **2** (1992) 539
- 14 D.K. Russell, I.M.T. Davidson, A.M. Ellis, G.P. Mills, M. Pennington, I.M. Povey, J.B. Raynor, S. Saydam and A.D. Workman, *Organometallics*, **14** (1995) 3717
- 15 A.G. Gaydon, *The Spectroscopy of Flames*, (Chapman and Hall, London, 1974)
- 16 J.M. Goodings, P.M. Patterson and A.N. Hayhurst, *J. Chem. Soc. Faraday Trans.*, **91** (1995) 2257
- 17 R.P. Wayne, *Chemistry of Atmospheres: An Introduction to the Chemistry of the Atmospheres of Earth, the Planets, and their Satellites*, (Clarendon Press, Oxford, 1991)
- 18 S. Chapman, *J. Astrophys.*, **90** (1939) 309
- 19 E. Murad, W. Snider and S.W. Benson, *Nature*, **289** (1981) 273
- 20 T. Tsuji, *Astron. Astrophys.*, **23** (1973) 411

- 21 K. Kawaguchi, E. Kagi, T. Hirano, S. Takano and S. Saito, *Astrophys. J.*, **403** (1993) L39
- 22 K. Ishii, T. Hirano, U. Nagashima, B. Weis and K. Yamashita, *Astrophys. J.*, **410** (1993) L43
- 23 L.M. Ziurys, A.J. Apponi, M. Guélin and J. Cernicharo, *Astrophys. J.*, **445** (1995) L47
- 24 K.P. Huber and G. Herzberg, *Molecular Spectra and Molecular Structure. IV. Constants of Diatomic Molecules* (Van Nostrand Reinhold, New York, 1979)
- 25 A.M. Bass, N.A. Keubler and L.S. Nelson, *J. Chem. Phys.*, **40** (1964) 3121
- 26 C.W. Von Rosenberg Jr. and K.L. Wray, *J. Quant. Spec. Rad. Trans.*, **12** (1972) 531
- 27 B. Rosen, *Nature*, **156** (1945) 570
- 28 R.K. Dhumwad and A.M. Bass, *Appl. Opt.*, **2** (1963) 1335
- 29 J.F.W. Herschel, *Trans. R. Soc. Edinburgh*, **9** (1823) 445
- 30 J.B. West, R.S. Bradford Jr., J.D. Eversole and C.R. Jones, *Rev. Sci. Instr.*, **46** (1975) 164
- 31 P.F. Bernath, *Science*, **254** (1991) 665
- 32 P.C.F. Ip, P.F. Bernath and R.W. Field, *J. Mol. Spec.*, **89** (1981) 53
- 33 P.F. Bernath, R.W. Field, B. Pinchemel, Y. Lefebvre and J. Schamps, *J. Mol. Spec.*, **88** (1981) 175
- 34 P.F. Bernath, B. Pinchemel and R.W. Field, *J. Chem. Phys.*, **74** (1981) 5508
- 35 M. Trkula, D.O. Harris and R.C. Hilborn, *Chem. Phys. Lett.*, **93** (1982) 345
- 36 R. Schlachta, V.E. Bondybey, G. Lask and S.H. Tsay, *Chem. Phys.*, **155** (1991) 267
- 37 T.C. Steimle, D.F. Nachman and D.A. Fletcher, *J. Chem. Phys.*, **87** (1987) 5680
- 38 R.S. Ram, P.F. Bernath and J.W. Brault, *J. Mol. Spec.*, **113** (1985) 269
- 39 M. Trkula and D.O. Harris, *J. Chem. Phys.*, **79** (1983) 1138
- 40 T.C. Steimle, M. Tanimoto, K. Namiki and S. Saito, *J. Chem. Phys.*, **108** (1998) 7616
- 41 D.M. Goodridge, R.T. Carter, J.M. Brown and T.C. Steimle, *J. Chem. Phys.*, **106** (1997) 4823
- 42 T.C. Steimle, J.E. Shirley, B. Simard, M. Vasseur and P. Hackett, *J. Chem. Phys.*, **95** (1991) 7179

- 43 C. Fosca, S. Firth, P.F. Bernath and R. Colin, *J. Chem. Phys.*, **109** (1998) 5795
- 44 T.C. Steimle and J.E. Shirley, *J. Chem. Phys.*, **91** (1989) 8000
- 45 Y. Azuma, W.J. Childs, G.L. Goodman and T.C. Steimle, *J. Chem. Phys.*, **93** (1990) 5533
- 46 W.J. Childs and T.C. Steimle, *J. Chem. Phys.*, **88** (1988) 6168
- 47 D.J. Clouthier, G. Huang, A.J. Merer and E.J. Friedmanhill, *J. Chem. Phys.*, **99** (1993) 6336
- 48 R.F. Wormsbecher, M. Trkula, C. Martner, R.E. Penn and D.O. Harris, *J. Mol. Spec.*, **97** (1983) 29
- 49 P.F. Bernath and S. Kinsey-Nielsen, *Chem. Phys. Lett.*, **105** (1984) 663
- 50 P.F. Bernath and C.R. Brazier, *Atrophys. J.*, **288** (1985) 373
- 51 C.R. Brazier, P.F. Bernath, S. Kinsey-Nielsen and L.C. Ellingboe, *J. Chem. Phys.*, **82** (1985) 1043
- 52 C.R. Brazier and P.F. Bernath, *J. Mol. Spec.*, **114** (1985) 163
- 53 S. Kinsey-Nielsen, C.R. Brazier and P.F. Bernath, *J. Chem. Phys.*, **84** (1986) 698
- 54 W.T.M.L. Fernando, M. Douay and P.F. Bernath, *J. Mol. Spec.*, **144** (1990) 344
- 55 R.A. Hailey, C.N. Jarman, W.T.M.L. Fernando and P.F. Bernath, *J. Mol. Spec.*, **147** (1991) 40
- 56 C.N. Jarman and P.F. Bernath, *J. Chem. Phys.*, **97** (1992) 1711
- 57 C.R. Brazier and P.F. Bernath, *J. Chem. Phys.*, **86** (1987) 5918
- 58 C.R. Brazier and P.F. Bernath, *J. Chem. Phys.*, **91** (1989) 4548
- 59 A.M.R.P. Bopegedera, C.R. Brazier and P.F. Bernath, *Chem. Phys. Lett.*, **136** (1987) 97
- 60 A.M.R.P. Bopegedera, C.R. Brazier and P.F. Bernath, *J. Mol. Spec.*, **129** (1988) 268
- 61 A.M.R.P. Bopegedera, C.R. Brazier and P.F. Bernath, *J. Phys. Chem.*, **91** (1987) 2779
- 62 L.C. Ellingboe, A.M.R.P. Bopegedera, C.R. Brazier and P.F. Bernath, *Chem. Phys. Lett.*, **126** (1986) 285
- 63 M. Douay and P.F. Bernath, *Chem. Phys. Lett.*, **174** (1990) 230
- 64 C.R. Brazier, L.C. Ellingboe, S. Kinsey-Nielsen and P.F. Bernath, *J. Am. Chem. Soc.*, **108** (1986) 2126
- 65 L.C. O'Brien, C.R. Brazier and P.F. Bernath, *J. Mol. Spec.*, **130** (1988) 33



- 66 W.T.M.L. Fernando, R.S. Ram, L.C. O'Brien and P.F. Bernath, *J. Phys. Chem.*, **95** (1991) 2665
- 67 L.C. O'Brien and P.F. Bernath, *J. Am. Chem. Soc.*, **108** (1986) 5017
- 68 A.M.R.P. Bopegedera, W.T.M.L. Fernando and P.F. Bernath, *J. Phys. Chem.*, **94** (1990) 4476
- 69 L.M. Ziurys, W.L. Barclay Jr., M.A. Anderson, D.A. Fletcher and J.W. Lamb, *Rev. Sci. Instr.*, **65** (1994) 1517
- 70 J. Xin and L.M. Ziurys, *J. Chem. Phys.*, **110** (1999) 4797
- 71 J. Xin and L.M. Ziurys, *Astrophys. J.*, **508** (1998) L109
- 72 A.J. Apponi, M.A. Brewster and L.M. Ziurys, *Chem. Phys. Lett.*, **298** (1998) 161
- 73 D.B. Grotjahn, A.J. Apponi, M.A. Brewster, J. Xin and L.M. Ziurys, *Angew. Chem.*, **37** (1998) 2678
- 74 J. Xin and L.M. Ziurys, *Astrophys. J.*, **501** (1998) L151
- 75 B.Z. Li and L.M. Ziurys, *Astrophys. J.*, **482** (1997) L215
- 76 B.P. Nuccio, A.J. Apponi and L.M. Ziurys, *Chem. Phys. Lett.*, **247** (1995) 283
- 77 M.A. Anderson and L.M. Ziurys, *Astrophys. J.*, **444** (1995) L57
- 78 M.A. Anderson and L.M. Ziurys, *Astrophys. J.*, **439** (1995) L25
- 79 J. Xin, J.S. Robinson, A.J. Apponi and L.M. Ziurys, *J. Chem. Phys.*, **108** (1998) 2703
- 80 M.D. Allen, T.C. Pesch, J.S. Robinson, A.J. Apponi, D.B. Grotjahn and L.M. Ziurys, *Chem. Phys. Lett.*, **293** (1998) 397
- 81 D.B. Grotjahn, T.C. Pesch, J. Xin and L.M. Ziurys, *J. Am. Chem. Soc.*, **119** (1997) 12368
- 82 B.Z. Li, J. Xin and L.M. Ziurys, *Chem. Phys. Lett.*, **280** (1997) 513
- 83 J.S. Robinson and L.M. Ziurys, *Astrophys. J.*, **472** (1996) L131
- 84 M.A. Anderson, J.S. Robinson and L.M. Ziurys, *Chem. Phys. Lett.*, **257** (1996) 471
- 85 M.A. Anderson and L.M. Ziurys, *Astrophys. J.*, **460** (1996) L77
- 86 M.A. Anderson and L.M. Ziurys, *Astrophys. J.*, **452** (1995) L157
- 87 J.S. Robinson, A.J. Apponi and L.M. Ziurys, *Chem. Phys. Lett.*, **278** (1997) 1
- 88 M.A. Anderson and L.M. Ziurys, *Chem. Phys. Lett.*, **231** (1994) 164
- 89 M.A. Anderson, T.C. Steimle and L.M. Ziurys, *Astrophys. J.*, **429** (1994) L41
- 90 L.M. Ziurys, D.A. Fletcher, M.A. Anderson and W.L. Barclay, *Astrophys. J. Supp. Ser.*, **102** (1996) 425

- 91 B.P. Nuccio, A.J. Apponi and L.M. Ziurys, *J. Chem. Phys.*, **103** (1995) 9193
- 92 P.R. Bunker, M. Kolbuszewski, P. Jensen, M. Brumm, M.A. Anderson, W.L. Barclay, L.M. Ziurys, Y. Ni and D.O. Harris, **239** (1995) 217
- 93 D.A. Fletcher, M.A. Anderson, W.L. Barclay and L.M. Ziurys, *J. Chem. Phys.*, **102** (1995) 4334
- 94 A.J. Apponi, W.L. Barclay and L.M. Ziurys, *Astrophys. J.*, **414** (1993) L129
- 95 M.A. Anderson, M.D. Allen, W.L. Barclay and L.M. Ziurys, *Chem. Phys. Lett.*, **205** (1993) 415
- 96 W.L. Barclay, M.A. Anderson and L.M. Ziurys, *Chem. Phys. Lett.*, **196** (1992) 225
- 97 M.A. Anderson, W.L. Barclay and L.M. Ziurys, *Chem. Phys. Lett.*, **196** (1992) 166
- 98 L.M. Ziurys, W.L. Barclay and M.A. Anderson, *Astrophys. J.*, **384** (1992) L63
- 99 M. Heaven, T.A. Miller and V.E. Bondeybey, *Chem. Phys. Lett.*, **84** (1981) 1
- 100 S. Sharp and P. Johnson, *Chem. Phys. Lett.*, **107** (1981) 35
- 101 J.R. Dunlop, J. Karolczak and D.J. Clouthier, *Chem. Phys. Lett.*, **151** (1988) 362
- 102 I.M. Povey, A.J. Bezant, G.K. Corlett and A.M. Ellis, *J. Phys. Chem.*, **98** (1994) 10427
- 103 S.J. Pooley and A.M. Ellis, *J. Mol. Spec.*, **185** (1997) 48
- 104 T.M. Cerny, X.Q. Tan, J.M. Williamson, E.S.J. Robles, A.M. Ellis and T.A. Miller, *J. Chem. Phys.*, **99** (1993) 9376
- 105 A.M. Ellis, E.S.J. Robles and T.A. Miller, *J. Phys. Chem.*, **97** (1993) 5809
- 106 T.G. Dietz, M.A. Duncan, D.E. Powers and R.E. Smalley, *J. Chem. Phys.*, **74** (1981) 6511
- 107 D.E. Powers, S.G. Hansen, M.E. Geusic, A.C. Puiu, J.B. Hopkins, T.G. Dietz, M.A. Duncan, P.R.R. Langridgesmith and R.E. Smalley, *J. Phys. Chem.*, **86** (1982) 2556
- 108 D.L. Michalopoulos, M.E. Geusic, S.G. Hansen, D.E. Powers and R.E. Smalley, *J. Phys. Chem.*, **86** (1982) 3914
- 109 J.B. Hopkins, P.R.R. Langridgesmith, M.D. Morse and R.E. Smalley, *J. Chem. Phys.*, **78** (1983) 1627
- 110 M.D. Morse, J.B. Hopkins, P.R.R. Langridgesmith and R.E. Smalley, *J. Chem. Phys.*, **79** (1983) 5316
- 111 P.R.R. Langridgesmith, M.D. Morse, G.P. Hansen, R.E. Smalley and A.J. Merer, *J. Chem. Phys.*, **80** (1984) 593

- 112 M.D. Morse, G.P. Hansen, P.R.R. Langridgesmith, L.S. Zheng, M.E. Geusic, D.L. Michalopoulos and R.E. Smalley, *J. Chem. Phys.*, **80** (1984) 5400
- 113 O. Cheshnovsky, S.H. Yang, C.L. Pettiette, M.J. Craycraft, Y. Lui and R.E. Smalley, *Chem. Phys. Lett.*, **138** (1987) 119
- 114 K.J. Taylor, C.L. Pettiette, M.J. Craycraft, O. Cheshnovsky and R.E. Smalley, *Chem. Phys. Lett.*, **152** (1988) 347
- 115 L. Lou, L. Wang, L.P.F. Chibante, R.T. Laaksonen, P. Nordlander and R.E. Smalley, *J. Chem. Phys.*, **94** (1991) 8015
- 116 D.E. Powers, S.G. Hansen, M.E. Geusic, D.L. Michalopoulos and R.E. Smalley, *J. Chem. Phys.*, **78** (1983) 2866
- 117 R.E. Smalley, *Ab. Pap. Am. Chem. Soc.*, **189** (1985) 115
- 118 C. Jin, K.J. Taylor, J. Conceicao and R.E. Smalley, *Chem. Phys. Lett.*, **175** (1990) 17
- 119 J.L. Gole, J.H. English and V.E. Bondybey, *J. Phys. Chem.*, **86** (1982) 2560
- 120 V.E. Bondybey and J.H. English, *Chem. Phys. Lett.*, **94** (1983) 11
- 121 M.C. Heaven, T.A. Miller and V.E. Bondybey, *J. Phys. Chem.*, **87** (1983) 2072
- 122 V.E. Bondybey, *Science*, **227** (1985) 125
- 123 L.A. Heimbrook, N. Chestnoy, M. Basanen, G.P. Schwartz and V.E. Bondybey, *J. Chem. Phys.*, **83** (1985) 6091
- 124 M.F. Cai, T.P. Dzugan and V.E. Bondybey, *Chem. Phys. Lett.*, **155** (1989) 430
- 125 R. Schlachta, I. Fischer, P. Rosmus and V.E. Bondybey, *Chem. Phys. Lett.*, **170** (1990) 485
- 126 C.J. Whitham, B. Soep, J-P. Visticot and A. Keller, *J. Chem. Phys.*, **93** (1990) 991
- 127 K.C. Namiki, J.S. Robinson and T.C. Steimle, *J. Chem. Phys.*, **109** (1998) 5283
- 128 A.J. Marr, M. Tanimoto, D. Goodridge and T.C. Steimle, *J. Chem. Phys.*, **103** (1995) 4466
- 129 T.C. Steimle, A.J. Marr, J. Xin, A.J. Merer, K. Athanassenas and D. Gillet, *J. Chem. Phys.*, **106** (1997) 2060
- 130 K.Y. Jung, D.A. Fletcher and T.C. Steimle, *J. Mol. Spec.*, **165** (1995) 448
- 131 H.P. Looock, A. Berces, B. Simard and C. Linton, *J. Chem. Phys.*, **107** (1997) 2720
- 132 B. Simard and A.M. James, *J. Chem. Phys.*, **97** (1992) 4669
- 133 B. Simard, C. Masoni and P.A. Hackett, *J. Chem. Phys.*, **92** (1990) 7003
- 134 M.S. Beardah and A.M. Ellis, *J. Chem. Phys.*, **110** (1999) 11244

- 135 A.M. Little, G.K. Corlett and A.M. Ellis, *Chem. Phys. Lett.*, **286** (1998) 439
- 136 G.K. Corlett, A.M. Little and A.M. Ellis, *Chem. Phys. Lett.*, **249** (1996) 53
- 137 E.S.J. Robles, A.M. Ellis and T.A. Miller, *J. Am. Chem. Soc.*, **114** (1992) 7171
- 138 R. Rubino, J.M. Williamson and T.A. Miller, *J. Chem. Phys.*, **103** (1995) 5964
- 139 M.F. Cai, C.C. Carter, T.A. Miller and V.E. Bondeybey, *J. Chem. Phys.*, **95** (1991) 73
- 140 Z. Morbi, C.F. Zhao, J.W. Hepburn and P.F. Bernath, *J. Chem. Phys.*, **108** (1998) 8891
- 141 M. Barnes, A.J. Merer and G.F. Metha, *J. Mol. Spec.*, **181** (1997) 168
- 142 M. Barnes, P.G. Hajigeorgiou, R. Kasrai, A.J. Merer and G.F. Metha, *J. Am. Chem. Soc.*, **117** (1995) 2096
- 143 M. Barnes, D.A. Gillett, A.J. Merer and G.F. Metha, *J. Chem. Phys.*, **105** (1996) 6168
- 144 A.M. Ellis, *private communication*

## *Chapter Two*

### *Experimental*

## 2.1 *Introduction*

The chemical intermediates studied in this work were prepared under supersonic jet conditions using a pulsed laser ablation/photolysis technique. Three types of pulsed laser-based spectroscopy were used to record electronic spectra, namely laser-induced fluorescence (LIF), dispersed fluorescence (DF) and resonance-enhanced multi-photon ionisation (REMPI). The experimental apparatus for REMPI will be discussed separately in Chapter 7.

This chapter will commence with a general description of the experimental apparatus used to prepare and, subsequently, observe the chemical species of interest. For experiments that deviated from this general description, specific details can be found in the relevant chapter. By considering the laboratory as three individual sections, a basic understanding of how experiments were performed can be established. Fig. 2.1 depicts how the separate constituents of a general experiment link together and illustrates the complexity of the laboratory. In order to gain a full working knowledge of the laboratory it is necessary to consider individual constituents in some detail and this will be covered below.

Constituents coloured *blue* in the diagram involve the first part of an experiment and may be broadly described as ‘radical production’. Radicals were routinely produced within an aluminium ablation fixture, prior to supersonic expansion into a vacuum chamber. The second part of an experiment (coloured *red*) involved directing a probe laser beam into the supersonic jet to excite electronic transitions within the molecular species. The final part of an experiment was concerned with the detection and recording of the spectroscopic transitions (coloured *green*).

## 2.2 *Radical production*

All of the laser ablation/photolysis experiments performed in this work were carried out under high vacuum conditions. The principal incentive for using such conditions arose from the physical requirements for attaining supersonic cooling (see section 2.2.4). However, a vacuum was also required in order to minimise reaction of the radical species with residual background gas molecules during the laser ablation process. The main experimental apparatus consisted of two vacuum chambers. Radical production and LIF experiments were carried out in the LIF chamber, labelled (1) in Fig. 2.1 and REMPI

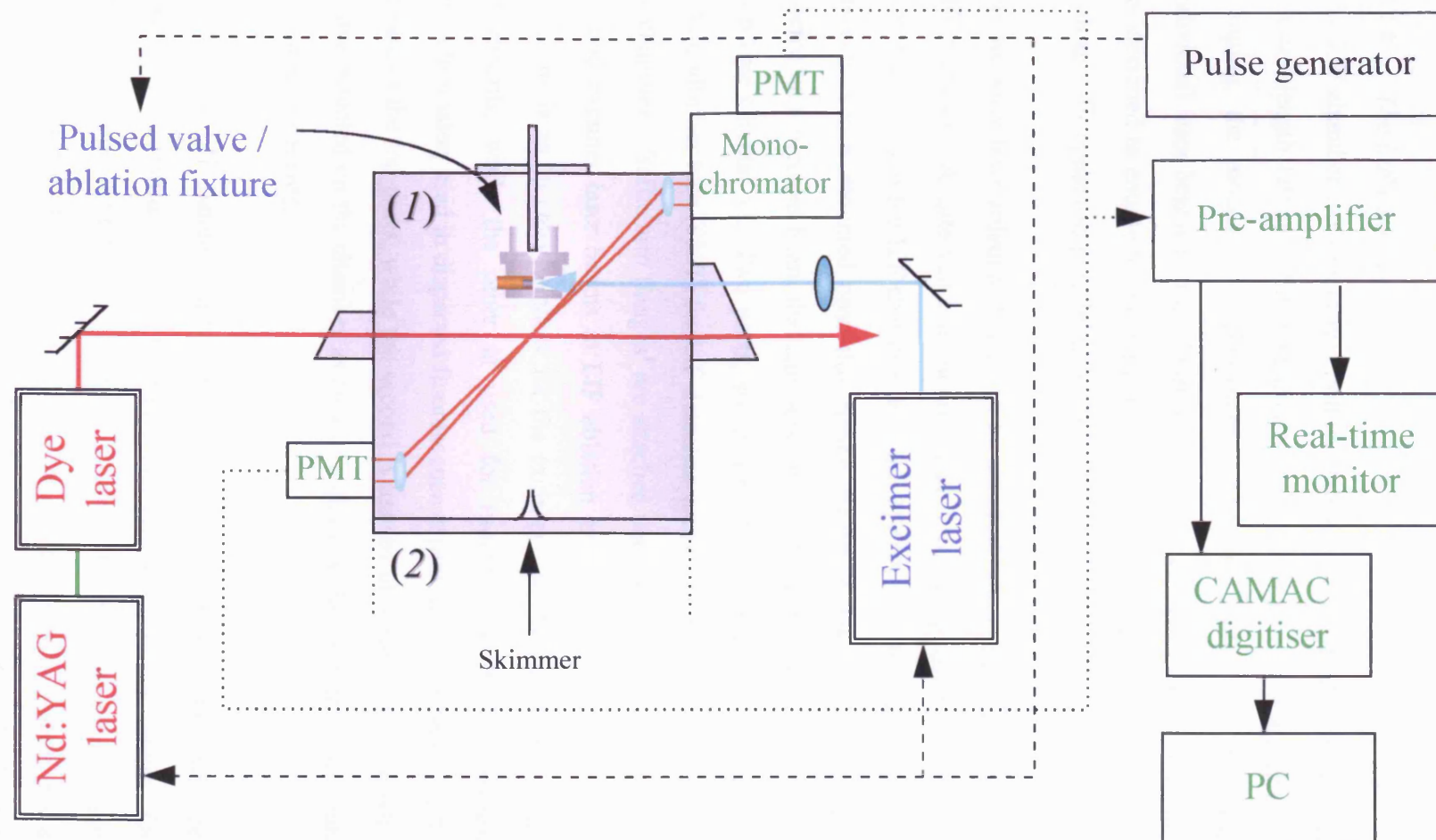


**Fig.2.1** Schematic diagram of experimental apparatus.

experiments were performed in the REMPI chamber, labelled (2) (but not shown in Fig. 2.1). A brief physical description of the LIF chamber will be outlined in this section, while a description of the REMPI chamber will be given in Chapter 7.

### 2.2.1 *The LIF chamber*

The LIF chamber is essentially a hollow stainless steel cylinder of external diameter 270 mm and length 410 mm. Situated around the chamber perimeter are nine ports for vacuum pumping, the mounting of fluorescence collection optics and for admission of the individual laser beams and the laser ablation fixture. All of the principal interface ports are designed to couple to standard stainless steel circular flanges (7.25" diameter), fitted with specific apparatus pertaining to the function of the port.

The working laser ablation flange can be attached, via a principal port, at one end of the LIF chamber. A gate-valve is incorporated into the opposite end of the chamber and allows isolation of the LIF chamber from the REMPI chamber during LIF experiments. A gas skimmer is mounted onto this flange, which is designed to produce a collimated supersonic molecular beam that can pass into the REMPI chamber when the gate-valve is open (see Chapter 7). Two ports, situated on the under side of the chamber, couple the photomultiplier tube (PMT) for LIF detection (see section 2.3.1) and the vacuum pumps to the chamber. Baffle arm flanges<sup>1</sup> are attached via two side ports and allow access for the dye and excimer laser beams in LIF ablation experiments. Of the two remaining side ports, one is as an entry window for the excimer laser beam when it is used in REMPI experiments, while the other is used for mounting a Pirani pressure gauge. A monochromator, used in dispersed fluorescence experiments (see section 2.3.2), is attached via one of the top ports, while the second is unused at present. Two small viewing ports are also situated on the chamber as an aid in aligning the excimer laser beam during laser ablation experiments.

The working LIF flange simply consists of a 0.25" diameter stainless steel tube that is passed, via a compression seal, through a stainless steel circular flange. On the vacuum side of the flange, the tube is connected to the pulsed valve/laser ablation fixture assembly, while the other end of the tube is connected to the gas delivery system (see section 2.2.3). All connections are made via Swagelok® fittings and a military style electrical connection adapter is attached to the flange to supply power to the pulsed valve.



The LIF chamber is pumped by a  $500 \text{ m}^3\text{h}^{-1}$  Leybold WAU501 roots pump, which in turn is backed by a  $40 \text{ m}^3\text{h}^{-1}$  Leybold Trivac D40B rotary pump. A resulting pressure of  $\sim 10^{-4}$  mbar, without gas load, can be routinely achieved using this configuration. As will be discussed in section 2.2.4, the pressure inside the vacuum chamber has a direct consequence upon the portion of the supersonic jet which can be usefully probed in an LIF experiment, namely the zone-of-silence. In a typical experiment, the distance from the end of the ablation fixture to the point of the dye laser probe, was in the region of 20 mm. Consequently, as will be seen later, a pressure of  $<1$  mbar was required to achieve a supersonic jet that could be spectroscopically probed well within the boundaries of the zone-of-silence.

### 2.2.2 Gas delivery

All of the radicals reported in this thesis were prepared directly from the reaction of organic, or small inorganic molecular fragments with metal atoms. An important requirement was to obtain sufficiently high concentrations of molecular radicals within the jet environment, while maintaining good cooling conditions. In a typical experiment the precursor was seeded into a high pressure inert carrier gas, such as 6-10 bar argon or helium, in ratios ranging from 0.1-5%. Fig. 2.2 illustrates the system that was used to prepare the precursor/carrier gas mixtures and deliver them to the pulsed valve. The apparatus can be considered as two distinct systems. Liquid precursor samples could be introduced into the inert gas via the system labelled *A* in the diagram, while gaseous precursor mixtures could be prepared via the system labelled *B*.

For experiments which involved the use of liquid precursors, gaseous mixtures could be attained by flowing carrier gas above the liquid precursor. All liquids possess a temperature related vapour pressure and this could be routinely exploited to prepare low concentration precursor/carrier gas mixtures. In many experiments the vapour pressure of a specific liquid was controlled using cold baths. An appropriate volume of liquid precursor was placed in the sample vessel. The entire gas delivery line could be evacuated via bypass valve 10, linking it to the main LIF chamber. In order to evacuate the sample vessel, without losing the liquid precursor, liquid nitrogen was used to freeze the liquid prior to the vessel being opened to vacuum. Carrier gas could be introduced to the system, via valves 1, 3, 4 and 5, with all other valves remaining closed. For experiments in which a precursor was not required, carrier gas could be directed to the pulsed valve via valve 2.

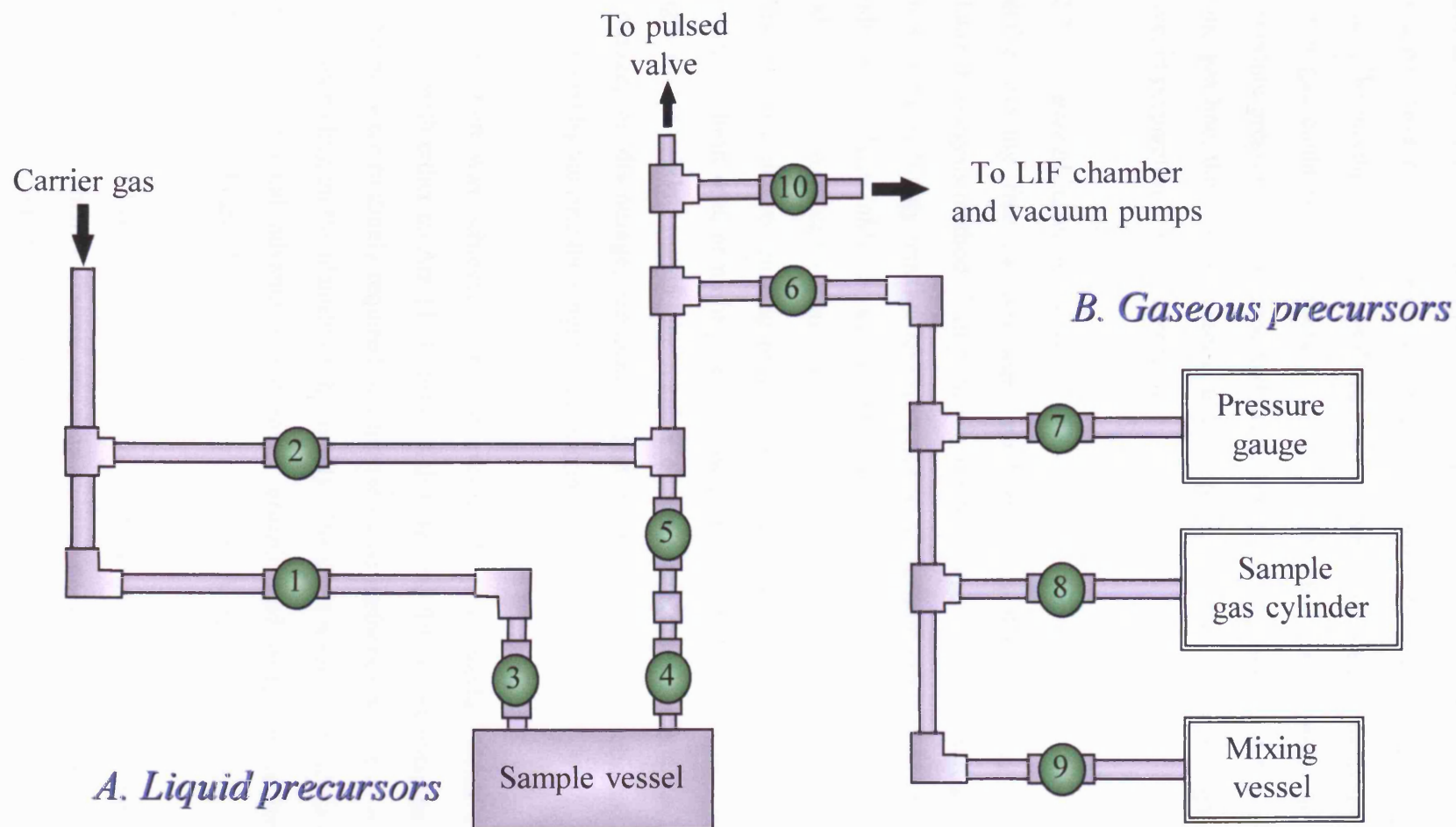


**Fig.2.2** Schematic diagram of gas delivery system. Valves are numbered and coloured in green.

In experiments involving gaseous precursors, gas premixtures were prepared in the section of the gas line, labelled *B*. Following evacuation of the gas line, the part of the system required for preparing gas mixtures was isolated using valve 6 and gaseous precursor could be introduced into the isolated system, via valve 8. With the desired pressure in the system, the mixing vessel was isolated, using valve 9, and the gas line could be evacuated. Carrier gas could be subsequently introduced into the mixing vessel until the desired premixture pressure was reached and the vessel could be isolated. After final evacuation of the gas line, the mixing vessel could be opened to allow passage of gas to the pulsed valve, in preparation for an experiment.

### 2.2.3 *Laser ablation/photolysis*

Metal-containing free radicals were synthesised, in the gas-phase, using the laser ablation/photolysis method.<sup>2,3</sup> In principle, the technique involves simultaneously creating two sources of highly reactive species prior to supersonic expansion. Metal atoms are produced by *laser ablation* of an appropriate metal target. Molecular fragments are produced via *photolysis* of an appropriate molecular precursor. Through subsequent collisions, in a defined mixing region, the metals atoms and photolysis fragments can combine to form one, or more products, including the desired radicals. By varying the length of the mixing region, the number of pre-expansion collisions can be altered to encourage, or discourage, reactions. The extent of rotational cooling can also be manipulated by varying the length of the mixing region.

Laser ablation was achieved using an excimer laser (Lambda Physik Compex 100) operating with either an ArF (193 nm) or KrF (248 nm) fill. Pulse energies ranging from 10-150 mJ were routinely required to vaporise metal surfaces (the actual optimum pulse energy depending on the identity of the metal). The short wavelength of the excimer laser gives the additional advantage that many organic and inorganic molecules can be photolysed by the beam, thereby potentially creating new reaction channels.

Fig. 2.3 shows a schematic diagram of the aluminium fixture used in the laser ablation experiments. The ablation fixture, which is screwed on to the faceplate of a pulsed valve (General Valve Series 9), is 45 mm in length and incorporates a 2 mm diameter flow channel that passes through its central axis. In a typical experiment, a metal sample was

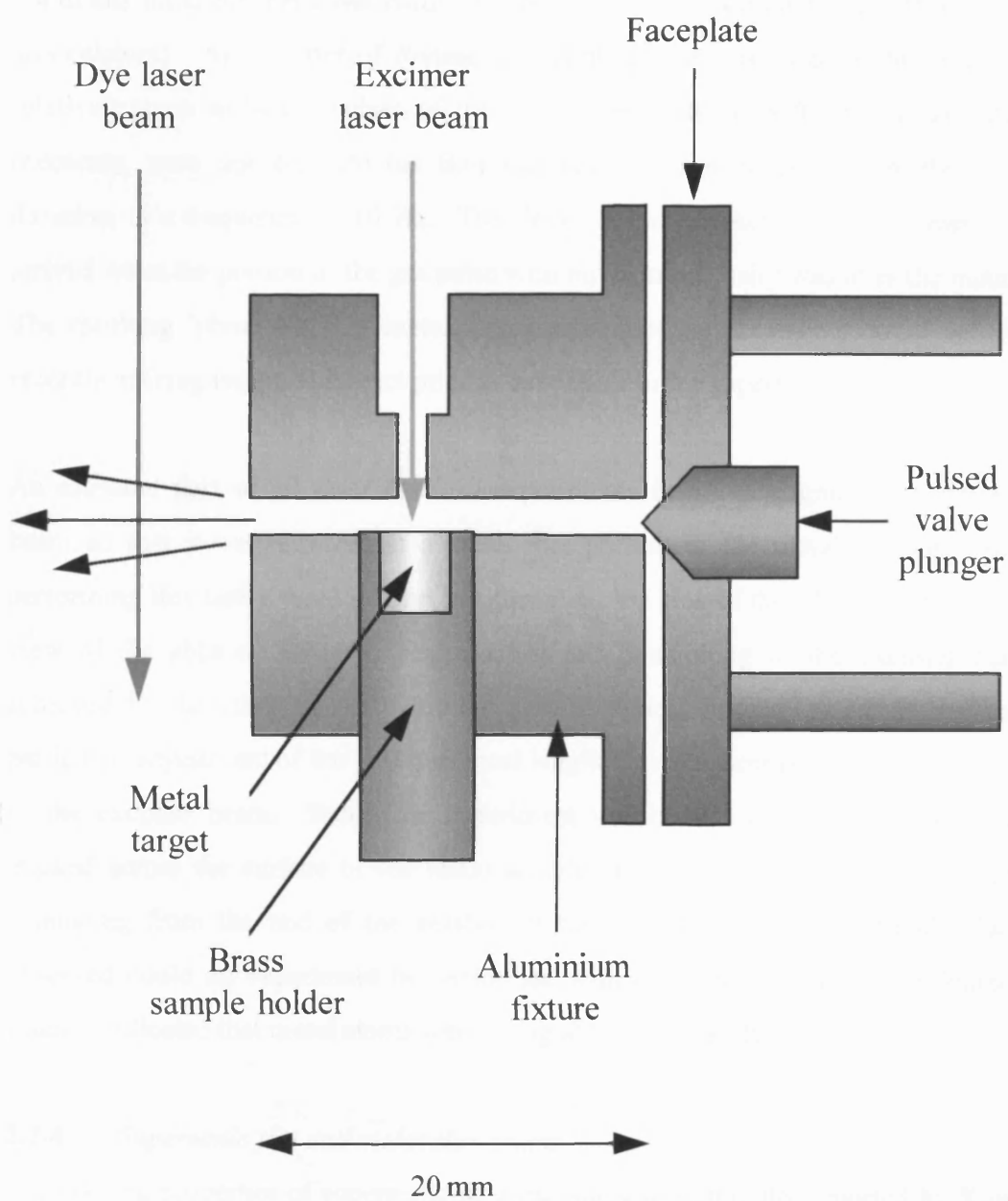


**Fig. 2.3** Laser ablation/photolysis fixture.

positioned near to the exit orifice of the fixture such that its end protruded slightly into the central channel. Some metal targets could be purchased as 6 mm diameter rods and these were clamped in the fixture without any further manipulation. For soft metals which were not in this form, the metal was hammered into a 6 mm brass holder (*e.g.* barium, strontium and calcium). As a matter of routine the metal sample was filed to obtain a clean and relatively even surface. Pulses of the carrier gas, with or without a small amount of precursor, were injected into the flow channel in pulses ranging from 300 to 700  $\mu$ s duration, at a frequency of 10 Hz. The firing of the excimer laser was timed so that it arrived when the portion of the gas pulse with maximum density was over the metal target. The resulting 'plume' of hot metal atoms and precursor fragments could subsequently enter the mixing region and react prior to expansion in the supersonic jet.

An essential part of all laser ablation experiments involved aligning the excimer laser beam so that it was directed at a clean, flat portion of the metal surface. To aid in performing this task a window port is situated on the side of the LIF chamber to enable a view of the ablation fixture. Fine control and positioning of the excimer beam was achieved by directing its path through several optics situated on an optical rail.<sup>1</sup> In particular, adjustment of the 700 mm focal length lens was normally used for fine steering of the excimer beam. Before an experiment was carried out, the excimer beam was tracked across the surface of the metal sample until a luminesce 'flame' was observed emanating from the end of the ablation fixture. Only when a reasonable flame was observed could an experiment be performed with confidence, since the coloured flame usually indicated that metal atoms were being ablated successfully.

#### 2.2.4 *Supersonic jets and molecular beams*

The cooling properties of supersonic jet expansions were initially reported by Kantrowitz and Grey in 1948.<sup>4</sup> It was recognised that the supersonic jet environment provides a source of extremely cold internal rotational and translational temperatures within an expanding jet of molecules. In a subsequent paper, Kistiakowsky and Slichter alluded to the importance of the supersonic expansion for investigating certain molecular energy levels in which there was an increase in population of states of low internal energy.<sup>5</sup> A great deal of early research using supersonic jets involved investigation of the dynamics of chemical reactions, since this took advantage of the narrow translational velocity

distribution that supersonic jets confer. Spectroscopic applications of supersonic jets were less common until it was recognised that jet cooling could be exploited to simplify molecular spectra. Band origins, vibrational progressions and rotational structure can be much more readily identified due to the depopulation of rotational, and often vibrational, energy levels.<sup>6</sup> However, until the early 1970's, the majority of molecular spectroscopy had dealt with stable molecules that could be identified using slow detection techniques. It was later recognised that supersonic jets provide an excellent environment for the preservation of short-lived species, although spectroscopic observation was difficult until lasers became commercially available. The field of supersonic jet free radical spectroscopy has rapidly expanded in recent years and, at present, is one of the most important areas of spectroscopic research.<sup>7</sup>

Fig. 2.4 shows the essence of a supersonic jet expansion. A high pressure gas reservoir is separated from a region of high vacuum by a small nozzle, or orifice. The orifice is usually circular, although slit nozzles have also been used.<sup>8</sup> A subtle, but very important, distinction can be made between the two types of jet that can be obtained by passing gas through a nozzle into vacuum. If the mean free path,  $\lambda_0$ , for molecular collisions passing through the nozzle, is much greater than the nozzle diameter, then few, if any, collisions will occur in, or beyond the nozzle. This type of jet is referred to as an effusive jet and offers little, or no molecular cooling. Conversely, if the mean free path is much smaller than the nozzle diameter, molecular collisions are abundant as the gas passes through the nozzle. The random Maxwellian distribution of molecular velocities that occurs in the reservoir gas is, consequently, converted to directed flow away from the nozzle, with a very narrow distribution of velocities. As a result, the translational temperature of the expanding gas can be lowered to as little as 1 K. This type of jet is referred to as a supersonic jet.<sup>6</sup>

Molecular collisions in the nozzle region also have profound cooling effects on the rotational and vibrational temperatures within the expanding gas. Fig. 2.4 shows the typical number of collision that have occurred, as a function of distance from the nozzle, in a typical expansion.<sup>7</sup> Collisions have almost ceased at a distance of sixty nozzle diameters from the end of the nozzle, at which time around one hundred collisions have occurred. Generally, the transfer between internal rotational energy of a molecule to translational energy is very rapid, although this is strongly dependent on the identity of the molecule.

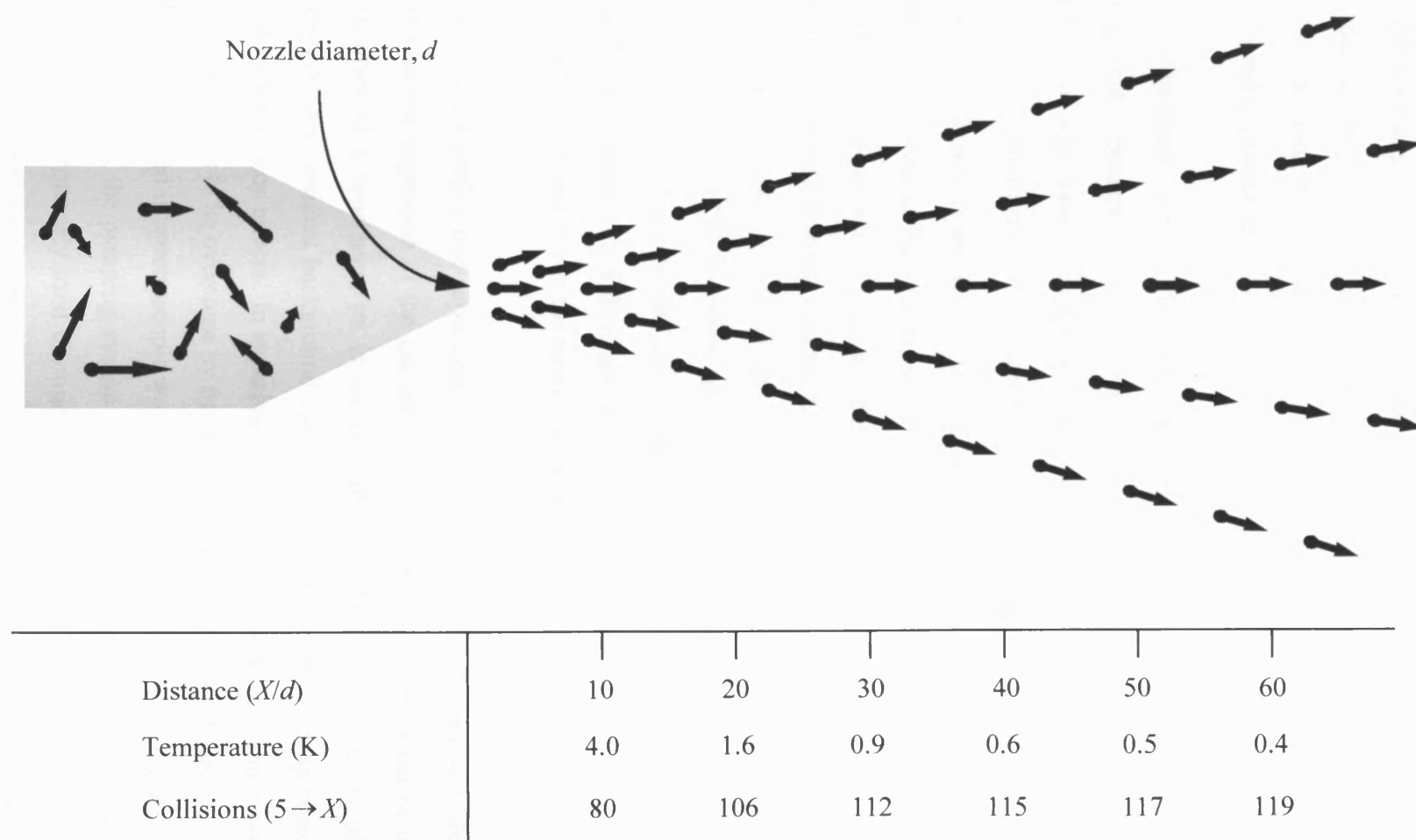


**Fig.2.4** Schematic diagram showing the essence of a supersonic jet expansion.

Clearly, the efficiency of this transfer can be extremely high and, consequently, molecular rotational temperatures as low as 1 K are attainable in supersonic jets. Transfer of vibrational energy is greatly dependent upon the nature of the molecular vibrations, but in general around one hundred collisions are required to transfer one quantum of vibrational energy to translational energy. The efficiency of this process will be less than that for rotational transfer, and typical vibrational temperatures of 100 K, or lower, are often achieved in supersonic jets.

The advantages to molecular spectroscopy that supersonic cooling offers are extremely important. Spectra involving complex vibrational and rotational structure, normally associated with room temperature, or warmer molecules, can be greatly simplified under supersonic conditions. This point is aptly illustrated in Fig. 2.5. Two laser-induced fluorescence spectra are shown for the  $A^2\Sigma^+ - X^2\Pi$  electronic transition of NO. The spectrum, shown in Fig. 2.5(a), was collected from a room temperature sample of NO contained in a gas cell. A large number of spectral lines are evident in the spectrum, with many overlapping features causing the spectrum to appear highly congested. Simulation of the rotational structure in the spectrum shows the rotational temperature to be around 300 K. A second LIF spectrum, shown in Fig. 2.5(b), was recorded in a supersonic jet containing 1% NO in a helium carrier gas. Clearly, the spectrum appears to be extensively simplified and relatively little rotational structure is observed. Simulation of the rotational structure in this case shows the rotational temperature was  $\sim 15$  K.

In practice, a perfect free supersonic jet expansion can never be realised, since to achieve this requires expansion of the gas into a perfect vacuum. The extent of the favourable properties of a supersonic jet is clearly linked to the pumping speed of the vacuum pump(s). Any residual background gas will severely disrupt the properties of the jet by creating turbulence effects. In experiments that employ continuous supersonic expansions this problem has to be overcome by using fast pumping systems. Pulsed nozzle supersonic jets are often used in spectroscopic work when pulsed lasers are employed, and in this case the demands on the pumping system are much less strenuous. This type of supersonic expansion was routinely used throughout the work described in this thesis. It has been shown that pulsed nozzle supersonic jets can often lead to superior rovibrational cooling than corresponding continuous jets.<sup>9</sup>



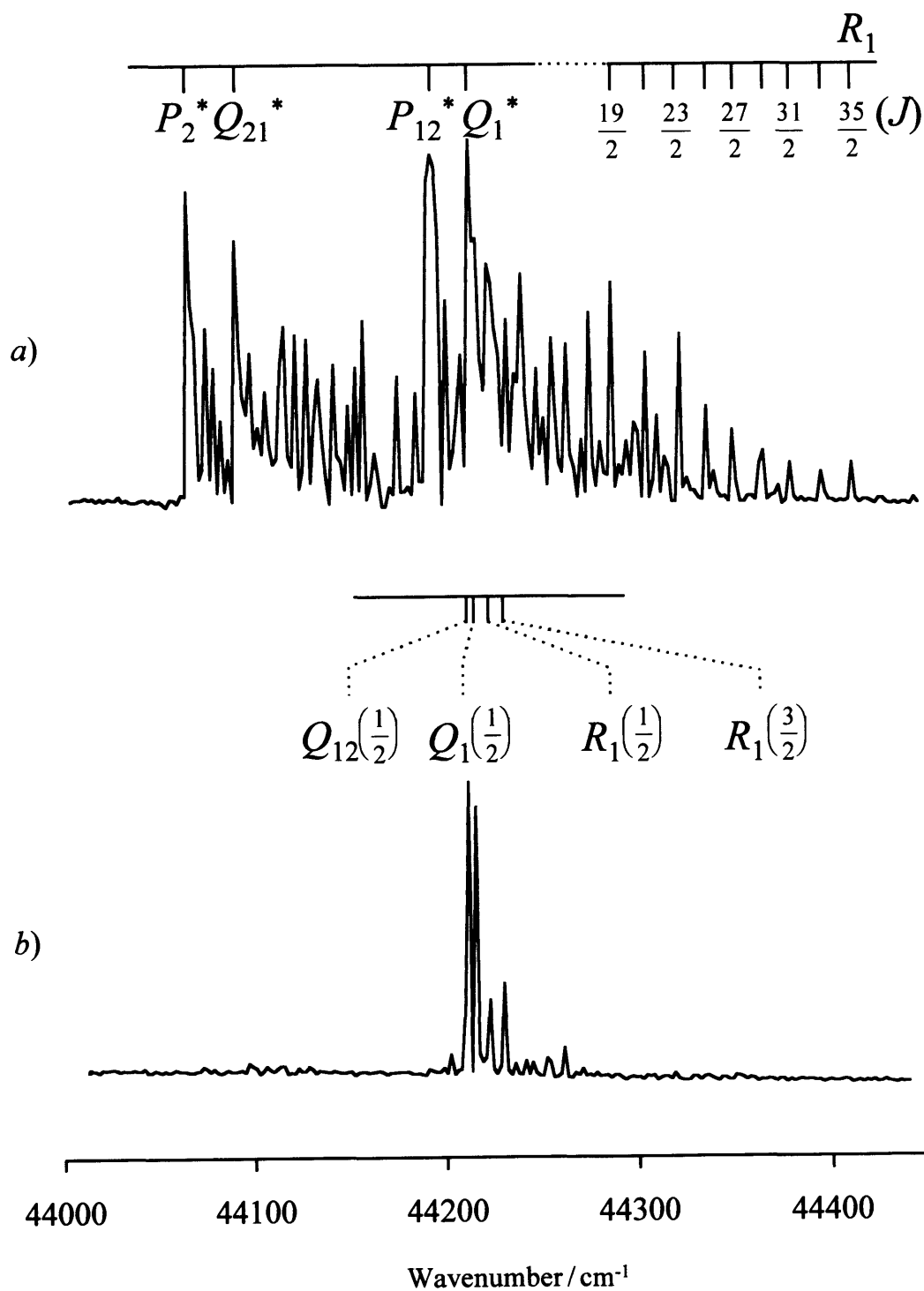


**Fig. 2.5** The LIF excitation spectrum of the  $A^2\Sigma^+ - X^2\Pi$  electronic transition of NO at a) a rotational temperature of  $\sim 300$  K, and b) after supersonic cooling to a rotational temperature of  $\sim 15$  K. The asterisks in a) identify  $P$  and  $Q$  branch bandheads.

The Mach number,  $M$ , of a flowing gas is given by,

$$M = \frac{u}{a} \quad (2.1)$$

where  $u$  = mass flow velocity and  $a$  = the local speed of sound. Since  $a$  varies with the square root of the translational temperature,  $T_{\text{trans}}$ , Mach numbers well in excess of unity can easily be obtained because of the dramatic translational cooling in the supersonic expansion.<sup>6</sup>

As the gas expands away from the nozzle region the velocities of gas molecules begin to exceed the speed of sound (Mach 1). A shock wave is formed around the jet when the cold, expanding gas collides with ‘warm’ residual gas in the chamber. The region of the supersonic jet, in which the intrinsic cooling properties are maintained, is defined by the so-called barrel shock and Mach disk. Fig. 2.6 illustrates the principal regions and dimensions of the expanding jet.<sup>10</sup> The distance of the Mach disk from the nozzle is extremely important in spectroscopic applications of supersonic jets, since it is important to probe the jet before the Mach disk is reached. Bier and Schmidt<sup>11</sup> characterised the dimensions of the barrel shock and Mach disk for a continuous supersonic jet in 1961. An approximate value for the nozzle-Mach disk distance can be calculated from,

$$x_M = 0.67d \left( \frac{p_0}{p_c} \right)^{1/2} \quad (2.2)$$

where  $d$  is the diameter of the nozzle,  $p_0$  is the stagnation pressure of the gas behind the nozzle and  $p_c$  is the background pressure in the chamber. For a pulsed supersonic jet expansion, the value for  $p_c$  is taken as an average over all pulses. As a result, an overestimate of  $x_M$  will be obtained, since the value of  $p_c$ , per pulse, will inevitably be higher than the average. Typically, experimental values for  $d$ ,  $p_0$  and  $p_c$  (average) were 2 mm, 6 bar and  $\sim 10^{-1}$  mbar, respectively, yielding a nozzle-Mach disk distance of  $\sim 300$  mm. Taking averaging into account, a more realistic value for  $x_M$  would probably be on the order of 100–200 mm. In all experiments the jet was probed 20–30 mm downstream of the nozzle, falling well within the boundaries of the zone-of-silence.

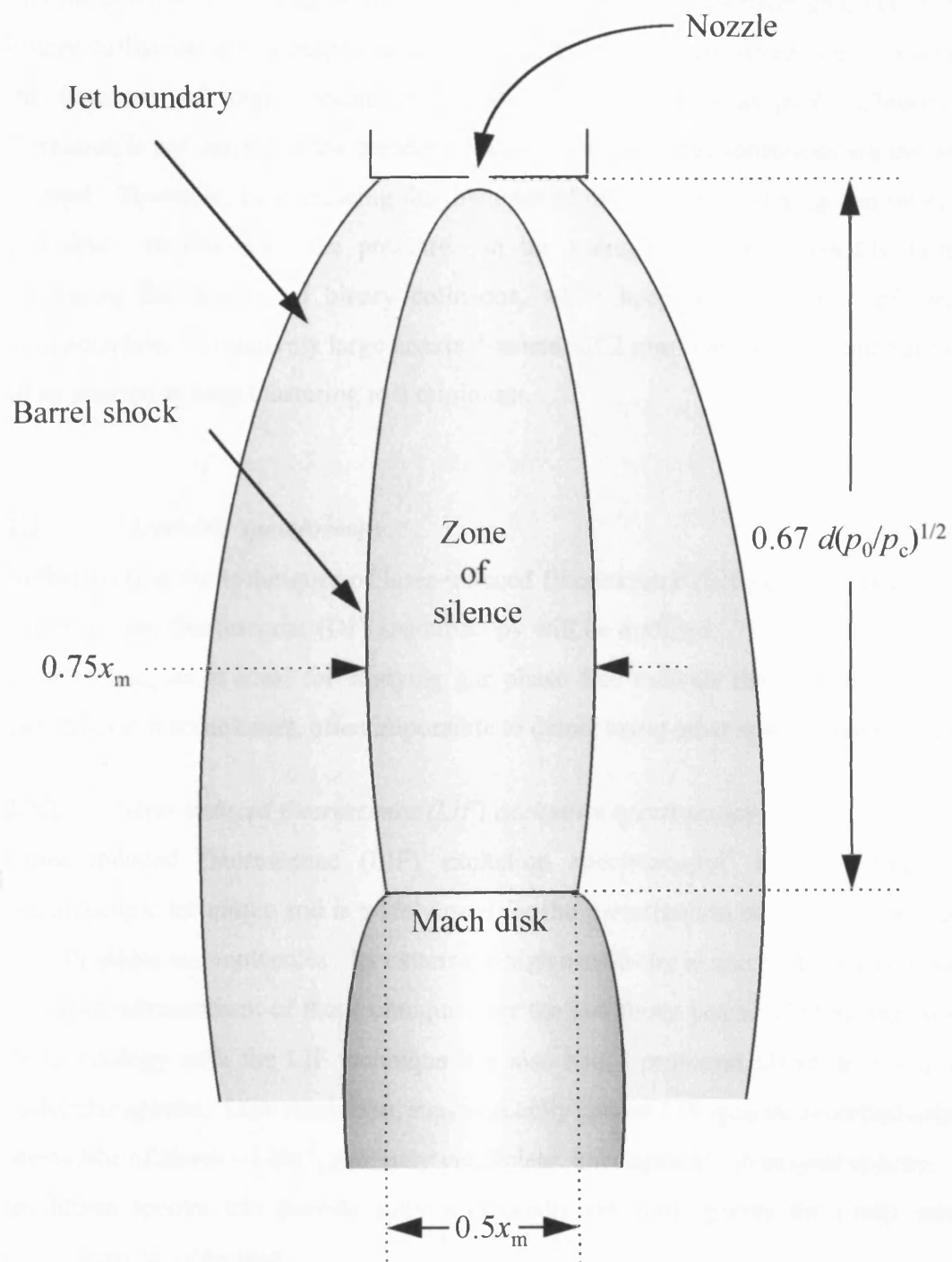


**Fig. 2.6** Structure of a continuous supersonic expansion, emanating from a circular nozzle.<sup>8</sup>

A final consideration must be given to the diameter of the circular nozzle. Kuth reported that the supersonic cooling of molecules, seeded into an inert carrier gas, occurs through binary collisions and is proportional to  $p_0 d$ .<sup>12</sup> Three-body collisions are accountable for the formation of weakly-bound molecular clusters and vary as  $p_0^2 d$ . Clearly, cluster formation is not desired in the present work, since unperturbed molecules are the source of interest. Therefore, by increasing the diameter of the nozzle, clustering can be made less probable. In this way, the pressure can be maintained at a reasonably high level, increasing the number of binary collisions, while keeping the number of three-body collisions low. A relatively large nozzle diameter of 2 mm was used throughout this work in an attempt to keep clustering to a minimum.

## 2.3 *Electronic spectroscopy*

In this section the techniques of laser-induced fluorescence (LIF) excitation spectroscopy and dispersed fluorescence (DF) spectroscopy will be outlined. The extreme sensitivity of these techniques is ideal for studying gas phase free radicals that would, otherwise, be difficult, or in some cases, often impossible to detect using other spectroscopic techniques.

### 2.3.1 *Laser induced fluorescence (LIF) excitation spectroscopy*

Laser induced fluorescence (LIF) excitation spectroscopy<sup>13</sup> is a relatively simple spectroscopic technique and is widely used for the investigation of optically excited states in both atoms and molecules. Its extremely high sensitivity is one of the major reasons for the rapid advancement of this technique over the last thirty years. Combining supersonic jet technology with the LIF technique has also had a profound effect on the quality of molecular spectra. Low resolution, supersonically cooled LIF spectra, recorded using laser linewidths of above  $\sim 1 \text{ cm}^{-1}$ , routinely yield clear, uncongested vibrational spectra. Higher resolution spectra can provide fully rotationally resolved spectra for many small and medium sized molecules.

In principle, any molecule can absorb a photon of light, resulting in promotion to a higher energy electronic state. Conventional absorption techniques observe molecular absorption by monitoring the decrease in light intensity on passage through a sample of molecules. A limitation is imposed on this technique by the ability of the detector to observe small changes in light intensity. Clearly, if a laser was used as the light source in such an experiment, small changes in the high laser intensity would be difficult to detect.

Laser induced fluorescence relies on the ability of an excited electronic state to decay via spontaneous emission of a photon. Fluorescence is clearly a marker of the initial absorption process and its detection is therefore an indirect observation of molecular absorption. One negative aspect of LIF spectroscopy is that not all excited states decay radiatively. Fluorescence spectroscopy will suffer if other decay processes have a rate comparable to, or greater than spontaneous emission. Fig. 2.7 illustrates the different decay processes that can potentially occur following absorption of a photon.

In this work, the laser beam from a tunable dye laser (Lambda Physik Scanmate 2E) was directed into the emerging supersonic expansion, 20–30 mm downstream from the end of the laser ablation fixture. In a typical experiment, the laser wavelength was scanned until it corresponded with the energy difference between two molecular energy levels. At these wavelengths absorption of a laser photon could occur, promoting the molecule to an excited electronic state. Fluorescence at many wavelengths can occur following excitation corresponding to decay to various rovibrational levels in lower lying electronic states, including the ground state. Fig. 2.8 illustrates the absorption and fluorescence processes involved in LIF spectroscopy. Since the fluorescence is observed as a means of monitoring an absorption process, the *total* fluorescence can be detected. Fluorescence was collected, perpendicularly to the laser beam, via a f/1.5 lens and imaged onto a Hamamatsu R562 photomultiplier tube (PMT). Positioning the PMT at right angles to the beam helped to minimise scattered light noise and, therefore, gave an improved sensitivity.

The output from the PMT was amplified by a Stanford Research Systems SR445 preamplifier and digitised using a CAMAC-based Lecroy 2262 transient digitiser. The digitised signal was passed to a PC on a shot-to-shot basis and integrated via a home written software package.<sup>1</sup> An excitation spectrum was obtained by plotting the total fluorescence intensity as a function of laser wavelength. The resulting spectrum is similar to a conventional absorption spectrum, although the signal intensity depends not only on the absorption probability, but also on the excited state fluorescence quantum yield. Spectral resolution was governed by the linewidth of the exciting dye laser and typically spectra were recorded with resolution ranging from 0.2-0.3 cm<sup>-1</sup>.

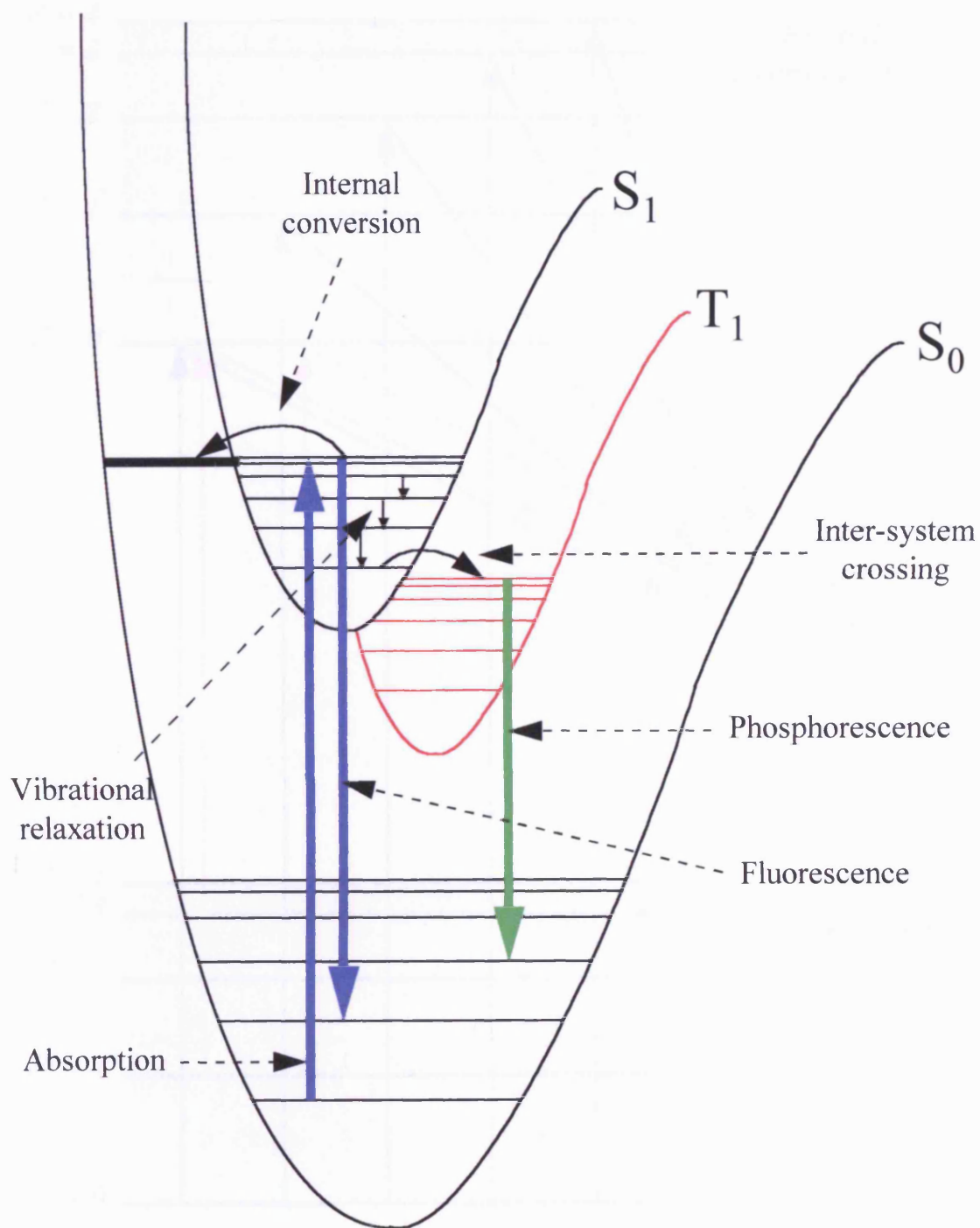


**Fig. 2.7** Decay processes which can occur following an absorption transition.

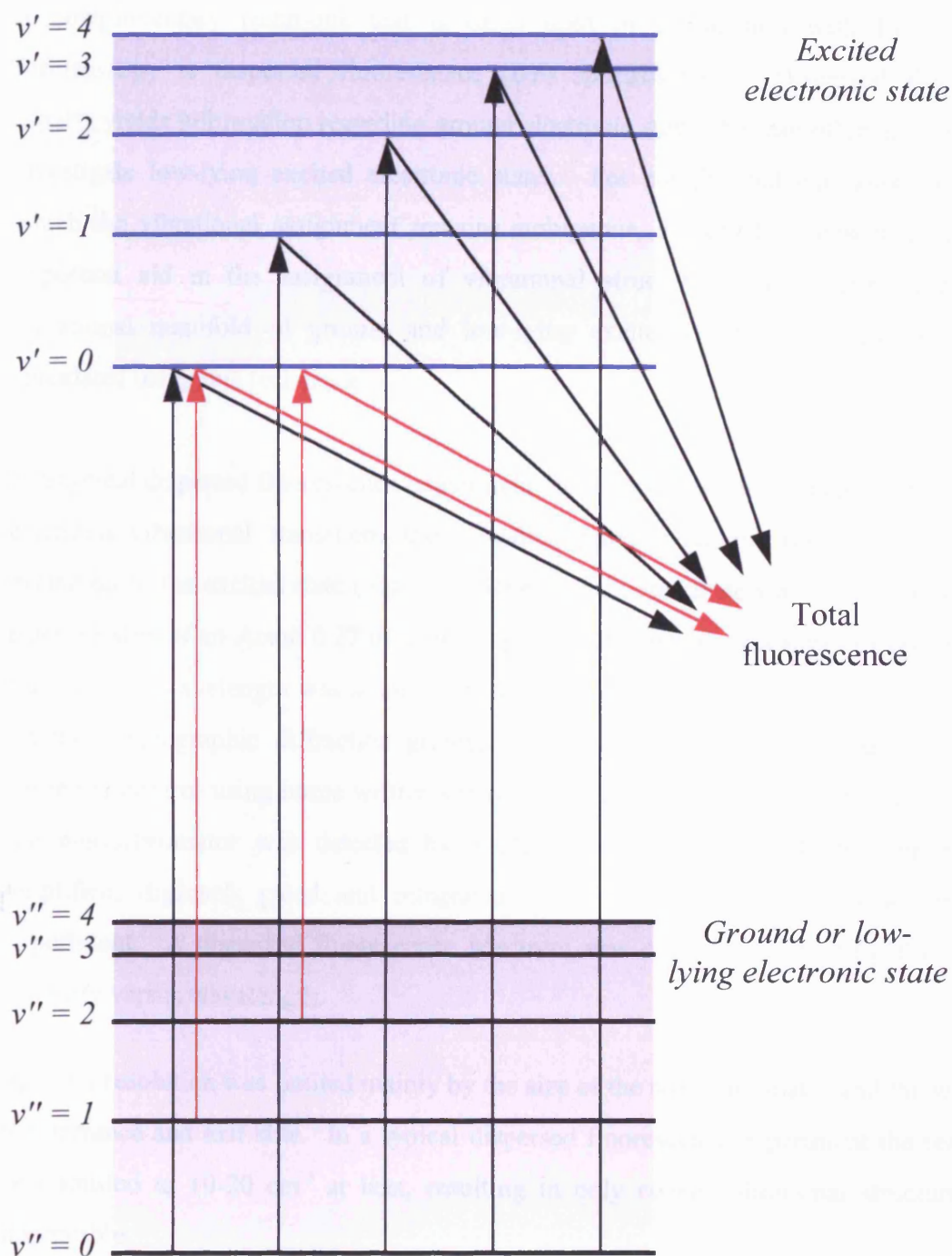


**Fig. 2.8** Schematic diagram showing the fundamental transitions involved in laser-induced fluorescence (LIF) excitation spectroscopy. Red arrows indicate hot band transitions.

### 2.3.2 *Dispersed fluorescence (DF) spectroscopy*

A complimentary technique that is often used in conjunction with LIF excitation spectroscopy is dispersed fluorescence (DF) spectroscopy.<sup>6</sup> Dispersed fluorescence usually yields information regarding ground electronic states, but can often also be used to investigate low-lying excited electronic states. For complicated excitation spectra, in which the vibrational assignment remains ambiguous, dispersed fluorescence can be an important aid in the assignment of vibrational structure in the excited state. The vibrational manifold of ground and low-lying excited electronic states can also be elucidated using this technique.

In a typical dispersed fluorescence experiment the laser wavelength was tuned to a specific electronic-vibrational transition, the so-called *pump* position, resulting in selective excitation to the excited state (Fig. 2.9). Resulting fluorescence was directed through the entrance slits of an Acton 0.27 m dispersing monochromator via a series of optics.<sup>14</sup> The fluorescence wavelength was scanned via a stepping motor in the monochromator, which rotates a holographic diffraction grating (1200 lines/mm). This was achieved under computer control using home-written software.<sup>1</sup> Light passing through the output slits of the monochromator was detected by a Hamamatsu R268 PMT detector and was amplified, digitised, gated and integrated in the same manner as for an excitation experiment. A dispersed fluorescence spectrum was obtained by plotting fluorescence intensity versus wavelength.

Spectral resolution was limited mainly by the size of the monochromator and the widths of the entrance and exit slits. In a typical dispersed fluorescence experiment the resolution was limited to 10-20 cm<sup>-1</sup> at best, resulting in only coarse vibrational structure being observable.

## 2.4 *Overview of the laser systems*

Details of the specific lasers used throughout this work will be given in this section, followed by a brief description of the equipment and optics that were used to deliver the laser beams into the experiment. Ablation/photolysis was carried out with an excimer laser. A pulsed dye laser, pumped by a Nd:YAG laser, was used to perform LIF, DF and REMPI spectroscopy.



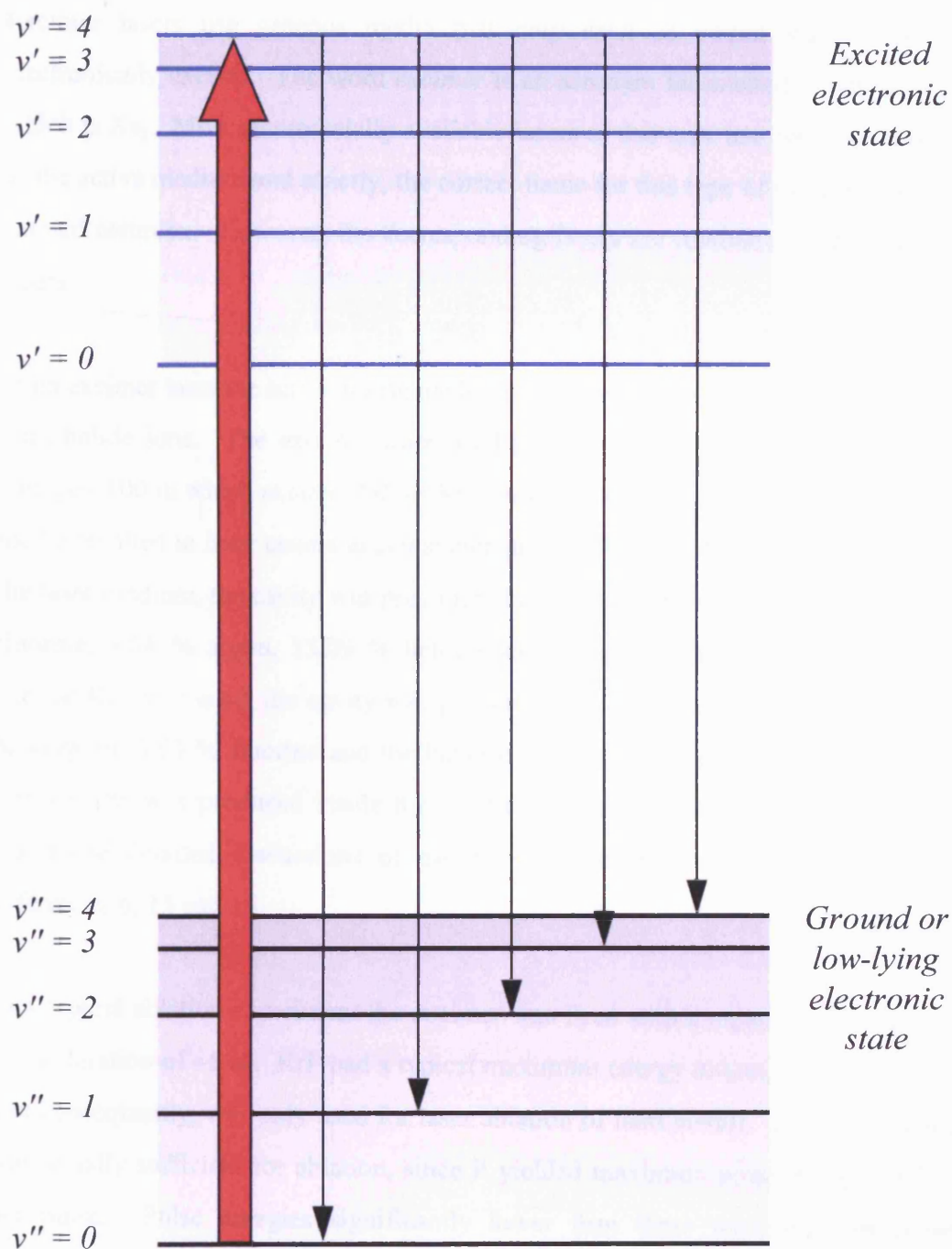


**Fig. 2.9** Transitions involved in laser-induced dispersed fluorescence (DF) spectroscopy. The red transition represents the laser excitation, or *pump*, transition.

### 2.4.1 The Excimer laser

Excimer lasers use gaseous media that only exist as bound states when they are electronically excited. The word *excimer* is an acronym for excited dimer, an example of which is  $\text{Xe}_2$ . Most commercially available lasers of this type use heteronuclear diatomics as the active medium and strictly, the correct name for this type of molecule is *exciplex*, or excited complex. However, the corresponding lasers are routinely referred to as excimer lasers.

In an excimer laser the active lasing medium is formed by chemical reaction of an inert gas with halide ions. The excimer laser used throughout this work was a Lambda Physik Compex 100 in which excited ArF or KrF was used as the active medium. The respective media resulted in laser emission at wavelengths of 193 and 248 nm. Using excited ArF as the laser medium, the cavity was pressurised to around 3 bar and was composed of 0.15 % fluorine, 4.88 % argon, 15.09 % helium and the balance made up with neon. When excited KrF was used, the cavity was pressurised to ~3.5 bar, with a composition of 0.12 % krypton, 3.03 % fluorine and the balance made up from neon. Electronically excited ArF or KrF was produced inside the laser cavity via a high energy electrical discharge. For more detailed discussions of excimer laser operation, the reader is referred to references 6, 15 and 16.

In a typical ablation experiment the excimer was fired with a repetition rate of 10 Hz and pulse duration of ~5 ns. KrF had a typical maximum energy output, per pulse, of ~300 mJ and consequently, was only used for laser ablation of hard metals. For softer metals, ArF was usually sufficient for ablation, since it yielded maximum pulse energies of ~200 mJ per pulse. Pulse energies significantly lower than these were used in experiments involving the alkaline-earth metals. The energies given above relate to the values obtained following a new cavity fill. Typically, the power output of the laser degraded continually over a period of around four weeks. Due to space confinements in the laboratory the excimer beam was reflected through ninety degrees via a prism, or mirror, and directed through a baffle arm, into the vacuum chamber. A 700 mm focal length lens was used to focus the beam onto the metal ablation target. The lens was held in a translational mount, enabling three dimensional movement of the lens to optimise the laser ablation process during routine experiments.

#### 2.4.2 *The Neodymium-YAG laser*

Optical pumping of the dye laser was achieved with a Continuum Surelite II Nd:YAG laser. As the name implies, the active laser medium consists of neodymium ions ( $\text{Nd}^{3+}$ ) doped into an yttrium aluminium garnet ( $\text{Y}_3\text{Al}_5\text{O}_{12}$ ) crystal host lattice. Laser action was induced by a broadband flashlamp, positioned adjacent to a rod of Nd:YAG crystal. By use of Q-switching, very high energy (600 mJ) pulses of  $\sim 5$  ns duration were output at the near IR wavelength of 1064.8 nm ( $9391.4 \text{ cm}^{-1}$ ). A number of detailed descriptions of Nd:YAG lasers, including the background photophysics, can be found in references 6, 16-18.

Since most organic dyes absorb visible, or ultra-violet radiation, non-linear optics were used to generate the first (532.4 nm) and second (354.9 nm) overtone wavelengths of the 1064.8 nm Nd:YAG fundamental emission. KDP (potassium dihydrogen phosphate) crystals were employed to generate the second and third harmonics, resulting in respective maximum pulse energies of  $\sim 310$  and  $\sim 145$  mJ. The laser pulse repetition frequency was fixed at 10 Hz in all experiments.

#### 2.4.3 *The Scanmate tunable dye laser*

Dye lasers are unusual, when compared to most other commercially available lasers, since the laser medium is a liquid, composed of an organic dye dissolved in an appropriate solvent. The fundamental properties of dye lasers are determined directly from the molecular structure of the dyes. Organic dyes are highly conjugated molecules which, when dissolved in the liquid phase, tend to have broad, diffuse rovibronic energy bands. In simple terms, laser action occurs between these broad electronic bands and it is this feature that leads to the smooth tunability of dye lasers over a relatively wide range. There are many dyes currently available that cover the whole of the visible region. Depending on the specific dye, tunability of a single dye solution can range between  $\sim 20$ -70 nm. For a more detailed discussion of tunable dye lasers the reader is referred to references 19 and 20.

The pulsed dye laser used in this work was a Lambda Physik Scanmate 2E dye laser. As described earlier, this was optically pumped by the second or third harmonic of a Nd:YAG laser. The important features of the Scanmate 2E dye laser are illustrated in Fig. 2.10. Laser action was produced in the oscillator and the output beam was amplified further via preamplification and main amplification stages.

The oscillator dye cuvette is optically pumped with ~5-10 % of the Nd:YAG pump beam. Stimulated emission is then amplified in the laser cavity, which is bound at one end by the resonator end mirror and at the other by a wavelength selective Littrow diffraction grating. Littrow dye lasers have the advantage that the entire spectral range (320-970 nm) can be covered by a single grating. A multiple prism beam expander, P, situated between the resonator end mirror and the grating, serves to illuminate as much of the grating as possible. This feature is an essential requirement for maximising the resolution of a dye laser, since the increased number of grating lines that are illuminated results in higher resolution. A laser linewidth of  $\sim 0.2 \text{ cm}^{-1}$  could be achieved with the Scanmate under normal cavity operation. An etalon, E, could also be inserted between the beam expander and the diffraction grating to reduce the linewidth of the dye laser output, from  $\sim 0.2 \text{ cm}^{-1}$  to  $\sim 0.03 \text{ cm}^{-1}$ , although operation of the etalon often proved problematical. Around 5 % of laser light was removed from the oscillator path at this stage, via a partially reflecting prism. The output oscillator beam was directed onto an output mirror which served to direct the beam through the oscillator dye cuvette in preparation for subsequent preamplification. Amplified stimulated emission (ASE) could be minimised at this stage by preventing it from hitting the output mirror with a beamblock, the so-called Edge. This could be achieved because the laser light and ASE traverse slightly different paths.

Preamplification was achieved by directing ~10 % of the Nd:YAG pump beam to coincide with the part of the first dye cuvette through which the oscillator output passes on its way out of the cavity. With preamplification, typical pulse energies of  $\sim 100\text{-}300 \text{ }\mu\text{J}$  were obtainable. However, pulse energies of 10-25 mJ could be obtained if the final stage of amplification was employed. Pulse energies of this magnitude were achieved by directing the remaining portion of the Nd:YAG pump beam (~80 %) onto the main amplifier dye cuvette. The amplified output then passes, through a frequency doubling unit (the crystals are removed if not required), before passing through a  $90^\circ$  prism and a baffle arm into the spectrometer vacuum chamber.

Frequency doubling allowed the output wavelength range of the Scanmate 2E to be extended from its normal operating range of 415-860 nm into the UV. The lowest wavelength attainable using commercially available Nd:YAG pumped dyes is  $\sim 415 \text{ nm}$  ( $24000 \text{ cm}^{-1}$ ). With frequency doubling, the Scanmate can operate at wavelengths down to

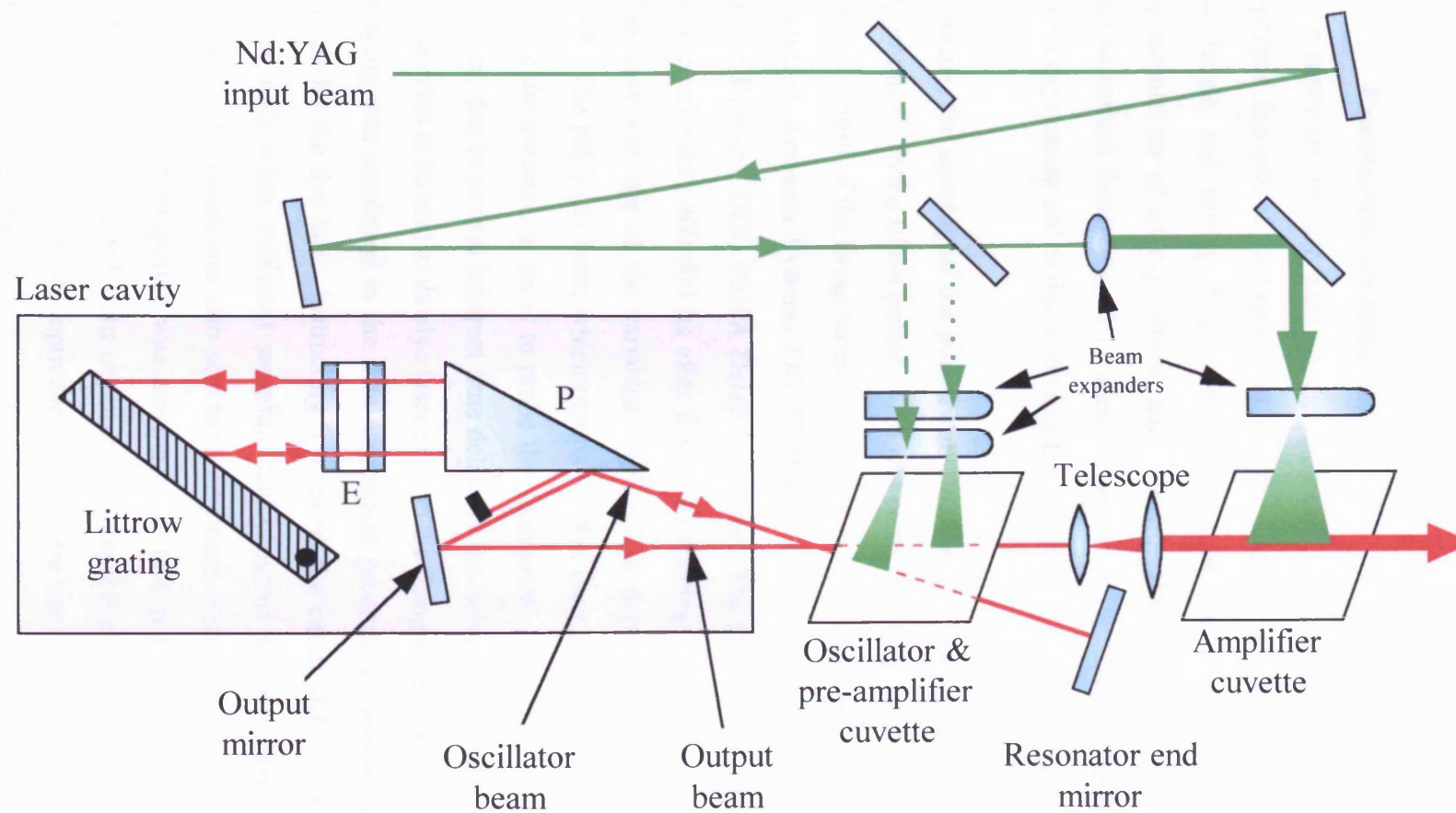


**Fig. 2.10** Schematic diagram of the Scanmate 2E dye laser.

$\sim 220$  nm ( $45000$  cm<sup>-1</sup>).  $\beta$ -phase barium borate (BBO) crystals were used for frequency doubling in the Scanmate 2E. A detailed description of the physics of non-linear optics may be found in reference 21.

## 2.5 *Experimental synchronisation*

Since many of the key parts of the apparatus were pulsed (10 Hz), one of the most important features of an experiment was the accurate synchronisation of all the pulses. The length and timing delays between various pulses were crucial for successful implementation of an experiment, and consequently, pulse-generation electronics were used to control these. Fig. 2.11 shows a schematic diagram of the timing aspects of a typical experiment and outlines some of the particular pulse lengths and timing delays.

Typically, the opening of the pulsed valve defined the start of an experiment ( $t = 0$ ), or trigger pulse. Firing of the pulsed valve was controlled by a General Valve Iota One pulse driver. Control of the firing times of the Nd:YAG and excimer lasers was achieved using a Stanford Research Systems DG535 Digital Delay/Pulse Generator and a Princeton Applied Research DDG 9050A Delay Generator. The excimer laser was programmed to fire approximately 400-600  $\mu$ s after the initial opening of the pulsed valve. The actual delay time was one of the variables employed in experiments to optimise the desired signal. The Nd:YAG laser, which pumps the dye laser, was set to fire approximately 25  $\mu$ s after the excimer, in order to probe the appropriate part of the supersonic expansion. However, due to several inherent time delays in the firing of the Nd:YAG laser, a trigger pulse needed to be sent to the dye laser prior to the firing of the excimer laser. Since shot-averaging was employed in the data acquisition process, an appropriate stop-pulse was required by the dye laser, instructing it to move the cavity diffraction grating to a new position only when sufficient sampling had occurred at the current wavelength. An appropriate stop-pulse was also sent to the digitiser, instructing it to cease data sampling while the diffraction grating was moving to its new position. Since the optimum pulse lengths and delays varied from experiment to experiment, all of the timing delays were manually adjusted to visually optimise the real-time laser induced fluorescence signal on a Tektronix TDS 320 digital oscilloscope.

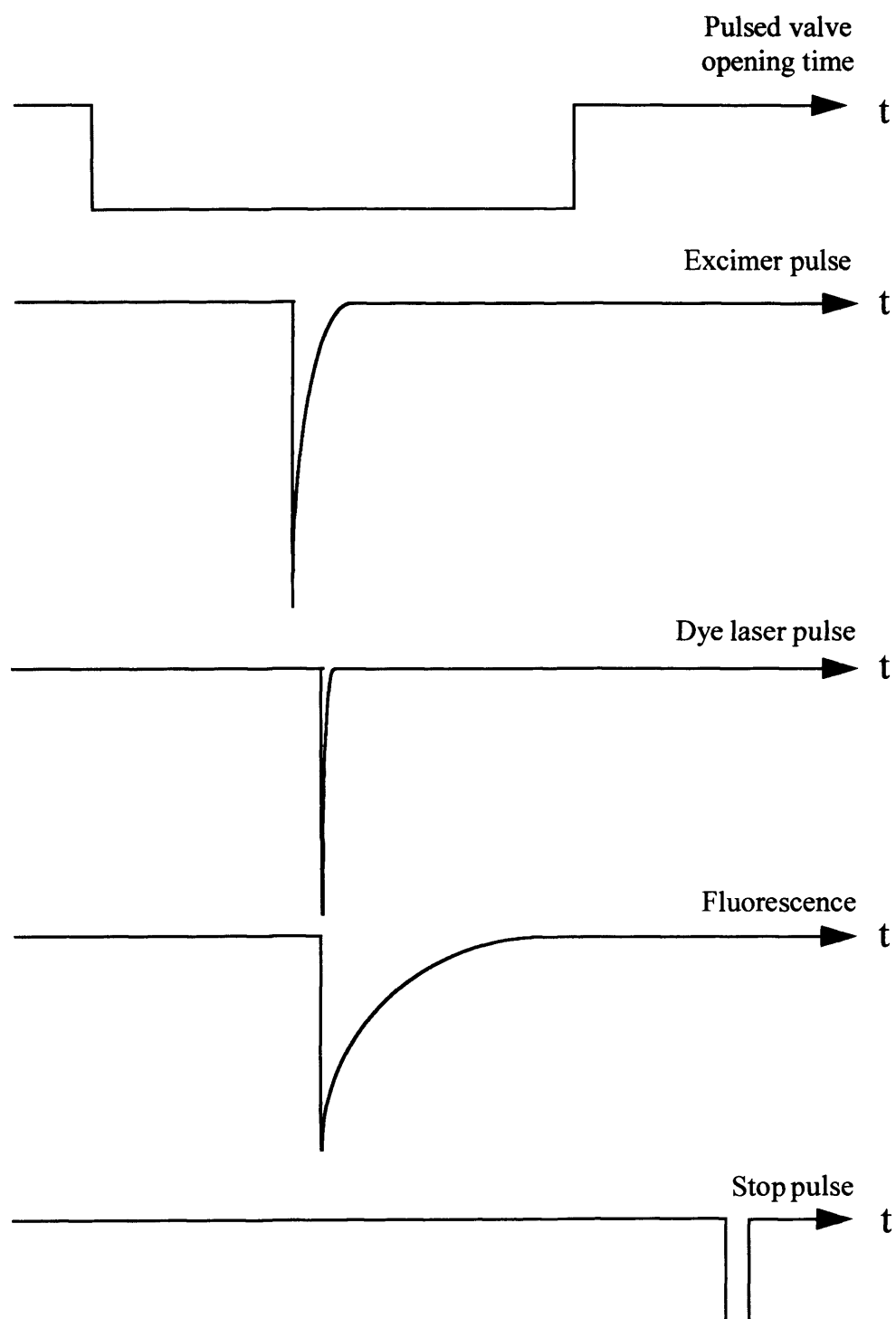


**Fig. 2.11** Timing aspects of experimental synchronisation (not to scale).

## References

- 1 G.K. Corlett, *Ph.D Thesis*, University of Leicester, 1997
- 2 T.G. Dietz, M.A. Duncan, D.E. Powers and R.E. Smalley, *J. Chem. Phys.*, **74** (1981) 6511
- 3 C.J. Whitham, B. Soep, J-P. Visticot and A. Keller, *J. Chem. Phys.*, **93** (1990) 991
- 4 A. Kantrowitz and J. Grey, *Rev. Sci. Instr.*, **22** (1951) 328
- 5 G.B. Kistiakowsky and W. P. Slichter, *Rev. Sci. Instr.*, **22** (1951) 333
- 6 J.M. Hollas, *High Resolution Spectroscopy*, (Wiley, London, 1998)
- 7 T.A. Miller, *Science*, **223** (1984) 545
- 8 P.C. Engelking, *Chem. Rev.*, **91** (1991) 399
- 9 M.G. Liverman, S. M. Beck, D. L. Monto and R. E. Smalley, *J. Chem. Phys.*, **70** (1979) 192
- 10 J.M. Hollas and D. Phillips (Ed.), *Jet Spectroscopy and Molecular Dynamics* (Blackie Academic and Professional, London, 1995)
- 11 K. Bier and B. Schmidt, *Angew. Phys.*, **13** (1961) 493
- 12 E.L. Kuth, *J. Chem. Phys.*, **66** (1977) 3315
- 13 D.L. Andrews and A.A. Demidov (Ed.), *An Introduction to Laser Spectroscopy*, (Plenum Press, London, 1995)
- 14 S.J. Pooley, *Ph.D Thesis*, University of Leicester, 1999
- 15 O. Svelto, *Principles of Lasers*, (Plenum Press, New York, 1982)
- 16 D.L. Andrews, *Lasers in Chemistry*, (Springer, Berlin, 1997)
- 17 A.E. Siegman, *Lasers*, (University Science Books, California, 1986)
- 18 K. Pátek, *Glass Lasers*, (Butterworths, London, 1970)
- 19 F.J. Duarte (Ed.), *Tunable Lasers Handbook*, (Academic Press, New York, 1995)
- 20 T.F. Johnston, Jr, *Encyclopedia of Physical Science and Technology*, Vol. **14**: *Tunable Dye Lasers*, (Academic Press, New York, 1987)
- 21 W. Demtröder, *Laser Spectroscopy: Basic Concepts and Instrumentation*, (Springer-Verlag, New York, 1981)



## *Chapter Three*

### *Monohydroxide derivatives of the alkaline-earth metals*

### 3.1 Background

The alkaline-earth monoxides and monohydroxides initially attracted attention in the early 1950's because of the intense colours that were observed from adding alkaline-earth salts to a flame. In 1955 James *et al.*<sup>1</sup> proposed that, while a number of emission bands in the visible and near-IR were due to the monoxides of the alkaline-earth metals, the most intense bands probably arose from electronic transitions in the metal monohydroxides. In subsequent, independent studies, Lagerqvist *et al.* and Charton *et al.* carried out more detailed work on the intense flame emission band systems in the visible and near-IR regions originating from addition of calcium, strontium and barium salts to a number of different high energy arc and flame environments.<sup>2-4</sup> The metal monohydroxides were assigned conclusively as the spectral carriers by observing small shifts in the emission lines due to deuterated analogues of these molecules.

The development of laser-induced fluorescence spectroscopy (LIF) in the mid-1970's introduced an alternative method for investigating short-lived molecules. Flame species could now be selectively excited using narrow laser bandwidths and studied with, potentially, much higher spectral resolution. However, although flames are an obvious source of short-lived molecules, they present a serious disadvantage to the high resolution spectroscopist. The high internal temperatures in flames can cause severe congestion in molecular spectra, making it very difficult to extract useful information. Haraguchi and co-workers observed strong fluorescence from a number of band systems in the red, green and near-IR regions, due to BaO/BaOH and SrO/SrOH, using LIF spectroscopy in an air-acetylene flame.<sup>5</sup> Emission bands originating from the monoxides could easily be differentiated from those of the monohydroxides by their strong red-shading. However, very little spectroscopic information regarding BaOH and SrOH could be extracted from the spectra, since the emission bands for these species were extremely broad and overlapped.

Throughout the 1980's and 1990's a number of relatively new production methods have been exploited to prepare alkaline-earth monohydroxides with low internal temperatures (see Chapter 1).<sup>6-9</sup> Subsequent detection, using highly sensitive lasers, has provided a powerful insight into the rovibronic energy levels of these molecules. This work has provided detailed information on electronic structure, vibrational properties and the interactions between angular momenta. For example, spin-orbit coupling, spin-rotation

coupling and the Renner-Teller effect are all potentially observable in the alkaline-earth monohydroxides. Although many LIF studies of the alkaline-earth monohydroxides have been carried out in recent years, almost all have focused on the ground and first two excited electronic states.

This chapter is intended to provide background information on the alkaline-earth monohydroxides as a prelude to later chapters describing work on new electronic transitions of BaOH and SrOH. Initially, a general discussion of the electronic structure of the alkaline-earth monohydroxides is presented, followed by a review of previous spectroscopic studies and an introduction to the present work. Additionally, a brief discussion of some of the angular momentum coupling and anharmonic vibrational effects, which are potentially observable in linear alkaline-earth monohydroxides is given.

### 3.2 *Electronic structure*

In general, metal monohydroxides (MOH) may be linear, bent or ‘quasilinear’. The nature of the M-O bonding can be broadly identified by the degree by which the molecule is bent. A linear structure is usually indicative of ionic bonding and the degree of deviation from linearity relates to the degree of covalency. Alkaline-earth metal-containing free radicals, such as MOH, MH, MF, MCH<sub>3</sub> and many related species tend to be highly ionic species in which the unpaired electron is mainly metal-localised. This is certainly true for the ground electronic state and is also known to be true for the lowest lying excited electronic states. The unpaired electron in the ground electronic state can be promoted to higher atomic orbitals on the metal and the spectroscopy which ensues is essentially that of an alkaline-earth cation perturbed by the electric field of the adjacent anion. The alkaline-earth cations undergo radiative emission with high quantum yields, making them ideal for probing by LIF spectroscopy.

Fig. 3.1 shows a simple, quantitative correlation diagram for the low-lying electronic states of Sr<sup>+</sup>, SrF and linear SrOH. Similar diagrams can be produced for all alkaline-earth diatomics and linear polyatomics. The diagram becomes more complicated for non-linear triatomics and polyatomic molecules with lower symmetries. On the left of the diagram are the atomic orbitals of Sr<sup>+</sup>. All ground state alkaline-earth metal ions have the outer electronic configuration  $ns^1$ , which give  $^2S$  electronic states. Promotion of the unpaired electron to previously vacant  $p$  or  $d$  atomic orbitals on the metal results in electronic states

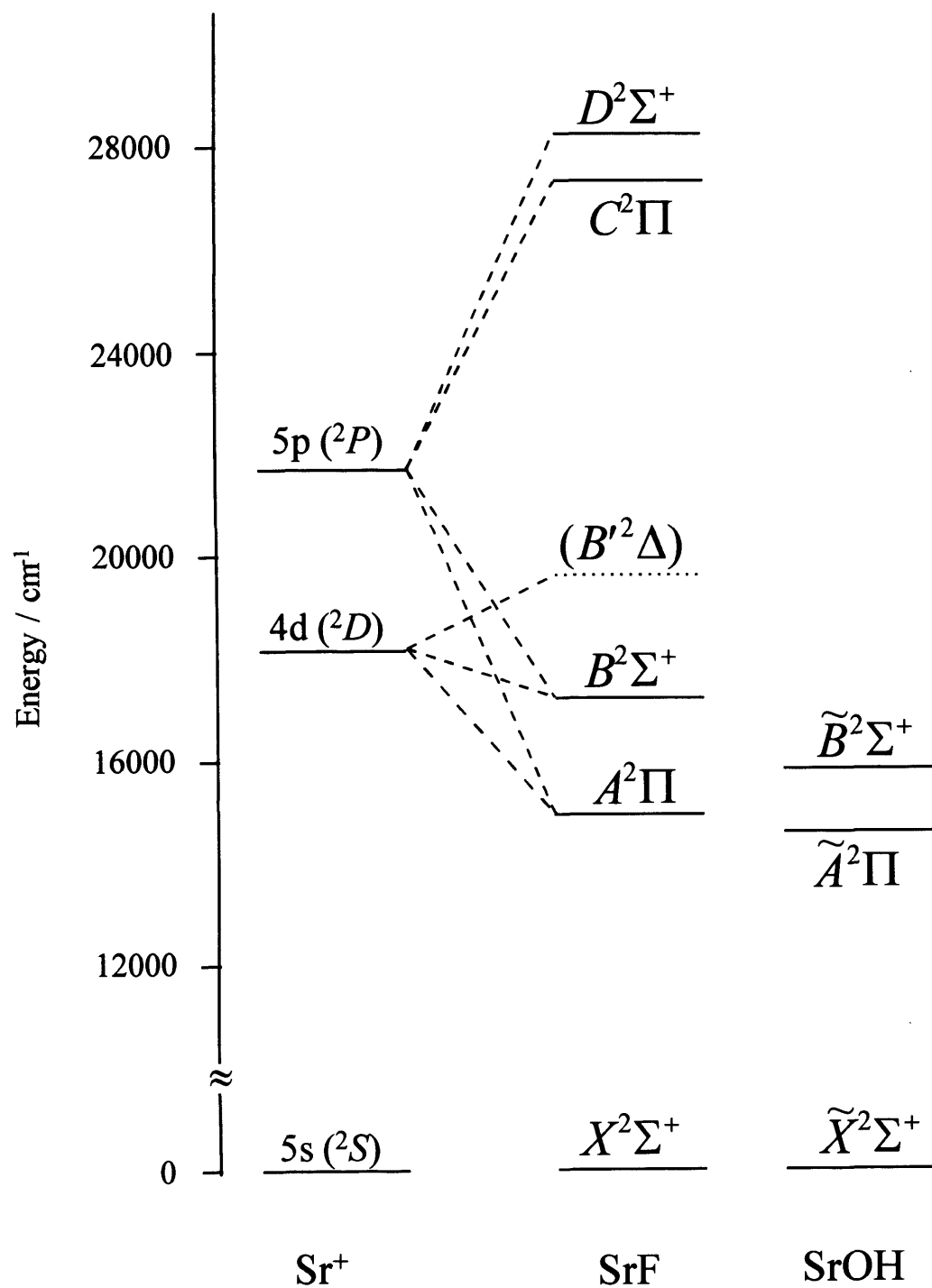


**Fig. 3.1** Correlation diagram illustrating the low-lying electronic states of Sr<sup>+</sup>, SrF and SrOH.

with  $^2P$  and  $^2D$  symmetries, respectively. Addition of a ligand to the metal, resulting in a diatomic molecule or linear polyatomic, e.g. SrF or SrOH, yields a ground electronic state of  $^2\Sigma^+$  symmetry. However, the effect of the ligand is more notable for excited states of the metal cations. The ligand has the effect of removing the degeneracy of the  $^2P$  state of the metal cation, resulting in both  $p\sigma$  and  $p\pi$  orbitals. These orbitals can mix with the  $d\sigma$  and  $d\pi$  orbitals, which correlate with the  $^2D$  state of the metal cation. The end result is five molecular electronic states, two  $^2\Sigma^+$  and two  $^2\Pi$  states, all of which have mixed metal  $p/d$  character, and one  $^2\Delta$  state which arises from the  $d\delta$  orbital.<sup>10</sup>

In attempting to understand the electronic structure of alkaline-earth monohydroxides, the alkaline-earth monofluorides are a very useful guide, since the  $\text{OH}^-$  ligand is isoelectronic with  $\text{F}^-$ . A great deal of experimental and theoretical information is available for the alkaline-earth monohalides.<sup>11-15</sup> Given that they are isoelectronic and the ligands possess the same masses, a good correlation can be made between molecular constants for the known low-lying electronic states of the alkaline-earth monohydroxides and those for the monohalides. Table 3.1 compares some of the spectroscopic constants of CaF and CaOH. Similar comparisons can be made for the heavier alkaline-earth analogues.

A number of molecular constants have been predicted for the low-lying states of the calcium monohalides in theoretical work by Rice *et al.*<sup>16</sup> Their calculations involved a simple semiempirical electrostatic model, based upon the assumptions of ligand field theory. Treating the ligand as a point charge, and explicitly evaluating the electrostatic interactions, the model clearly showed that most electronic properties (e.g. excited state energies, dissociation energies, transition moments and dipole moments) could be predicted with reasonable precision.

One of the more notable and interesting results of the calculations related to the dipole moments of CaF in its various low-lying electronic states. In the  $X^2\Sigma^+$ ,  $A^2\Pi$  and  $B^2\Sigma^+$  states the dipole moments were found to be quite similar. Figs. 3.2(a-c) show qualitative orbital representations of the  $X^2\Sigma^+$ ,  $A^2\Pi$  and  $B^2\Sigma^+$  states in CaF, an idea which can be extended to the other alkaline-earth monohalides.<sup>17</sup> In all three of these states the unpaired electron is concentrated in an orbital polarised *away* from the ligand and this results in modest dipole moments, even though the molecule is highly ionic. However, the dipole

**Table 3.1** Comparison of spectroscopic constants ( $\text{cm}^{-1}$ ) in low-lying electronic states of CaF and CaOH.

<i>Electronic state</i>	<i>Spectroscopic constant</i>	<i>CaF</i> <sup>a)</sup>	<i>CaOH</i>
$\tilde{X}^2\Sigma^+$	$\nu_{00}$	0	0
	$\omega_e$	581.1	612.8 <sup>b)</sup>
	$B_e$	0.338	0.3345 <sup>c)</sup>
$\tilde{A}^2\Pi$	$\nu_{00}$	16493.1	15998 <sup>c)</sup>
	$A$	72.5	66 <sup>c)</sup>
	$\omega_e$	586.8	621 <sup>d)</sup>
	$B_e$	0.343	0.3405 <sup>c)</sup>
$\tilde{B}^2\Sigma^+$	$\nu_{00}$	18834.2	18022.3 <sup>e)</sup>
	$\omega_e$	566.1	606 <sup>e)</sup>
	$B_e$	0.336	0.339 <sup>e)</sup>

a) Taken from reference 18.

d) Taken from reference 21.

b) Taken from reference 19.

e) Taken from reference 22.

c) Taken from reference 20.

moment in the  $C^2\Pi$  electronic state of CaF was calculated by Rice *et al.* to be approximately twice as large as those in the  $X^2\Sigma^+$ ,  $A^2\Pi$  and  $B^2\Sigma^+$  states. Experimental confirmation of this difference was subsequently achieved by Ernst *et al.* in their Stark investigation of CaF in 1989.<sup>17</sup> In their work, the  $C^2\Pi$  state dipole moment of CaF was found to be *three* times larger (9.24 D) than in the ground electronic state (3.07 D). The reason for the apparent difference in the dipole moment of the  $C^2\Pi$  state was described in terms of a reverse polarised electronic state wave function (see Fig. 3.2(d)). In this case the electron is concentrated in an orbital polarised *towards* the ligand, resulting in a significant increase in dipole moment. It seems entirely reasonable that a similar effect will be seen for the alkaline-earth monohydroxides. Indeed, the idea of opposite orbital polarisations will be discussed more thoroughly in Chapters 4 and 5 when it will be shown that it has significant implications for particular electronic states of the BaOH and SrOH molecules.

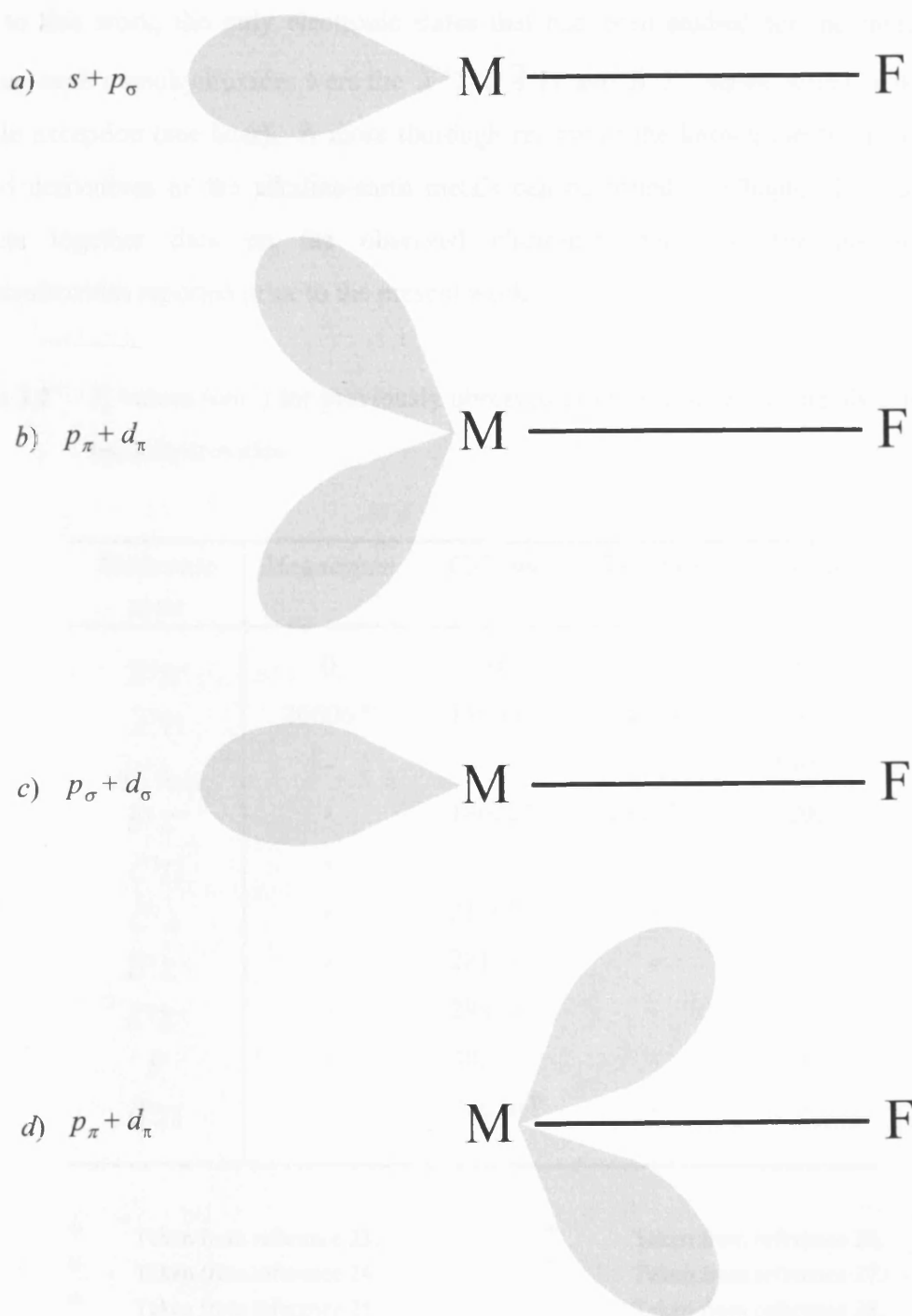


**Fig. 3.2** Diagram showing approximate orbital shapes for the unpaired electron in an alkaline-earth monofluoride. a)  $X^2\Sigma^+$ , b)  $A^2\Pi$ , c)  $B^2\Sigma^+$  and d)  $C^2\Pi$  electronic states.<sup>17</sup> The main contributions of atomic functions to the single electron orbital are shown for each state.

### 3.3 Previous spectroscopic studies of the alkaline-earth monohydroxides

Prior to this work, the only electronic states that had been studied for the majority of alkaline-earth monohydroxides were the  $\tilde{X}^2\Sigma^+$ ,  $\tilde{A}^2\Pi$  and  $\tilde{B}^2\Sigma^+$  states, with CaOH as the notable exception (see later). A more thorough review of the known electronic states of related derivatives of the alkaline-earth metals can be found in Chapter 1. Table 3.2 collects together data on the observed electronic states of the alkaline-earth monohydroxides reported prior to the present work.

**Table 3.2**  $T_e$  values ( $\text{cm}^{-1}$ ) for previously observed electronic states of the alkaline-earth monohydroxides.

<i>Electronic state</i>	<i>Magnesium</i>	<i>Calcium</i>	<i>Strontium</i>	<i>Barium</i>
$\tilde{X}^2\Sigma^+$	0	0	0	0
$\tilde{A}^2\Pi$	26606 <sup>a)</sup>	15999 <sup>b)</sup>	14675 <sup>b)</sup>	11762 <sup>b)</sup>
$\tilde{A}',^2\Delta_{5/2}$	-	-	-	11307 <sup>c)</sup>
$\tilde{B}^2\Sigma^+$	-	18022 <sup>b)</sup>	16377 <sup>b)</sup>	13200 <sup>b)</sup>
$\tilde{C}^2\Pi$	-	-	-	-
$\tilde{C}^2\Delta$	-	21907 <sup>d)</sup>	-	-
$\tilde{D}^2\Sigma^+$	-	28153 <sup>e)</sup>	-	-
$\tilde{E}^2\Sigma^+$	-	29879 <sup>e)</sup>	-	-
$\tilde{F}$	-	30215 <sup>e)</sup>	-	-
$\tilde{G}^2\Pi$	-	32630 <sup>f)</sup>	-	-

a) Taken from reference 23.

b) Taken from reference 24.

c) Taken from reference 25.

d) Taken from reference 26.

e) Taken from reference 27.

f) Taken from reference 28.

#### 3.3.1 MgOH

To date, there has been little spectroscopic work on MgOH. Ziurys and co-workers recorded the pure rotational spectrum for the  $\tilde{X}^2\Sigma^+$  ground state of MgOH, using millimetre-wave spectroscopy.<sup>29-30</sup> The ground state equilibrium geometry of MgOH was found to be linear, although the bending potential was found to be unusually flat.



The only electronic system of MgOH that has been observed using LIF is the  $\tilde{A} - \tilde{X}$  system, reported by Ni in his PhD thesis of 1986.<sup>23</sup> The findings of this work indicate that the degeneracy of the  $\tilde{A}^2\Pi$  electronic state of MgOH, which correlates with a linear equilibrium geometry, is lifted, due to the  $\tilde{A}$  state assuming a bent equilibrium geometry. However, only the lower Renner-Teller component was identified in this study.

### 3.3.2 CaOH

CaOH has been the most extensively investigated member of the alkaline-earth monohydroxides. To date, eight electronic states have been identified. The three lowest excited states,  $\tilde{A}^2\Pi$ ,  $\tilde{B}^2\Sigma^+$  and  $\tilde{C}^2\Delta$ , have been characterised in several LIF studies,<sup>19-22,24,26-28,31-38</sup> while the ground ( $^2\Sigma^+$ ) state has been studied in detail using millimetre-wave and dispersed fluorescence spectroscopy.<sup>19-20,39-40</sup> Of these states, the  $\tilde{A}^2\Pi$  and  $\tilde{C}^2\Delta$  states are the most interesting because of the possibility of Renner-Teller activity. In fact, detailed studies have shown that the Renner-Teller effect in these states is small.<sup>26,33</sup> In CaF the unpaired electron, which is the source of the net orbital angular momentum, is thought to be in metal-localised orbitals polarised *away* from the fluoride ligand in the  $A^2\Pi$  and  $C^2\Delta$  states (see Fig. 3.2). Since CaF is isoelectronic with CaOH, a similar orbital picture should be applicable to CaOH. The remoteness of the unpaired electron from the Ca–O–H bending motion, which is dominated by movement of the H atom, does not lend itself to efficient coupling of orbital and vibrational angular momenta. Consequently, it is unsurprising that the Renner-Teller effect is small in the  $\tilde{A}^2\Pi$  and  $\tilde{C}^2\Delta$  states of CaOH.

The four highest known electronic states of CaOH, the  $\tilde{D}^2\Sigma^+$ ,  $\tilde{E}^2\Sigma^+$ ,  $\tilde{F}$  and  $\tilde{G}^2\Pi$  states, have only recently been reported. The  $\tilde{D}$ ,  $\tilde{E}$  and  $\tilde{F}$  states were observed by Pereira and Levy, using both LIF and mass-resolved REMPI spectroscopies.<sup>27</sup> Vibrational structure was resolved for each of these states together with some partially resolved rotational structure in the  $\tilde{D} - \tilde{X}$  system. The symmetries of the  $\tilde{D}$  and  $\tilde{E}$  states were readily established as  $^2\Sigma^+$ . However, the  $\tilde{F}$  state, whose symmetry was not determined, proved to be more interesting, showing evidence for a bent equilibrium geometry. The  $\tilde{G}^2\Pi$  state of CaOH was reported by Hailey *et al.* from an optical-optical double resonance experiment using the  $\tilde{B} - \tilde{X}$  transition as the first resonant step.<sup>28</sup> As in the four lowest

states of CaOH, the unpaired electron seems to be largely metal-localised in the  $\tilde{D}$ ,  $\tilde{E}$  and  $\tilde{G}$  states (the situation is less clear for the  $\tilde{F}$  state). Given that the ligand is largely a spectator in these electronic transitions, with the possible exception of the  $\tilde{F}$  state, this suggests that comparable new metal-localised transitions might be observed for many other alkaline-earth containing free radicals.

### 3.3.3 *BaOH and SrOH*

The  $\tilde{X}^2\Sigma^+$ ,  $\tilde{A}^2\Pi$ ,  $\tilde{A}'^2\Delta$  and  $\tilde{B}^2\Sigma^+$  states of BaOH have all been investigated in some detail in previous studies.<sup>25,41-43</sup> As expected, their equilibrium geometries are found to be linear. Interestingly, spectroscopic evidence recorded by Bernath and co-workers indicates that the optically forbidden  $\tilde{A}'^2\Delta - \tilde{X}^2\Sigma^+$  transition gains intensity through vibronic coupling of the  $\tilde{A}'^2\Delta$  state with the  $\tilde{A}^2\Pi$  and  $\tilde{B}^2\Sigma^+$  states.<sup>25</sup> Apart from these states, the only other excited electronic state of BaOH which has been identified is the  $\tilde{C}$  state. As mentioned in an earlier section, Haraguchi and co-workers observed fluorescence in their low resolution LIF study of barium flames.<sup>5</sup> They tentatively assigned the transition responsible to the  $\tilde{C} - \tilde{X}$  transition of BaOH, although the symmetry of the  $\tilde{C}$  state was not deduced and no spectroscopic constants could be extracted.

Similar electronic states have been observed for SrOH, including the  $\tilde{X}^2\Sigma^+$ ,  $\tilde{A}^2\Pi$  and  $\tilde{B}^2\Sigma^+$  states, although no evidence of a  $^2\Delta$  excited state has been reported.<sup>24,44-52</sup> Coxon and co-workers have also shown that the  $\tilde{A}^2\Pi$  state of SrOH undergoes perturbations arising from the combined effects of Renner-Teller coupling, Fermi resonance and spin-orbit coupling.<sup>52</sup>

## 3.4 *Present work*

The aim of this work has been to identify higher electronic states of alkaline-earth monohydroxides in an attempt to investigate the role of the OH ligand on their electronic structure, vibrational properties and the interaction between various angular momenta. As mentioned above, evidence obtained for the CaOH radical would seem to suggest that the unpaired electron in at least one of its higher electronic states, while still predominantly metal-localised, is more strongly perturbed by the ligand field than in lower states. Such perturbations may give rise, in those states which possess net orbital angular momentum,

to increased Renner-Teller activity. ‘Competition’ between these processes and, for example, spin-orbit coupling, is potentially easy to study in alkaline-earth monohydroxides since the atomic spin-orbit coupling constants increase as group 2 is descended (see section 3.5.1).

In the present work several new electronic transitions have been observed for both the BaOH and SrOH free radicals. In Chapter 4, an LIF investigation of a new electronic transition ( $\tilde{D}^2\Sigma^+ - \tilde{X}^2\Sigma^+$ ) of BaOH will be discussed, along with a re-investigation of the supersonically cooled  $\tilde{C} - \tilde{X}$  system. In addition, five new UV electronic transitions of the SrOH free radical, the  $\tilde{B}'^2\Sigma^+ - \tilde{X}^2\Sigma^+$ ,  $\tilde{C}^2\Pi - \tilde{X}^2\Sigma^+$ ,  $\tilde{D}^2\Sigma^+ - \tilde{X}^2\Sigma^+$ ,  $\tilde{E}^2\Sigma^+ - \tilde{X}^2\Sigma^+$  and  $\tilde{F}^2\Pi - \tilde{X}^2\Sigma^+$  systems, have been observed for the first time and these will be discussed in Chapter 5.

### 3.5 Angular momentum coupling in linear molecules

The occurrence of angular momentum coupling, including spin-orbit and Renner-Teller coupling, has been alluded to in the previous sections. In subsequent chapters, the observation of these effects and others, will be discussed in detail for specific systems. A brief qualitative description of a number of these phenomena are presented here as background for the forthcoming discussions.

#### 3.5.1 Spin-orbit coupling

Considerations of electronic angular momentum in linear triatomics can be treated in the same way as those for diatomic molecules.<sup>53</sup> In a linear molecule, a strong electrostatic field occurs between the atomic nuclei along the direction of the internuclear axis. Consequently, electrons are free to precess with an orbital angular momentum,  $L$ , around the internuclear axis. This orbital motion creates a well-defined component of angular momentum along the internuclear axis, given by  $M_L \hbar$ .  $M_L$  is a projection quantum number which can only take values of,

$$M_L = L, L - 1, L - 2 \dots -L. \quad (3.1)$$

The sign of  $M_L$  can be thought of as representing the direction in which the electrons are circulating about the internuclear axis, i.e. clockwise or anticlockwise, and therefore the

*energy* is determined by the magnitude of  $M_L$ , not its sign. If  $L$  is so strongly coupled to the internuclear axis that its magnitude is no longer well-defined,  $L$  is no longer a good quantum number, but  $|M_L|$  remains well defined. Consequently, it is more appropriate to define the orbital angular momentum according to the value of  $M_L$ , rather than the value of  $L$ .

It is usual to represent the orbital angular momentum along the internuclear axis in a linear molecule by the quantum number,  $\Lambda$ , where  $\Lambda = |M_L|$ . The corresponding angular momentum,  $\pm\Lambda\hbar$ , represents the *component of the electronic orbital angular momentum along the internuclear axis*. Consequently,  $\Lambda$  can take values of 0, 1, 2 ....  $L$ , which correspond to  $\Sigma$ ,  $\Pi$ ,  $\Delta$  ...., molecular states, where all states except  $\Sigma$  states are doubly degenerate.

In addition to orbital angular momentum, there is a spin angular momentum,  $S$ , associated with electrons. The corresponding total spin quantum number,  $S$ , depends on the number of unpaired electrons in the molecule and may be integer or half-integer. In electronic states with  $\Lambda \neq 0$ , a magnetic field exists in the direction of the internuclear axis, due to the orbital motion of the electrons. If sufficiently strong, this can cause  $S$  to precess around the internuclear axis, with a component,  $\Sigma$ , (see Fig. 3.3(i)) the projected spin quantum number, given by,

$$\Sigma = S, S - 1, S - 2 \dots - S. \quad (3.2)$$

The situation, in which the orbital angular momentum,  $L$ , and the spin angular momentum,  $S$ , are weakly coupled is commonly referred to as Hund's case (a), and is shown in Fig. 3.3(i). In this case, the spin-orbit coupling is not strong enough to uncouple  $S$  from the internuclear axis and so  $\Sigma$  (and  $\Lambda$ ) are good quantum numbers. The total electronic (orbital and spin) angular momentum about the internuclear axis is defined as  $\Omega$  and the corresponding quantum number,  $\Omega$ , is given by  $\Omega = |\Lambda + \Sigma|$ . For example, a  $\Pi$  electronic state ( $\Lambda = 1$ ) with one unpaired electron ( $\Sigma = \pm 1/2$ ) splits into two components, where  $\Omega = 1/2$  and  $3/2$ . Note that, for a given value of  $\Omega$ , the state is doubly degenerate. Another extreme coupling case, referred to as Hund's case (c), occurs when  $L$  and  $S$  are strongly coupled to each other. In this case,  $\Lambda$  and  $\Sigma$  are not defined. Rather,  $L$  and  $S$  form a resultant,  $J$ , which is then coupled to the internuclear axis (see Fig. 3.3(ii)).

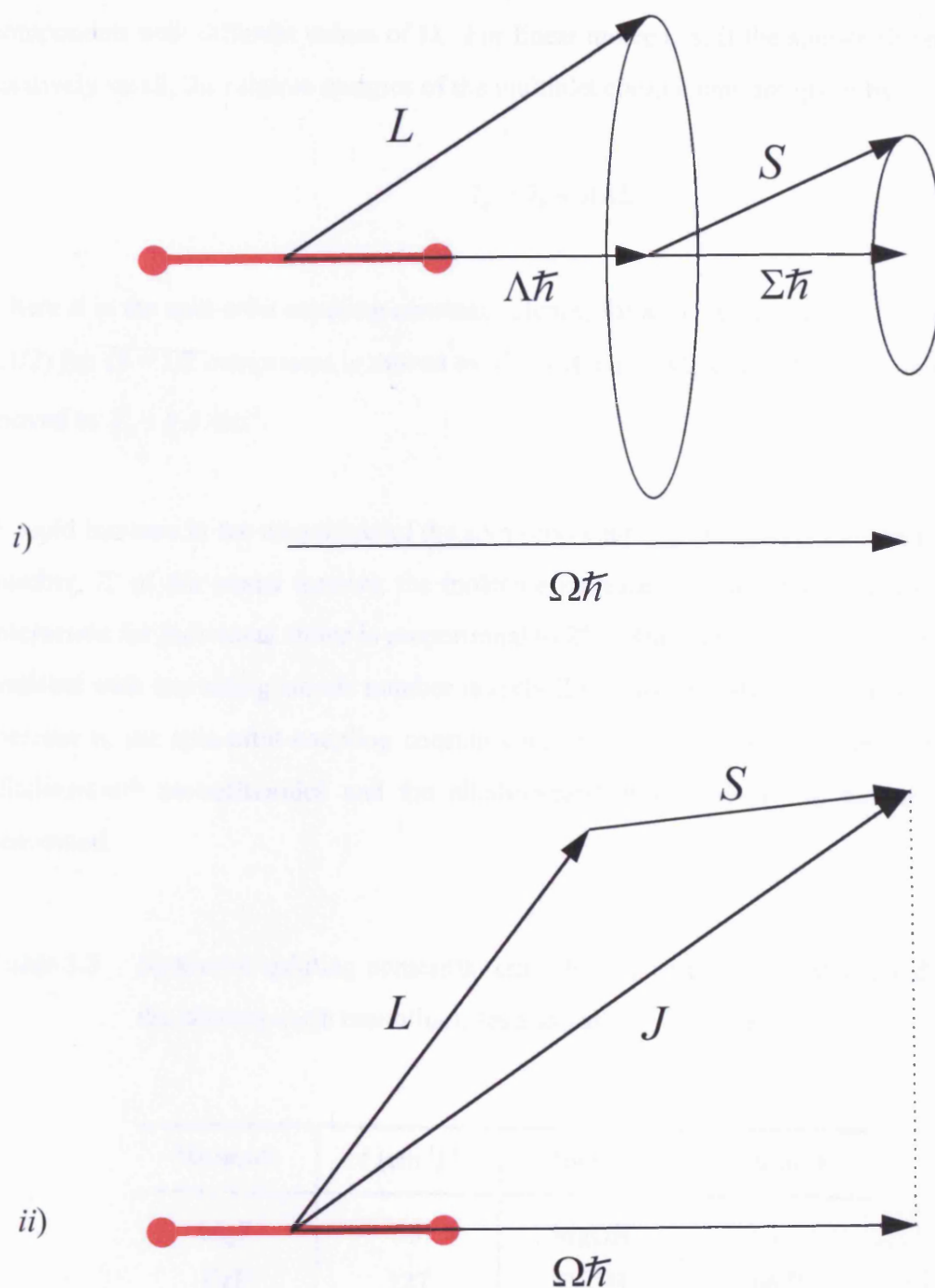


**Fig. 3.3** *i)* Hund's case (a), in which the orbital angular momentum,  $L$ , and spin angular momentum,  $S$ , are weakly coupled. *ii)* Hund's case (c), in which the interaction between  $L$  and  $S$  is sufficiently strong that they are not uncoupled by the strong electrostatic field along the internuclear axis.

The result of spin-orbit coupling is to split an electronic state into a multiplet of components with different values of  $\Omega$ . For linear molecules, if the spin-orbit coupling is relatively small, the relative energies of the multiplet components are given by,

$$T_e = T_0 + A\Lambda\Sigma \quad (3.3)$$

where  $A$  is the spin-orbit coupling constant. Hence, for a  $^2\Pi$  electronic state ( $\Lambda = 1$ ,  $\Sigma = \pm 1/2$ ) the  $\Omega = 1/2$  component is moved to  $T_0 - \frac{1}{2}A \text{ cm}^{-1}$ , while the  $\Omega = 3/2$  component is moved to  $T_0 + \frac{1}{2}A \text{ cm}^{-1}$ .

A rapid increase in the magnitude of the spin-orbit coupling constant occurs as the atomic number,  $Z$ , of the atoms forming the molecule increase. In fact, the magnitude of the interaction for individual atoms is proportional to  $Z^4$ .<sup>53</sup> The increase in spin-orbit coupling constant with increasing atomic number is aptly illustrated in Table 3.3, which shows the increase in the spin-orbit coupling constants for the respective first excited states of the alkaline-earth monofluorides and the alkaline-earth monohydroxides, as the group is descended.

**Table 3.3** Spin-orbit splitting constants ( $\text{cm}^{-1}$ ) for the respective first excited states of the alkaline-earth monofluorides and monohydroxides.

Molecule	$A \text{ (cm}^{-1}\text{)}^{\text{a)}$	Molecule	$A \text{ (cm}^{-1}\text{)}$
MgF	35	MgOH	-
CaF	127	CaOH	66 <sup>b)</sup>
SrF	281	SrOH	265 <sup>c)</sup>
BaF	368	BaOH	569 <sup>d)</sup>

a) Taken from reference 18.

b) Taken from reference 20.

c) Taken from reference 46.

d) Taken from reference 25.

### 3.5.2 The Renner-Teller effect

The Renner-Teller effect<sup>54</sup> in linear molecules is a direct result of the interaction of electronic orbital angular momentum with the vibrational angular momentum associated with doubly degenerate bending vibrations. For linear triatomic molecules there is only one such vibration, traditionally labelled as normal mode  $\nu_2$ . The bending motion has the effect of lifting the double degeneracy associated with the electronic orbital angular momentum and, consequently, the potential curves representing the action of the bending motion split into two curves. There are three general ways in which the potential curves are affected and these are shown in Fig. 3.4. Fig. 3.4(a) illustrates the limiting case in which both curves have an identical minimum in the linear configuration. A second limiting case (Fig. 3.4(b)) pertains to the situation where one component of the electronic state is linear and the other is bent. The third limiting case (Fig. 3.4(c)) shows the situation where the equilibrium configurations of both components are bent, but the states become degenerate for linear geometries.

Excitation of  $\nu_2$  can result in the generation of vibrational angular momentum,  $l$ , around the internuclear axis. The component in the direction of the internuclear axis is denoted by the quantum number,  $l$ , and may take on the values

$$l = \nu_2, \nu_2 - 2, \nu_2 - 4, \dots, -\nu_2. \quad (3.4)$$

where,  $\nu_2$  is the vibrational quantum number for the normal vibration,  $\nu_2$ . Consequently,  $l$  can take values of  $\pm 1, \pm 2, \pm 3, \dots$ , corresponding to  $\Pi, \Delta, \Phi, \dots$ , vibrational states.

As a result of the interaction between orbital and vibrational angular momentum, there is a breakdown of the Born-Oppenheimer approximation and it is necessary to consider *vibronic* energy levels. The vibronic angular momentum,  $K$ , around the internuclear axis, resulting from coupling of the orbital and vibrational angular momenta, is given by  $K = |\pm \Lambda + l|$ . For example, the vibronic levels associated with a  $\Pi$  electronic state ( $\Lambda = 1$ ) in which one quantum of the bending mode,  $\nu_2$ , is excited ( $l = 1$ ) are  $K = 0, 0, 2$  and  $2$ , corresponding to two  $\Sigma$  states and the doubly degenerate  $\Delta$  state (see Fig. 5.8). In fact, as can be seen in Fig. 5.8, the two  $\Sigma$  states have different symmetries,  $\Sigma^+$  and  $\Sigma^-$ , respectively.

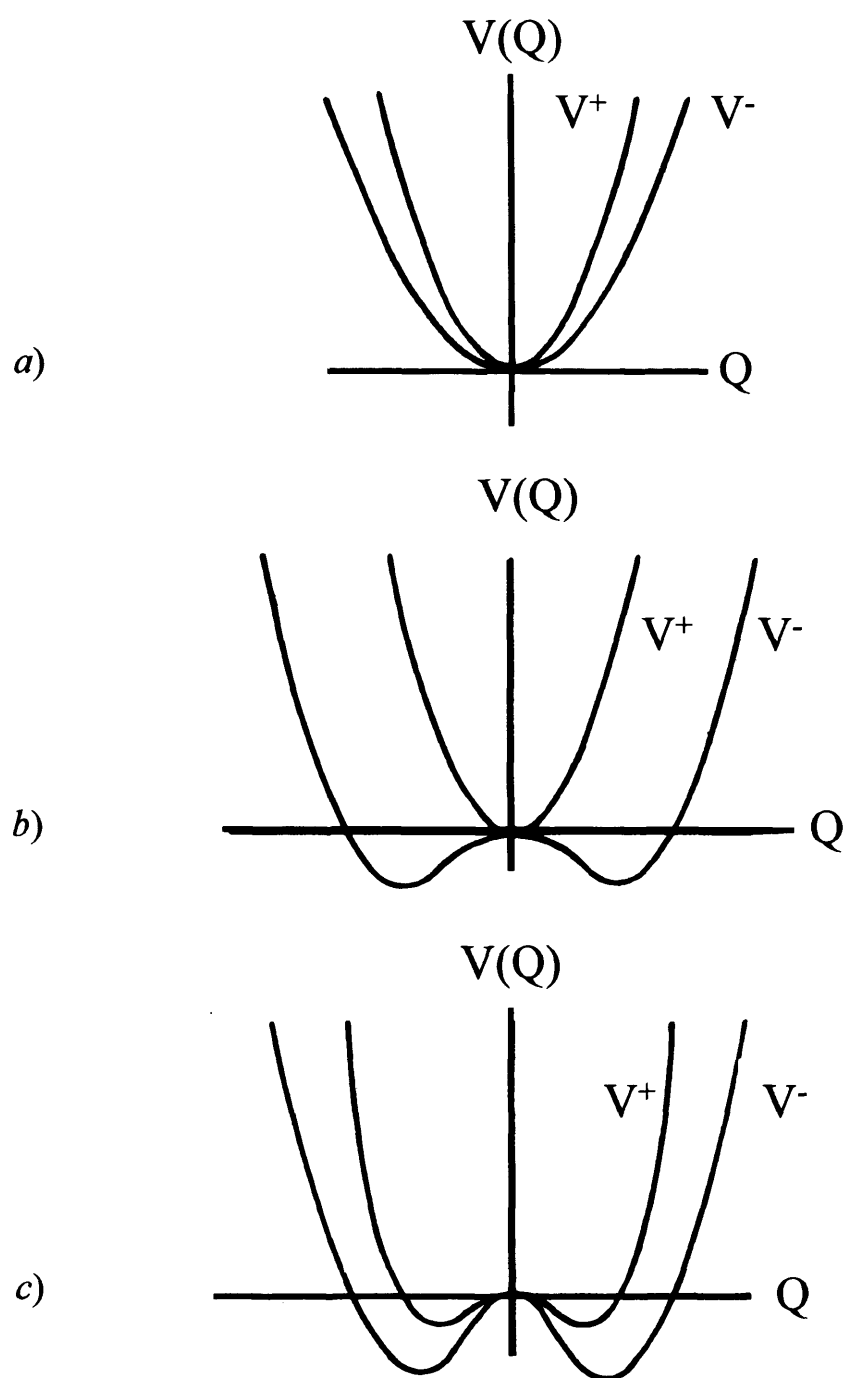


**Fig. 3.4** The three general ways in which the potential curves, representing the bending co-ordinate in linear triatomic molecules, behave under Renner-Teller coupling. *a)* represents the limiting case in which both curves have an identical minimum in the linear configuration, *b)* the case where one component of the electronic state is linear and the other is bent, and *c)* the case where the equilibrium configurations of both components are bent.<sup>54</sup>



Renner-Teller coupling has been identified experimentally in many linear molecules, including several of the alkaline-earth monohydroxides.<sup>27,34</sup> As will be seen in Chapters 4 and 5, the Renner-Teller effect is thought to have significant consequences for the spectroscopy of BaOH and SrOH, in their respective  $\tilde{C}^2\Pi$  states.

### 3.5.3 *Other types of angular momentum interactions*

#### 3.5.3.1 *Lambda-type doubling*<sup>54</sup>

In the discussion of Hund's case (a) for linear molecules (section 3.5.1) it was implicitly assumed that any interaction between the rotation of nuclei and the orbital angular momentum could be neglected. For small rotational speeds this assumption is usually acceptable, but for faster rotation this interaction can be important, since it produces a doublet splitting for each  $J$  value in states which are nominally doubly degenerate ( $\Lambda > 0$ ). In multiplet states, the rotational levels of each component of the multiplet split into two  $\Lambda$ -type components, denoted by the parity labels +/- or e/f (see Fig. 3.5(a)). In general, the doublet splitting increases with increasing  $J$ . Fig. 3.5(b) illustrates the extent of the splitting with increasing  $J$  for the two spin-orbit components of a  $^2\Pi$  state, but is significantly exaggerated. In most cases, the splitting is small, usually very much less than  $1\text{ cm}^{-1}$ . Consequently, very high resolution spectroscopy is normally required to see the effect of lambda doubling. In this work lambda doubling was not observable.

#### 3.5.3.2 *Spin-rotation interaction*<sup>55</sup>

Another form of angular momentum coupling arises through the interaction of electron spin angular momentum with rotational angular momentum. The result is for each rotational level to be split into multiplets, depending on the number of unpaired electrons. Clearly, for singlet states, in which  $S = 0$ , there can be no spin-rotation interaction. For doublet states, in which  $S = 1/2$ , the rotational levels are split into pairs corresponding to  $J \pm 1/2$ . These pairs share a common rotational quantum number,  $N$ , which, strictly speaking, is not a good quantum number in the presence of spin-rotation coupling. However, the coupling between the two angular momenta is extremely weak and the resulting spin-rotation splitting, usually defined by the spin-rotation constant,  $\gamma$ , is very small. Indeed, such small splittings will be unresolvable at the resolution of the laser used in this work.

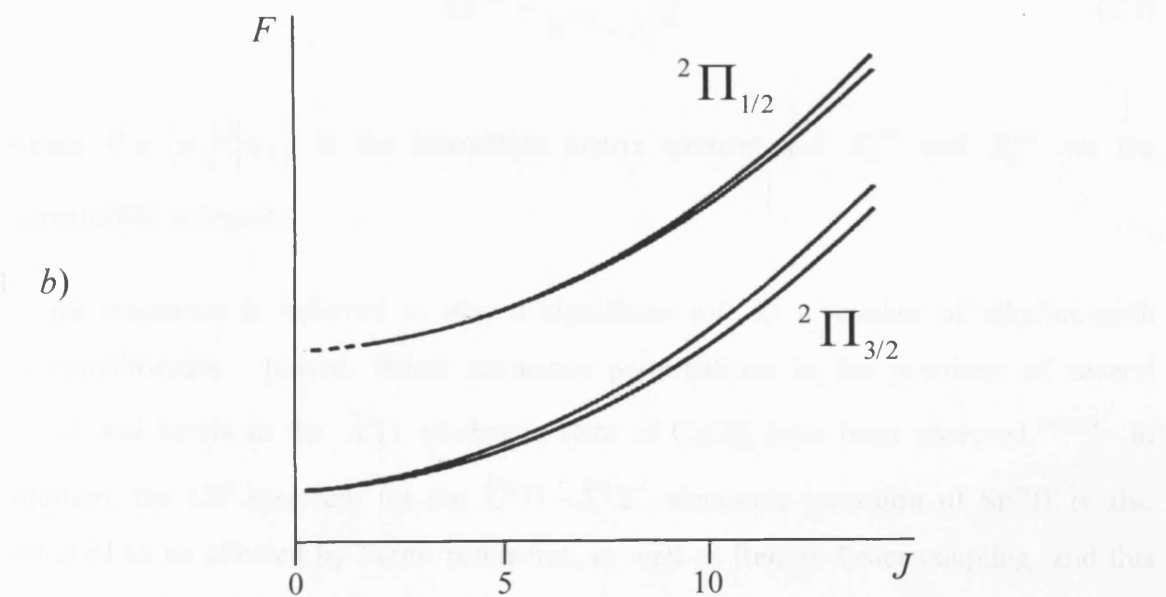
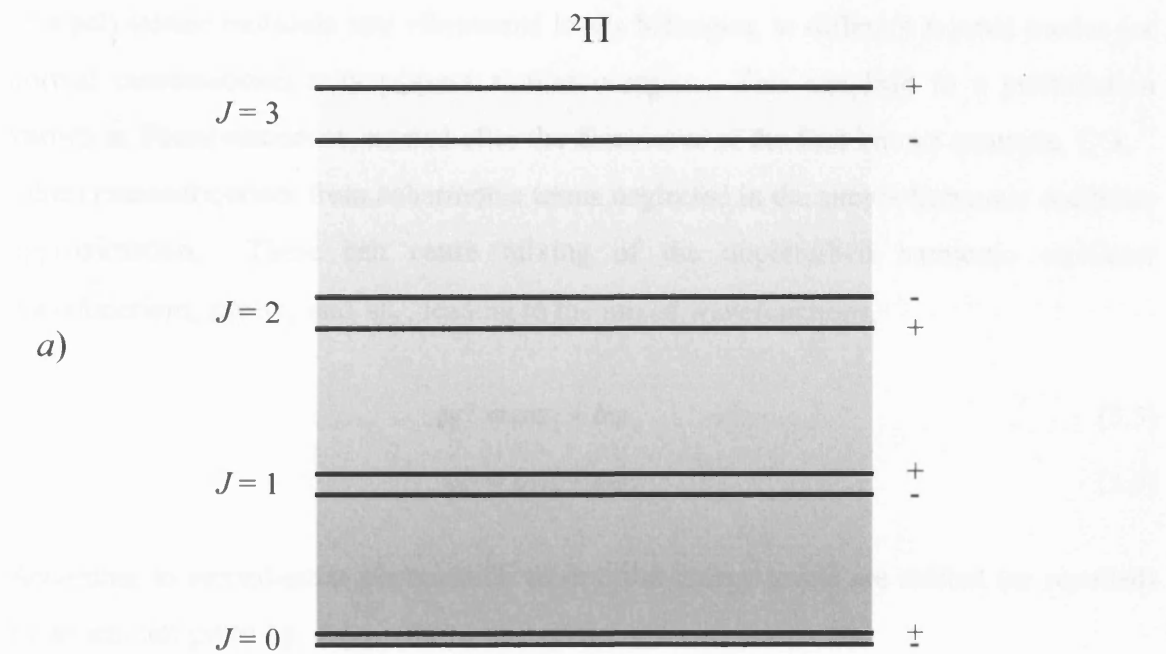


**Fig. 3.5** a) Energy level diagram showing the multiplet  $\Lambda$ -type splitting for respective  $J$  levels of a  $^2\Pi$  state. The labels  $\pm$  refer to the parities of the rotational bands. b) Diagram illustrating the increase in  $\Lambda$ -type doubling for a  $^2\Pi$  state. The  $\Lambda$ -type doubling increases as  $J$  increases.

### 3.6 *Fermi resonance*<sup>56</sup>

In a polyatomic molecule two vibrational levels belonging to different normal modes (or normal combinations) may possess similar energies. This can lead to a perturbation known as Fermi resonance, named after the discoverer of the first known example, CO<sub>2</sub>.<sup>57</sup> Fermi resonance arises from anharmonic terms neglected in the simple harmonic oscillator approximation. These can cause mixing of the unperturbed harmonic oscillator wavefunctions, say  $\psi_1$  and  $\psi_2$ , leading to the mixed wavefunctions,

$$\psi^+ = a\psi_1 + b\psi_2 \quad (3.5)$$

$$\psi^- = b\psi_1 - a\psi_2 \quad (3.6)$$

According to second-order perturbation theory, the energy levels are shifted (or repelled) by an amount given by,

$$\Delta E^{(2)} = \frac{V^2}{E_2^{(0)} - E_1^{(0)}} \quad (3.7)$$

where  $V = \langle \psi_1 | \hat{V} | \psi_2 \rangle$  is the interaction matrix element and  $E_2^{(0)}$  and  $E_1^{(0)}$  are the unperturbed energies.

Fermi resonance is believed to play a significant role in a number of alkaline-earth monohydroxides. Indeed, Fermi resonance perturbations in the positions of several vibrational levels in the  $\tilde{A}^2\Pi$  electronic state of CaOH have been observed.<sup>22,34,38</sup> In addition, the LIF spectrum for the  $\tilde{C}^2\Pi - \tilde{X}^2\Sigma^+$  electronic transition of SrOH is also believed to be affected by Fermi resonance, as well as Renner-Teller coupling, and this will be considered in more detail in Chapter 5.

## References

- 1 C.G. James and T.M. Sugden, *Nature*, **175** (1955) 133.
- 2 A.G. Gaydon, *Proc. Phys. Soc. A.*, **231** (1955) 437
- 3 M. Charton and A.G. Gaydon, *Proc. Phys. Soc. A.*, **69** (1956) 520
- 4 A. Lagerqvist and L. Hultdt, *Naturwissenschaften*, **42** (1955) 365
- 5 H. Haraguchi, S.J. Weeks and J.D. Winefordner, *Spectrochim. Acta A*, **35** (1979) 391
- 6 R.F. Wormsbecher, M. Trkula, C. Martner, R.E. Penn and D.O. Harris, *J. Mol. Spec.*, **97** (1983) 29
- 7 J. Nakagawa, R.F. Wormsbecher and D.O. Harris, *J. Mol. Spec.*, **97** (1983) 37
- 8 R.F. Wormsbecher, R.E. Penn and D.O. Harris, *J. Mol. Spec.*, **97** (1983) 65
- 9 R.C. Hilborn, Z. Qingshi and D.O. Harris, *J. Mol. Spec.*, **97** (1983) 73
- 10 P.F. Bernath, *Science*, **254** (1991) 665
- 11 A. Bernard, C. Effantin, E. Andrianavalona, J. Verges and R.F. Barrow, *J. Mol. Spec.*, **152** (1992) 174
- 12 M.A. Anderson and L.M. Ziurys, *Chem. Phys. Lett.*, **224** (1994) 381
- 13 A.R. Allouche, G. Wannous and M. Aubert-Frecon, *Chem. Phys.*, **170** (1993) 11
- 14 P.F. Bernath, R.W. Field, B. Pinchemel, Y. Lefebvre and J. Schamps, *J. Mol. Spec.*, **88** (1981) 175
- 15 O. Launila, P. Royen and M. Zackrisson, *Mol. Phys.*, **78** (1993) 763
- 16 S.F. Rice, H. Martin and R.W. Field, *J. Chem. Phys.*, **82** (1985) 5023
- 17 W.E. Ernst and J. Kandler, *Phys. Rev. A.*, **39** (1989) 1575
- 18 K.P. Huber and G. Herzberg, *Molecular Spectra and Molecular Structure. IV. Constants of Diatomic Molecules* (Van Nostrand Reinhold, New York, 1979)
- 19 J.A. Coxon, M. Li and P.I. Presunka, *Mol. Phys.*, **76** (1992) 1463
- 20 R.C. Hilborn, Z. Qingshi and D.O. Harris, *J. Mol. Spec.*, **97** (1983) 73
- 21 J.A. Coxon, M.G. Li and P.I. Presunka, *J. Mol. Spec.*, **150** (1991) 33
- 22 P.F. Bernath and S. Kinsey-Nielsen, *Chem. Phys. Lett.*, **105** (1984) 663
- 23 Y. Ni, *Ph.D Thesis*, University of California (Santa Barbara), 1986
- 24 C.R. Brazier, L.C. Ellingboe, S. Kinsey-Nielsen and P.F. Bernath, *J. Am. Chem. Soc.*, **108** (1986) 2126
- 25 W.T.M.L. Fernando, M. Douay and P.F. Bernath, *J. Mol. Spec.*, **144** (1990) 344

- 26 C.N. Jarman and P.F. Bernath, *J. Chem. Phys.*, **97** (1992) 1711
- 27 R. Pereira and D.H. Levy, *J. Chem. Phys.*, **105** (1996) 9733
- 28 R.A. Hailey, C. Jarman and P.F. Bernath, *J. Chem. Phys.*, **107** (1997) 669
- 29 W.L. Barclay Jr., M.A. Anderson and L.M. Ziurys, *Chem. Phys. Lett.*, **196** (1992) 225
- 30 P.R. Bunker, M. Kolbuszewski, P. Jensen, M. Brumm, M.A. Anderson, W.L. Barclay Jr., L.M. Ziurys, Y. Ni and D.O. Harris, *Chem. Phys. Lett.*, **239** (1995) 217
- 31 P.F. Bernath and C.R. Brazier, *Astrophys. J.*, **288** (1985) 373
- 32 T.C. Steimle, D.A. Fletcher, K.Y. Jung and C.T. Scurlock, *J. Chem. Phys.*, **96** (1992) 2556
- 33 M.G. Li and J.A. Coxon, *J. Chem. Phys.*, **97** (1992) 8961
- 34 Z.J. Jakubek and R.W. Field, *J. Chem. Phys.*, **98** (1993) 6574
- 35 J.A. Coxon, M.G. Li and P.I. Presunka, *J. Mol. Spec.*, **164** (1994) 118
- 36 M.G. Li and J.A. Coxon, *J. Chem. Phys.*, **102** (1995) 2663
- 37 M.G. Li and J.A. Coxon, *J. Chem. Phys.*, **104** (1996) 4961
- 38 M.G. Li and J.A. Coxon, *Can. J. Phys.*, **72** (1994) 1200
- 39 C.T. Scurlock, D.A. Fletcher and T.C. Steimle, *J. Mol. Spec.*, **159** (1993) 350
- 40 L.M. Ziurys, W.L. Barclay and M.A. Anderson, *Astrophys. J.*, **384** (1992) L63
- 41 M.A. Anderson, M.D. Allen, W.L. Barclay and L.M. Ziurys, *Chem. Phys. Lett.*, **205** (1993) 415
- 42 T. Gustavsson, C. Alcaraz, J. Berlande, J. Cuvelier, J.-M. Mestdagh, P. Meynadier, P. de Pujo, O. Sublemontier and J.-P. Visticot, *J. Mol. Spec.*, **145** (1991) 210
- 43 S. Kinsey-Nielson, C.R. Brazier and P.F. Bernath, *J. Chem. Phys.*, **84** (1986) 698
- 44 J. Nakawaga, R.F. Wormsbecher and D.O. Harris, *J. Mol. Spec.*, **97** (1983) 37
- 45 C.R. Brazier and P.F. Bernath, *J. Mol. Spec.*, **114** (1985) 163
- 46 P.A. Bonczyk, *Appl. Opt.*, **28** (1989) 1529
- 47 T.C. Steimle, D.A. Fletcher, K.Y. Jung and C.T. Scurlock, *J. Chem. Phys.*, **96** (1992) 2556
- 48 M.A. Anderson, W.L. Barclay Jr. and L.M. Ziurys, *Chem. Phys. Lett.*, **196** (1992) 166

- 49 D.A. Fletcher, K.Y. Jung, C.T. Scurlock and T.C. Steimle, *J. Chem. Phys.*, **98**  
(1993) 1837
- 50 P.I. Presunka and J.A. Coxon, *Can. J. Chem.*, **71** (1993) 1689
- 51 P.I. Presunka and J.A. Coxon, *Chem. Phys.*, **190** (1995) 97
- 52 P.I. Presunka and J.A. Coxon, *J. Chem. Phys.*, **101** (1994) 201
- 53 G. Herzberg, *Molecular Spectra and Molecular Structure. I. Spectra of  
Diatomic Molecules* (Van Nostrand Reinhold, New York, 1967).
- 54 G. Herzberg, *Molecular Spectra and Molecular Structure. III. Electronic  
Spectra and Electronic Structure of Polyatomic Molecules* (Van Nostrand  
Reinhold, New York, 1966)
- 55 H. Lefebvre-Brion and R.W. Field, *Perturbations in the Spectra of Diatomic  
Molecules*, (Academic Press, Inc., London, 1986)
- 56 J.M. Hollas, *High Resolution Spectroscopy*, (Wiley, London, 1998)
- 57 E. Fermi, *Z. Physik*, **71** (1931) 250

## *Chapter Four*

*Electronic spectroscopy of the  $\tilde{C} - \tilde{X}$   
and  $\tilde{D} - \tilde{X}$  transitions of BaOH*

## 4.1 Introduction

In 1979, Haraguchi and co-workers<sup>1</sup> re-investigated the BaOH band systems in the green and near-IR regions that James and Sugden had studied in barium-containing flames during the 1950's.<sup>2</sup> Their laser-induced fluorescence study revealed overlapping spectra, attributed to contributions from both BaO and BaOH, in the 18500-21000 cm<sup>-1</sup> region of the spectrum. Bands arising from the  $A^1\Sigma^+ - X^1\Sigma^+$  system of BaO were easily identified by their strong red-shading. Two broad bands were also observed, centred at  $\sim 19500$  cm<sup>-1</sup> and  $\sim 20500$  cm<sup>-1</sup> respectively, which are at the same positions as the  $\tilde{C}^2\Pi - \tilde{X}^2\Sigma^+$  bands of BaOH assigned by James and Sugden.<sup>2</sup> The resolution was insufficient for a rigorous assignment in the LIF work of Haraguchi *et al.*, and therefore the two bands were attributed to BaOH by analogy with the earlier work of James and Sugden.

As outlined in the previous chapter, these very low resolution investigations are the only studies of BaOH that have been carried out for electronic states other than the  $\tilde{X}^2\Sigma^+$ ,  $\tilde{A}^2\Pi$ ,  $\tilde{A}'^2\Delta$  and  $\tilde{B}^2\Sigma^+$  states.<sup>3,4</sup> In this chapter a new electronic transition of BaOH, identified as the  $\tilde{D}^2\Sigma^+ - \tilde{X}^2\Sigma^+$  system, is reported for the first time.<sup>5</sup> The  $\tilde{D} - \tilde{X}$  spectrum is dominated by a single vibrational progression, which has been assigned to the Ba-O stretching vibration in the  $\tilde{D}$  state.

Secondly, the findings from a re-investigation, under supersonic conditions, of the  $\tilde{C} - \tilde{X}$  system of BaOH are presented.<sup>5</sup> Surprisingly, the LIF spectrum of this system is more complicated than expected by analogy with related molecules, notably BaF. Two band systems, very close to each other and each apparently showing a spin-orbit splitting, were observed. Possible explanations for this behaviour are discussed.

## 4.2 Experimental

Details of the laboratory apparatus and general experimental procedure for laser ablation experiments can be found in Chapter 2.

BaOH was produced by laser ablation of barium metal. In a typical experiment, ArF excimer laser pulses, with energies in the region of 30 mJ, were softly focused onto the barium surface in synchronisation with the arrival of gas pulses from the pulsed valve. In initial experiments, hydrogen peroxide was seeded into helium carrier gas to help form



BaOH, but it was subsequently found that this had little impact on the BaOH concentration in the supersonic jet.

The post-ablation mixture was expanded into a Roots-pumped vacuum chamber to form a supersonic jet. In this work, for both laser excitation and dispersed fluorescence spectroscopy, the jet was crossed  $\sim 25$  mm downstream from the nozzle by the dye laser beam. The dye laser was operated without an intracavity etalon (giving a linewidth of  $\sim 0.2$  cm $^{-1}$ ). All other details are as given in Chapter 2.

### 4.3 *Results and discussion*

#### 4.3.1 *The $\tilde{D}^2\Sigma^+ - \tilde{X}^2\Sigma^+$ system*

##### 4.3.1.1 *Vibrational structure*

An LIF excitation spectrum covering the range 22700-24400 cm $^{-1}$  is shown in Fig. 4.1. Three distinct band groups can be identified in the spectrum, centred at 23057, 23622 and 24172 cm $^{-1}$ . The spectral carrier is undoubtedly barium-containing since no LIF signal was observed when the barium target was removed. Possible candidates are limited since in most experiments no precursor molecules were seeded into the carrier gas. As mentioned earlier, when hydrogen peroxide, or water, was used as the precursor no significant enhancement in the magnitude of the LIF signal was observed. Therefore, it is most likely that the spectral carrier originates from laser ablation of BaO or Ba(OH) $_2$  on the barium surface. Consequently, possible identities for the spectral carrier include Ba $_2$ , BaO, BaH, or BaOH, but it is easily confirmed to be BaOH using dispersed fluorescence spectroscopy.

The dispersed fluorescence spectrum obtained by pumping the 23057 cm $^{-1}$  band, shown in Fig. 4.2(a), exhibits a short progression of interval  $495 \pm 5$  cm $^{-1}$ . Kinsey-Nielson *et al.*<sup>3</sup> obtained a value of 492.4 cm $^{-1}$  for the Ba-O stretch ( $\nu_3$ ) in the  $\tilde{X}^2\Sigma^+$  ground electronic state of BaOH and so the progression in Fig. 4.2(a) is assigned to  $\nu_3$  in BaOH. Kinsey-Nielson *et al.* also reported a frequency of 661.1 cm $^{-1}$  for two quanta in the Ba-O-H bending mode ( $\nu_2$ ). This correlates well with a weak peak some  $660 \pm 5$  cm $^{-1}$  to the red of the pump position in our dispersed fluorescence spectrum. The Ba-O-H bend is a non-totally symmetric vibrational mode and therefore, from symmetry arguments, single quantum excitation of this mode is forbidden in the Franck-Condon limit.<sup>6</sup> In fact, a very weak but reproducible band, identified in Fig. 4.2(a), is observed at the single quantum

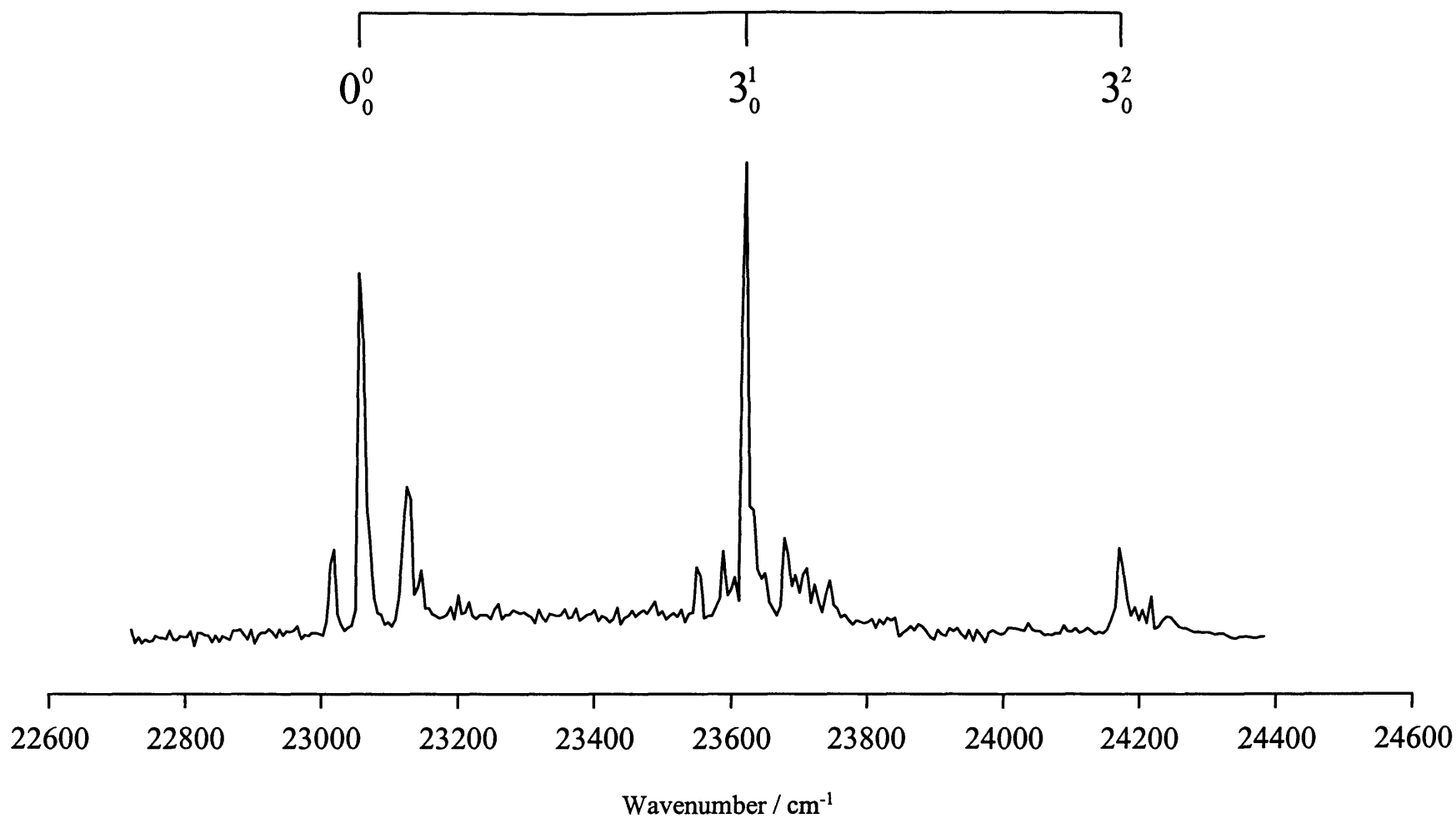


**Fig. 4.1** Jet-cooled laser excitation spectrum of the  $\tilde{D}^2\Sigma^+ - \tilde{X}^2\Sigma^+$  transition of BaOH. Mode  $\nu_3$  is the Ba-O stretching vibration. Sequence structure is seen surrounding each main member of the  $\nu_3$  progression (see text for more details).

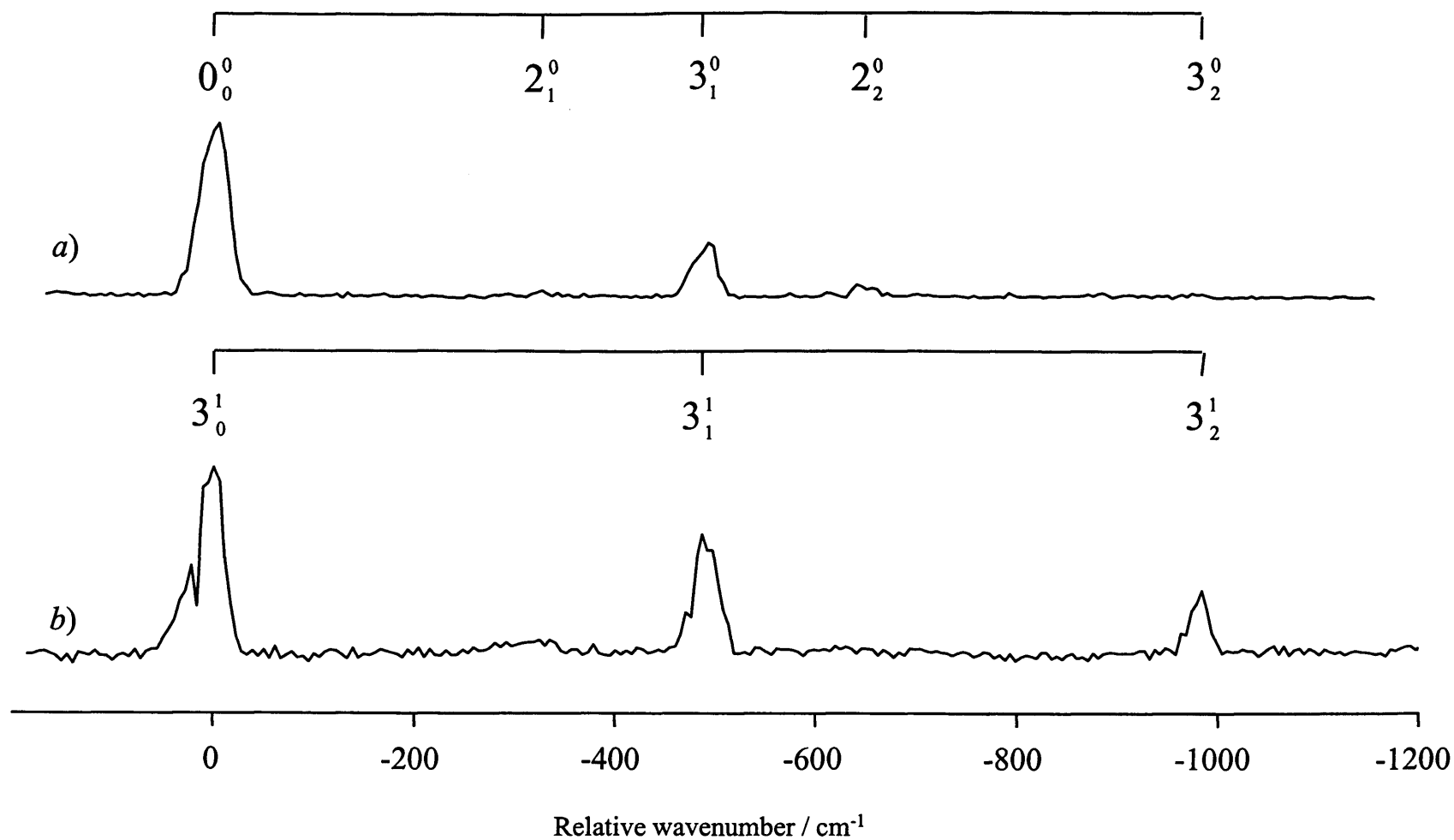


**Fig.4.2** Dispersed fluorescence spectra obtained pumping transitions at *a*) 23057  $\text{cm}^{-1}$  and *b*) 23622  $\text{cm}^{-1}$ .

position for the Ba-O-H bend. The increased intensity for this transition must be achieved via a Herzberg-Teller intensity stealing mechanism.<sup>7</sup>

The peak at 23057 cm<sup>-1</sup> in the excitation spectrum is assigned as the 0<sub>0</sub><sup>0</sup> band of this new BaOH electronic transition, since no additional bands of any significant intensity were observed in the 22000-23000 cm<sup>-1</sup> region. Since the Ba-O stretch is the major Franck-Condon active mode in the dispersed fluorescence spectrum, the same should be true in the excitation spectrum. The bands at 23057, 23622, and 24172 cm<sup>-1</sup> are therefore assigned to a vibrational progression in the Ba-O stretching mode. This gives a Ba-O stretching frequency in the excited state of 563 cm<sup>-1</sup>, significantly larger than the ground electronic state. Confirmation of this assignment is provided by the dispersed fluorescence spectrum obtained by pumping the 23622 cm<sup>-1</sup> transition, assigned to the 3<sub>0</sub><sup>1</sup> transition, which as expected shows a clear enhancement in the Ba-O stretching progression (see Fig. 4.2(b)).

In addition to the main progression, sequence bands can also be seen in the excitation spectrum. The band immediately to the blue (+69 cm<sup>-1</sup>) of the 0<sub>0</sub><sup>0</sup> band is consistent with the 3<sub>1</sub><sup>1</sup> transition using the Ba-O stretching frequencies of the  $\tilde{X}$  and  $\tilde{D}$  states quoted earlier.<sup>3</sup> The band to the red (-40 cm<sup>-1</sup>) may be a sequence transition in the Ba-O-H bending mode, since the only other unaccounted for mode, the O-H stretch, will have a much higher frequency and its excited vibrational levels are therefore unlikely to have significant populations. If correct, this would give a frequency of 290 cm<sup>-1</sup> for the Ba-O-H bend in the  $\tilde{D}$  state when combined with the known frequency of this mode in the ground electronic state.<sup>3</sup>

#### 4.3.1.2 *Electronic state assignment*

The spectrum shown in Fig. 4.1 is a new electronic band system of BaOH. To assign the excited state symmetry, a comparison with the well-studied molecule BaF is valuable. Since BaOH is isoelectronic with BaF, it is reasonable to assume that their electronic states will show strong similarities. A comparison of the energies of the known electronic states of the two molecules is given in Fig. 4.3. This figure shows that the origin of the new state of BaOH observed in this work, at 23057 cm<sup>-1</sup>, is at a similar wavenumber to that of the  $D^2\Sigma^+$  state of BaF (24177 cm<sup>-1</sup> for the  $D-X$  0-0 transition).<sup>8</sup> Since all other

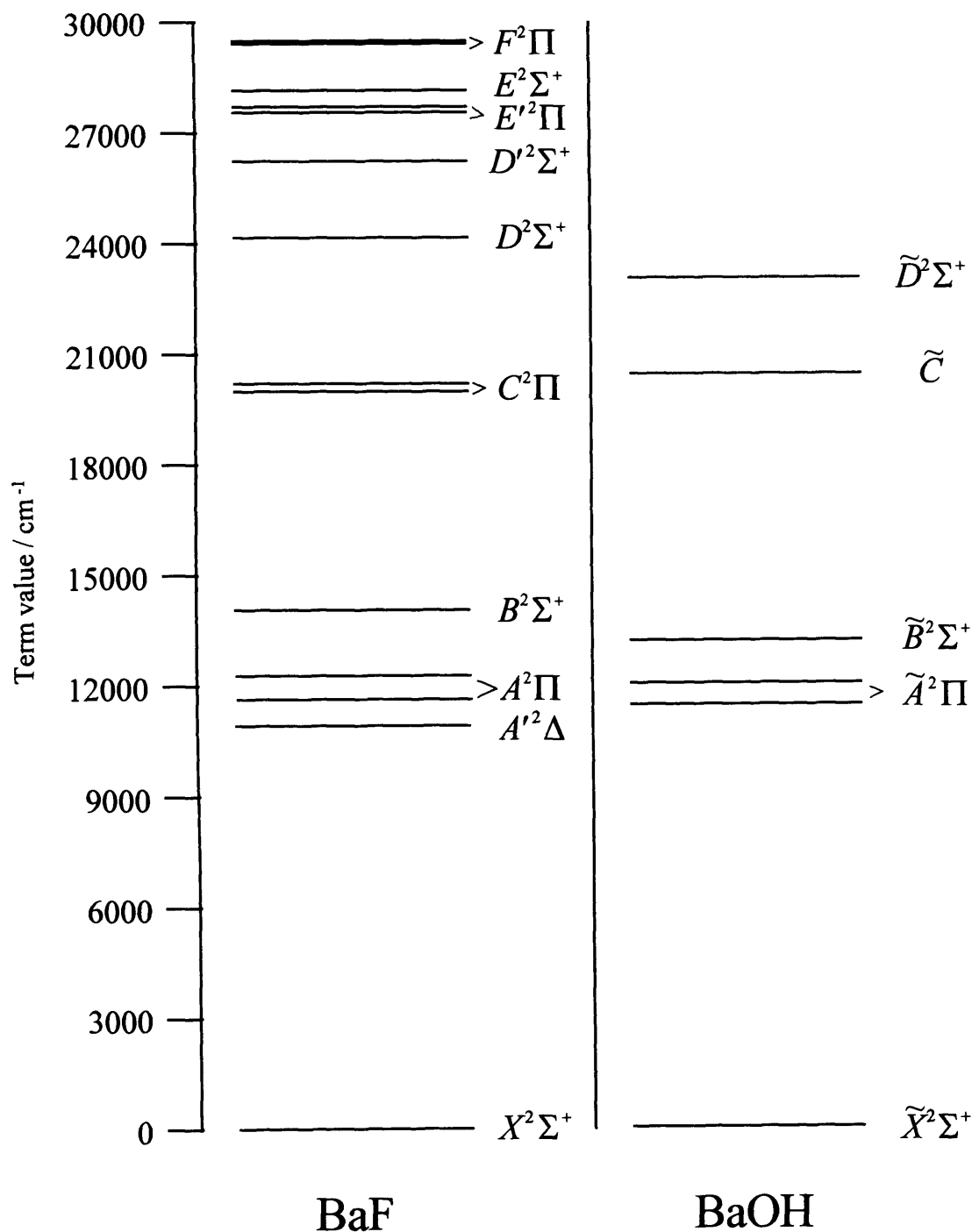


**Fig. 4.3** Comparison of the energies of the known electronic states of BaF and BaOH.  $T_e$  term values, taken from reference 8, are shown for BaF. The spin-orbit splitting of  $^2\Pi$  states is shown. For BaOH the term values correspond to the electronic origin transition wavenumbers. The symmetry of the  $\tilde{C}$  state of BaOH is not shown for reasons discussed in the text. Electronic states of BaOH marked in red have been observed in this work.

known states of BaF are either much higher, or much lower in energy, the BaOH excitation spectrum in Fig. 4.1 is most likely due to the  $\tilde{D}^2\Sigma^+ - \tilde{X}^2\Sigma^+$  transition of BaOH. Since there is no orbital electronic angular momentum associated with a  $^2\Sigma^+$  electronic state, this assignment is consistent with the lack of any observable spin-orbit splitting in the spectrum.

#### 4.3.1.3 Rotational structure

In the current work, the linewidth of the dye laser prevented full rotational resolution, but some structure is resolved in parts of the BaOH bands and is readily assigned. Fig. 4.4(a) shows an expanded view of the  $0_0^0$  band, along with a rotational simulation. At this resolution the rotational structure is entirely consistent with a  $^2\Sigma^+ - ^2\Sigma^+$  electronic transition, showing clear *P*- and *R*-branches, but no *Q*-branch.

A simulation of the rotational structure for the  $\tilde{D} - \tilde{X}$  origin band, assuming a  $^2\Sigma^+ - ^2\Sigma^+$  transition, has been carried out and the result is shown in Fig. 4.4(b). The program SpecSim, developed by Panov and Miller and containing models for  $^2\Pi$  and  $^2\Sigma$  states, was employed for the simulation.<sup>9</sup> This program combines matrix diagonalisation of the appropriate rotational Hamiltonian with transition intensity calculations, non-linear least-squares fitting, and plotting routines, all in a single standardised package. Using the known rotational constant of the  $\tilde{X}^2\Sigma^+$  ground electronic state of BaOH ( $B'' = 0.2166 \text{ cm}^{-1}$ ),<sup>3</sup> the rotational constant in the excited electronic state, together with the temperature, were adjusted. Although the quality of the experimental spectrum is insufficient to obtain a least-squares fit of the simulated spectrum to the assigned structure, a visual best fit yields an approximate value in the excited state rotational constant of  $B' \approx 0.220 \text{ cm}^{-1}$ .

If it is assumed that the O-H bond length does not alter significantly on electronic excitation, the increase in rotational constant is due to a decrease in the Ba-O bond length. This is consistent with the increase in the Ba-O stretching vibrational frequency seen on  $\tilde{D} \leftarrow \tilde{X}$  excitation, implying a strengthening of the Ba-O bond. Comparable behaviour is observed for BaF,<sup>8</sup> thus further supporting the BaOH assignment.

#### 4.3.2 The $\tilde{C} - \tilde{X}$ region

Attention is now turned to the  $\tilde{C} - \tilde{X}$  electronic system of BaOH. As mentioned in the introduction, this system, in conjunction with BaO, is thought to be responsible for the

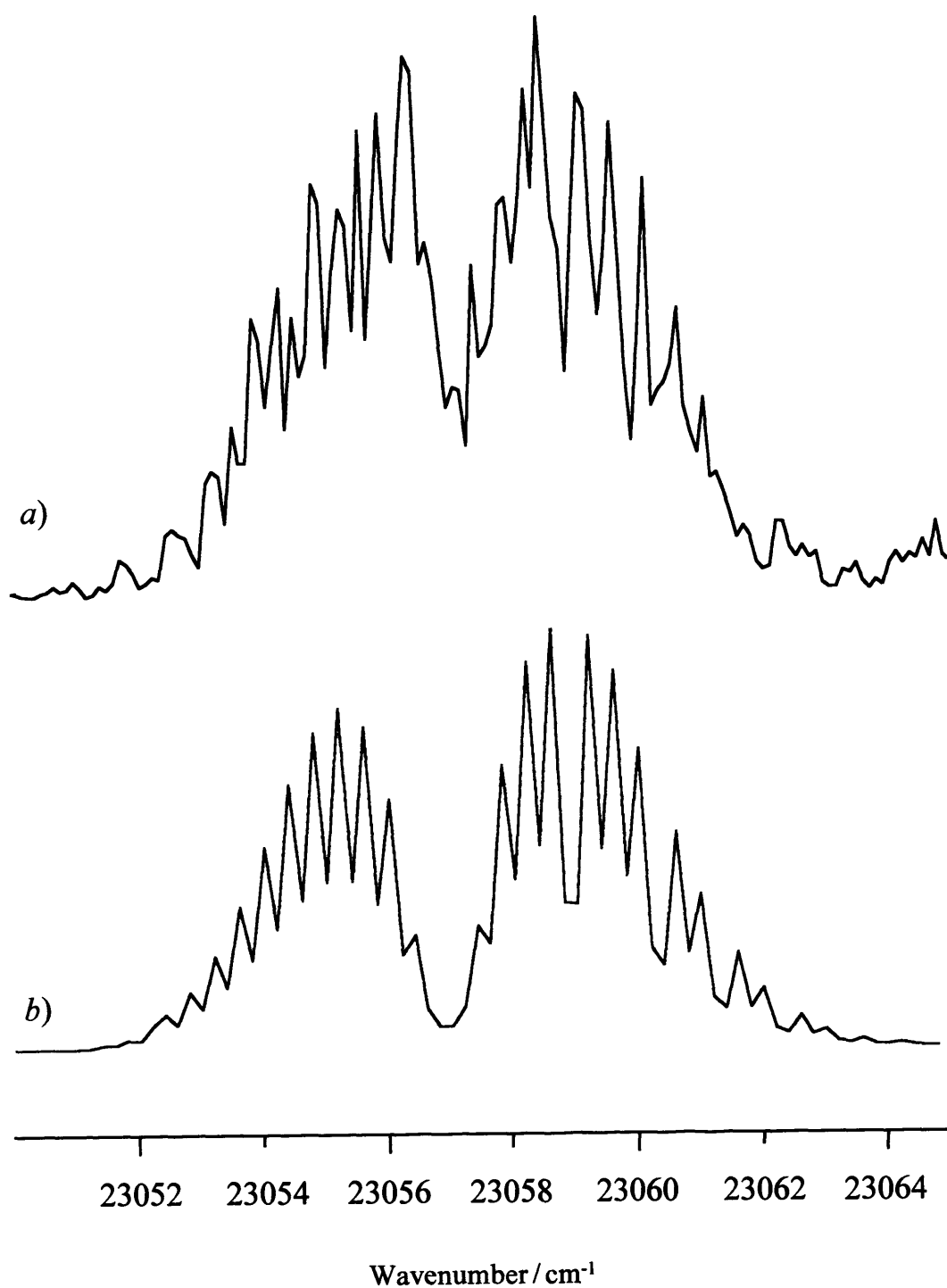


**Fig. 4.4** a) Rotational contour of the band centred at  $23057\text{ cm}^{-1}$ , assigned to the  $\tilde{D}^2\Sigma^+ - \tilde{X}^2\Sigma^+ 0_0^0$  transition. b) Simulation assuming a  $^2\Sigma^+ - ^2\Sigma^+$  transition, a rotational temperature of 25 K,  $B'' = 0.2166\text{ cm}^{-1}$  and  $B' = 0.220\text{ cm}^{-1}$ .

green colour of barium-containing flames and is therefore of considerable interest. However, in earlier spectroscopic studies no firm assignments were made other than identifying bands at 487 and 512 nm (20530 and 19530  $\text{cm}^{-1}$  respectively) as being due to BaOH.<sup>1,2,10</sup> In the current work LIF survey scans of supersonically cooled BaOH were carried out which included the green region of the visible spectrum. The coarse structure in the spectrum is considered initially, followed by a discussion of the rotational structure and possible assignments.

#### 4.3.2.1 *Identifying the BaOH bands*

Fig. 4.5 shows the LIF excitation spectrum recorded between 19750 and 22200  $\text{cm}^{-1}$ . Several strong bands are observed together with many weaker ones. There are two contributors to this spectrum, BaO and BaOH. The BaO  $A^1\Sigma^+ - X^1\Sigma^+$  electronic transition overlaps this region. This system is characterised by a long vibrational progression and strongly red-shaded vibronic bands.<sup>11</sup> In Fig. 4.5 it is not easy to see these characteristic band contours, since the intensities of BaO bands in the excitation spectrum are relatively weak. However, in excitation spectra recorded in this region under slightly different conditions, the BaO bands have considerably stronger intensities and it is relatively simple to identify these transitions. However, it is clear that the strong bands in Fig. 4.5 do not arise from BaO and are therefore attributed to BaOH.

The four strongest bands are found in the 20240-20620  $\text{cm}^{-1}$  region. These would appear to form two spin-orbit doublets, one being the 20270/20548  $\text{cm}^{-1}$  pair and the other the 20355/20605  $\text{cm}^{-1}$  pair. If correct, these imply spin-orbit splittings of 278 and 250  $\text{cm}^{-1}$ , respectively. One way of checking this assignment is to search for other doublets which exhibit these characteristic splittings. Scans to lower wavenumbers revealed no such pairings, and indeed no bands of significant intensities other than those due to BaO were found in the 16000-20000  $\text{cm}^{-1}$  region. However, on the high wavenumber side at least one vibrational progression could be identified showing the 250  $\text{cm}^{-1}$  splitting. Since, apparent spin-orbit splitting is observed for the vibrational members of this progression, this points to the transitions originating from a doubly degenerate electronic state. The selection rule governing electronic transitions in polyatomics requires that  $\Delta\Lambda = 0, \pm 1$ , where  $\Lambda$  is the orbital angular momentum quantum number.<sup>6</sup> As a result, the only allowed transition from the ground  $^2\Sigma^+$  state to an orbitally degenerate excited state is to a  $^2\Pi$  state, assuming forbidden transitions do not gain transition probability through some perturbation. Hence, the symmetry of the excited electronic state is initially assigned as



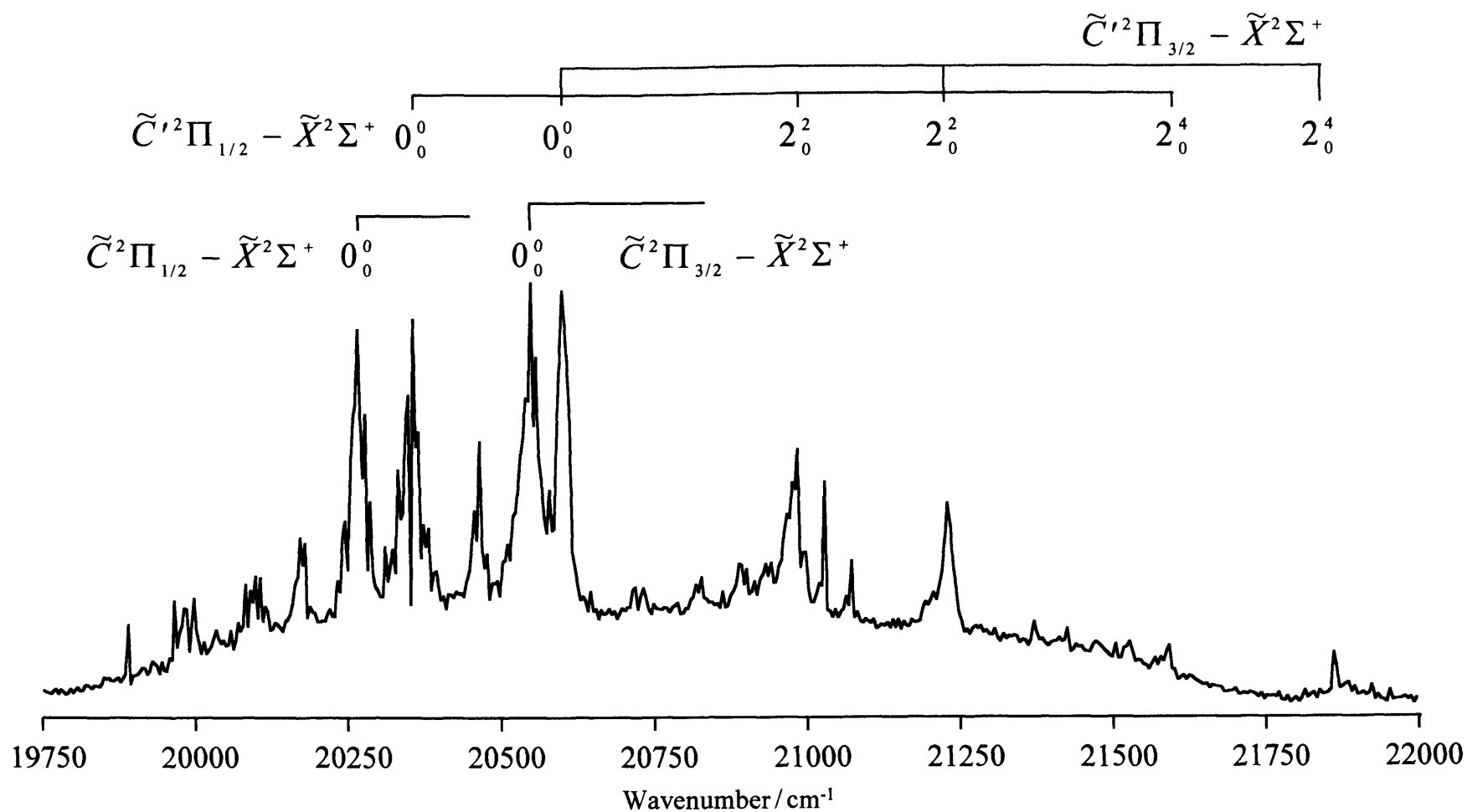


**Fig.4.5** Survey laser excitation scan of the ' $\tilde{C}$ - $\tilde{X}$ ' region of BaOH. This scan covers the full range of the Coumarin 480 laser dye, hence the variation in the background intensity. Note that the labels for the two identified  $^2\Pi$ - $^2\Sigma$  systems have assumed positive spin-orbit coupling constants in both cases since the spin-orbit coupling arises from a single unpaired electron in a  $\pi$  orbital (i.e. the shell is less than half full).

$^2\Pi$ . For reasons discussed later, the progression identified in Fig. 4.5 has been labelled as the  $\nu_2$  bending mode progression in the  $\tilde{C}'^2\Pi - \tilde{X}^2\Sigma^+$  system of BaOH. Any other bands are too weak or too heavily overlapped to be convincingly assigned to specific vibrational progressions.

It is interesting at this point to compare the observations seen in the excitation spectrum with those reported by other groups for this spectral region and also with what would be expected from an analogy with BaF. Considering BaF first, a single observed excited electronic state, the  $C^2\Pi$  state, has been seen in the region under consideration. This state is well-isolated from the  $B$  and  $D$  states, as can be seen by inspecting Fig. 4.3. The  $C^2\Pi$  state has a  $T_e$  value of  $20091\text{ cm}^{-1}$  and a spin-orbit splitting constant of  $195\text{ cm}^{-1}$  in the  $\nu=0$  level.<sup>8</sup> Assuming that the analogy with BaOH is valid, it is difficult to reconcile this with the observations of the BaOH  $\tilde{C}-\tilde{X}$  system by previous workers.<sup>1,2,10</sup> If there is only a single excited electronic state involved, the separation between the two prominent bands reported at  $20534\text{ cm}^{-1}$  (487 nm) and  $19531\text{ cm}^{-1}$  (512 nm) must be due to either a vibrational interval or a spin-orbit splitting. If it is a spin-orbit splitting it would be dramatically different from that of the  $C^2\Pi$  state of BaF. If it is a vibrational interval, it would be too large for single quantum excitation of the Ba-O stretch or the Ba-O-H bend, but far too low for the O-H stretch. Alternatively, the interval may be due to two quanta in the Ba-O stretch, but again this is unlikely since there is no evidence for single quantum excitation between the 487 and 512 nm bands. Although a strong band near to 487 nm is observed, no trace of any band that might correspond to the 512 nm feature has been found in the current excitation spectra, despite repeated attempts to find it. It is possible that the flame spectra contain one, or more, 'hot bands' of BaOH that are not observable in a supersonic jet. However, it is difficult to be convinced of this because of the vibrational interval arguments outlined above. Alternatively, it is possible that the band at 512 nm, attributed to BaOH by previous workers, is not due to BaOH. The second of these two scenarios would seem more likely.

Comparison of the current observations with BaF is more favourable. The quartet of strong bands in the  $20240\text{-}20620\text{ cm}^{-1}$  region are close in energy to the BaF  $C^2\Pi - X^2\Sigma^+$  electronic origin. Furthermore, the two apparent spin-orbit splittings, although larger than

that in the BaF  $C^2\Pi$  state ( $195\text{ cm}^{-1}$ ),<sup>8</sup> are not dissimilar. This observation can be taken as strong evidence that these bands are due to BaOH. However, there is clearly a problem with this assignment since there would appear to be *two* distinct electronic transitions, when comparison with BaF would lead us to expect only one. This point will be returned to later.

#### 4.3.2.2 *Vibrational structure*

As mentioned above, a vibrational progression has been identified in the system labelled  $\tilde{C}'^2\Pi - \tilde{X}^2\Sigma^+$  in Fig. 4.5. The first member, consisting of the pair of bands at 20967 and 21225  $\text{cm}^{-1}$ , is reasonably strong and corresponds to an average vibrational interval of 616  $\text{cm}^{-1}$ . One possibility is that this doublet arises from excitation of one quantum in the Ba-O stretching mode. If correct, this would result in a substantial increase in frequency over the corresponding mode in the ground electronic state of BaOH ( $492.4\text{ cm}^{-1}$ ),<sup>3</sup> thus implying a major strengthening of the Ba-O bond on excitation to the  $\tilde{C}'^2\Pi$  state.

To check this assignment, dispersed fluorescence spectra have been recorded. If the Ba-O stretch is responsible for the major vibrational activity in the excitation spectrum, the Franck-Condon principle suggests that a prominent progression in this mode should be observed in the dispersed fluorescence spectra. Laser excitation at wavelengths corresponding to the four  $0_0^0$  transitions in the  $\tilde{C}^2\Pi - \tilde{X}^2\Sigma^+$  and  $\tilde{C}'^2\Pi - \tilde{X}^2\Sigma^+$  systems yielded qualitatively similar dispersed fluorescence spectra. Fig. 4.6 shows the dispersed fluorescence spectrum obtained by exciting the  $\tilde{C}'^2\Pi_{1/2} - \tilde{X}^2\Sigma^+ 0_0^0$  transition. The Ba-O stretching mode is relatively inactive in this spectrum, the main progression arising from even quantum number changes in the Ba-O-H bending mode,  $\nu_2$ . Even quantum number changes in  $\nu_2$  were also seen in the  $\tilde{D}^2\Sigma^+ - \tilde{X}^2\Sigma^+$  dispersed fluorescence spectra (see Fig. 4.2(a)), but are much weaker in that system.

Given the dominance of the  $\nu_2$  progression in the  $\tilde{C}'^2\Pi - \tilde{X}^2\Sigma^+$  and  $\tilde{C}^2\Pi - \tilde{X}^2\Sigma^+$  dispersed fluorescence spectra, the main progression in the excitation spectrum must also arise from even quantum number changes in  $\nu_2$ , hence the assignment given in Fig. 4.5. This is confirmed by further dispersed fluorescence experiments, which show a dramatic enhancement in the bending progression when laser excitation of the bands at 20967 and 21225  $\text{cm}^{-1}$  is employed (see Fig. 4.7). The vibrational interval in the excitation spectrum

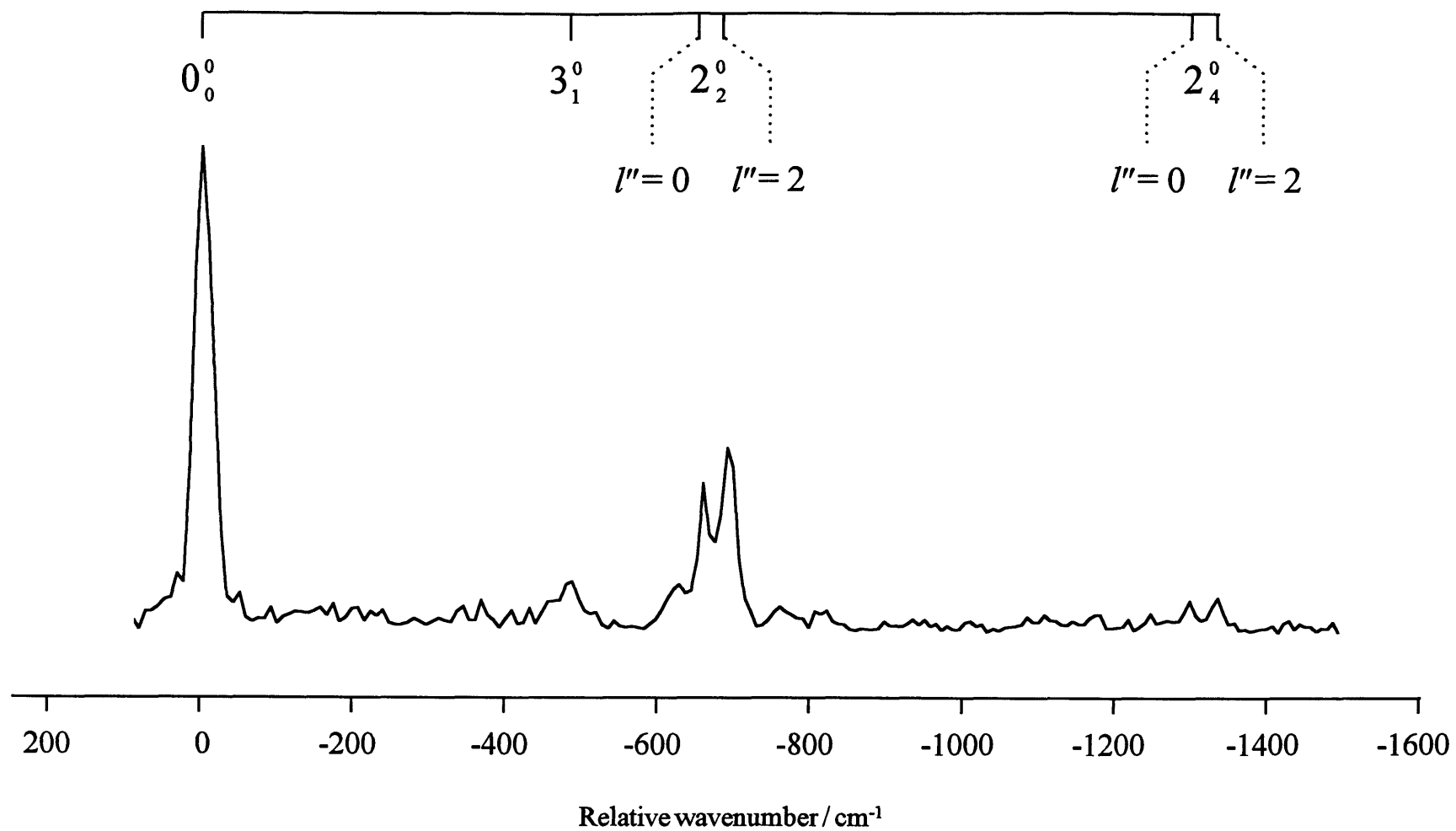


**Fig.4.6** Dispersed fluorescence spectrum following laser excitation of the transition at 20355 cm<sup>-1</sup>.

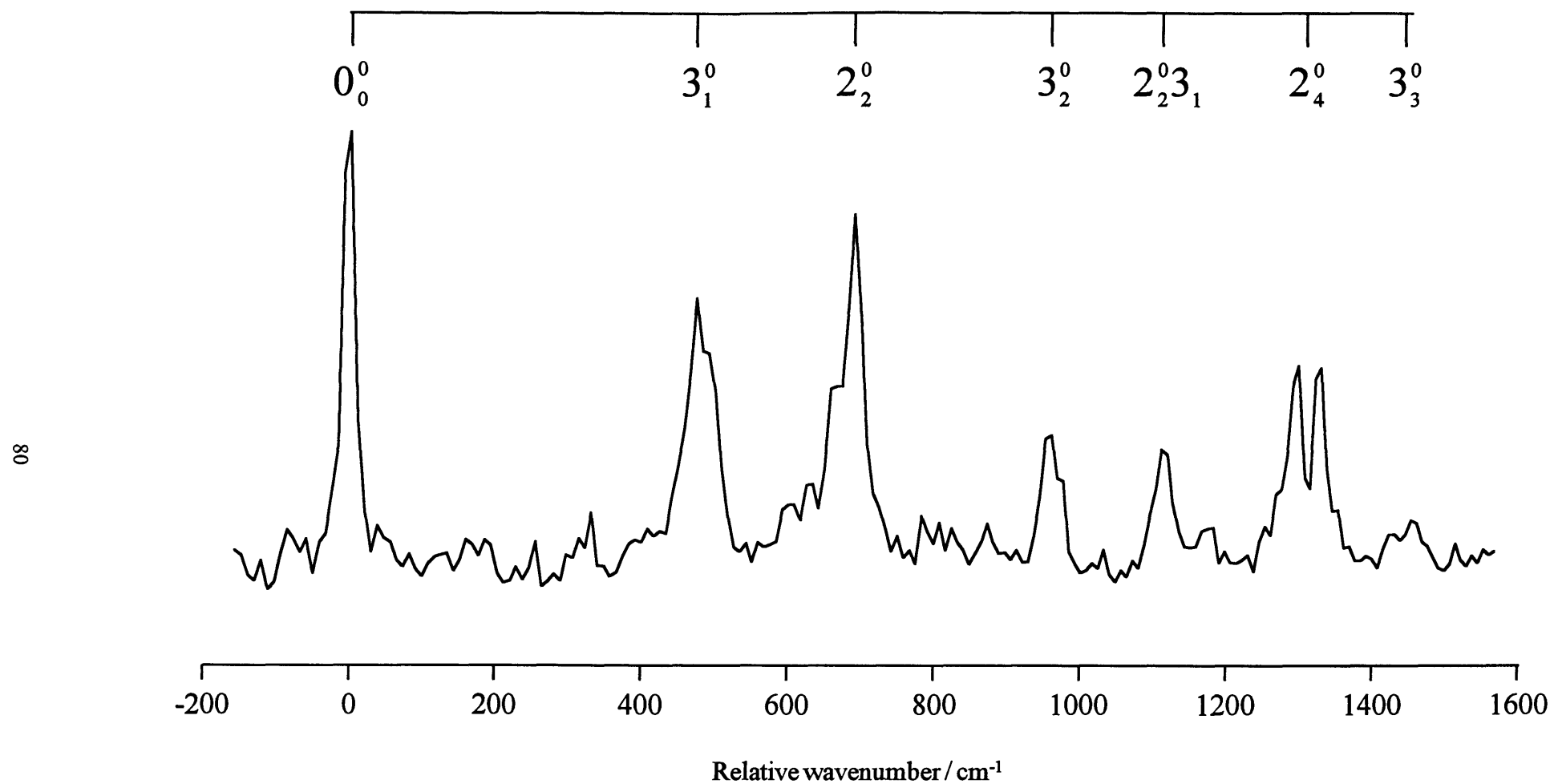


**Fig. 4.7** Dispersed fluorescence spectrum obtained by pumping the transition at 20967 cm<sup>-1</sup>.

(616 cm<sup>-1</sup>) implies a moderate decrease in the bending frequency in the  $\tilde{C}'^2\Pi$  state compared with the  $\tilde{X}^2\Sigma^+$  state ( $2\nu_2 = 661.1$  cm<sup>-1</sup>).<sup>3</sup>

A further member of the  $\tilde{C}'^2\Pi - \tilde{X}^2\Sigma^+$  progression has been identified in the excitation spectrum in Fig. 4.5. Two weak bands, at 21585 and 21853 cm<sup>-1</sup>, respectively, have a doublet splitting (268 cm<sup>-1</sup>) and vibrational interval (average 623 cm<sup>-1</sup>) compatible with the next even quanta member of the  $\nu_2$  progression. However, dispersed fluorescence spectra from the upper states of these bands were too weak to prove useful in assigning them conclusively.

To close this section, the dispersed fluorescence spectrum, shown in Fig. 4.6, is reconsidered. The  $2_2^0$  and  $2_4^0$  bands are both split by  $\sim 30$  cm<sup>-1</sup> into two components due to vibrational anharmonicity. Neglecting off-diagonal anharmonicity, the term value of a doubly degenerate bending vibration is given by,<sup>6</sup>

$$G(\nu_2, l) = \omega_2(\nu_2 + 1) + x_{22}(\nu_2 + 1)^2 + g_{22}l^2 \quad (4.1)$$

where  $l$  is the vibrational angular momentum (see section 3.5.2). For  $\nu_2 = 2$ ,  $l$  can be 0 or 2, giving rise to  $^2\Sigma^+$  and  $^2\Delta$  vibronic states, respectively, in the  $\tilde{X}^2\Sigma^+$  electronic state manifold. For  $\nu_2 = 4$ , three vibronic levels are possible but, as made clear in Fig. 4.8, only the  $l = 0$  and  $l = 2$  levels have the correct vibronic symmetry to be optically accessible from an upper state of  $^2\Pi$  vibronic symmetry. Thus, the same splitting (arising from the  $g_{22}l^2$  term in equation (4.1)) is expected for the  $2\nu_2$  and  $4\nu_2$  bands in the dispersed fluorescence spectrum and this is indeed observed in Fig. 4.6, although the  $4\nu_2$  doublet is very weak. A value of *ca.* 8 cm<sup>-1</sup> is obtained for  $g_{22}$ , which is close to that previously reported for the ground electronic state of SrOH.<sup>12</sup>

#### 4.3.2.3 Rotational analysis

As mentioned earlier, the linewidth of the dye laser prevented full rotational resolution but, as for the  $\tilde{D} - \tilde{X}$  system, some structure is resolved in parts of the BaOH bands and can be readily assigned. Fig. 4.9(a) shows an expanded view of the band assigned to the  $\tilde{C}'^2\Pi_{1/2} - \tilde{X}^2\Sigma^+ 0_0^0$  transition in the excitation spectrum (see Fig. 4.5), and clearly shows

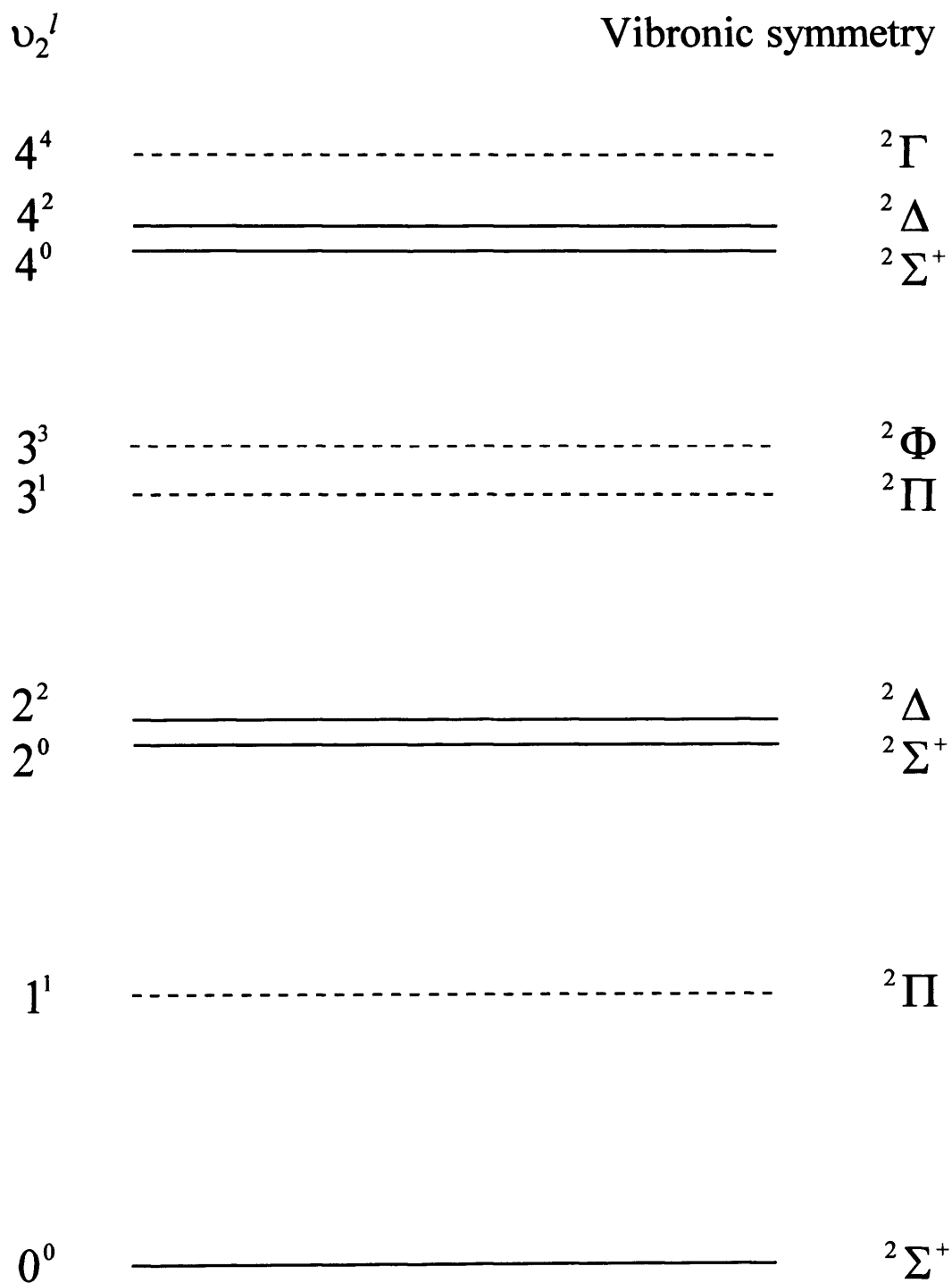


**Fig. 4.8** Illustration of the low-lying vibrational levels of the Ba-O-H bending mode in the ground electronic state. The dotted lines correspond to those levels that are optically forbidden in transitions from the zero point level of a  $^2\Pi$  electronic state.





the coarse '3B, B, -B, -3B' structure expected for a  ${}^2\Pi(a)-{}^2\Sigma^+$  transition.<sup>6</sup> The apparent spin-orbit splitting seen in the excited state is more than large enough to satisfy the Hund's case (a) limit ( $A \gg BJ$ ) and, since a  ${}^2\Pi-{}^2\Sigma^+$  transition is expected, by analogy with BaF, the rotational structure seems perfectly reasonable.

Assuming  ${}^2\Pi-{}^2\Sigma^+$  transitions, simulations of the rotational structure in the two spin-orbit pairs (20270/20548 and 20355/20605  $\text{cm}^{-1}$ ) have been carried out. The rotational simulation of the  $\tilde{C}'^2\Pi - \tilde{X}^2\Sigma^+ 0_0^0$  transition (20355  $\text{cm}^{-1}$ ) is shown in Fig. 4.9(b). Using the known rotational constant for the  $\tilde{X}^2\Sigma^+$  ground electronic state of BaOH ( $B'' = 0.2166 \text{ cm}^{-1}$ ),<sup>3</sup> the spin-orbit splitting and rotational constants in the excited electronic state, together with the temperature, were adjusted. A least-squares fit of the simulated spectrum to the assigned structure in the experimental spectrum gives excited state rotational constants of  $B' = 0.2132 \pm 0.0002 \text{ cm}^{-1}$  and  $A' = 278.41 \pm 0.03 \text{ cm}^{-1}$  for the 20270/20548 pair, and  $B' = 0.2136 \pm 0.0003 \text{ cm}^{-1}$  and  $A' = 249.19 \pm 0.03 \text{ cm}^{-1}$  for the 20355/20605 pair. Simulations were also carried out for other possible pairings of the four bands to ascertain if there is any probability that other band pairs are more likely to be spin-orbit doublets. The results of these simulations were inconclusive, since the values obtained for the rotational constants in each case were too similar, within experimental error, to draw any useful conclusions.

It is evident from the rotational structure that, as for the  $\tilde{D}^2\Sigma^+$  state of BaOH, there is no substantial change in rotational constant on electronic excitation, since there is no significant shading of the bands to the red or blue. This is borne out by the rotational constants which, as can be seen on inspection of Table 4.1, are very similar to the ground state value. Once again, this is in line with BaF which shows only a small decrease in the rotational constant on  $\tilde{C} \leftarrow \tilde{X}$  excitation.<sup>8</sup> It is also entirely consistent with the absence of any significant structure in the Ba-O stretching vibration in the excitation spectrum.

For reasons that will be discussed in the next section, there is a possibility that some of the bands in the excitation spectrum (Fig. 4.5) could be due to a nominally forbidden  ${}^2\Delta-{}^2\Sigma^+$  transition of BaOH. The overall rotational structure for  ${}^2\Pi-{}^2\Sigma^+$  and  ${}^2\Delta-{}^2\Sigma^+$  transitions is expected to be similar, but the two could be distinguished by

identifying ‘missing’ rotational lines in fully resolved rotational spectra.<sup>6</sup> For a  ${}^2\Pi - {}^2\Sigma^+$  transition, undergoing Hund’s case (a) coupling in the excited state, the  $P_{12}(\frac{1}{2})$  transition does not exist and will be missing from a rotationally-resolved  ${}^2\Pi_{1/2} - {}^2\Sigma^+$  spectrum. The same is true for  $P_2(\frac{1}{2})$  and  $P_2(\frac{3}{2})$  rotational transitions in a  ${}^2\Pi_{3/2} - {}^2\Sigma^+$  spectrum. In the case of a  ${}^2\Delta - {}^2\Sigma^+$  transition, the  $P_{12}(\frac{1}{2})$  and  $P_{12}(\frac{3}{2})$  transitions do not exist and will be missing from the  ${}^2\Delta_{3/2} - {}^2\Sigma^+$  spectrum. Again, the same is true for the  $P_2(\frac{1}{2})$ ,  $P_2(\frac{3}{2})$ ,  $P_2(\frac{5}{2})$  and  $R_{21}(\frac{1}{2})$  rotational transitions of the  ${}^2\Delta_{5/2} - {}^2\Sigma^+$  transition.

Unfortunately, since the four bands in question are only partially resolved, identification of these ‘missing’ lines is impossible under current resolution. Consequently, the assignment of each band as a  ${}^2\Pi - {}^2\Sigma^+$  or  ${}^2\Delta - {}^2\Sigma^+$  electronic transition cannot be firmly made on the basis of the present data.

**Table 4.1** Molecular constants ( $\text{cm}^{-1}$ ) determined for BaOH compared to those for the analogous states in BaF.

State	Molecular constants <sup>b)</sup>	BaOH	BaF <sup>c)</sup>
$\tilde{D}^2\Sigma^+$	$B_0$	$\approx 0.220 \text{ cm}^{-1}$	0.2273
$\tilde{C}'^2\Pi^a)$	$B_0$	$0.2136 \pm 0.0003$	
	$A$	$249.19 \pm 0.03$	
$\tilde{C}^2\Pi^a)$	$B_0$	$0.2132 \pm 0.0002$	0.2148
	$A$	$278.41 \pm 0.03$	198.8
$\tilde{X}^2\Sigma^+$	$B_0$	$0.216571(11)^d)$	0.2158

a) The assignments of these states are uncertain. See text for further details.

b)  $B_0$  is the rotational constant in the zero point vibrational level and  $A$  is the spin-orbit coupling constant.

c) Taken from references 8 and 13.

d) Taken from reference 3.

#### 4.3.2.4 The BaOH $\tilde{C}$ state: linear or bent?

Finally, the reasons for why two band systems, with apparently similar spin-orbit splittings, and very similar transition energies ( $\Delta T_e \approx 71 \text{ cm}^{-1}$ ) might arise in the ' $\tilde{C}-\tilde{X}$ ' region are considered. Up until this point the two systems have been referred to as the  $\tilde{C}^2\Pi - \tilde{X}^2\Sigma^+$  and  $\tilde{C}'^2\Pi - \tilde{X}^2\Sigma^+$  transitions. However, only one  $^2\Pi - ^2\Sigma^+$  transition is expected in this region by comparison with BaF. Assuming that this comparison holds, and there is no reason to expect that it will not given its success in predicting the positions of other electronic states in BaOH, it seems that two distinct  $^2\Pi - ^2\Sigma^+$  systems are *not* responsible for the spectrum in Fig. 4.5.

An alternative possibility is that there is a  $^2\Delta$  state, with a very similar energy, lying near to the  $\tilde{C}^2\Pi$  state and we are observing a  $^2\Pi - ^2\Sigma^+$  system and a  $^2\Delta - ^2\Sigma^+$  system in close proximity, rather than two different  $^2\Pi - ^2\Sigma^+$  systems. As mentioned above, without full rotational resolution it is impossible to distinguish between these two possibilities. There is no  $^2\Delta$  state known for BaF at the required energy, although a much lower lying  $^2\Delta$  state has been identified in both BaF<sup>14</sup> and BaOH.<sup>4</sup> A transition to a  $^2\Delta$  state from the  $^2\Sigma^+$  ground electronic state is nominally forbidden. However, off-diagonal spin-orbit induced mixing of the  $^2\Delta$  state with the nearby  $^2\Pi$  state could provide the necessary transition moment for a  $^2\Delta - ^2\Sigma^+$  transition. This mechanism has been identified as being responsible for the  $A'^2\Delta - X^2\Sigma^+$  system observed for BaH.<sup>15</sup> It is therefore possible that a  $^2\Delta - ^2\Sigma^+$  transition lies in the ' $\tilde{C}-\tilde{X}$ ' region, although it is pertinent to point out that the corresponding transition has not been observed for BaF.

An alternative mechanism for inducing transition probability, one that is not open to BaF, is vibronic coupling. It might be expected that the Renner-Teller effect (see section 3.5.2) will play a significant role in what is nominally the  $\tilde{C}^2\Pi$  state of BaOH. This can be seen, once again, by drawing on the analogy between the electronic states of BaF and BaOH. In the two lowest optically accessible excited states of BaF, and indeed of all the alkaline-earth monohalides, the unpaired electron is located primarily on the metal atom but, as detailed in Chapter 3, *is in a largely non-bonding orbital polarised away from the halide*. These orbitals are essentially metal  $np/(n-1)d$  hybrid orbitals.<sup>16</sup> The bonding in the

two lowest obtainable electronic states, the  $A^2\Pi$  and  $B^2\Sigma^+$  states, is strongly ionic.<sup>17,18</sup> In the alkaline-earth monohydroxides the bonding remains highly ionic in the first two excited electronic states and, in order to minimise repulsion between the unpaired electron on the metal and the negative charge on the hydroxyl, a linear geometry is adopted. Renner-Teller coupling is possible in the first excited  $^2\Pi$  state, but it would be expected to be weak given the remote, non-bonding nature of the unpaired electron. This is borne out by experiments on several alkaline-earth containing radicals, including  $\text{MgOH}$ <sup>19</sup>,  $\text{CaOH}$ <sup>20,21</sup> and  $\text{CaCCH}$ .<sup>22,23</sup>

In the  $C^2\Pi$  state of the monohalides the unpaired electron is once again mainly metal-localised *but the  $\pi$  orbital is now expected to be polarised towards the halide*; this state is sometimes referred to as being reverse-polarised.<sup>24,25</sup> This confers more electron density on the halide ion than is the case for the lower electronic states and leads, for example, to a strong variation in spin-orbit coupling constant as a function of the halide identity.<sup>18</sup>

Since  $\text{BaF}$  is isoelectronic with  $\text{BaOH}$ , it is reasonable to assume that the analogous state in  $\text{BaOH}$ , the  $\tilde{C}^2\Pi$  state, will also be reverse-polarised. In contrast to the  $\tilde{A}^2\Pi$  state, the unpaired electron will be more sensitive to distortion from a non-linear geometry in the  $\tilde{C}^2\Pi$  state and one might expect the Renner-Teller effect to play a larger role. Indeed, it is even conceivable that a non-linear equilibrium geometry might be favoured for one of the states of the bent molecule correlating with the  $^2\Pi$  state in the linear molecule (see section 3.5.2). As shown in Fig. 4.10, a deviation from linearity would allow the hydrogen  $1s$  orbital to overlap with one of the lobes of the in-plane metal-centred  $\pi$  orbital, thus creating a bonding interaction. If significant, the reverse-polarised  $^2\Pi$  state would be resolved into two distinct electronic states, a bent  $^2A'$  state and a  $^2A''$  state (the latter favouring a linear equilibrium geometry).<sup>6</sup> These will clearly be coupled by the Renner-Teller effect.

The deviation from linearity, if it occurs, must be small for two reasons. First, since  $\text{BaOH}$  is known to be linear in its ground electronic state, a long progression in the Ba-O-H bending mode, with both  $\Delta v_2 = \text{even}$  and  $\Delta v_2 = \text{odd}$  transitions now being prominent, would be observed if there was a significant change in the equilibrium Ba-O-H angle. No such progression is observed. Second, the observation of a large spin-orbit splitting would

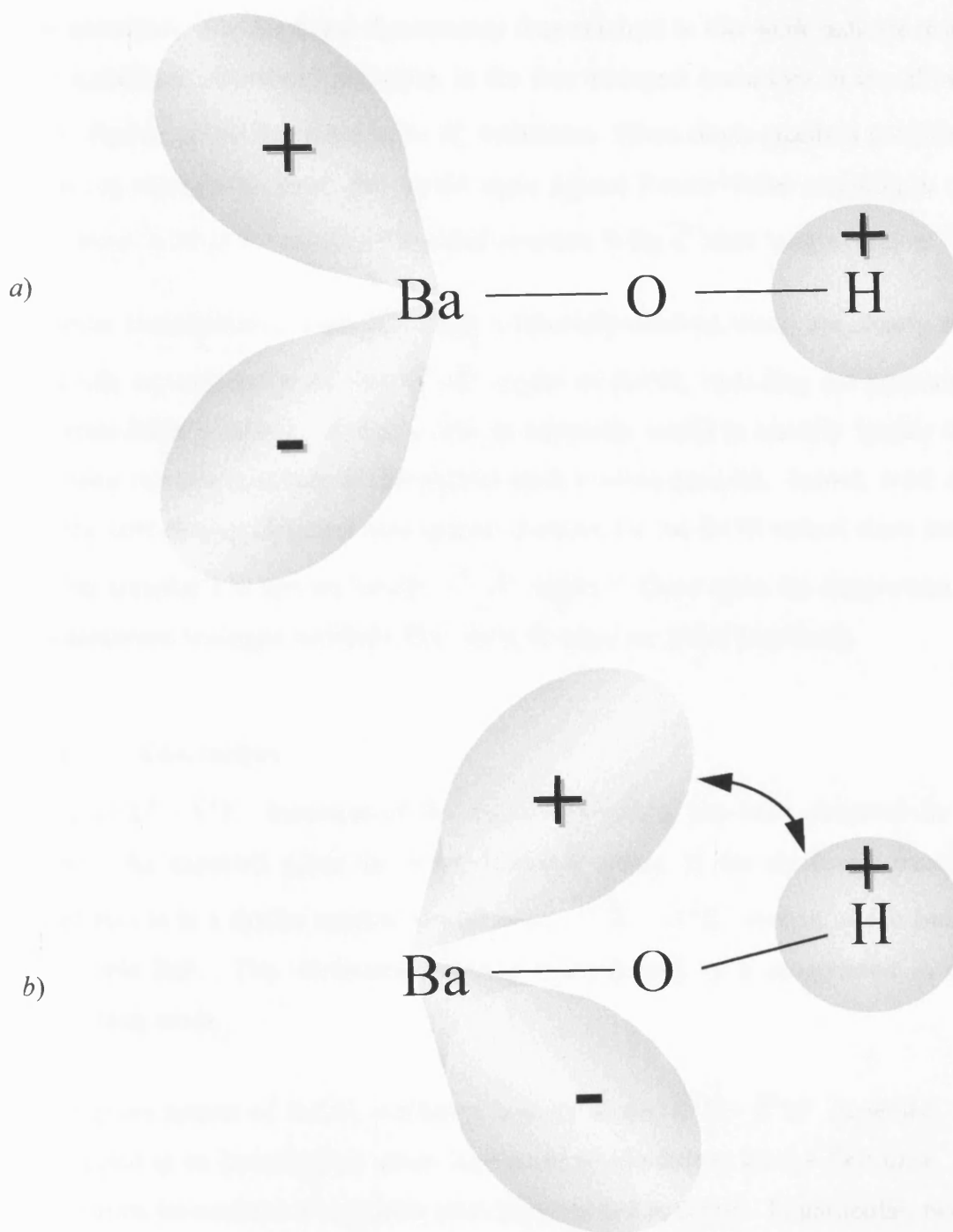


**Fig. 4.10** Illustration of the change in orientation of the orbital containing the unpaired electron in *a*) the linear configuration for the  $\tilde{A}^2\Pi$  state of barium monohydroxide and *b*) the slightly bent configuration for the BaOH  $\tilde{C}^2\Pi$  state.

be inconsistent with a strongly bent molecule, since the orbital angular momentum would be quenched. The dispersed fluorescence data obtained in this work indicate that there is no significant vibrational excitation in the four strongest transitions in the 20240-20620  $\text{cm}^{-1}$  region, *i.e.* all four seem to be  $0_0^0$  transitions. Since single quantum excitation of the bending mode is not seen, this would argue against Renner-Teller coupling in the upper electronic state as the cause of the added structure in the  $\tilde{C}$  state ‘origin’ region.

Further investigations, especially fully rotationally-resolved work, are clearly needed to provide an explanation of the ‘ $\tilde{C}-\tilde{X}$ ’ region of BaOH, including the possible role of Renner-Teller coupling. It would also be extremely useful to identify similar electronic systems in other members of the alkaline-earth monohydroxides. Indeed, work described in the next chapter describes how spectra recorded for the SrOH radical show intense and rather complex LIF spectra for the ‘ $\tilde{C}-\tilde{X}$ ’ region.<sup>26</sup> Once again, by comparison with the isoelectronic analogue molecule, SrF, these findings are rather surprising.

#### 4.4 Conclusions

The  $\tilde{D}^2\Sigma^+ - \tilde{X}^2\Sigma^+$  transition of the BaOH free radical has been observed for the first time. As expected given the metal-localised nature of the electronic transition, the spectrum is in a similar spectral region to the  $D^2\Sigma^+ - X^2\Sigma^+$  system of the isoelectronic molecule BaF. The vibrational structure is dominated by a progression in the Ba-O stretching mode.

The green system of BaOH, attributed initially to the  $\tilde{C}^2\Pi - \tilde{X}^2\Sigma^+$  transition, has been subjected to an investigation under supersonic jet conditions for the first time. The low resolution jet-cooled LIF spectrum possesses unusual structure. In particular, two distinct band systems, showing similar spin-orbit splittings and similar transition energies, were observed. Two possible explanations have been put forward to explain the spectrum. In one, it is suggested that a  $^2\Delta$  state is very close to the  $\tilde{C}^2\Pi$  state and that two electronic transitions, one  $^2\Pi - ^2\Sigma^+$  and one  $^2\Delta - ^2\Sigma^+$ , are seen in this region, the latter probably being induced by spin-orbit mixing of the  $^2\Pi$  and  $^2\Delta$  excited states. Alternatively, the unusual vibronic structure may arise from the Renner-Teller effect in the  $\tilde{C}^2\Pi$  state. Further work is necessary to establish which, if either, of these two possibilities is correct.

## References

- 1 H. Haraguchi, S.J. Weeks and J.D. Winefordner, *Spectrochim. Acta A*, **35** (1979) 391.
- 2 C.G. James and T.M. Sugden, *Nature*, **175** (1955) 133.
- 3 S. Kinsey-Nielson, C.R. Brazier and P.F. Bernath, *J. Chem. Phys.*, **84** (1986) 698.
- 4 W.T.M.L. Fernando, M. Douay and P.F. Bernath, *J. Mol. Spec.*, **144** (1990) 344.
- 5 S.J. Pooley, M.S. Beardah and A.M. Ellis, *J. Elec. Spec. Rel. Phen.*, **97** (1998) 77
- 6 G. Herzberg, *Molecular Spectra and Molecular Structure. III. Electronic Spectra and Electronic Structure of Polyatomic Molecules* (Van Nostrand Reinhold, New York, 1966)
- 7 J.M. Hollas, *High Resolution Spectroscopy*, (Butterworths, London, 1982)
- 8 A. Bernard, J. Verges and R.F. Barrow, *J. Mol. Spec.*, **152** (1992) 174
- 9 S. Panov, X.Q. Tan and T.A. Miller, *48th Ohio State University International Symposium on Molecular Spectroscopy*, paper RA06 (1993)
- 10 M. Charton and A.G. Gaydon, *Proc. Phys. Soc. A*, **7** (1956) 520
- 11 R.A. Gottscho, *J. Chem. Phys.*, **70** (1979) 3554
- 12 P.I. Presunka and J.A. Coxon, *Chem. Phys.*, **190** (1995) 97
- 13 K.P. Huber and G. Herzberg, *Molecular Spectra and Molecular Structure. IV. Constants of Diatomic Molecules* (Van Nostrand Reinhold, New York, (1979)
- 14 R.F. Barrow, A. Bernard, C. Effantin, J. d'Incan, G. Fabre, A. El Hachimi, R. Stringat and J. Verges, *Chem. Phys. Lett.*, **147** (1988) 535
- 15 A. Bernard, C. Effantin, J. d'Incan, G. Fabre, R. Stringat and R.F. Barrow, *Mol. Phys.*, **67** (1989) 1
- 16 W.E. Ernst and J. Kandler, *Phys. Rev. A*, **39** (1989) 1575
- 17 T. Topping, W.E. Ernst, and J. Kandler, *J. Chem. Phys.*, **90** (1989) 4927
- 18 S.F. Rice, H. Martin, and R.W. Field, *J. Chem. Phys.*, **82** (1985) 5023
- 19 Y. Ni, *Ph.D Thesis*, University of California (Santa Barbara), 1986
- 20 M.G. Li and J.A. Coxon, *J. Chem. Phys.*, **97** (1992) 8961
- 21 M.G. Li and J.A. Coxon, *J. Chem. Phys.*, **102** (1995) 2663
- 22 M.G. Li and J.A. Coxon, *J. Mol. Spec.*, **180** (1996) 287
- 23 M.G. Li and J.A. Coxon, *J. Mol. Spec.*, **183** (1997) 250

- 24 P. Bungden, B. Engels, and S.D. Peyerimhoff, *J. Chem. Phys.*, **176** (1991) 407
- 25 N.A. Harris and R.W. Field, *J. Chem. Phys.*, **98** (1993) 2642
- 26 M.S. Beardah and A.M. Ellis, *J. Chem. Phys.*, **110** (1999) 11244



## *Chapter Five*

*Observation of several new electronic  
transitions of the SrOH free radical*

## 5.1 Introduction

At present, only three electronic states of the SrOH free radical, the  $\tilde{X}^2\Sigma^+$ ,  $\tilde{A}^2\Pi$  and  $\tilde{B}^2\Sigma^+$  states, have been spectroscopically observed.<sup>1-9</sup> As mentioned in Chapter 3, the bonding in these low-lying states is thought to be highly ionic, with movement of the electron being localised on the metal and the ligand being regarded as a ‘spectator’. The possibility of greater (or lesser) interaction between the metal and ligand in higher-lying electronic states of alkaline-earth monohydroxides is intriguing. This is especially true in view of the recent observation of the  $\tilde{F}$  electronic state of CaOH, which is thought to favour a bent equilibrium geometry.<sup>10</sup> In addition, observation of significant perturbations in the nominal  $\tilde{C}^2\Pi$  state of BaOH<sup>11</sup> (see Chapter 4), offers strong evidence to support the idea of a change in metal-ligand interactions in higher electronic states. Clearly, the identification and characterisation of higher-energy electronic states in other alkaline-earth monoligated molecules would help to clarify this matter and allow any bonding trends to be elucidated and explained.

In this chapter, five new UV electronic transitions of SrOH are reported for the first time. Four of these, the  $\tilde{B}'^2\Sigma^+ - \tilde{X}^2\Sigma^+$ ,  $\tilde{D}^2\Sigma^+ - \tilde{X}^2\Sigma^+$ ,  $\tilde{E}^2\Sigma^+ - \tilde{X}^2\Sigma^+$  and  $\tilde{F}^2\Pi - \tilde{X}^2\Sigma^+$  states, show mostly simple vibrational structure, although the  $\tilde{B}'^2\Sigma^+ - \tilde{X}^2\Sigma^+$  and  $\tilde{D}^2\Sigma^+ - \tilde{X}^2\Sigma^+$  transitions do yield evidence of excited state vibronic perturbations due to their close proximity to the  $\tilde{C}^2\Pi$  state. The  $\tilde{C}^2\Pi - \tilde{X}^2\Sigma^+$  transition gives extensive and complex vibronic structure and yields evidence of significant Renner-Teller activity. Excitation and dispersed fluorescence spectra are presented for the five new electronic systems of SrOH. Furthermore, the character of the  $\tilde{C}^2\Pi$  state and the origin of its Renner-Teller effect are discussed.

## 5.2 Experimental

Details of the laboratory apparatus and experimental procedure for a general laser ablation experiment can be found in Chapter 2.

SrOH was prepared in the gas phase by laser ablation of strontium metal. An intense and stable laser induced fluorescence signal for SrOH was obtained by seeding hydrogen

peroxide, or water, into a helium carrier gas. The LIF signal could also be obtained with a comparable intensity with no precursor present in the carrier gas, though in this case the shot-to-shot stability of the signal was much less reproducible. In view of these observations, it seems likely that the bulk of the SrOH comes from the laser ablation of strontium hydroxide,  $\text{Sr}(\text{OH})_2$ , on the surface of the strontium target, rather than from a gas phase reaction between strontium atoms and added reagent.

A stagnation pressure of 12 bar was typically used behind the pulsed valve for these experiments. In addition, a 10 mm extension piece was attached to the end of the fixture, thereby increasing the length of the pre-expansion, post-ablation mixing zone to approximately 20 mm. In a typical experiment  $\sim 20$  mJ pulses from an ArF or KrF excimer laser were used to ablate the strontium. The excimer laser beam was softly focused onto the metal surface, and firing was timed to coincide with the arrival of a gas pulse from the pulsed valve. Subsequently, a supersonic jet was formed by expanding the resulting gas mixture into a Roots-pumped vacuum chamber (base pressure of  $\sim 10^{-4}$  mbar), as described in Chapter 2.

The expanding jet was crossed by the beam from a pulsed dye laser about 25 mm downstream of the fixture. The optimum SrOH LIF signal stability was achieved by synchronising the dye laser pulse with the trailing edge of the gas pulse. In the current work the dye laser was operated without an intracavity etalon, resulting in a linewidth of  $\sim 0.2 \text{ cm}^{-1}$ . For all excitation experiments a 500 nm long-pass filter was placed between the lens and PMT to reduce scattered light interference from both the dye and excimer lasers. All other experimental details are as given in Chapter 2.

### 5.3 *Results and discussion*

The  $25500\text{--}34000 \text{ cm}^{-1}$  region was scanned in a search for new SrOH bands. Many intense peaks were observed and at least five different electronic transitions were identified within this region. A variety of evidence supports the assignment of these transitions to SrOH, but the simplest means of firmly establishing the carrier was to record dispersed fluorescence spectra. When applied to each prominent vibronic transition the dispersed fluorescence spectra, several of which are presented later, showed vibrational structure characteristic of the ground electronic state of SrOH.

**Table 5.1** Major vibronic bands in the 25990-28500 cm<sup>-1</sup> region and their assignments.

Wavenumber	Rotational contour	Assignment
25994	$\Sigma - \Sigma$	$\tilde{B}'^2\Sigma^+ - \tilde{X}^2\Sigma^+ 0_0^0$
26391	$\Pi - \Sigma$	$\tilde{B}'^2\Sigma^+ - \tilde{X}^2\Sigma^+ 2_0^1$
26571	$\Sigma - \Sigma$	$\tilde{B}'^2\Sigma^+ - \tilde{X}^2\Sigma^+ 3_0^1$
26931	$\Pi - \Sigma$	$\tilde{B}'^2\Sigma^+ - \tilde{X}^2\Sigma^+ 3_0^1 2_0^1$
27121	$\Sigma - \Sigma$	$\tilde{B}'^2\Sigma^+ - \tilde{X}^2\Sigma^+ 3_0^2$
27291	$\Pi - \Sigma$	$\tilde{C}^2\Pi_{1/2} - \tilde{X}^2\Sigma^+ 0_0^0$
27315	$\Pi - \Sigma$	$\tilde{C}^2\Pi_{3/2} - \tilde{X}^2\Sigma^+ 0_0^0$
27422	$\Pi - \Sigma^a)$	
27522	$\Sigma - \Sigma$	$ \tilde{C}^2\Pi(010)\mu^2\Sigma - \tilde{X}^2\Sigma^+(000) ^b)$
27588	$\Sigma - \Sigma$	$ \tilde{C}^2\Pi(010)\kappa^2\Sigma - \tilde{X}^2\Sigma^+(000) $
27698	$\Sigma - \Sigma$	$\tilde{D}^2\Sigma^+ - \tilde{X}^2\Sigma^+ 0_0^0^c)$
27714	$\Sigma - \Sigma$	
27725	$\Sigma - \Sigma$	
27756	$\Pi - \Sigma$	$\tilde{C}^2\Pi - \tilde{X}^2\Sigma^+ 2_0^2 / 3_0^1$ region <sup>d)</sup>
27768	$\Pi - \Sigma$	
27781	$\Pi - \Sigma$	
27788	$\Pi - \Sigma$	
27862	$\Pi - \Sigma ?$	
27873	$\Pi - \Sigma$	
27890	$\Pi - \Pi ?$	
28203	$\Sigma - \Sigma$	
28237	$\Sigma - \Sigma$	
28317	$\Sigma - \Sigma$	$\tilde{D}^2\Sigma^+ - \tilde{X}^2\Sigma^+ 3_0^1^e)$

- a) The 27422 cm<sup>-1</sup> feature is actually composed of at least three bands, but the dominant transition, at 27429 cm<sup>-1</sup>, is a  $^2\Pi - ^2\Sigma$  transition.
- b) This assignment must be considered as tentative since dispersed fluorescence data indicate that it is possibly a sequence band.
- c) This assignment is tentative.
- d) See text for further details.
- e) The vibrational quantum numbering here is based on the tentative assignment of the band at 27698 cm<sup>-1</sup> as the origin of the  $\tilde{D} - \tilde{X}$  system.

### 5.3.1 The $\tilde{C}^2\Pi - \tilde{X}^2\Sigma^+$ system

#### 5.3.1.1 Overview

An LIF excitation spectrum covering 26350-28800  $\text{cm}^{-1}$  is shown in Fig. 5.1. A considerable number of bands appear in the spectrum, with several notable strong and medium intensity bands appearing alongside many weaker ones. As discussed later, most of these bands do not seem to fit into any obvious pattern. The wavenumbers of strong and medium intensity bands are collected in Table 5.1. Justification of the assignments in Table 5.1 will be given later in this chapter.

To make some sense of this and other SrOH spectra, a useful starting point is to compare the relative positions of electronic transitions of SrOH with those of its isoelectronic analogue, SrF. The known electronic transitions of SrF are predominantly metal-localised. Consequently, the electronic spectra of SrF and SrOH would be expected to have some similarities. The electronic spectroscopy of SrF is well documented<sup>12</sup> and the relative positions and symmetries of its electronic states are illustrated in Fig. 5.2. Prior to the present work, the only reported excited states of SrOH were the  $\tilde{A}^2\Pi$  and  $\tilde{B}^2\Sigma^+$  states.<sup>3-9</sup> Notice that the  $\tilde{A}^2\Pi$  and  $\tilde{B}^2\Sigma^+$  states of SrOH and the  $A^2\Pi$  and  $B^2\Sigma^+$  states of SrF have, as expected, similar energies. There are other similarities. For example, the spin-orbit coupling constants in the first excited states of both molecules are comparable, being 281 and 263  $\text{cm}^{-1}$  for SrF and SrOH, respectively. Also, as shown in Table 5.2 the Sr-O and Sr-F stretching vibrations have similar frequencies in the ground and first two excited electronic states. All of these observations are consistent with the non-bonding character of the unpaired electron.

If the similarity between SrF and SrOH also holds for higher electronic states, the  $\tilde{C} - \tilde{X}$  system of SrOH should be a  $^2\Pi - ^2\Sigma^+$  transition with an origin in the region of 27400  $\text{cm}^{-1}$ . Furthermore, comparison with SrF would lead us to expect a spin-orbit coupling constant of  $\sim 60 \text{ cm}^{-1}$  in the  $\tilde{C}^2\Pi$  state.

#### 5.3.1.2 Electronic origin

The strongest bands in Fig. 5.1 appear at 27291 and 27315  $\text{cm}^{-1}$  and have nearly equal intensities. Given their proximity to the predicted origin of the  $\tilde{C} - \tilde{X}$  system, it is possible that these form a spin-orbit pair in the  $\tilde{C}^2\Pi - \tilde{X}^2\Sigma^+$  manifold of SrOH. If

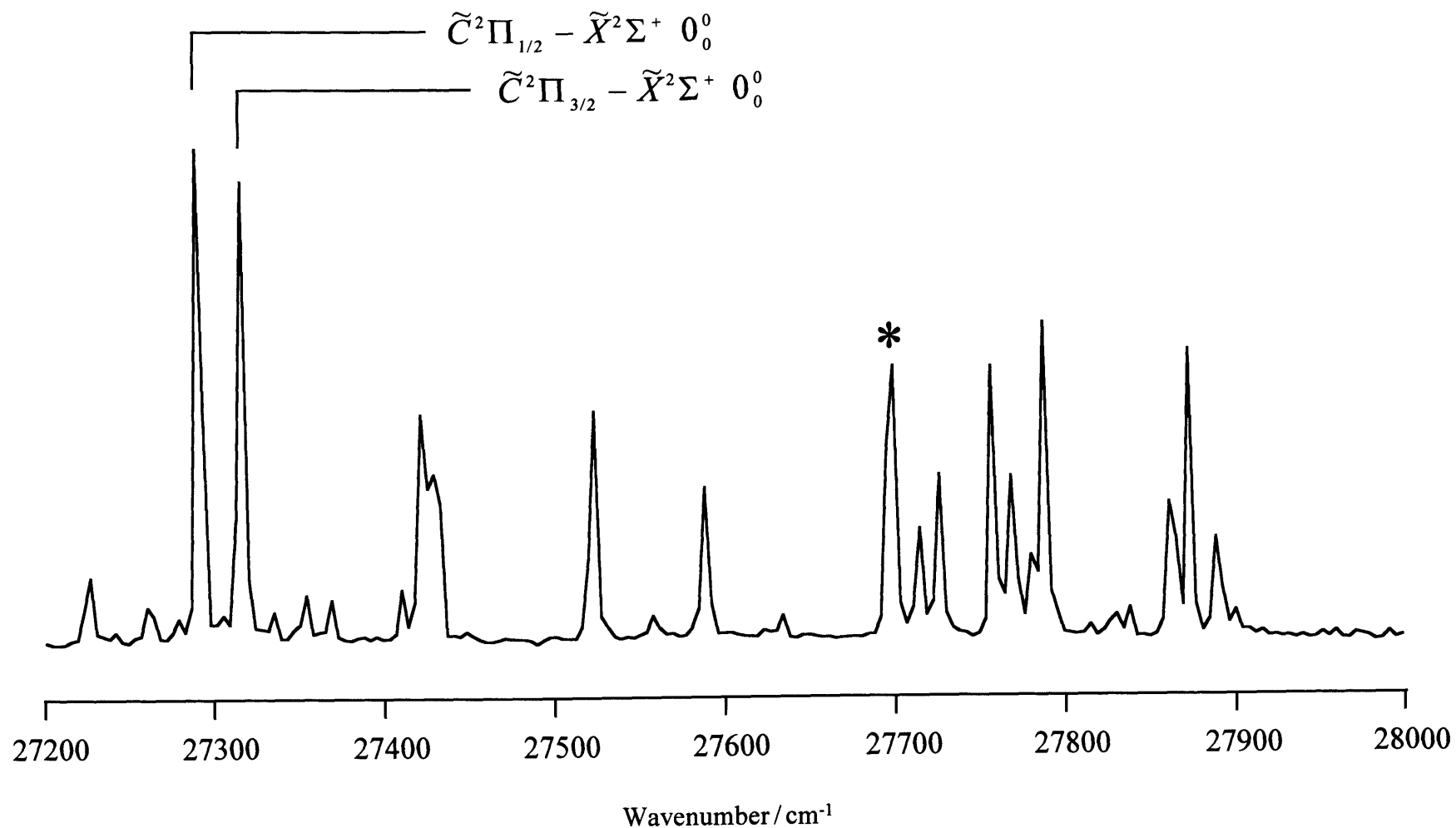


**Fig. 5.1** Laser excitation spectrum showing the  $\tilde{C}^2\Pi - \tilde{X}^2\Sigma^+$  system and part of the  $\tilde{D}^2\Sigma^+ - \tilde{X}^2\Sigma^+$  system of SrOH. The spectrum is a composite of scans using three different laser dyes; band intensities have not been corrected for variations in laser output. The asterisked band identifies a peak that is thought to belong to the  $\tilde{D} - \tilde{X}$  system.

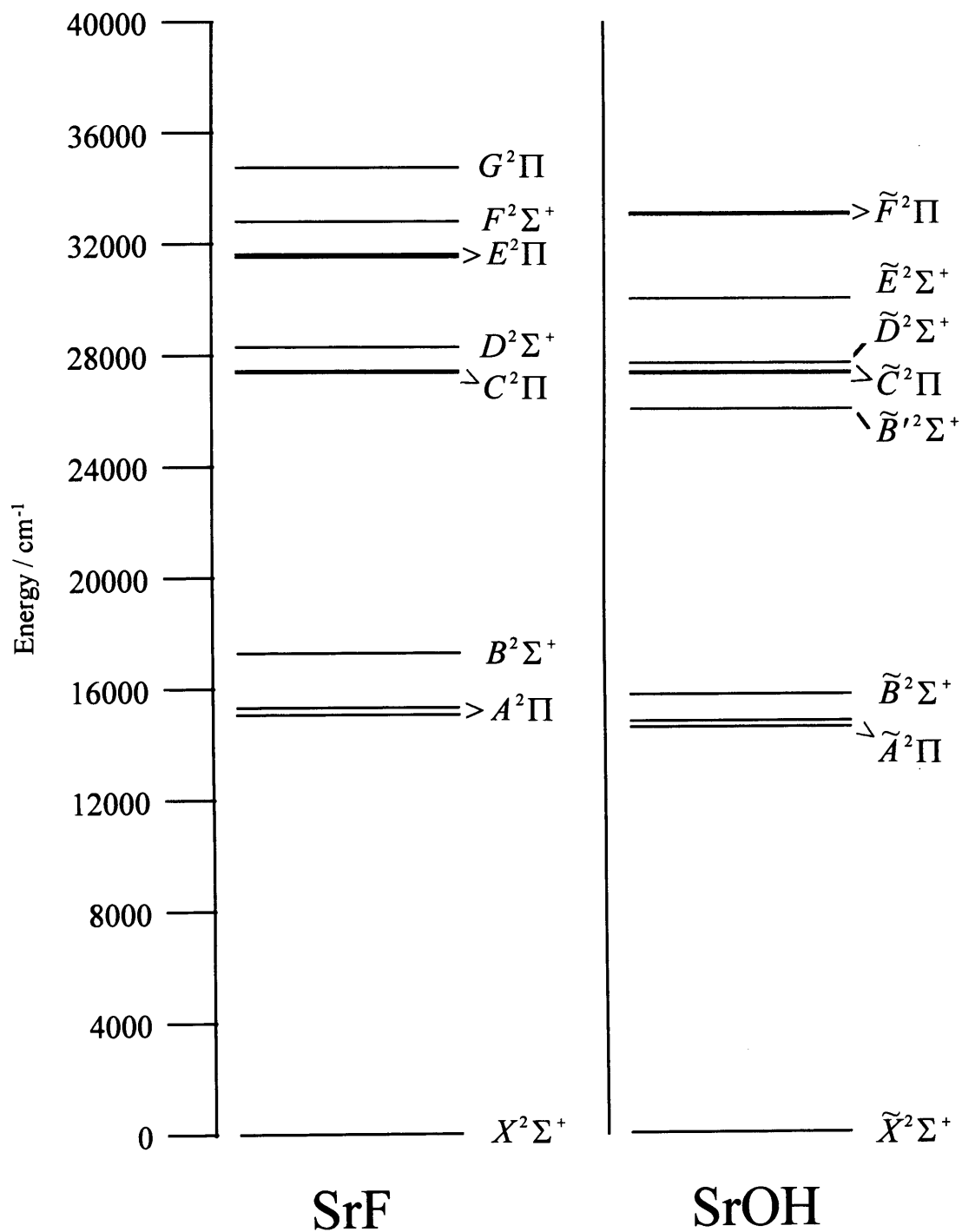


**Fig. 5.2** Comparison of the energies of electronic states of SrF and SrOH. The energies of SrF states were taken from Huber and Herzberg,<sup>12</sup> while those of the  $\tilde{A}^2\Pi$  and  $\tilde{B}^2\Sigma^+$  states of SrOH are from refs. 3 and 9. The energies of the five highest states of SrOH shown in this diagram have been determined in the present work.

**Table 5.2** Comparison of the Sr-O and Sr-F stretching vibrational frequencies ( $\text{cm}^{-1}$ ) in SrOH and SrF.

Electronic state	Sr-O	Electronic state	Sr-F <sup>c)</sup>
$\tilde{X}^2\Sigma^+$	528 <sup>a)</sup>	$X^2\Sigma^+$	502.4
$\tilde{A}^2\Pi$	544 <sup>a)</sup>	$A^2\Pi$	507.6
$\tilde{B}^2\Sigma^+$	522 <sup>b)</sup>	$B^2\Sigma^+$	495.8

a) Taken from reference 4.

b) Taken from reference 9.

c) Taken from reference 12.

correct, this would imply a spin-orbit coupling constant of  $24 \text{ cm}^{-1}$  in the  $\tilde{C}^2\Pi$  state, a value considerably smaller than the *ca.*  $60 \text{ cm}^{-1}$  suggested above in the analogy with SrF. One way of checking this assignment is to search for other spin-orbit doublets in this spectral region that show the same characteristic splitting. Scans to lower wavenumbers revealed several bands originating from SrOH, but none with the appropriate  $24 \text{ cm}^{-1}$  splitting. On the high wavenumber side there are several possible candidates, each displaying a splitting of  $\sim 30 \text{ cm}^{-1}$ . However, some of these doublets may result from the accidental proximity of very different bands, especially in the  $27700\text{-}27850 \text{ cm}^{-1}$  region where there are several bands relatively close together. Consequently, to try and obtain firmer assignments of the  $27291/27315 \text{ cm}^{-1}$  pair, (i) dispersed fluorescence spectra and (ii) the rotational structure of each band has been investigated.

Given the high intensities of the bands at  $27291$  and  $27315 \text{ cm}^{-1}$ , the most likely assignment is that they form the origin of the  $\tilde{C}^2\Pi - \tilde{X}^2\Sigma^+$  system. The dispersed fluorescence data are consistent with this assignment. Apart from a shift in band positions due to excited state spin-orbit splitting, virtually identical dispersed fluorescence spectra are expected on excitation of these two transitions. As shown in Fig. 5.3, this is precisely what is observed. The dominant band is due to emission at the pump wavelength, as expected for excitation of the origin of a transition involving movement of a primarily non-bonding electron. However, there are also other, much weaker features, including peaks at  $368 \pm 7 \text{ cm}^{-1}$  and  $724 \pm 7 \text{ cm}^{-1}$  to the red of the respective pump positions.



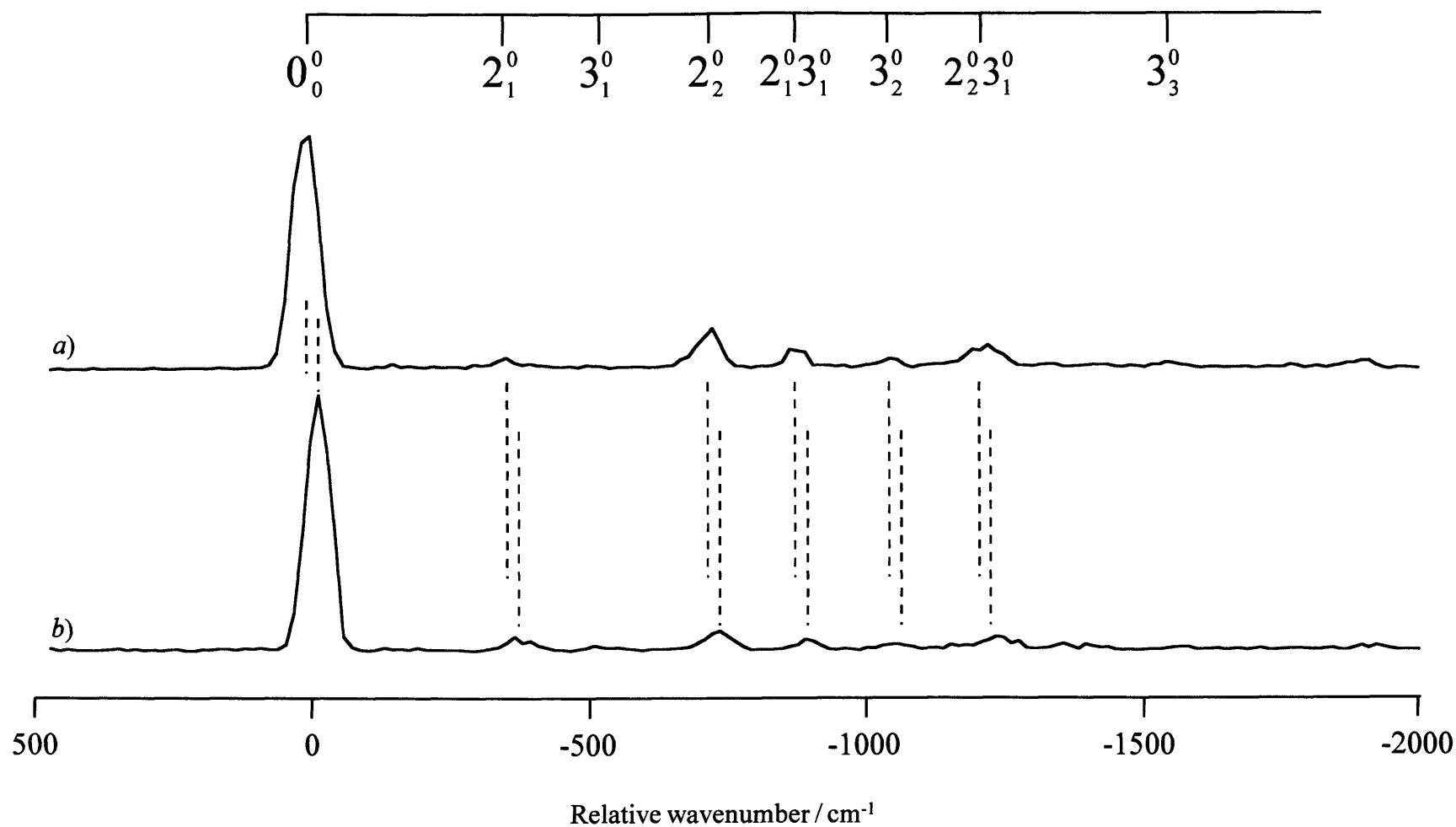


**Fig. 5.3** Dispersed fluorescence spectra obtained by pumping the a)  $\tilde{C}^2\Pi_{1/2} - \tilde{X}^2\Sigma^+$  and b)  $\tilde{C}^2\Pi_{3/2} - \tilde{X}^2\Sigma^+$   $0_0^0$  transitions. The small shift in the relative positions of the bands in the two spectra, indicated by dashed lines, is due to the excited state spin-orbit splitting (*ca.* 24 cm<sup>-1</sup>).

Brazier and Bernath<sup>4</sup> reported values of 361 and 727 cm<sup>-1</sup>, respectively, for the fundamental and first overtone of the Sr-O-H bending mode ( $\nu_2$ ) in the  $\tilde{X}^2\Sigma^+$  ground electronic state of SrOH. These assignments were subsequently confirmed in a much higher resolution dispersed fluorescence study by Presunka and Coxon.<sup>7</sup> The bands at  $368 \pm 7$  cm<sup>-1</sup> and  $724 \pm 7$  cm<sup>-1</sup> bands in Fig. 5.3 are therefore assigned to these bending mode transitions. Very weak peaks at  $520 \pm 10$  cm<sup>-1</sup> and  $1046 \pm 7$  cm<sup>-1</sup> are also observed in the spectrum. These correlate well with the values of 528 and 1048 cm<sup>-1</sup> obtained by Brazier and Bernath for  $\nu_3$  and  $2\nu_3$ , where  $\nu_3$  is the Sr-O stretch, in the electronic ground state.<sup>4</sup> The peaks at 891 and 1230 cm<sup>-1</sup> are assigned to the  $\nu_2+\nu_3$  and  $2\nu_2+\nu_3$  combination bands.

Expanded views of the 27291 and 27315 cm<sup>-1</sup> bands are shown in Fig. 5.4, together with simulations of the rotational structure.<sup>13</sup> The dye laser linewidth of  $\sim 0.2$  cm<sup>-1</sup> prevented full rotational resolution, but some structure is resolved in parts of the bands and is readily assigned. The rotational structure is entirely consistent with the assignment to a  $^2\Pi - ^2\Sigma^+$  transition in which the  $^2\Pi$  state undergoes Hund's case (a) coupling<sup>14</sup> (see section 3.5.1). At the present resolution four out of the six possible branches should be observed for each band, and all four can be seen in Fig. 5.4 (although only the two outer branches are specifically identified in the figure). Using the known rotational constant of the  $\tilde{X}^2\Sigma^+$  state of SrOH ( $B'' = 0.24920$  cm<sup>-1</sup>),<sup>4</sup> the observed rotational structure can be simulated by varying the rotational and spin-orbit coupling constants in the excited state together with the ground state rotational temperature. A least squares fit of the simulated spectrum to the assigned structure in the experimental spectrum gives excited state constants of  $B' = 0.2564 \pm 0.0009$  cm<sup>-1</sup> and  $A' = 24.52 \pm 0.04$  cm<sup>-1</sup>.

### 5.3.1.3 Higher vibronic bands

Although the  $\tilde{C}^2\Pi_{1/2} - \tilde{X}^2\Sigma^+$  and  $\tilde{C}^2\Pi_{3/2} - \tilde{X}^2\Sigma^+ 0_0^0$  transitions are relatively easy to assign, the remaining bands in Fig. 5.1 are more difficult to deal with. The excitation spectrum is remarkably complex for a transition which is thought to be dominated by promotion of a largely non-bonding electron. In fact, it will be seen later that this simple picture of the electronic transition requires modification. To aid the assignment process the same approach has been followed as was employed for the origin, *i.e.* information from rotational contours and from dispersed fluorescence spectra has been used. Unfortunately, as will be seen, in most cases the latter do not give clear-cut information about vibrational

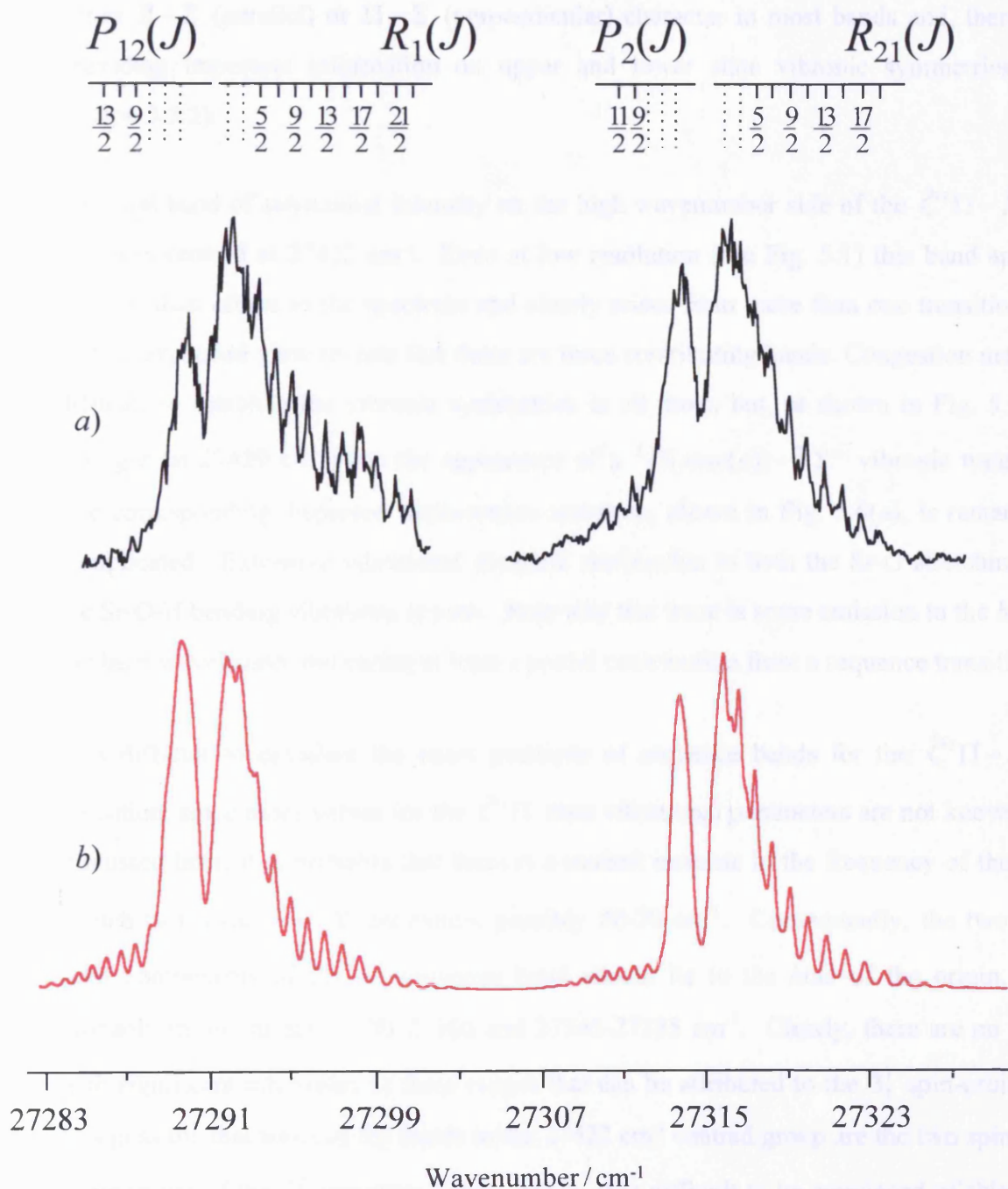


**Fig. 5.4** a) Rotational contours of the bands centred at 27291 and 27315 cm<sup>-1</sup>. These bands are assigned to the  $\tilde{C}^2\Pi_{1/2} - \tilde{X}^2\Sigma^+$  and  $\tilde{C}^2\Pi_{3/2} - \tilde{X}^2\Sigma^+$   $0_0^0$  transitions, respectively. The coarse  $3B$ ,  $B$ ,  $-B$ ,  $-3B$  branches expected for a  $^2\Pi(case(a)) - ^2\Sigma^+$  transition<sup>14</sup> are easily identified, although individual rotational components are only resolved for the  $3B$  and  $-3B$  branches. b) Simulation assuming a  $^2\Pi - ^2\Sigma^+$  transition, a rotational temperature of 15 K,  $B'' = 0.2492$  cm<sup>-1</sup>,  $B' = 0.2564$  cm<sup>-1</sup> and  $A' = 24.52$  cm<sup>-1</sup>.

assignments. The rotational structure has proved more valuable, allowing identification of either  $\Sigma - \Sigma$  (parallel) or  $\Pi - \Sigma$  (perpendicular) character in most bands and, therefore, providing important information on upper and lower state vibronic symmetries (see section 3.5.2).

The first band of substantial intensity on the high wavenumber side of the  $\tilde{C}^2\Pi - \tilde{X}^2\Sigma^+$  origin is centred at 27422  $\text{cm}^{-1}$ . Even at low resolution (see Fig. 5.1) this band appears broader than others in the spectrum and clearly arises from more than one transition. In fact an expanded view reveals that there are three contributing bands. Congestion makes it difficult to establish the vibronic symmetries in all three, but, as shown in Fig. 5.5, the stronger (at 27429  $\text{cm}^{-1}$ ) has the appearance of a  $^2\Pi(case(a)) - ^2\Sigma^+$  vibronic transition. The corresponding dispersed fluorescence spectrum, shown in Fig. 5.6(a), is remarkably complicated. Extensive vibrational structure attributable to both the Sr-O stretching and the Sr-O-H bending vibrations is seen. Note also that there is some emission to the *blue* of the laser wavelength, indicating at least a partial contribution from a sequence transition.

It is difficult to calculate the exact positions of sequence bands for the  $\tilde{C}^2\Pi - \tilde{X}^2\Sigma^+$  transition, since exact values for the  $\tilde{C}^2\Pi$  state vibrational parameters are not known. As discussed later, it is probable that there is a modest increase in the frequency of the Sr-O stretch ( $\nu_3$ ) upon  $\tilde{C} \leftarrow \tilde{X}$  excitation, possibly 30-70  $\text{cm}^{-1}$ . Consequently, the two spin-orbit components of the  $3_1^1$  sequence band should lie to the *blue* of the origin, most probably in the ranges 27320-27360 and 27345-27385  $\text{cm}^{-1}$ . Clearly, there are no bands with significant intensities in these ranges that can be attributed to the  $3_1^1$  spin-orbit pair. It is possible that some of the bands in the 27422  $\text{cm}^{-1}$  centred group are the two spin-orbit components of the  $3_2^2$  sequence band. Again, it is difficult to be convinced of this since there is no evidence of the  $3_1^1$  sequence bands. Under supersonic conditions the  $3_2^2$  sequence transition would be considerably less probable than the  $3_1^1$  transition.

It is inconceivable that the bands centred at 27422  $\text{cm}^{-1}$  are due to sequence bands in the  $\nu_2$  Sr-O-H bending mode since, again as discussed later, it is proposed that there is a significant decrease (*ca.* 100  $\text{cm}^{-1}$ ) in the vibrational frequency of this mode in the  $\tilde{C}^2\Pi$  state compared with the  $\tilde{X}^2\Sigma^+$  state. This would place sequence bands involving the

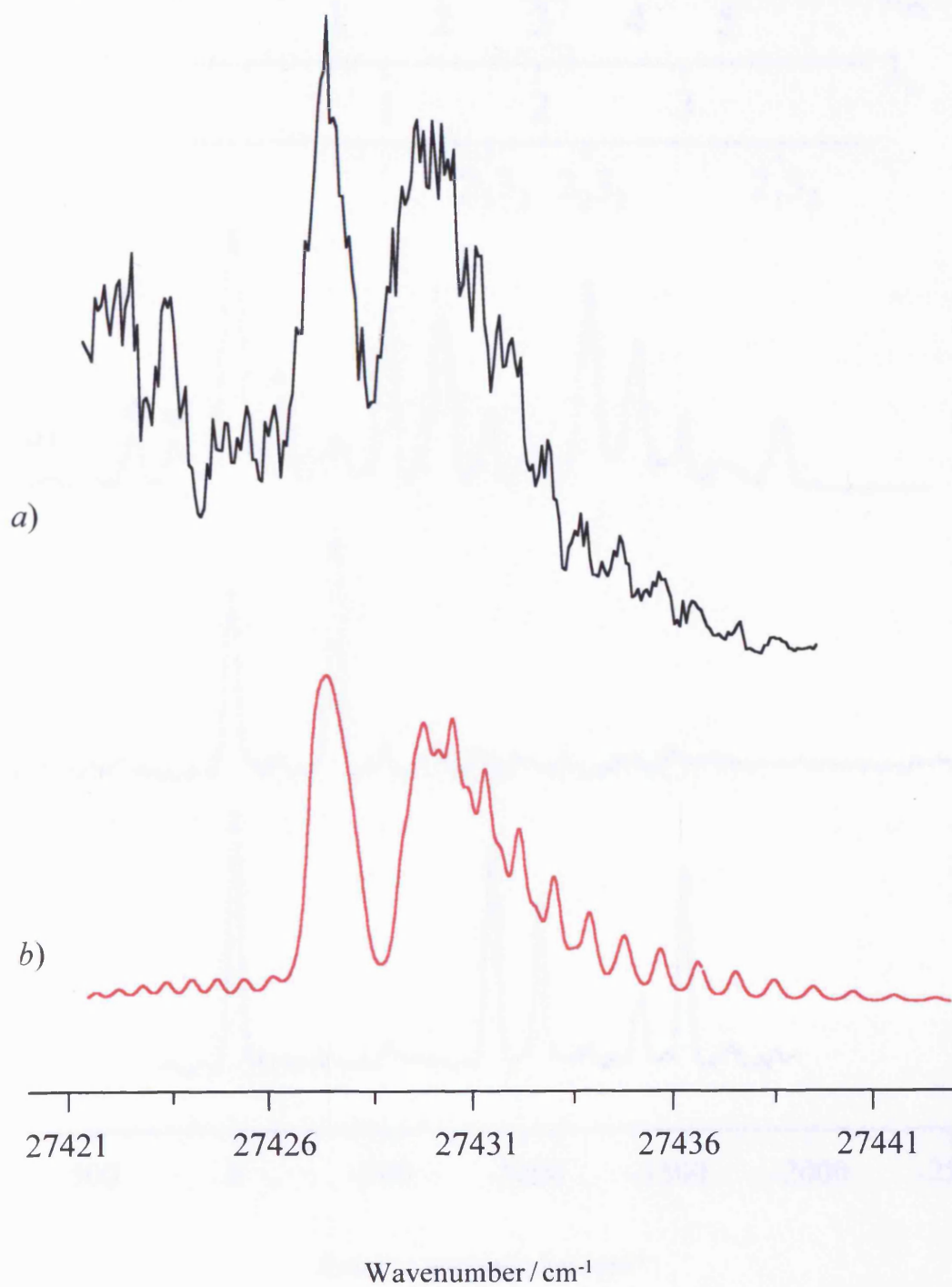


**Fig. 5.5** *a)* Expanded view of the band centred at 27429 cm<sup>-1</sup> and *b)* simulation assuming a  $^2\Pi - ^2\Sigma^+$  transition, a rotational temperature of 20 K,  $B'' = 0.2492$  cm<sup>-1</sup> and  $B' = 0.256$  cm<sup>-1</sup>.

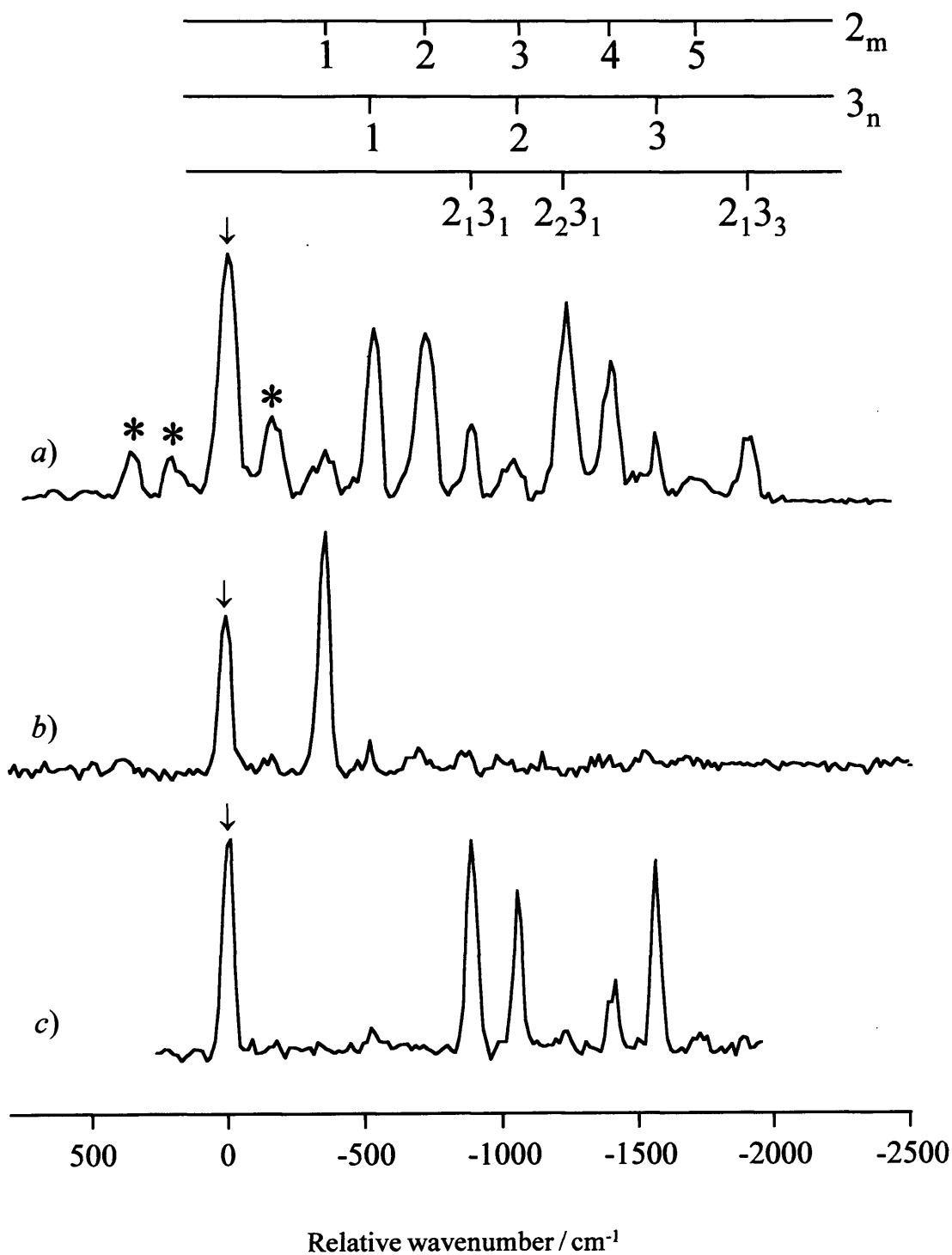


**Fig. 5.6** Dispersed fluorescence spectra obtained by laser excitation of a) 27429 cm<sup>-1</sup>, b) 27522 cm<sup>-1</sup> and c) 27588 cm<sup>-1</sup>. The arrows indicate the laser wavenumber. Modes  $\nu_2$  and  $\nu_3$  are the Sr-O-H bend and Sr-O stretch, respectively. The asterisked bands show blue shifted emission, indicating possible hot/sequence band activity.

bending mode to the *red* of the excited state origin. One final possibility is that some of the 27422 cm<sup>-1</sup> centred group of bands arise through combination sequence bands. It should be noted that the shifts of combination sequence bands from the origin would be small, since the shifts for  $\nu_2$  and  $\nu_3$  are apposite. Without precisely knowing the upper state vibrational frequencies for  $\nu_2$  and  $\nu_3$  it is virtually impossible to make a positive statement regarding any sequence band activity.

The next two bands, centred at 27522 and 27588 cm<sup>-1</sup>, can be identified as parallel bands from their rotational structure (see Fig. 5.7) and are assigned to  $^2\Sigma^+ - ^2\Sigma^+$  transitions on account of their missing *Q*-branches. The corresponding dispersed fluorescence spectra are shown in Figs 5.6(b) and 5.6(c). Like the 27429 cm<sup>-1</sup> peak, the 27522 cm<sup>-1</sup> peak also shows some possible emission to the blue of the pump wavelength, although it is very weak and difficult to distinguish from the noise. Clearly, there is a possibility that this band is due to a sequence band, although it is unlikely given its high intensity and displacement from the origin. As indicated above,  $\nu_3$  sequence bands would be relatively close to the origin (the band at 27522 cm<sup>-1</sup> would have to be at least the 3<sub>4</sub><sup>4</sup> sequence band). Sequence bands involving  $\nu_2$  would be *red*-shifted from the origin. The only other possibility is that the 27522 cm<sup>-1</sup> band is due to a combination sequence band but, as stated above, this is unlikely since combination sequence bands would lie very close in energy to the  $\tilde{C}^2\Pi$  state electronic origin.

The dispersed fluorescence spectrum for the 27522 cm<sup>-1</sup> band is otherwise completely different from the 27429 cm<sup>-1</sup> band, the single dominant feature to the red of the pump position arising from single quantum excitation of the Sr-O-H bending mode. The dispersed fluorescence spectrum obtained by exciting the 27588 cm<sup>-1</sup> transition is different again, showing activity in both the Sr-O stretch and the bending mode. Unlike the 27522 cm<sup>-1</sup> transition, excitation of the 27588 cm<sup>-1</sup> transition does not yield any emission to the blue of the laser wavelength.

The 27695-27900 cm<sup>-1</sup> region contains *at least* ten bands with substantial intensities. The conclusions from the rotational contours are summarised in Table 5.1. The first three bands in this group are parallel bands and are attributed to  $^2\Sigma^+ - ^2\Sigma^+$  transitions. However, the majority of the remaining bands are consistent with  $^2\Pi(case(a)) - ^2\Sigma^+$

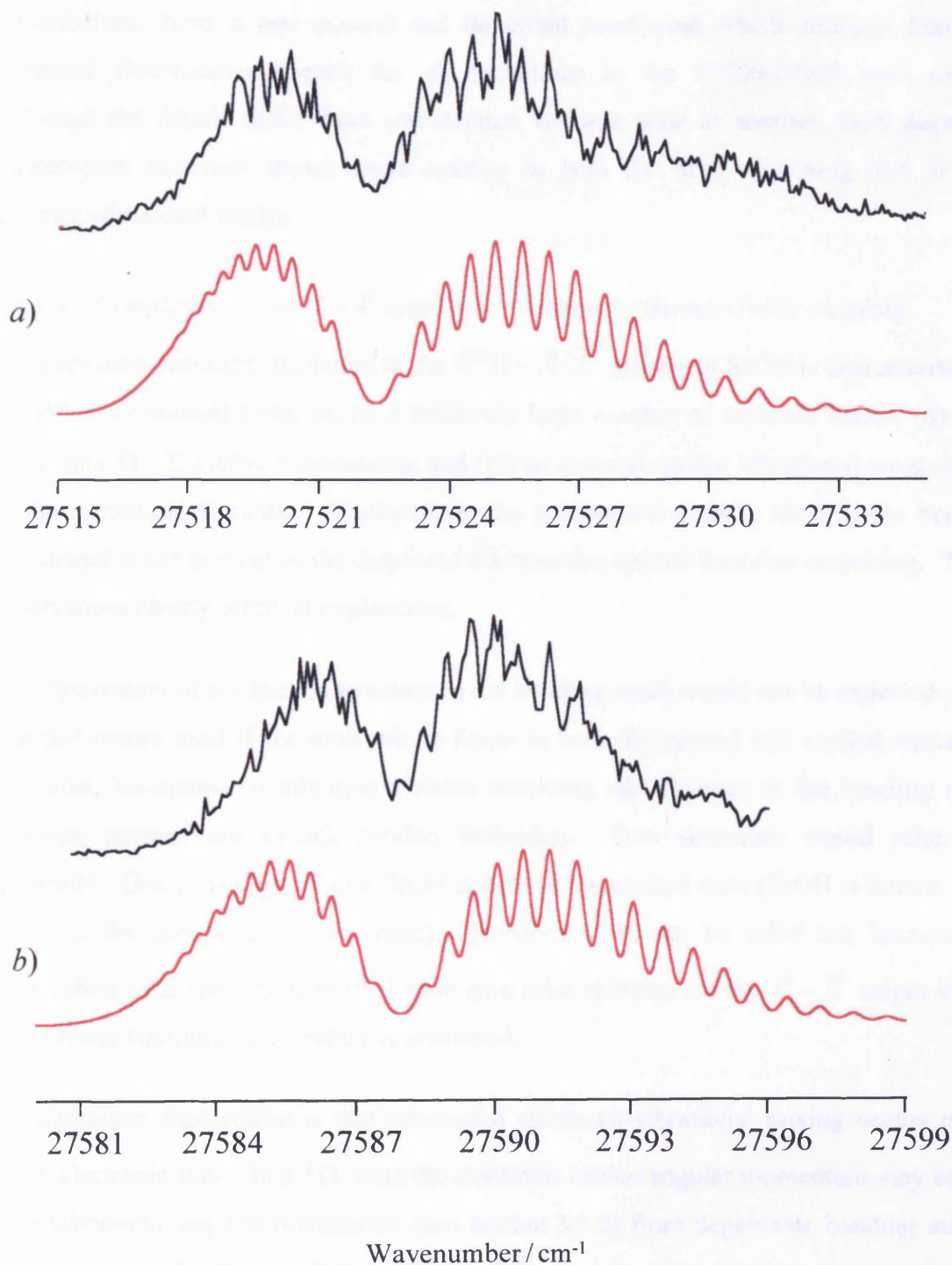


**Fig. 5.7** Rotational contours of the bands at a) 27522 cm<sup>-1</sup> and b) 27588 cm<sup>-1</sup>. The lower spectrum in each case is a simulation assuming a  $^2\Sigma^+ - ^2\Sigma^+$  transition ( $B'' = 0.2492$  cm<sup>-1</sup>,  $B' = 0.258$  cm<sup>-1</sup> and  $T = 15$  K).



transitions. The information from dispersed fluorescence spectra is less specific. Nevertheless, there is one general and important conclusion which emerges from the dispersed fluorescence spectra for all transitions in the 27700-27920 cm<sup>-1</sup> region. Although the details differ from one excited vibronic state to another, each dispersed fluorescence spectrum shows some activity in *both* the Sr-O stretching and Sr-O-H bending vibrational modes.

#### 5.3.1.4 Complexity of the $\tilde{C} - \tilde{X}$ spectrum: evidence for Renner-Teller coupling

The excitation spectrum attributed to the  $\tilde{C}^2\Pi - \tilde{X}^2\Sigma^+$  system of SrOH is characterised by a number of unusual features: (i) a relatively large number of vibronic bands, (ii) both  $\Sigma - \Sigma$  and  $\Pi - \Sigma$  vibronic transitions, and (iii) no obvious regular vibrational progressions in the excitation spectrum. Furthermore, the pronounced activity seen in the bending vibrational mode in most of the dispersed fluorescence spectra was also surprising. These observations clearly merit an explanation.

The observation of substantial structure in the bending mode would not be expected in the Franck-Condon limit if the molecule is linear in both the ground and excited states. In particular, transitions to vibrational states involving odd changes in the bending mode quantum number are Franck-Condon forbidden. Two scenarios would relax this constraint. One possibility is that SrOH is bent in the excited state (SrOH is *known* to be linear in the ground electronic state). However, this can be ruled out because the observation of a substantial excited state spin-orbit splitting for the  $\tilde{C} - \tilde{X}$  origin shows that a linear equilibrium geometry is preserved.

An alternative explanation is that substantial electronic-vibrational mixing occurs in the  $\tilde{C}^2\Pi$  electronic state. In a  $^2\Pi$  state the electronic orbital angular momentum may couple with vibrational angular momentum (see section 3.5.2) from degenerate bending modes, giving rise to the Renner-Teller effect. One consequence that can be seen in low resolution spectra is that some transitions which are nominally forbidden in the Franck-Condon limit may gain intensity through Renner-Teller coupling.<sup>14</sup> For SrOH this means that odd quantum number changes of the bending vibration become partially allowed. These transitions are very weak in the  $\tilde{A}^2\Pi - \tilde{X}^2\Sigma^+$  system of SrOH but, as detailed in the final section of this chapter, there are good reasons to expect these bands to be much stronger in the  $\tilde{C}^2\Pi - \tilde{X}^2\Sigma^+$  system.

Pople initially investigated the effect of vibronic interaction on the multiplet structure of a  $^2\Pi$  state in 1960.<sup>15</sup> Fig. 5.8 illustrates the results of his calculations. On the left of the diagram (Fig. 5.8(a)), are the energy levels for a  $^2\Pi$  state in which there is no Renner-Teller interaction, but a non-zero spin-orbit splitting interaction. To the right of the diagram, in Fig. 5.8(c), is the situation in which there is no spin-orbit interaction, but a non-zero Renner-Teller interaction. Fig. 5.8(b) illustrates the perturbed energy levels that arise through both non-zero spin-orbit and Renner-Teller interactions. In the situation where there is strong spin-orbit coupling, the quantum number defining the component of the orbital-plus-spin angular momentum along the internuclear axis is  $\Omega$ . Since the resultant spin-orbit vector can couple to the vibrational angular momentum, the vibronic angular momentum, along the internuclear axis, is defined by the quantum number  $P$ , where  $P = |\pm\Omega + l|$ . Notice that for the situation in which the spin-orbit splitting is zero, the vibronic quantum number,  $K$ , is still a good quantum number.<sup>14</sup>

With the introduction of spin-orbit coupling, to a first approximation the component levels with  $K = \nu_2 + 1$  split in the same way as if there were no vibronic interaction, and the vibronic term function, corresponding to the levels shown in Fig 5.8(b), may be written as,

$$G(\nu_2, K, \pm \frac{1}{2}) = \omega_2(\nu_2 + 1) \pm \frac{1}{2}A - \frac{1}{8}\epsilon^2\omega_2 K(K+1) \quad (5.1)$$

where  $\pm \frac{1}{2}$  stands for the spin quantum number,  $\Sigma$ , and  $A$  is the spin-orbit coupling constant. In this approximation the spin splitting for the  $K = \nu_2 + 1$  component is,

$$\Delta \nu_{K=\nu_2+1} = A \quad (5.2)$$

In a higher approximation, determined by Hougen<sup>16</sup> in 1962, the spin splitting was found to have a slight dependence on  $K$ ,

$$\Delta \nu_{K=\nu_2+1} = A \left[ 1 - \frac{1}{8}\epsilon^2 K(K+1) \right] \quad (5.3)$$

For  $K < \nu_2 + 1$ , a modification of Pople's expression for the vibronic energy levels is given by,

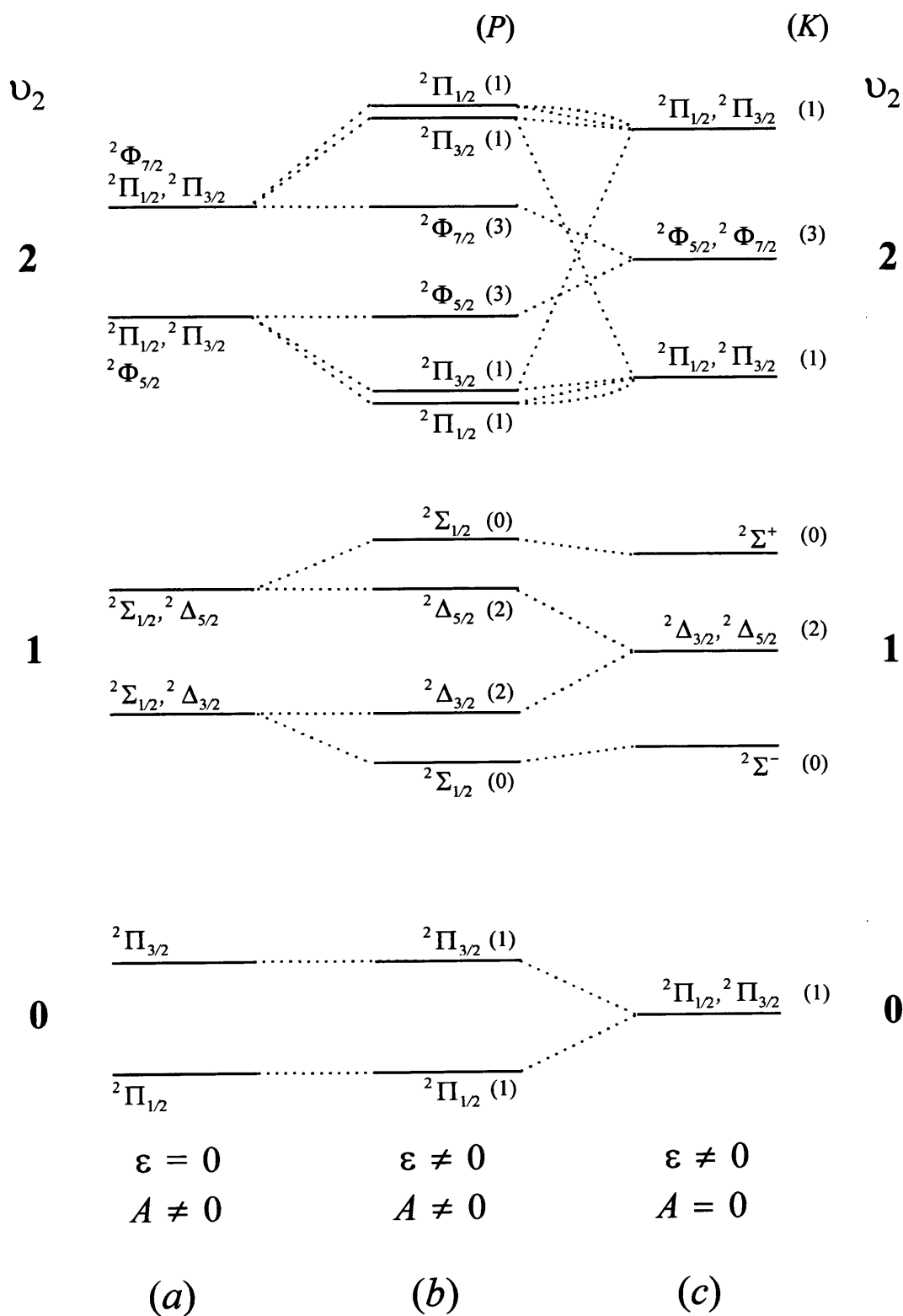


**Fig. 5.8** Correlation of the vibronic levels of a  $^2\Pi$  electronic state for *a*) zero Renner-Teller, *b*) non-zero spin-orbit and Renner-Teller and *c*) zero spin-orbit interactions.

$$G^+(\nu_2, K, \pm 1/2) = \omega_2(1 - \frac{1}{8}\epsilon^2)(\nu_2 + 1) + \frac{1}{2}A_{\nu_2, K}^* \mp \frac{\epsilon^2 A \omega_2 K(\nu_2 + 1)}{8A_{\nu_2, K}^*} \quad (5.4)$$

$$G^-(\nu_2, K, \pm 1/2) = \omega_2(1 - \frac{1}{8}\epsilon^2)(\nu_2 + 1) - \frac{1}{2}A_{\nu_2, K}^* \pm \frac{\epsilon^2 A \omega_2 K(\nu_2 + 1)}{8A_{\nu_2, K}^*} \quad (5.5)$$

where the + and - labels indicate levels associated with the upper and lower spin-orbit components, respectively.  $A_{\nu_2, K}^*$  is an effective spin-orbit coupling constant modified by vibronic interaction, given by,

$$A_{\nu_2, K}^* = \sqrt{A^2 + \epsilon^2 \omega_2^2 [(\nu_2 + 1)^2 - K^2]} \quad (5.6)$$

Assuming substantial Renner-Teller activity in the  $\tilde{C}^2\Pi$  state of SrOH, the above expressions can be used to begin tackling band assignments. However, it must be emphasised from the outset that the assignments made below are provisional and represent a best explanation for *some* of the bands in the  $\tilde{C} - \tilde{X}$  system. A complete explanation for all of the structure seen in the spectrum is currently very difficult to achieve given the relatively low resolution of the LIF spectra.

In terms of vibrational modes attention can be restricted to the Sr-O stretch ( $\nu_3$ ) and the Sr-O-H bend ( $\nu_2$ ), since the O-H stretching frequency will be too high to be responsible for any structure in Fig. 5.1. Since earlier rotational analysis shows that the rotational constant increases on excitation from the  $\tilde{X}^2\Sigma^+$  state to the  $\tilde{C}^2\Pi$  state, it is reasonable to assume that the Sr-O stretching frequency also increases. Given that the ground state value is 528 cm<sup>-1</sup>, an excited state value in the range 550-600 cm<sup>-1</sup> is likely in view of the modest increase of rotational constant. Consequently, using these arguments, a pair of bands would be expected to appear within, or close to, the 27850-27900 cm<sup>-1</sup> region, arising from excitation of the two spin-orbit components of the  $\tilde{C}^2\Pi - \tilde{X}^2\Sigma^+ 3_0^1$  transition. These perpendicular bands should show rotational structure characteristic of a  $^2\Pi(case(a)) - ^2\Sigma^+$  transition. There is a clear candidate for one of the spin-orbit components, the band at 27873 cm<sup>-1</sup>, but there is no obvious spin-orbit partner. There are, however, several other perpendicular bands near this region (see Table 5.1) which complicates this picture.

A plausible source of some of these additional perpendicular bands is that they arise from double quantum excitation of the bending mode. As can be seen from Fig. 5.8(b), six vibronic components with different energies, four  $^2\Pi$  and two  $^2\Phi$ , arise from double quantum excitation of the Sr-O-H vibrational manifold. Transitions to the  $^2\Phi$  levels from the  $^2\Sigma^+$  ground electronic state will be optically forbidden, but all four  $^2\Pi$  components are accessible. Consequently, as shown in Fig. 5.9, combining the two  $^2\Pi$  components of the  $3_0^1$  transition with the four  $^2\Pi$  vibronic components of  $2_0^2$  leads one to expect a total of *six* perpendicular bands in this region. As illustrated in Table 5.1, five perpendicular bands have definitely been found between 27750 and 27890  $\text{cm}^{-1}$  and there may well be at least one more, although this cannot be firmly identified at present due to band congestion. If these bands arise from the  $2_0^2$  and  $3_0^1$  transitions, then the proximity of the  $2\nu_2$  and  $\nu_3$  vibrational levels will inevitably give rise to Fermi resonance<sup>17</sup> (see section 3.5.3). This may explain why, if our general assignment is correct, the  $2_0^2$  bands are relatively strong, since intensity can be ‘borrowed’ from the  $3_0^1$  transition. Fermi resonance will also perturb the (020)/(001) vibronic energy level structure and this in turn may explain why the perpendicular transitions in the 27750-27890  $\text{cm}^{-1}$  region do not seem to fit into any obvious pattern. Because of this, and because of the limited spectral resolution, specific assignment of individual bands has not been attempted in the 27695-27900  $\text{cm}^{-1}$  region.

Although specific band assignments have not been made, some information on the proposed Renner-Teller effect in the  $\tilde{C}^2\Pi$  state can be extracted from the spectra. As shown in Fig. 5.8(b), the four  $^2\Pi$  vibronic components in the (020) manifold will split into two groups of levels, the  $\mu^2\Pi_{1/2,3/2}$  and  $\kappa^2\Pi_{1/2,3/2}$  levels. In the absence of Fermi resonance the splitting between the  $\mu$  and the  $\kappa$  levels is given approximately by the effective spin-orbit coupling constant,  $A_{v_2,K}^*$ , represented by equation (5.6).

In equation (5.6),  $K$  is the quantum number for projection of the vibronic angular momentum along the internuclear axis (equals one for  $^2\Pi$  vibronic components),  $A$  is the true spin-orbit coupling constant,  $\varepsilon$  is the Renner parameter, and  $\omega_2$  is the harmonic frequency of the bending vibration. The separation between the 27756 and 27873  $\text{cm}^{-1}$  bands, which are the outer members of the group of observed  $^2\Pi-^2\Sigma^+$  bands in the

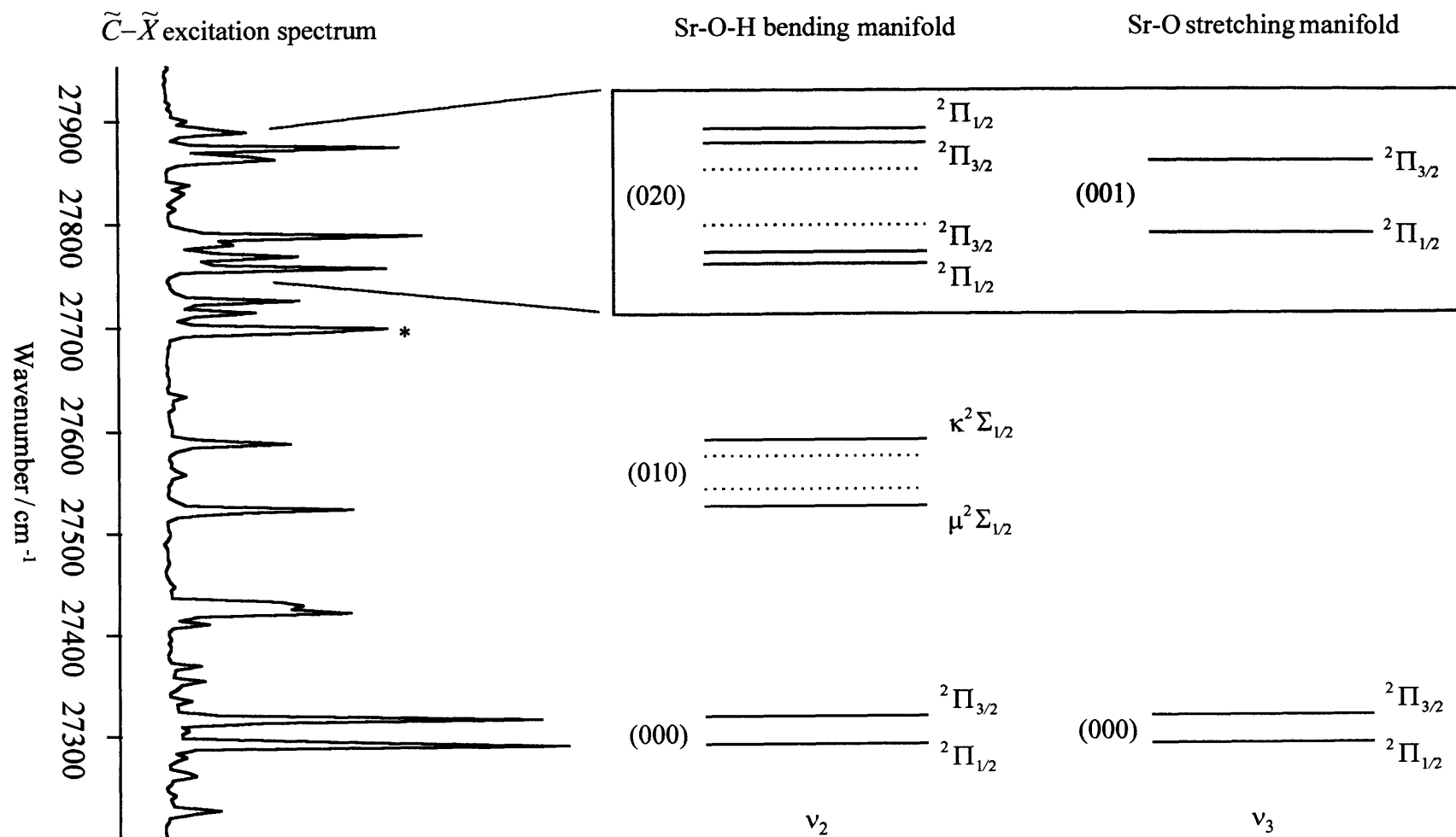


**Fig. 5.9** Illustration showing the correlation between excitation bands in the  $\tilde{C}^2\Pi - \tilde{X}^2\Sigma^+$  LIF spectrum and the predicted  $v_2$  and  $v_3$  vibrational manifolds of SrOH. The asterisk indicates a band thought to be associated with the  $\tilde{D}^2\Sigma^+ - \tilde{X}^2\Sigma^+$  transition. Dashed lines indicate vibronic levels which are optically inaccessible from the ground electronic state.

$2_0^2/3_0^1$  region, provides an *upper* limit for  $A^*$ . Using  $A = 24.52 \text{ cm}^{-1}$ , which was extracted from the  $\tilde{C} - \tilde{X} \ 0_0^0$  transition, equation (5.6) yields  $|\varepsilon\omega_2| \leq 40 \text{ cm}^{-1}$ . Furthermore, the mid-point of this cluster of bands gives a crude estimate of  $255 \text{ cm}^{-1}$  for  $\omega_2$ . This is a much lower frequency for the bending mode than in the ground electronic state of SrOH ( $\omega_2 = 361 \text{ cm}^{-1}$ ).<sup>4</sup>

Having extracted tentative information from the  $2_0^2/3_0^1$  region, it is possible to try and identify bands in the region expected for the  $2_0^1$  transition. If the parameters extracted above are reasonable, then the  $2_0^1$  transition should be centred at around  $27560 \text{ cm}^{-1}$ . The  $\tilde{C}^2\Pi(010)$  vibronic manifold will be composed of two  $^2\Delta$  and two  $^2\Sigma$  vibronic components (Fig. 5.8(b)), of which only the latter are optically accessible from the zero point level of the ground  $^2\Sigma^+$  electronic state. According to equation (5.6), the separation between the two  $^2\Sigma$  components will be  $\leq 84 \text{ cm}^{-1}$  using  $|\varepsilon\omega_2| \leq 40 \text{ cm}^{-1}$ . Consequently, two vibronic transitions are expected, the  $\tilde{C}(010)\mu^2\Sigma - \tilde{X}^2\Sigma^+(000)$  transition at around  $27520 \text{ cm}^{-1}$  and the  $\tilde{C}(010)\kappa^2\Sigma - \tilde{X}^2\Sigma^+(000)$  transition at around  $27600 \text{ cm}^{-1}$ .

Plausible candidates for these transitions can be found in the excitation spectrum (Fig. 5.9). The band at  $27588 \text{ cm}^{-1}$  has rotational structure consistent with a  $\Sigma - \Sigma$  vibronic transition. Furthermore, the emission spectrum from the upper vibronic level shows prominent activity in the ground state bending mode (see Fig. 5.6(c)), albeit in combination with one quantum in the Sr-O stretch. Thus, it is likely that the  $27588 \text{ cm}^{-1}$  band is due to the  $\tilde{C}(010)\kappa^2\Sigma - \tilde{X}^2\Sigma^+(000)$  transition. There is a band at almost exactly the position expected for the transition to the  $\mu^2\Sigma$  component, namely the band at  $27522 \text{ cm}^{-1}$ . It too shows rotational structure consistent with a  $\Sigma - \Sigma$  transition. It also shows very prominent excitation in a single quantum of the bending mode in the dispersed fluorescence spectrum (see Fig. 5.6(b)). Unfortunately, the dispersed fluorescence spectrum also registers very weak emission to the blue of the laser wavelength, suggesting that the  $27522 \text{ cm}^{-1}$  is possibly a sequence band, instead of the  $\tilde{C}(010)\mu^2\Sigma - \tilde{X}^2\Sigma^+(000)$  transition. It is perhaps conceivable that there are two transitions contributing to the  $27522 \text{ cm}^{-1}$  band, the main  $\mu^2\Sigma - \tilde{X}^2\Sigma^+$  transition and a weak underlying sequence band.

However, the expanded view of the band in Fig. 5.7(a) provides no convincing evidence in support of this suggestion.

If, instead of using the largest splitting between perpendicular bands in the  $2_0^2/3_0^1$  region, it is assumed that the 27522 and 27588  $\text{cm}^{-1}$  bands are due to the  $\tilde{C}(010)\mu^2\Sigma - \tilde{X}^2\Sigma^+(000)$  and  $\tilde{C}(010)\kappa^2\Sigma - \tilde{X}^2\Sigma^+(000)$  transitions, a value of  $\sim 30 \text{ cm}^{-1}$  is obtained for  $|\varepsilon\omega_2|$  from equation (5.6). The mid-point of the two bands, 27555  $\text{cm}^{-1}$ , yields a value of  $\sim 252 \text{ cm}^{-1}$  for  $\omega_2$ , which is very similar to the value obtained above. Consequently, the Renner parameter is found to be 0.12. If this value is used in equations (5.4) and (5.5), it is possible to obtain an estimate for the small splitting between the  $^2\Pi_{1/2}$  and  $^2\Pi_{3/2}$  components of the four  $\Pi - \Sigma$  transitions associated with two quanta of the bending vibration. A value of  $\sim 1 \text{ cm}^{-1}$  is obtained for this splitting, which is considerably smaller than any of the spacings between adjacent  $\Pi - \Sigma$  bands in Fig. 5.9. Typical spacings between bands in this region of the spectrum are on the order of 10-20  $\text{cm}^{-1}$ . One possibility is that the four  $\Pi - \Sigma$  transitions are shifted away from their nominal positions by different amounts because of Fermi resonance with one quantum of the stretching vibration,  $\nu_3$ .

To conclude this section, arguments have been presented which provide plausible assignments for several bands in the  $\tilde{C} - \tilde{X}$  region. However, there are other bands for which no assignments have been made. The Renner-Teller effect has been employed to explain part of the complexity in the excitation spectrum, but this is clearly not the whole story. As will be discussed in section 5.3.2, there is good reason to believe that one of the bands below 28000  $\text{cm}^{-1}$  is part of the  $\tilde{D}^2\Sigma^+ - \tilde{X}^2\Sigma^+$  system. However, to explain the remaining unassigned bands it seems that at least one additional, and as yet unidentified, electronic system of SrOH must overlap this region.

#### 5.3.1.5 Bands to the red of the $\tilde{C} - \tilde{X}$ origin: Evidence for a separate $^2\Sigma^+ - ^2\Sigma^+$ electronic transition

Four bands with significant intensities have been seen on the low wavenumber side of the  $\tilde{C} - \tilde{X}$  origin. These bands, which are shown in Fig. 5.10, were found at 26931, 26571, 26391 and 25997  $\text{cm}^{-1}$ . At first glance they appear to be in approximately the correct



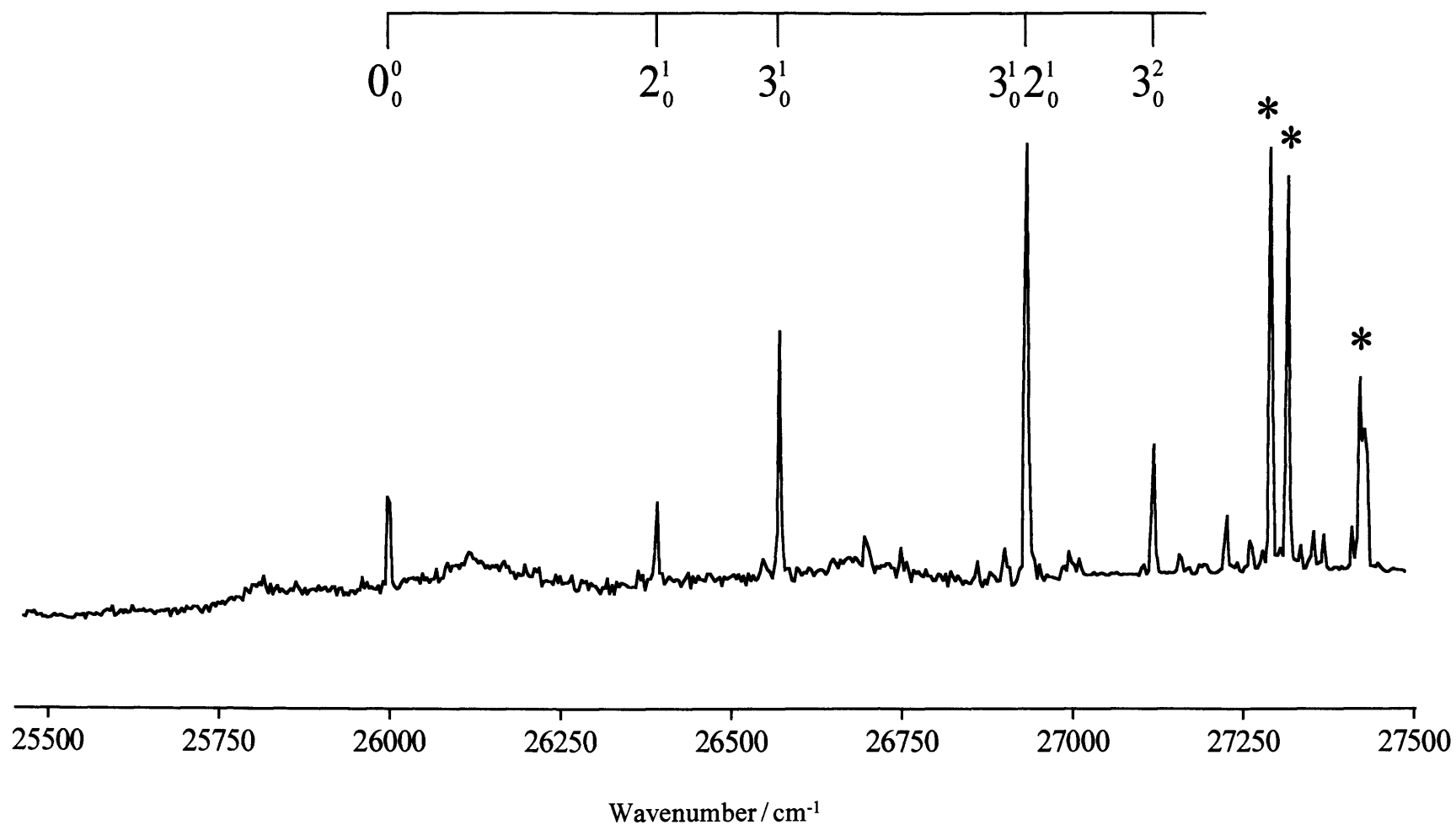


**Fig. 5.10** Laser excitation spectrum showing the  $\tilde{B}'^2\Sigma^+ - \tilde{X}^2\Sigma^+$  system and part of the  $\tilde{C}^2\Pi - \tilde{X}^2\Sigma^+$  system (marked with asterisks) of SrOH.

positions for certain hot bands in the  $\tilde{C} - \tilde{X}$  system. There are, however, firm arguments against the assignment of these bands as  $\tilde{C} - \tilde{X}$  hot bands.

The two spin-orbit components for the  $\tilde{C}^2\Pi - \tilde{X}^2\Sigma^+ 0_0^0$  transition lie at 27291 and 27315  $\text{cm}^{-1}$ . As mentioned earlier, the fundamental frequencies of  $\nu_2$  and  $\nu_3$  in the  $\tilde{X}^2\Sigma^+$  state have been determined as 361 and 528  $\text{cm}^{-1}$ .<sup>4</sup> Consequently, hot bands involving the  $\nu_2$  bending mode should result in spin-orbit pairs at 26930/26954  $\text{cm}^{-1}$  for the  $2_1^0$  transition and 26564/26588  $\text{cm}^{-1}$  for the  $2_2^0$  transition. The band at 26931  $\text{cm}^{-1}$  lies very close to the correct position for the  $\tilde{C}^2\Pi_{1/2} - \tilde{X}^2\Sigma^+ 2_1^0$  transition. However, it is evident from the excitation spectrum (Fig. 5.10) that the other spin-orbit component for this transition is missing. A similar discrepancy arises for the  $2_2^0$  transition. The band at 26571  $\text{cm}^{-1}$  is fairly close to the estimated positions of both spin-orbit components of the  $2_2^0$  hot band, but once again the other spin-orbit partner is missing.

The two spin-orbit components of the  $3_1^0$  hot band should appear at 26763 and 26787  $\text{cm}^{-1}$ , respectively, according to the ground state vibrational values obtained by Brazier.<sup>4</sup> These transitions are also missing from the excitation spectrum. Consequently, there is no evidence for any significant intensity in hot bands associated with the  $\tilde{C} - \tilde{X}$  system and therefore the four bands mentioned above must arise from a different source.

To extract further information their rotational structure was investigated. Fig. 5.11(a) shows an expanded view of the band centred at 25997  $\text{cm}^{-1}$ . The resolution of the dye laser was insufficient to resolve the rotational structure fully, but some structure is resolved in the wings and the contours allow the state symmetries to be readily assigned. The 25997  $\text{cm}^{-1}$  band arises from a  $^2\Sigma - ^2\Sigma$  vibronic transition. Using the known rotational constant of the  $\tilde{X}^2\Sigma^+$  state of SrOH ( $B'' = 0.24920 \text{ cm}^{-1}$ ),<sup>4</sup> the observed rotational structure has been simulated by varying the rotational constant of the upper electronic state and the ground state rotational temperature (see Fig. 11(b)). A least squares fit of the simulated spectrum to the assigned structure in the excitation spectrum gives an excited state rotational constant of  $B' = 0.2658 \pm 0.0009 \text{ cm}^{-1}$ .

Similar rotational analyses were performed for the other three bands situated to the red of the  $\tilde{C} - \tilde{X}$  origin. The band, centred at 26571  $\text{cm}^{-1}$  is also easily identified as a  $^2\Sigma - ^2\Sigma$

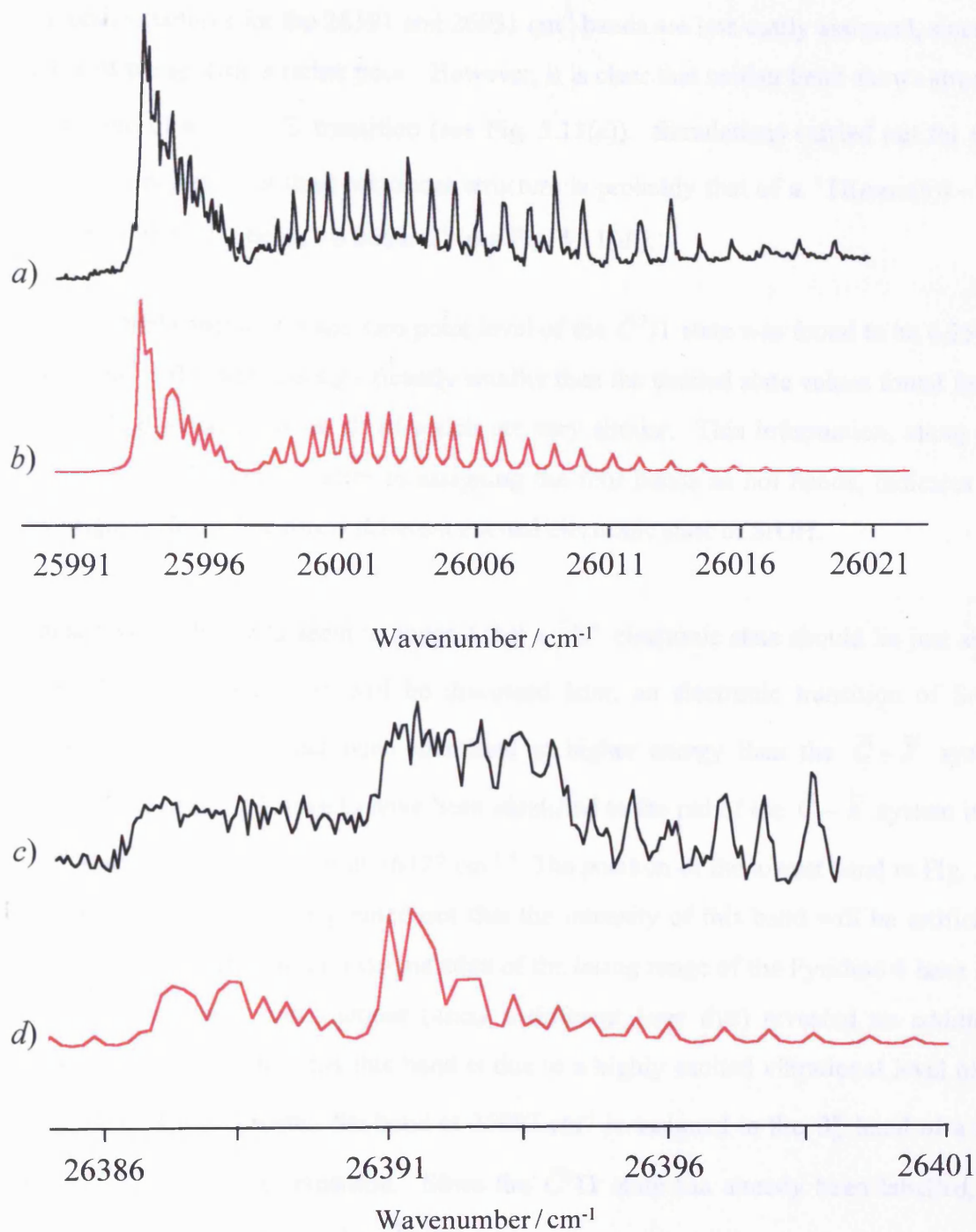


**Fig. 5.11** a) Expanded view of the band at 25997 cm<sup>-1</sup>. b) Simulation assuming a  $^2\Sigma - ^2\Sigma$  transition ( $T = 20$  K,  $B'' = 0.2492$  cm<sup>-1</sup> and  $B' = 0.2658$  cm<sup>-1</sup>). c) Expanded view of the band at 26391 cm<sup>-1</sup>. d) Simulation assuming a  $^2\Pi(\text{Hund's case}(b)) - ^2\Sigma$  transition ( $T = 20$  K,  $B'' = 0.2492$  cm<sup>-1</sup> and  $B' = 0.266$  cm<sup>-1</sup>).

transition, with a least squares fit yielding a value of  $B' = 0.2653 \pm 0.0009 \text{ cm}^{-1}$ . The rotational structures for the 26391 and 26931  $\text{cm}^{-1}$  bands are less easily assigned, since the quality of the spectra is rather poor. However, it is clear that neither band shows structure reminiscent of a  $^2\Sigma - ^2\Sigma$  transition (see Fig. 5.11(c)). Simulations carried out for these two bands indicate that their rotational structure is probably that of a  $^2\Pi(\text{case}(b)) - ^2\Sigma^+$  transition,<sup>18</sup> with  $B'$  being  $\sim 0.266 \text{ cm}^{-1}$  (see Fig. 5.11(d)).

The rotational constant for the zero point level of the  $\tilde{C}^2\Pi$  state was found to be  $0.2564 \pm 0.0009 \text{ cm}^{-1}$ . This value is significantly smaller than the excited state values found for the four bands discussed above, all of which are very similar. This information, along with the difficulties discussed earlier in assigning the four bands as hot bands, indicates that they originate from an entirely different excited electronic state of SrOH.

Analogy with SrF would seem to suggest that a  $^2\Sigma^+$  electronic state should lie just above the  $C^2\Pi$  state. Indeed, as will be discussed later, an electronic transition of SrOH, labelled  $\tilde{D}^2\Sigma^+ - \tilde{X}^2\Sigma^+$ , has been identified at higher energy than the  $\tilde{C} - \tilde{X}$  system. However, the only  $^2\Sigma^+$  state to have been identified to the red of the  $\tilde{C} - \tilde{X}$  system is the  $\tilde{B}^2\Sigma^+$  state, whose origin lies at  $16377 \text{ cm}^{-1}$ .<sup>9</sup> The position of the lowest band in Fig. 5.10 is  $25997 \text{ cm}^{-1}$ . It should be pointed out that the intensity of this band will be artificially low, since it is situated at the extreme edge of the lasing range of the Pyridine 4 laser dye. Since scans to lower wavenumber (using a different laser dye) revealed no additional bands, it is inconceivable that this band is due to a highly excited vibrational level of the  $\tilde{B}^2\Sigma^+$  state. Consequently, the band at  $25997 \text{ cm}^{-1}$  is assigned to the  $0_0^0$  band of a new  $^2\Sigma^+ - \tilde{X}^2\Sigma^+$  electronic transition. Since the  $\tilde{C}^2\Pi$  state has already been labelled, the new excited state is designated as  $\tilde{B}'^2\Sigma^+$ .

The increase in rotational constant ( $\sim 0.017 \text{ cm}^{-1}$ ) indicates that there is a decrease in Sr-O bond length upon  $\tilde{B}' \leftarrow \tilde{X}$  excitation, assuming that the O-H bond length does not alter significantly. Consequently, an increase in the Sr-O stretching vibrational frequency should also be seen upon electronic excitation. Given that the ground state Sr-O stretching frequency is  $528 \text{ cm}^{-1}$ , a clear candidate for  $3_0^1$  is the band at  $26571 \text{ cm}^{-1}$ , which lies 574

$\text{cm}^{-1}$  above the origin band. A possibility for the second member of the  $\nu_3$  progression is the weak band situated at  $27121 \text{ cm}^{-1}$ . The spacing between this band and the  $3_0^1$  band is  $550 \text{ cm}^{-1}$ , which is not unreasonable assuming moderate anharmonicity. The rotational contour of the  $27121 \text{ cm}^{-1}$  band is found to be  $^2\Sigma^+ - ^2\Sigma^+$ . Consequently, the band at  $27121 \text{ cm}^{-1}$  is tentatively assigned as the  $3_0^2$  transition.

Having assigned a progression in the  $\nu_3$  vibrational mode, it is necessary to assign the other two bands in Fig. 5.10, situated at  $26391$  and  $26931 \text{ cm}^{-1}$ . For a metal-localised  $^2\Sigma^+ - ^2\Sigma^+$  electronic transition in which the upper and lower state equilibrium geometries are linear, the main vibrational progression should be in  $\nu_3$  in the absence of significant vibronic coupling. As mentioned above, the rotational structure for the  $26391$  and  $26931 \text{ cm}^{-1}$  bands suggests that both arise from  $^2\Pi - ^2\Sigma^+$  transitions, where the  $^2\Pi$  state conforms to Hund's case (b). In addition, simulations of the two bands yield approximate values for the respective upper state rotational constants which are very similar to those obtained for the  $0_0^0$  and  $3_0^1$  bands, although the quality of data is insufficient to obtain a fit. Consequently, it seems likely that the  $26391$  and  $26931 \text{ cm}^{-1}$  bands originate from the same electronic system as the  $0_0^0$  and  $3_0^1$  bands.

The spacing between the  $0_0^0$  band and that at  $26391 \text{ cm}^{-1}$  is  $\sim 394 \text{ cm}^{-1}$ . In ground state SrOH, the bending frequency,  $\nu_2$ , is  $361 \text{ cm}^{-1}$ .<sup>4</sup> Consequently, it is possible that the  $26391 \text{ cm}^{-1}$  band arises from single quantum excitation of  $\nu_2$  in the  $\tilde{B}'^2\Sigma^+$  state of SrOH. If the equilibrium geometry of the  $\tilde{B}'^2\Sigma^+$  state was bent, a lengthy progression in  $\nu_2$  would be observed in the excitation spectrum. No such progression is seen. For a linear equilibrium geometry in the  $\tilde{B}'^2\Sigma^+$  state, transitions involving  $\Delta v_2 = \text{odd}$  are Franck-Condon forbidden.<sup>14</sup> If the band at  $26391 \text{ cm}^{-1}$  is due to the  $2_0^1$  transition, then it must gain intensity through vibronic coupling. The  $2_0^1$  transition would possess  $^2\Pi$  vibronic symmetry, with the excited state subject to Hund's case (b) coupling, and this is the conclusion drawn from the rotational contour. It is conceivable that the unusually large intensity of the  $2_0^1$  band arises through mixing with  $^2\Pi$  vibronic levels in the  $\tilde{C}^2\Pi$  state manifold of SrOH.<sup>14</sup> Consequently, the band at  $26391 \text{ cm}^{-1}$  is tentatively assigned to the  $2_0^1$  transition in the  $\tilde{B}'^2\Sigma^+ - \tilde{X}^2\Sigma^+$  system of SrOH.

Finally, the intense band at 26931 cm<sup>-1</sup> is considered. Although this band does not appear to fit into a progression for  $\nu_2$  or  $\nu_3$ , it is in a reasonable place for the  $3_0^1 2_0^1$  combination band. As shown in Fig. 5.12, the bending vibration,  $\nu_2$ , is the predominant active mode in the dispersed fluorescence of this band, although there is a weak band *ca.* 890 cm<sup>-1</sup> to the red of the pump position which correlates to the  $3_1^1 2_1^1$  combination band. The  $3_0^1 2_0^1$  transition should show rotational structure which is characteristic of a  ${}^2\Pi(case(b)) - {}^2\Sigma^+$  transition and, once again, the rotational contour supports evidence of this. The spacing between the  $3_0^1 2_0^1$  and  $3_0^1$  transitions is  $\sim 360$  cm<sup>-1</sup>, which is smaller than would be expected since the  $\nu_2$  vibrational frequency for the  $\tilde{B}'^2\Sigma^+$  state was deduced as 394 cm<sup>-1</sup> earlier. However, as for the band at 26391 cm<sup>-1</sup>, the proximity of the 26931 cm<sup>-1</sup> band to the nearby Renner-Teller  $\tilde{C}^2\Pi$  state could allow substantial electronic-vibronic mixing to occur, resulting in a shift to lower wavenumber.<sup>14</sup> This may also be the reason for the relatively high intensity of this band. Indeed, the  $3_0^1 2_0^1$  band has a significantly higher intensity than the  $2_0^1$  band. This may partly be because the  $3_0^1 2_0^1$  band is situated at the maximum of the laser dye curve, but it may also be due to a greater degree of vibronic mixing because of its closer proximity to the  $\tilde{C}^2\Pi$  state origin (*ca.* 400 cm<sup>-1</sup>).

### 5.3.2 The $\tilde{D}^2\Sigma^+ - \tilde{X}^2\Sigma^+$ system

By analogy with SrF a  ${}^2\Sigma^+$  electronic state of SrOH is expected slightly above the  $\tilde{C}^2\Pi$  state. A band system due to excitation to this new  ${}^2\Sigma^+$  state, the  $\tilde{D}^2\Sigma^+$  state, has been observed and Fig. 5.13 shows the key region. A series of bands showing no evidence of spin-orbit structure, but forming a clear vibrational progression, have been identified and these bands are assigned to the  $\tilde{D}^2\Sigma^+ - \tilde{X}^2\Sigma^+$  transition. The vibrational progression, with an interval of  $\sim 630$  cm<sup>-1</sup>, is clearly due to the Sr-O stretch since the O-H stretch and Sr-O-H bending modes are expected to have much higher and lower frequencies, respectively. The Sr-O stretching frequency in the  $\tilde{D}^2\Sigma^+$  state is approximately 20% higher than in the ground state, showing that the Sr-O bond is significantly strengthened by electronic excitation.

Although it is straightforward to identify the Sr-O stretching progression, it is not easy to locate the origin of the  $\tilde{D} - \tilde{X}$  system. The strongest band lies at 28317 cm<sup>-1</sup>, but extrapolation to the red yields another possible candidate, the band at 27698 cm<sup>-1</sup>. The

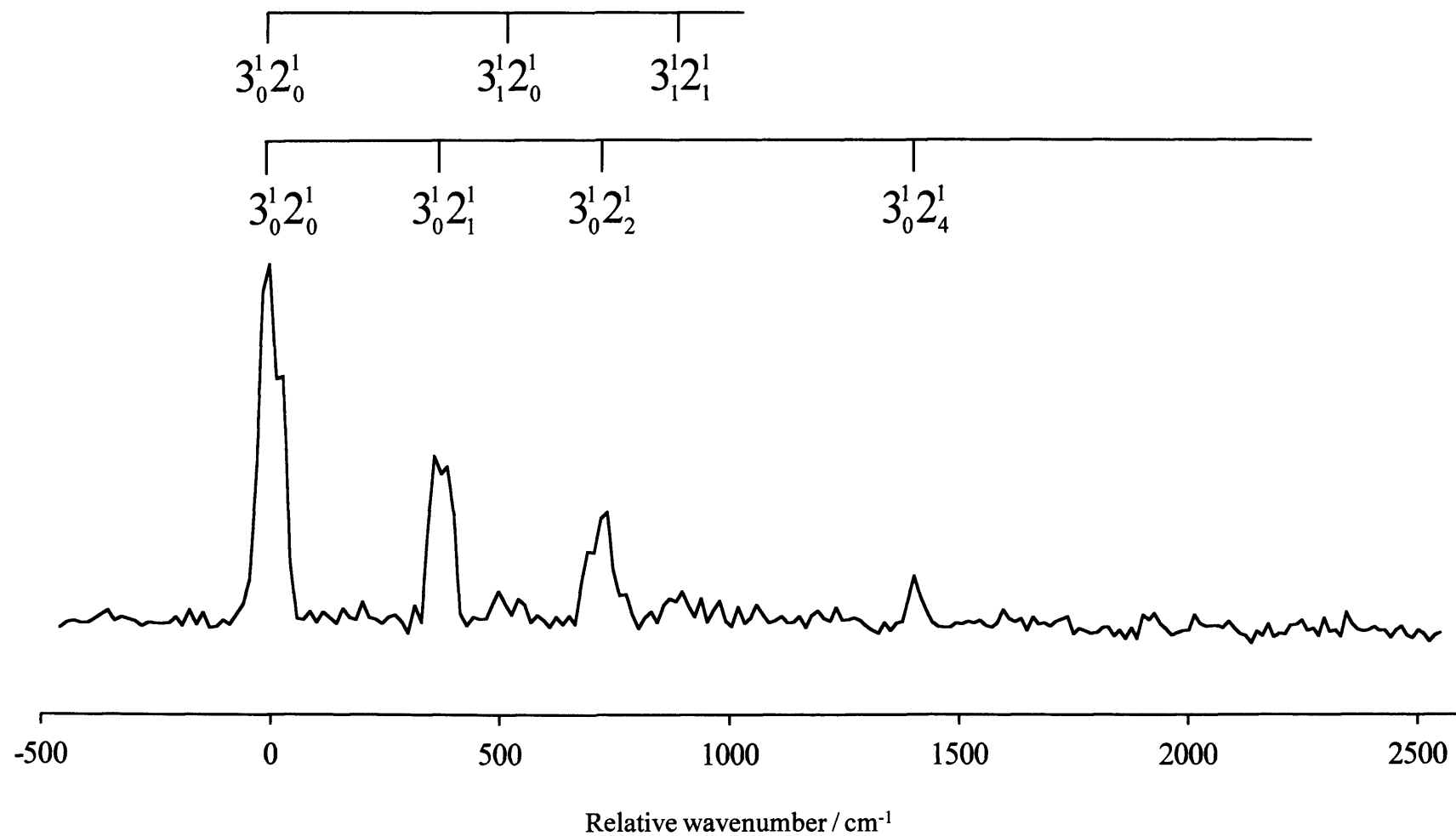


**Fig. 5.12** Dispersed fluorescence spectrum obtained by pumping the  $\tilde{B}'^2\Sigma^+ - \tilde{X}^2\Sigma^+ 3^1_0 2^1_0$  transition at  $26931 \text{ cm}^{-1}$ .

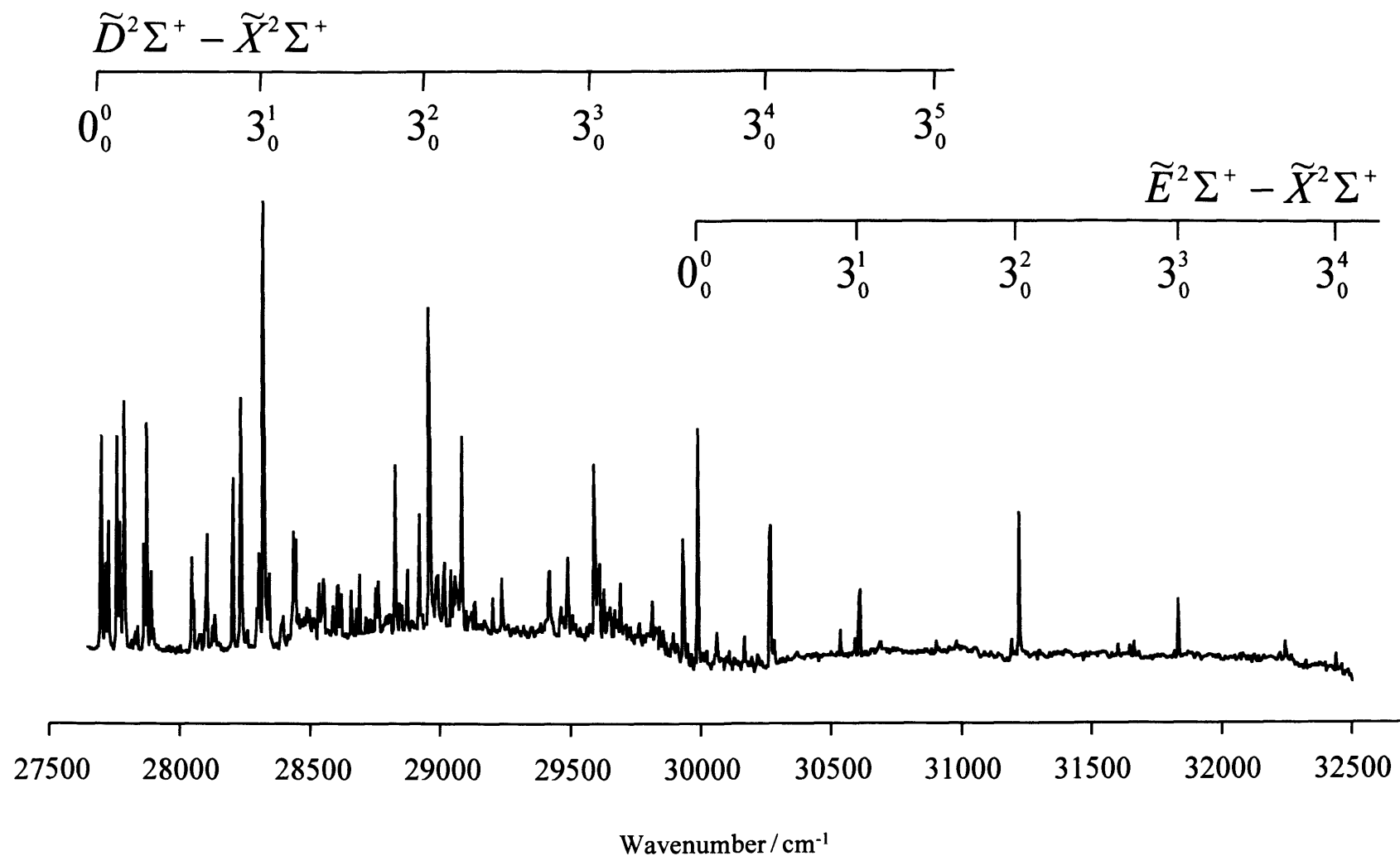


**Fig. 5.13** Laser excitation spectrum showing the  $\tilde{D}^2\Sigma^+ - \tilde{X}^2\Sigma^+$  and  $\tilde{E}^2\Sigma^+ - \tilde{X}^2\Sigma^+$  transitions of SrOH. In both cases the only significant vibrational structure is a progression in the Sr-O stretching mode. This spectrum was obtained by joining scans of three different laser dyes, hence the uneven background signal.



latter, whose rotational contour clearly shows that it arises from a  ${}^2\Sigma^+ - {}^2\Sigma^+$  transition, lies amongst the densest group of bands in the  $\tilde{C} - \tilde{X}$  system. Fig. 5.15(a) shows a partially resolved rotational spectrum of the band at 27698 cm<sup>-1</sup>, while Fig. 5.15(b) shows a simulation assuming a  ${}^2\Sigma^+ - {}^2\Sigma^+$  transition. Although the quality of the experimental spectrum is rather poor, a visual best fit of the rotational structure to the simulation yields an excited state rotational constant of  $\sim 0.257$  cm<sup>-1</sup>. This value for  $B'$  is very similar to that obtained for the  $\tilde{C}^2\Pi$  excited state, which is relatively unsurprising since there is a strong possibility that if the 27698 cm<sup>-1</sup> band is associated with the  $\tilde{D}^2\Sigma^+$  manifold, it will be perturbed by levels of  ${}^2\Sigma^+$  vibronic symmetry in the  $\tilde{C}^2\Pi$  manifold. Consequently, no clear conclusions can be made from the rotational structure of the band at 27698 cm<sup>-1</sup> regarding its assignment to the  $\tilde{D} - \tilde{X}$  system.

In the absence of vibronic coupling, dispersed fluorescence spectra would help confirm the assignment of the bands at 27698 and 28317 cm<sup>-1</sup>, since no significant bending mode activity would be expected for the  $\tilde{D}^2\Sigma^+ - \tilde{X}^2\Sigma^+$  transition. The dispersed fluorescence spectra arising from excitation of the 28956 (see Fig. 5.14(c)) and 29590 cm<sup>-1</sup> transitions, which are rather distant from the  $\tilde{C} - \tilde{X}$  manifold, show precisely this scenario, namely a progression in only the Sr-O stretch. However, dispersed fluorescence spectra obtained by pumping the 27698 and 28317 cm<sup>-1</sup> transitions (see Fig. 5.14(a) and (b)), both show more complex vibrational structure with substantial activity in both the Sr-O stretch *and* the bending mode. Clearly the dispersed fluorescence spectra for these four bands do not provide a definitive assignment. Consequently, even though the 27698 cm<sup>-1</sup> band is claimed as the  $0_0^0$  transition in Table 5.1, it is not clear whether it, or the 28317 cm<sup>-1</sup> band can legitimately be assigned to the  $\tilde{D}^2\Sigma^+ - \tilde{X}^2\Sigma^+$  origin.

The rotational structure for the band at 28956 cm<sup>-1</sup>, assigned to the  $\tilde{D}^2\Sigma^+ - \tilde{X}^2\Sigma^+ 3_0^2$  transition, is shown in Fig 5.15(c). The simulation below it (Fig. 5.15(d)), assumes a  ${}^2\Sigma^+ - {}^2\Sigma^+$  transition. Since this band is relatively removed from the dense group of bands associated with the  $\tilde{C} - \tilde{X}$  system, extraction of an excited state rotational constant from its rotational structure should yield a value characteristic of the  $\tilde{D}^2\Sigma^+$  state. Once again, the quality of the experimental spectrum is insufficient to obtain a statistical fit of the observed rotational structure to the simulation, but a visual best fit yields an excited

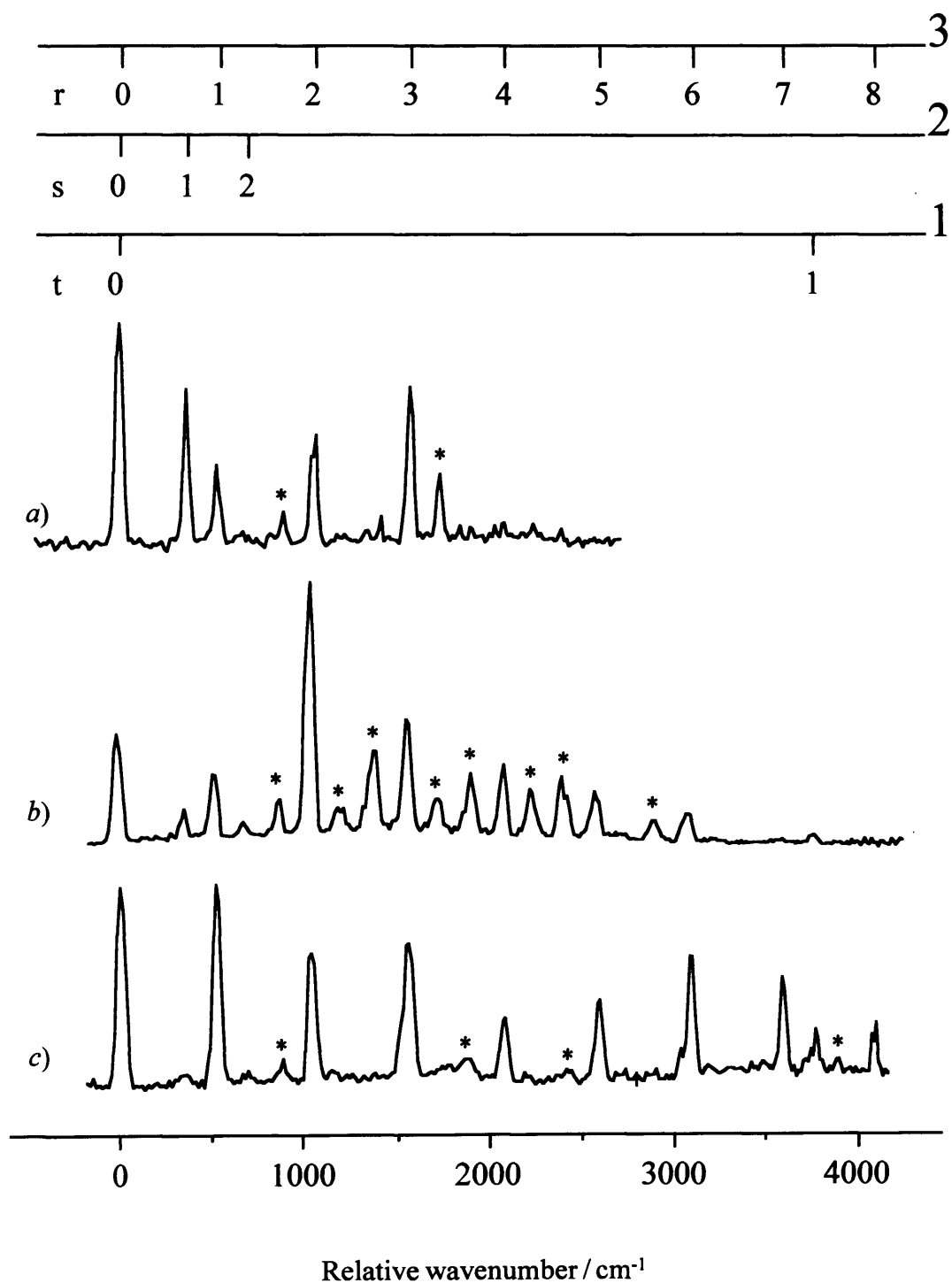


**Fig. 5.14** Dispersed fluorescence spectra obtained by pumping the bands at a) 27698  $\text{cm}^{-1}$ , b) 28317  $\text{cm}^{-1}$  and c) 28956  $\text{cm}^{-1}$ . Modes  $\nu_1$ ,  $\nu_2$  and  $\nu_3$  are the O-H stretch, Sr-O-H bend and Sr-O stretch, respectively. Asterisked bands indicate  $\nu_2\nu_3$  combination bands.

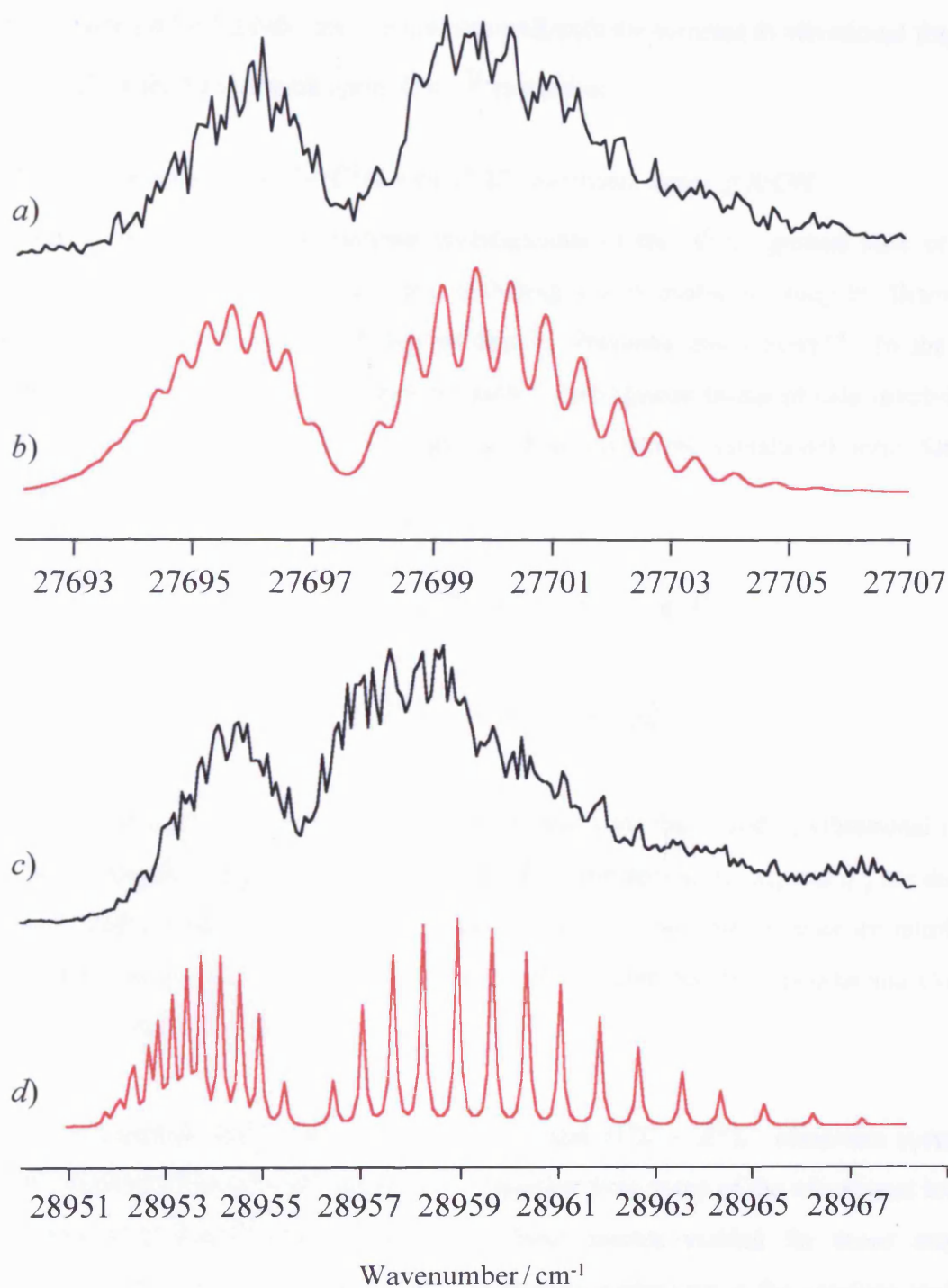


**Fig. 5.15** *a)* Rotational contour of the tentatively assigned  $\tilde{D}^2\Sigma^+ - \tilde{X}^2\Sigma^+ 0_0^0$  transition at 27698 cm<sup>-1</sup>. *b)* Simulation assuming a  $^2\Sigma^+ - ^2\Sigma^+$  transition ( $B'' = 0.2492$  cm<sup>-1</sup>,  $B' \sim 0.257$  cm<sup>-1</sup> and  $T = 15$  K). *c)* Rotational contour of the tentatively assigned  $\tilde{D}^2\Sigma^+ - \tilde{X}^2\Sigma^+ 3_0^2$  transition at 28956 cm<sup>-1</sup>. *d)* Simulation assuming a  $^2\Sigma^+ - ^2\Sigma^+$  transition ( $B'' = 0.2492$  cm<sup>-1</sup>,  $B' \sim 0.265$  cm<sup>-1</sup> and  $T = 15$  K).

state rotational constant of  $\sim 0.265 \text{ cm}^{-1}$ . The increase in rotational constant relative to the  $\tilde{X}^2\Sigma^+$  state ( $B'' = 0.24920 \text{ cm}^{-1}$ )<sup>4</sup> correlates well with the increase in vibrational frequency observed for the Sr-O stretch upon  $\tilde{D} \leftarrow \tilde{X}$  excitation.

### 5.3.2.1 Emission from the $\tilde{C}^2\Pi$ and $\tilde{D}^2\Sigma^+$ electronic states of SrOH

A number of dispersed fluorescence investigations of the  $\tilde{X}^2\Sigma^+$  ground state of SrOH have been carried out in recent years, including a low-resolution study by Brazier and Bernath<sup>4</sup> and several high-resolution studies by Presunka and Coxon.<sup>6-8</sup> In the latter, molecular constants were extracted from global least-squares fitting of data involving the ( $\nu_2$ ) bending and ( $\nu_3$ ) stretching modes to their respective vibrational term functions (referred to the (000) level), given by,

$$G_0(0, \nu_2, 0) = \omega_2^0 \nu_2 + x_{22}^0 \nu_2^2 + g_{22} l_2^2 \quad (5.7)$$

$$G_0(0, 0, \nu_3) = \omega_3^0 \nu_3 + x_{33}^0 \nu_3^2 \quad (5.8)$$

where  $\nu_2$  and  $\nu_3$  are the vibrational quantum numbers for the  $\nu_2$  and  $\nu_3$  vibrational modes,  $\omega_2$  and  $\omega_3$  are the respective harmonic vibrational frequencies,  $x_{22}$ ,  $x_{33}$  and  $g_{22}$  are diagonal anharmonicity constants, and  $l$  is the vibrational angular momentum quantum number for the degenerate bending mode. The experimental data obtained by Presunka and Coxon is collected together in Table 5.3.

During the current analysis of the  $\tilde{C}^2\Pi - \tilde{X}^2\Sigma^+$  and  $\tilde{D}^2\Sigma^+ - \tilde{X}^2\Sigma^+$  electronic systems of SrOH, dispersed fluorescence spectra were recorded from many of the vibrational levels in the respective excited state manifolds. These spectra yielded far more extensive vibrational structure in the ground electronic state than was seen in the previous studies of both Bernath and Presunka, although the resolution in the work of Presunka was much higher. Many of these spectra (see Fig. 5.14(a)-(c)) show significant vibrational activity in the Sr-O stretch ( $\nu_3$ ), the Sr-O-H bend ( $\nu_2$ ), several  $\nu_2\nu_3$  combination bands and also the O-H stretch ( $\nu_1$ ). Presunka and Coxon observed vibrational members of up to  $3\nu_2$  and  $2\nu_3$  in their dispersed fluorescence studies of the  $\tilde{A}^2\Pi - \tilde{X}^2\Sigma^+$  and  $\tilde{B}^2\Sigma^+ - \tilde{X}^2\Sigma^+$  electronic transitions, while in the current study up to  $4\nu_2$  and  $8\nu_3$  have been observed. No attempt is

made to improve the vibrational constants reported by Presunka, since the resolution of the monochromator used in the current work was insufficient to make a valid comparison with their high-resolution measurements. However, since the dispersed fluorescence spectra show strong activity in relatively high quanta of the Sr-O-H bending and Sr-O stretching modes, they can be used to verify the ground state molecular constants reported by Presunka.

**Table 5.3** Molecular constants for the  $\tilde{X}^2\Sigma^+$  state of SrOH.

Constant	Value (cm <sup>-1</sup> )
$\omega_2^0$	360.605 <sup>a)</sup>
$x_{22}^0$	-4.480 <sup>a)</sup>
$g_{22}$	7.5646 <sup>a)</sup>
$\omega_3^0$	529.446 <sup>b)</sup>
$x_{33}^0$	-2.455 <sup>b)</sup>

<sup>a)</sup> Taken from reference 8

<sup>b)</sup> Taken from reference 7

Figs. 5.14(c) and 5.16 show dispersed fluorescence spectra obtained by laser excitation of the  $\tilde{D}^2\Sigma^+ - \tilde{X}^2\Sigma^+ 3_0^2$  transition of SrOH at 28956 cm<sup>-1</sup> and the transition at 27422 cm<sup>-1</sup> (an unidentified transition of the  $\tilde{C}^2\Pi - X^2\Sigma^+$  system). In Fig. 5.14(c) up to 8 $\nu_3$  are excited, while the legend above the spectrum in Fig. 5.16 clearly indicates considerable activity in  $\nu_2$ ,  $\nu_3$  and  $\nu_2\nu_3$ , including up to 5 $\nu_2$ . In order to collect statistically meaningful data for the positions of each vibrational member, information from a number of independent dispersed fluorescence spectra was used. Tables 5.4 and 5.5 show the relative values obtained for  $n\nu_2$  and  $n\nu_3$ , along with their mean values, one standard deviation and the sample size. The respective tables also show the calculated relative positions for each quantum of  $\nu_2$  and  $\nu_3$  using the molecular constants reported by Presunka.<sup>6-8</sup>

A weighted least-squares fit of all values of  $n\nu_2$  and  $n\nu_3$  to the respective  $\nu_2$  and  $\nu_3$  term functions of equations (5.7) (ignoring the  $g_{22}l^2$  term) and (5.8), yields values of  $\omega_2 = 368.1$

$\pm 3.4 \text{ cm}^{-1}$ ,  $x_{22} = -4.81 \pm 0.55 \text{ cm}^{-1}$ ,  $\omega_3 = 529.1 \pm 0.7 \text{ cm}^{-1}$  and  $x_{33} = -2.55 \pm 0.09 \text{ cm}^{-1}$ . Clearly, the value of  $\omega_2$  is significantly higher than that reported by Presunka ( $360.605 \text{ cm}^{-1}$ ), while the value of  $x_{22}$  compares more favourably ( $-4.480 \text{ cm}^{-1}$ ). However, it must be pointed out that the doublet splitting, due to the  $g_{22}l^2$  term in equation (5.7), is not resolved in any of the dispersed fluorescence spectra obtained in the present work and so the experimental position of bands involving this splitting are taken as the average of the two components. This will inevitably introduce significant errors into the value obtained for  $\omega_2$ . As would be expected, comparison of  $\omega_3$  and  $x_{33}$  with the values obtained by Presunka is much more favourable.

**Table 5.4** Comparison of experimental values for  $n\nu_2$  with those calculated using the molecular constants from reference 8.

$\nu_1, \nu_2, \nu_3$	$\bar{x} \text{ (cm}^{-1}\text{)}$	$\sigma \text{ (cm}^{-1}\text{)}$	Sample	Calc. value (cm <sup>-1</sup> )
0,1,0	363.3	4.7	12	363.69
0,2,0	717.0	5.1	7	703.29, 733.55 <sup>a)</sup>
0,4,0	1395.5	7.1	4	1370.74, 1401.00 <sup>a)</sup>

<sup>a)</sup> The calculated values of  $(0,\nu_2,0)$  arise through  $l$ -type doubling.

**Table 5.5** Comparison of experimental values for  $n\nu_3$  with those calculated using the molecular constants from reference 7.

$\nu_1, \nu_2, \nu_3$	$\bar{x} \text{ (cm}^{-1}\text{)}$	$\sigma \text{ (cm}^{-1}\text{)}$	Sample	Calc. value (cm <sup>-1</sup> )
0,0,1	526.2	2.7	24	526.99
0,0,2	1049.3	5.8	16	1049.07
0,0,3	1567.2	4.7	13	1566.24
0,0,4	2075.1	4.5	7	2078.50
0,0,5	2581.6	8.2	5	2585.86
0,0,6	3074.3	12.3	3	3088.30
0,0,7	3588.0	-	1	3585.83
0,0,8	4078.0	-	1	4078.45

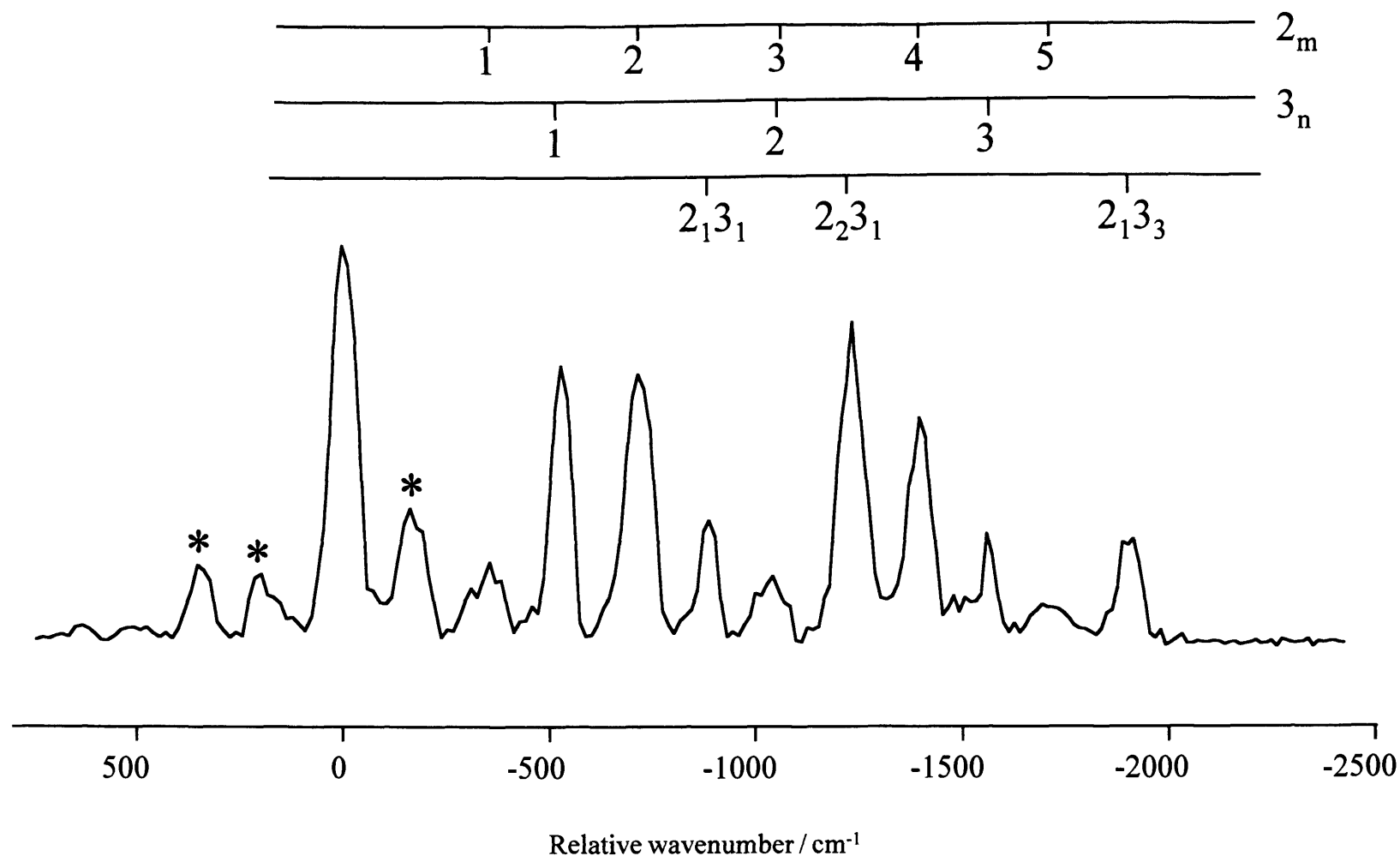


**Fig. 5.16** Dispersed fluorescence spectra obtained by laser excitation of 27422 cm<sup>-1</sup>. Modes  $\nu_2$  and  $\nu_3$  are the Sr-O-H bend and Sr-O stretch, respectively. The asterisked bands show blue shifted emission, indicating possible hot/sequence band activity.

Strictly speaking the expression for the vibrational levels should include off-diagonal anharmonicity, i.e.,

$$G_0(0, \nu_2, \nu_3) = \omega_2^0 \nu_2 + x_{22}^0 \nu_2^2 + \omega_3^0 \nu_3 + x_{33}^0 \nu_3^2 + g_{22} \nu_2^2 + x_{23} \nu_2 \nu_3 + g_{22} l_2^2 \quad (5.9)$$

where  $x_{23}$  represents the coupling between modes  $\nu_2$  and  $\nu_3$ . In principle it should be possible to determine  $x_{23}$  from the combination bands seen in Figs. 5.14(a), 5.14(b) and 5.16. However, in practice the resolution in the present work is insufficient to obtain a meaningful value for  $x_{23}$ . Hopefully, this work may stimulate higher resolution dispersed fluorescence studies in the future.

The most interesting finding from the dispersed fluorescence spectra is a band apparently due to excitation of the O-H stretch ( $\nu_1$ ) in the  $\tilde{X}^2\Sigma^+$  state. The frequency of this mode in SrOH has not been previously reported. The corresponding vibration in CaOH has been identified, although there is a considerable discrepancy between the value obtained by Bernath and co-workers ( $3847 \text{ cm}^{-1}$ )<sup>19</sup> and that reported by Pereira and Levy ( $3778 \text{ cm}^{-1}$ ).<sup>10</sup> In the dispersed fluorescence spectrum shown in Fig. 5.14(b) there is a weak peak at  $3764 \pm 3 \text{ cm}^{-1}$ , which is unassignable in terms of  $\nu_2$ ,  $\nu_3$  or combinations of these two vibrations. Consequently, this peak must be due to excitation of  $\nu_1$ , the O-H stretch. It is hardly surprising that this peak is very weak given that the O-H bond is unlikely to be significantly perturbed by a mainly metal-localised electronic transition.

Little change in the frequency of  $\nu_1$  is expected between SrOH and CaOH. Therefore, it seems likely that the correct value for CaOH is that reported by Pereira and Levy. However, it is interesting that the O-H stretching frequency for SrOH is slightly lower than that of CaOH. One would expect, on the basis of the electronegativities of the metals, that the OH group in SrOH should be closer to the OH<sup>-</sup> ionic limit than in CaOH. In fact, the value obtained for SrOH is only  $26 \text{ cm}^{-1}$  above that reported for free OH<sup>-</sup> ( $3738 \text{ cm}^{-1}$ ),<sup>20</sup> confirming the picture of a strongly ionic molecule.

### 5.3.3 The $\tilde{E}^2\Sigma^+ - \tilde{X}^2\Sigma^+$ system

In addition to the  $\tilde{D}^2\Sigma^+ - \tilde{X}^2\Sigma^+$  system, Fig. 5.13 also shows another new system of SrOH. If the electronic state ordering for SrF is assumed for SrOH, the next highest optically accessible excited state of SrOH would be the analogue of the  $E^2\Pi$  state of SrF



( $T_e = 31600 \text{ cm}^{-1}$ ).<sup>12</sup> The  $E^2\Pi$  state of SrF has a spin-orbit coupling constant of  $\sim 85 \text{ cm}^{-1}$  and so a substantial spin-orbit splitting should also be seen for SrOH. However, no evidence of any spin-orbit splitting is seen for this new system in Fig. 5.13. Consequently, the upper electronic state is assigned as another  $^2\Sigma^+$  state, presumably the analogue of the  $F^2\Sigma^+$  state of SrF ( $T_e = 32820 \text{ cm}^{-1}$ ).<sup>12</sup> This assignment is confirmed by the rotational contours of individual bands (see, for example, Fig. 5.17) which clearly arise from  $^2\Sigma^+ - ^2\Sigma^+$  transitions. A visual best fit of the experimental spectrum to a  $^2\Sigma^+ - ^2\Sigma^+$  transition simulation results in an upper state rotational constant of  $\sim 0.268 \text{ cm}^{-1}$ . The rotational temperature of the simulation is 15 K. To be consistent with the labels used for the other excited states, the new excited state of SrOH is designated as the  $\tilde{E}^2\Sigma^+$  state.

Unlike the  $\tilde{D}^2\Sigma^+ - \tilde{X}^2\Sigma^+$  system, the origin of the  $\tilde{E}^2\Sigma^+ - \tilde{X}^2\Sigma^+$  system is easy to locate. The band at  $29990 \text{ cm}^{-1}$  corresponds to the  $0_0^0$  transition since it is intense and no bands are found at lower wavenumbers which fit into the clear Sr-O stretching progression seen on the high wavenumber side. Consequently, the bands at  $30610$ ,  $31222$ ,  $31834$  and  $32439 \text{ cm}^{-1}$  are respectively assigned to one, two, three and four quanta in the Sr-O stretch. This gives an  $\tilde{E}^2\Sigma^+$  excited state Sr-O stretching frequency of *ca.*  $612 \text{ cm}^{-1}$ . As for the  $\tilde{D}^2\Sigma^+$  state, this is a significant increase from the  $528 \text{ cm}^{-1}$  frequency observed for the ground state. Again, the correlation between increased Sr-O vibrational frequency and increased rotational constant, upon  $\tilde{E} \leftarrow \tilde{X}$  excitation, is consistent. Comparable findings are found for the metal-ligand stretch in the alkaline-earth monohalides, with all electronic states above the  $\tilde{C}^2\Pi$  state showing an increase in frequency compared with the ground state.<sup>12</sup> This is presumably due to an increase in ionic bonding as the electron gains more Rydberg character.

### 5.3.4 The $\tilde{F}^2\Pi - \tilde{X}^2\Sigma^+$ system

Scans to higher wavenumbers revealed yet another new electronic transition of SrOH. The spectrum, shown in Fig. 5.18, is dominated by the pair of bands at  $32974$  and  $32996 \text{ cm}^{-1}$ . These appear to form a spin-orbit doublet which, if correct, would imply an excited state spin-orbit splitting of  $22 \text{ cm}^{-1}$ . Consequently, these bands are assigned to the  $^2\Pi_{1/2} - \tilde{X}^2\Sigma^+$  and  $^2\Pi_{3/2} - \tilde{X}^2\Sigma^+$   $0_0^0$  transitions of the new transition of SrOH. This

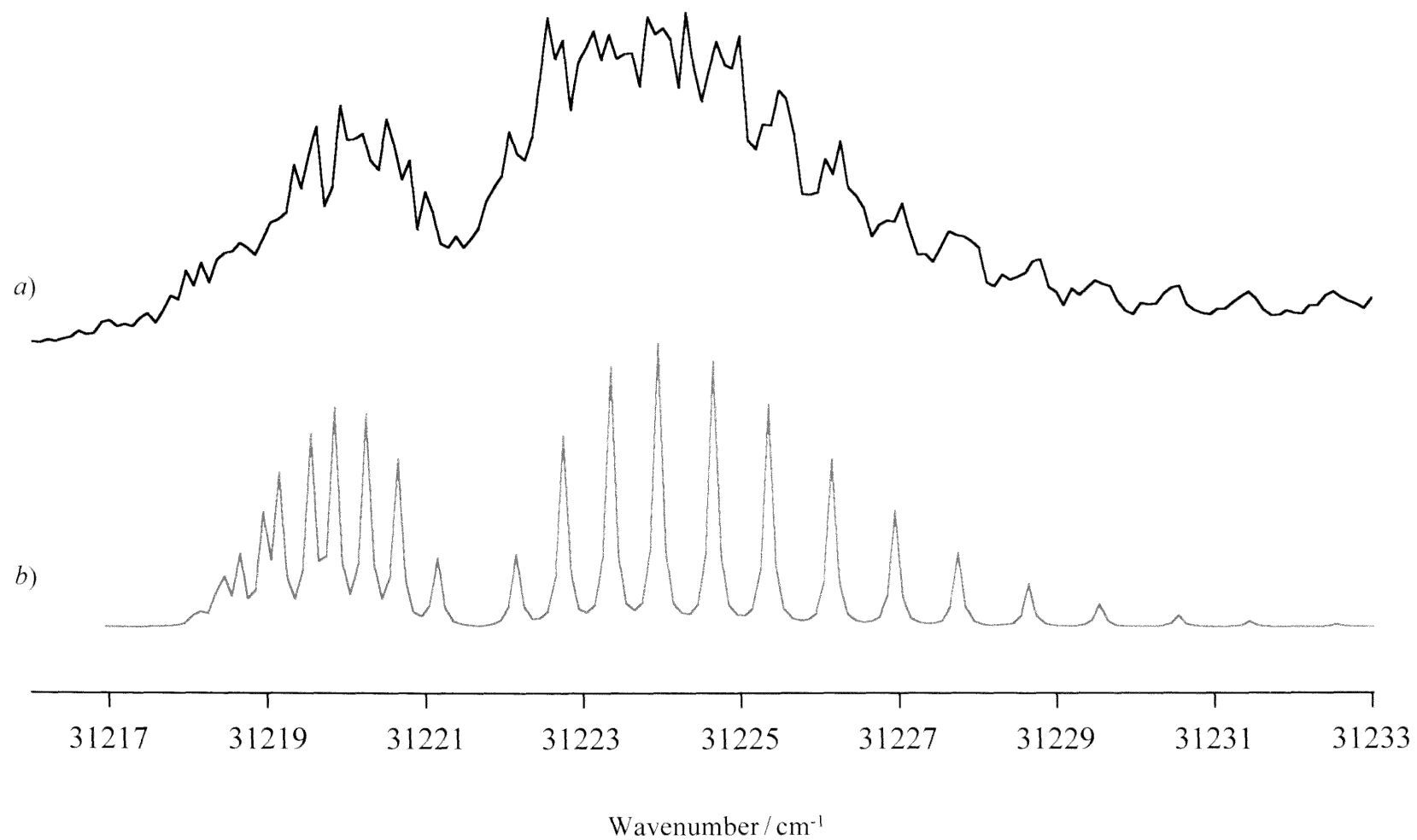


**Fig. 5.17** *a)* Rotational contour of the  $\tilde{E}^2\Sigma^+ - \tilde{X}^2\Sigma^+ 3_0^2$  transition at 31222 cm<sup>-1</sup>. *b)* Simulation assuming a  $^2\Sigma^+ - ^2\Sigma^+$  transition ( $B'' = 0.2492$  cm<sup>-1</sup>,  $B' = 0.2679$  cm<sup>-1</sup> and  $T = 15$  K).

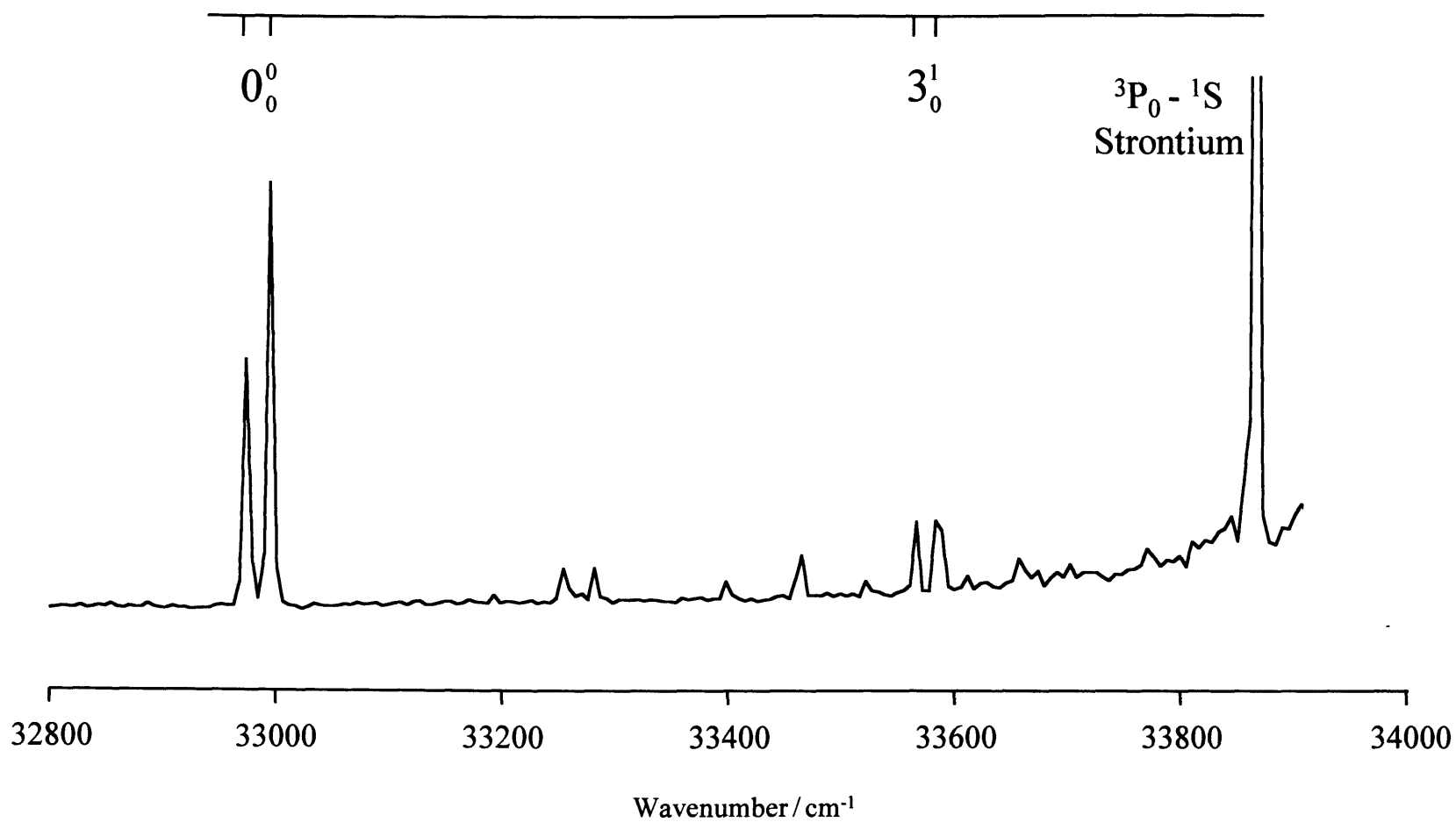


**Fig. 5.18** Laser excitation spectrum showing the  $\tilde{F}^2\Pi - \tilde{X}^2\Sigma^+$  transition of SrOH. At the high wavenumber end of the spectrum a strong atomic strontium transition is seen.

assignment is supported by the rotational contours, which have the profiles expected for a  ${}^2\Pi - {}^2\Sigma^+$  transition in which the  ${}^2\Pi$  state undergoes Hund's case (a) coupling. Although the quality of the rotational contours were relatively poor, and were insufficiently resolved to obtain a fit to the rotational simulation, a visual best fit yields an upper state rotational constant of  $\sim 0.255\text{ cm}^{-1}$  for both spin-orbit components. The rotational temperature in both simulations was 20 K.

There is one other doublet in the spectrum with a  $22\text{ cm}^{-1}$  splitting, namely the two weak peaks near  $33600\text{ cm}^{-1}$ . These two peaks, at  $33567$  and  $33589\text{ cm}^{-1}$ , most probably arise from excitation of the Sr-O stretch, giving an excited state frequency of  $592\text{ cm}^{-1}$  for this mode. However, this assignment should be viewed as a tentative one given the relatively low intensities of these features.

The upper state is labelled as the  $\tilde{F}^2\Pi$  state. The spin-orbit splitting is small, even smaller than in the  $\tilde{C}^2\Pi$  state. The  $\tilde{F}^2\Pi$  state of SrOH is approximately midway between that of the  $E^2\Pi$  and  $G^2\Pi$  states of SrF. However, the latter is known to possess a much smaller spin-orbit coupling constant,  $A = 22.94\text{ cm}^{-1}$ ,<sup>21</sup> a value almost identical with that reported here for SrOH. Consequently, it seems likely that the  $\tilde{F}^2\Pi$  state of SrOH is the analogue of the  $G^2\Pi$  state of SrF. This would leave the SrOH analogue of the  $E^2\Pi$  state unaccounted for.

### 5.3.5 Character of excited electronic states of SrOH

The  $\tilde{D}^2\Sigma^+$ ,  $\tilde{E}^2\Sigma^+$  and  $\tilde{F}^2\Pi$  electronic states of SrOH have much in common with the  $\tilde{A}^2\Pi$  and  $\tilde{B}^2\Sigma^+$  states. Transitions to these states from the ground electronic state yield simple LIF spectra in which the only significantly Franck-Condon active mode is the Sr-O stretching vibration. The  $\tilde{B}'^2\Sigma^+$  state undergoes significant vibronic perturbations, presumably brought about by mixing with the  $\tilde{C}^2\Pi$  state. The Sr-O stretching frequencies (see Table 5.6) are larger in the  $\tilde{B}'$ ,  $\tilde{D}$ ,  $\tilde{E}$  and  $\tilde{F}$  states than in the  $\tilde{X}$ ,  $\tilde{A}$  and  $\tilde{B}$  states, but the increase is modest ( $<20\%$ ) and is explicable in terms of increased ionic character in the higher states. It is therefore reasonable to assume that transitions between these states involve movement of the unpaired electron between different largely non-bonding metal-centred orbitals.

**Table 5.6** Summary of spectroscopic constants (in  $\text{cm}^{-1}$ ) for the new electronic states of SrOH.

State	Constant <sup>a)</sup>	Value <sup>b)</sup>
$\tilde{B}^2\Sigma^+$	$T_{00}$	25997
	$\nu_{\text{Sr-O-H}}$	394
	$\nu_{\text{Sr-O}}$	574
	$B$	$0.2658 \pm 0.0009$
$\tilde{C}^2\Pi$	$T_{00}$	27303
	$A$	$24.52 \pm 0.04$
	$B$	$0.2564 \pm 0.0009$
	$ \epsilon\omega_2 $	$\leq 40$ <sup>c)</sup>
	$\omega_{\text{Sr-O-H}}$	<i>ca.</i> 255 <sup>c)</sup>
$\tilde{D}^2\Sigma^+$	$T_{00}$	27698 <sup>c)</sup>
	$\nu_{\text{Sr-O}}$	630
	$B$	$\sim 0.265$ <sup>d)</sup>
$\tilde{E}^2\Sigma^+$	$T_{00}$	29990
	$\nu_{\text{Sr-O}}$	612
	$B$	$\sim 0.268$
$\tilde{F}^2\Pi$	$T_{00}$	32985
	$A$	22
	$\nu_{\text{Sr-O}}$	[592] <sup>e)</sup>
	$B$	$\sim 0.255$

a) Unless stated otherwise all rotational constants are  $B_0$  values.

b) All errors are derived from a least squares fit of rotational structure and represent one standard deviation.

c) See text for details.

d) This value is for the  $\tilde{D}^2\Sigma^+$  state (002) level.

e) This value is based on a tentative band assignment.

However, it would appear at first sight that the situation for the  $\tilde{C}^2\Pi$  state is quite different given the far more complex LIF spectrum. To try and understand this, analogy between the alkaline-earth monohalides and the monohydroxides is, once again, a good starting point. In the alkaline-earth monohalides there is strong evidence that the unpaired electron in the  $\pi$  orbitals in the  $A^2\Pi$  and  $C^2\Pi$  states have similar metal atomic orbital characters.<sup>21-23</sup> However, as discussed in Chapters 3 and 4, there is also an important difference. In order for the two  $\pi$  orbitals to be orthogonal they must possess opposite polarisations. In the  $A^2\Pi$  state the  $\pi$  orbital is known to be polarised *away* from the ligand. Consequently, the  $\pi$  orbital in the  $C^2\Pi$  state should be polarised *towards* the ligand, i.e. it will be 'reverse polarised'.<sup>22-26</sup>

Making the reasonable assumption that the same process occurs in the alkaline-earth monohydroxides, the  $\tilde{C}^2\Pi$  state of SrOH should also be reverse-polarised. In the alkaline-earth monohalides the reverse-polarised state possesses a much larger electric dipole moment than the other known electronic states. This is because the reverse-polarisation prevents the build up of significant unpaired electron density on the opposite side of the metal from the ligand. In other known states this lobe of negative charge goes some way towards cancelling the dipole moment generated by the polar metal ligand bond. In the reverse-polarised  $\tilde{C}^2\Pi$  state of SrOH a relatively large electric dipole moment would be expected. This in turn has important implications for the spectroscopy of the  $\tilde{C} - \tilde{X}$  system.

Bolman and Brown<sup>27</sup> have described a mechanism by which vibronically-induced parallel bands, which represent vibrationally forbidden components of the main, electronically allowed transition, can gain intensity. This model was developed for transitions between  $^2\Pi$  and  $^2\Sigma$  electronic states in a linear triatomic molecule. The  $^2\Pi$  state can gain some  $^2\Sigma$  character through Renner-Teller interaction when the bending vibration is excited and, this in turn, confers a non-zero probability to transitions which involve single quantum excitation of the bending mode. According to Bolman and Brown, the intensity of these Franck-Condon forbidden bands, which includes the  $2_0^1$  band of SrOH, is proportional to the square of the difference in dipole moments between the upper and lower electronic states, i.e.

$$\text{Intensity} \propto \left\{ \langle {}^2\Pi | \mu_z | {}^2\Pi \rangle - \langle {}^2\Sigma | \mu_z | {}^2\Sigma \rangle \right\}^2 \quad (5.10)$$

Given the proximity of electronic states surrounding the  $\tilde{C}^2\Pi$  state, several of which have  ${}^2\Sigma^+$  character, the two-state model is likely to be a severe oversimplification for the  $\tilde{C}-\tilde{X}$  system of SrOH. However, as pointed out by Bolman and Brown, the same qualitative arguments will apply to a multi-state model, the quantitative difference being that each  ${}^2\Sigma^+$  state will contribute a dipole difference term weighted by an appropriate coefficient describing the degree of mixing with the  $\tilde{C}^2\Pi$  state. Since all nearby  ${}^2\Sigma^+$  states are expected to possess much smaller dipole moments than the  $\tilde{C}^2\Pi$  state, this mechanism could give substantial intensity to transitions involving  $\Delta v_2 = \pm 1$  in the  $\tilde{C}-\tilde{X}$  system. In fact, a combination of experimental and theoretical data<sup>24-25,28-29</sup> for various alkaline-earth monohalides and monohydroxides indicates that the dipole moment of the  $\tilde{C}^2\Pi$  state of SrOH will be close to the limit expected for  $\text{Sr}^+\text{-OH}$  and will be three to four times larger than in most nearby electronic states (including the  $\tilde{A}^2\Pi$  state). On this basis we would expect, for example, the Franck-Condon forbidden  $\Delta v_2 = \pm 1$  transitions in the  $\tilde{C}^2\Pi - \tilde{X}^2\Sigma^+$  system to be at least an order of magnitude more intense than in the  $\tilde{A}^2\Pi - \tilde{X}^2\Sigma^+$  system. Since such transitions are seen with substantial intensities in the  $\tilde{C}-\tilde{X}$  excitation spectrum and in several dispersed fluorescence spectra, these observations support the suggestion that the  $\tilde{C}^2\Pi$  state is reverse-polarised.

To close this section we consider the effect the reverse-polarised character of the  $\tilde{C}^2\Pi$  state is likely to have on the Renner parameter. Since the bending vibration will be dominated by motion of the hydrogen atom, the coupling between vibrational and electronic angular momenta should be weak if the unpaired electron is strongly metal-localised. On these grounds it would be expected that the  $\tilde{C}^2\Pi$  state would have a larger Renner parameter than for the  $\tilde{A}^2\Pi$  state because the polarisation of the HOMO in the former favours greater delocalisation of the unpaired electron density onto the ligand. Comparison of the reported Renner parameter for the  $\tilde{A}^2\Pi$  state ( $\epsilon = -0.0791$ )<sup>5</sup> with the limits we have deduced in this work for the  $\tilde{C}^2\Pi$  state ( $\epsilon \leq 0.16$ ) is consistent with this idea. Nevertheless, it seems likely that the unpaired electron is still predominantly metal-localised in the  $\tilde{C}^2\Pi$  state.

### 5.3.6 Comparison with other MOH molecules

It is interesting that  $^2\Pi$  excited electronic states have been observed for both SrOH and BaOH, given that no analogous state of CaOH was identified in the work of Pereira and Levy.<sup>10</sup> However, Pereira and Levy did report an intriguing new electronic state of CaOH, the  $\tilde{F}$  state, which was judged to be non-linear on the basis of bending mode structure seen in dispersed fluorescence spectra which would be forbidden in the Franck-Condon limit for a linear molecule. This bending mode structure was relatively weak, indicating that any deviation from linearity in the  $\tilde{F}$  state is modest. The suspicion must be that the  $\tilde{F}$  state of CaOH correlates with the reverse-polarised  $C^2\Pi$  of CaF, a correlation supported by their similar electronic energies (the  $T_0$  values are 30215 and 30217  $\text{cm}^{-1}$  for CaOH and CaF, respectively). It is speculated that the non-linear geometry results from increased metal-ligand overlap due to the reverse-polarised character of the excited state. A greater degree of covalency is expected for CaOH than for SrOH or BaOH and this may be sufficiently large in the case of CaOH to favour a non-linear equilibrium geometry.

## 5.4 Conclusions

Vibrationally-resolved spectra of several new electronic transitions of the SrOH free radical have been reported. Five transitions have been firmly identified of which three, the,  $\tilde{D}^2\Sigma^+ - \tilde{X}^2\Sigma^+$ ,  $\tilde{E}^2\Sigma^+ - \tilde{X}^2\Sigma^+$  and  $\tilde{F}^2\Pi - \tilde{X}^2\Sigma^+$  systems, yield relatively simple spectra dominated by progressions in the Sr-O stretching vibration. The  $\tilde{B}'^2\Sigma^+ - \tilde{X}^2\Sigma^+$  system also has relatively simple vibrational structure, but in this case there is evidence of significant perturbations, probably arising through vibronic coupling with the  $\tilde{C}^2\Pi$  state.

Far more complex spectra are observed for the  $\tilde{C}^2\Pi - \tilde{X}^2\Sigma^+$  system. The origin of this system has been firmly identified, but higher frequency bands do not fit into regular vibrational progressions and their assignment, in most cases, is uncertain. Laser excitation of several of these transitions yield marked Sr-O-H bending mode activity in dispersed fluorescence spectra. One source of this complexity is thought to be a substantial Renner-Teller effect in the  $\tilde{C}^2\Pi$  state. It has been proposed that this is brought about by the reverse-polarised character of the unpaired electron in this state.



All of the new SrOH transitions yield strong LIF spectra and so all should be excellent candidates for higher resolution work. Such studies will be essential for providing a complete band assignment. Fully rotationally-resolved spectra should also yield further insight into the character of the  $\tilde{C}^2\Pi$  state, especially for clarifying the extent of Renner-Teller coupling.

Comparable and higher electronic states of other alkaline-earth metal-containing free radicals, such as the metal monomethyls, monoacetylides, monocyclopentadienides, and many others should, in principle, also be observable using LIF spectroscopy. Resonance-enhanced multiphoton ionisation (REMPI) spectroscopy is an alternative method which could prove equally successful. Indeed, REMPI spectra of CaOH in a supersonic jet were recently reported by Pereira and Levy.<sup>10</sup> Laser ablation sources routinely generate a variety of species when an organic precursor is present over the metal target and so the mass-selective detection capability of REMPI may prove essential in establishing the spectral carrier in more complicated systems. Although not yet explored, there is little doubt that ZEKE spectroscopy, via resonant intermediate states such as those investigated in the present work, will also be possible. This is particularly important since there is little or no spectroscopic information on the corresponding cationic species.

## References

- 1 M.A. Anderson, W.L. Barclay Jr. and L.M. Ziurys, *Chem. Phys. Lett.*, **196** (1992) 166
- 2 D.A. Fletcher, K.Y. Jung, C.T. Scurlock and T.C. Steimle, *J. Chem. Phys.*, **98** (1993) 1837
- 3 R.C. Hilborn, Z. Qingshi and D.O. Harris, *J. Mol. Spec.*, **97** (1983) 73
- 4 C.R. Brazier and P.F. Bernath, *J. Mol. Spec.*, **114** (1985) 163
- 5 J. Nakawaga, R.F. Wormsbecher and D.O. Harris, *J. Mol. Spec.*, **97** (1983) 37
- 6 P.I. Presunka and J.A. Coxon, *J. Chem. Phys.*, **101** (1994) 201
- 7 P.I. Presunka and J.A. Coxon, *Chem. Phys.*, **190** (1995) 97
- 8 P.I. Presunka and J.A. Coxon, *Can. J. Chem.*, **71** (1993) 1689
- 9 P.F. Bernath and S. Kinsey-Nielson, *Chem. Phys. Lett.*, **105** (1984) 663
- 10 R. Pereira and D.H. Levy, *J. Chem. Phys.*, **105** (1996) 9733
- 11 S.J. Pooley, M.S. Beardah, and A.M. Ellis, *J. Elec. Spec. Rel. Phen.*, **97** (1998) 77
- 12 K.P. Huber and G. Herzberg, *Molecular Spectra and Molecular Structure. IV. Constants of Diatomic Molecules* (Van Nostrand Reinhold, New York, (1979)
- 13 S. Panov, X.Q. Tan, and T.A. Miller, 48th Ohio State University International Symposium on Molecular Spectroscopy, paper RA06 (1993).
- 14 G. Herzberg, *Molecular Spectra and Molecular Structure. III. Electronic Spectra and Electronic Structure of Polyatomic Molecules* (Van Nostrand Reinhold, New York, 1966)
- 15 J.A. Pople, *Mol. Phys.*, **3** (1960) 16
- 16 J.T. Hougen, *J. Chem. Phys.*, **36** (1962) 519
- 17 G. Herzberg, *Molecular Spectra and Molecular Structure. II. Infrared and Raman Spectra of Polyatomic Molecules* (Van Nostrand Reinhold, New York, 1968).
- 18 G. Herzberg, *Molecular Spectra and Molecular Structure. I. Spectra of Diatomic Molecules* (Van Nostrand Reinhold, New York, 1967).
- 19 R.A. Hailey, C. Jarman and P.F. Bernath, *J. Chem. Phys.*, **107** (1997) 669
- 20 N.H. Rosenbaum, J.C. Owruksy, L.M. Tack and R.J. Saykally, *J. Chem. Phys.*, **84** (1986) 5308
- 21 C. Nitsch, J.O. Schröder, and W.E. Ernst, *Chem. Phys. Lett.*, **148** (1988) 130

- 22 L. Klynning and H. Martin, *Phys. Scr.*, **24** (1981) 33
- 23 S.F. Rice, H. Martin, and R.W. Field, *J. Chem. Phys.*, **82** (1985) 5023
- 24 P. Bundgen, B. Engels, and S.D. Peyerimhoff, *Chem. Phys. Lett.*, **176** (1991) 407
- 25 W.E. Ernst and J. Kändler, *Phys. Rev. A*, **39** (1989) 1575
- 26 W.E. Ernst, J. Kändler, C. Noda, J. S. McKillop and R. N. Zare, *J. Chem. Phys.*, **85** (1986) 3735
- 27 P.S.H. Bolman, and J.M. Brown, *Chem. Phys. Lett.*, **21** (1973) 213
- 28 T. Törring, W.E. Ernst and J. Kändler, *J. Chem. Phys.*, **90** (1989) 4927
- 29 A.R. Allouche, G. Wannous and M. Aubert-Frécon, *Chem. Phys.*, **170** (1993) 11

## *Chapter Six*

*A dispersed fluorescence investigation  
of the low frequency vibrations of  
 $MgCCH \left( \tilde{X}^2\Sigma^+ \right)$*

## 6.1 Introduction

The first observations of alkaline-earth containing monoacetylides were reported in 1987 by Bernath and co-workers, who recorded low resolution LIF spectra of the respective  $\tilde{A}^2\Pi - \tilde{X}^2\Sigma^+$  electronic transitions of CaCCH and SrCCH following their production in a Broida oven.<sup>1</sup> A subsequent rotationally-resolved study of the  $\tilde{A}^2\Pi - \tilde{X}^2\Sigma^+$  transition of CaCCH was also carried out by the Bernath group in 1988.<sup>2</sup> Their work indicated that both of these molecules show ionic bonding character ( $M^+CCH^-$ ), similar to that in the alkaline-earth monohydroxides, and adopt a linear geometry in their lowest and first excited electronic states. Whitham and co-workers were the first workers to prepare an alkaline-earth monoacetylide (CaCCH) using the laser ablation method, in 1990.<sup>3</sup> Several additional high resolution studies, focusing predominantly upon the  $\tilde{A}^2\Pi - \tilde{X}^2\Sigma^+$  transition of CaCCH have been carried out in recent years in the groups of Coxon<sup>4-8</sup> and Steimle.<sup>9</sup> Steimle reported the  $\tilde{A}^2\Pi$  state of CaCCH to be subject to a small Renner-Teller effect and determined the Renner parameter to be 0.035.<sup>9</sup> Pure rotational, millimetre-wave spectra of the  $\tilde{X}^2\Sigma^+$  ground electronic states of MgCCH, CaCCH and SrCCH have also been recorded by Ziurys and co-workers,<sup>10-12</sup> yielding very precise rotational constants. Interestingly, the  $\tilde{B}^2\Sigma^+ - \tilde{X}^2\Sigma^+$  transitions of CaCCH and SrCCH have not been spectroscopically observed, despite repeated attempts by Bernath and co-workers<sup>1</sup> and members of the Ellis group.<sup>13</sup> Analysis of the high resolution spectrum of the  $\tilde{A}^2\Pi - \tilde{X}^2\Sigma^+$  transition of CaCCH is consistent with a distant, or dissociative,  $\tilde{B}^2\Sigma^+$  state.<sup>1</sup>

The first observation of an excited electronic state of MgCCH was reported by Corlett and co-workers.<sup>14</sup> The low-resolution LIF excitation spectrum of the  $\tilde{A}^2\Pi - \tilde{X}^2\Sigma^+$  system yielded structure in only one vibrational mode, the Mg-C stretch ( $\nu_3$ ). A fundamental frequency of 552  $\text{cm}^{-1}$  was obtained for the Mg-C stretch in the  $\tilde{A}^2\Pi$  state. This represented a small increase from the approximate ground ( $\tilde{X}^2\Sigma^+$ ) state value of 496  $\text{cm}^{-1}$  reported in the 1997 Ph.D thesis of Corlett.<sup>15</sup> Thompson and Andrews reported a similar value (492  $\text{cm}^{-1}$ ) for single quantum excitation of  $\nu_3$  in their independent IR study of matrix isolated MgCCH.<sup>16</sup> Corlett and co-workers<sup>14</sup> recorded a partially resolved rotational spectrum for the  $\tilde{A}^2\Pi_{1/2} - \tilde{X}^2\Sigma^+ 0_0^0$  transition of MgCCH, yielding an approximate excited state rotational constant of 0.175  $\text{cm}^{-1}$ . This represents a small, but

significant, increase from the value of  $0.167\text{ cm}^{-1}$  in the ground state, obtained from a millimetre wave study by Ziurys.<sup>10</sup> The increase in the rotational constant upon electronic excitation suggests a decrease in the Mg–C bond length, which is consistent with the observed increase in vibrational frequency upon  $\tilde{A} \leftarrow \tilde{X}$  excitation.

In the matrix isolation study of MgCCH reported by Thompson and Andrews<sup>16</sup> IR bands attributable to the C≡C–H bend and, tentatively, the C≡C stretch, were identified in addition to the Mg–C stretch. MgCCH was assigned as the spectral carrier from a combination of isotope shifts and *ab initio* calculations. In order to obtain additional information on the vibrational structure of MgCCH in its  $\tilde{X}^2\Sigma^+$  ground electronic state, dispersed fluorescence spectra have been recorded. This work represents a more extensive investigation of the preliminary dispersed fluorescence study reported by Corlett in his thesis of 1997.<sup>15</sup>

## 6.2 *Experimental*

The experimental apparatus and procedure was described in Chapter 2. MgCCH was prepared by laser ablation of magnesium metal in the presence of a mixture of 0.1 % acetone in helium. Dispersed fluorescence spectra were recorded by passing the fluorescence through an Acton 0.27 m scanning monochromator.

## 6.3 *Results and discussion*

Fig. 6.1 shows the dispersed fluorescence spectrum obtained by laser excitation of the  $\tilde{A}^2\Pi_{1/2} - \tilde{X}^2\Sigma^+ 0_0^0$  transition at  $22790\text{ cm}^{-1}$ . The excitation spectrum of the  $\tilde{A} - \tilde{X}$  system<sup>14</sup> shows the Mg–C stretch to be the major Franck-Condon active mode and therefore the same should be true in the dispersed fluorescence spectrum. Clearly, Fig. 6.1 shows a dispersed fluorescence spectrum that is dominated by a short progression in a single vibrational mode, and this is assigned to the Mg–C stretch,  $\nu_3$ . A vibrational frequency of  $496 \pm 2\text{ cm}^{-1}$  is deduced for this mode in the  $\tilde{X}^2\Sigma^+$  ground electronic state. This is essentially the harmonic frequency, since the limited progression shows little anharmonicity. Thompson and Andrews reported a value of  $492\text{ cm}^{-1}$  for the Mg–C stretching fundamental, which agrees well with the dispersed fluorescence value, especially given the expectation of a small (red) matrix shift. The Mg–C stretching

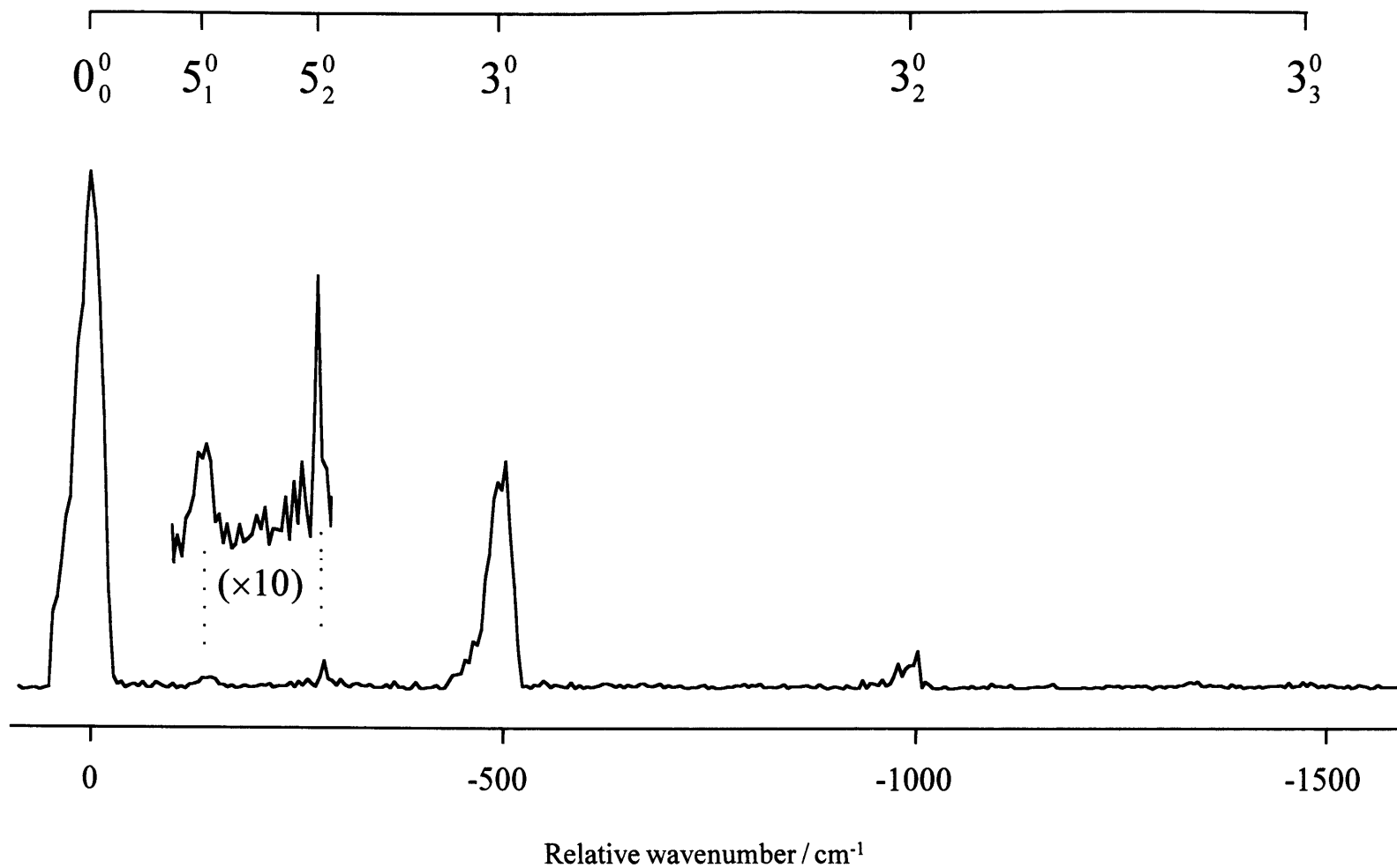


**Fig. 6.1** Dispersed fluorescence spectrum obtained by laser excitation of the  $\tilde{A}^2\Pi_{1/2} - \tilde{X}^2\Sigma^+ 0_0^0$  transition at 22790 cm<sup>-1</sup>.

frequency is lowered considerably from the  $\tilde{A}^2\Pi$  state value of  $552\text{ cm}^{-1}$ ,<sup>14</sup> which suggests a significant strengthening of the Mg-C bond upon  $\tilde{A} \leftarrow \tilde{X}$  excitation.

In addition to the Mg-C stretching progression, several weak bands can be identified in Fig. 6.1. Two of these, at  $143 \pm 2\text{ cm}^{-1}$  and  $285 \pm 2\text{ cm}^{-1}$ , lie between the strong  $0_0^0$  and  $3_1^0$  bands and have been observed reproducibly in several independent scans of this region. Scans in the comparable region in the IR spectrum, which would be in the far-IR, were not attempted by Thompson and Andrews. *Ab initio* calculations on MgCCH by Woon<sup>17</sup> and by Thompson and Andrews<sup>16</sup> both show that the only mode with a lower frequency than the Mg-C stretch is the Mg-C $\equiv$ C bend,  $\nu_5$ . The harmonic frequencies predicted by both sets of calculations are similar and are shown in Table 6.1. Comparison with the calculated values leaves no doubt that the two weak bands at 143 and  $285\text{ cm}^{-1}$  in the dispersed fluorescence spectrum are due to the  $5_1^0$  and  $5_2^0$  transitions. The fact that the  $\nu_5$  features are very weak is unsurprising given that MgCCH is linear in both upper and lower states.<sup>8</sup> Furthermore, the  $5_1^0$  transition is Franck-Condon forbidden and must gain intensity through vibronic coupling.

A dispersed fluorescence spectrum from the  $\tilde{A}^2\Pi_{1/2}\ 3^1$  level, which is accessed by laser excitation at  $23359\text{ cm}^{-1}$ , was also recorded and is shown in Fig. 6.2. As was the case for excitation of the origin transition, the spectrum is dominated by a progression in the Mg-C stretching mode. Clearly, the intensity of the band correlating to one quantum in the stretch is significantly enhanced, as would be expected for emission from the  $3^1$  level. This confirms the assignment of the excitation spectrum reported by Ellis and co-workers.<sup>14</sup> This spectrum also shows the two weak bands at  $143\text{ cm}^{-1}$  and  $285\text{ cm}^{-1}$  relative to the pump position, and these are assigned to the  $3_0^15_1^0$  and  $3_0^15_2^0$  transitions.

In their IR matrix isolation study of MgCCH, Thompson and Andrews<sup>16</sup> reported weak bands at  $1982.7$  and  $1984.2\text{ cm}^{-1}$ , which they tentatively assigned to the C $\equiv$ C stretching mode. In addition, a tentative dispersed fluorescence assignment for the C $\equiv$ C stretch was made in the PhD thesis of Corlett.<sup>15</sup> A very weak band at  $\sim 1990\text{ cm}^{-1}$  was observed, which is in fair agreement with the IR matrix isolated values for the C $\equiv$ C stretch. Again, expectation of a small (red) shift could account for the difference in the two values. Single



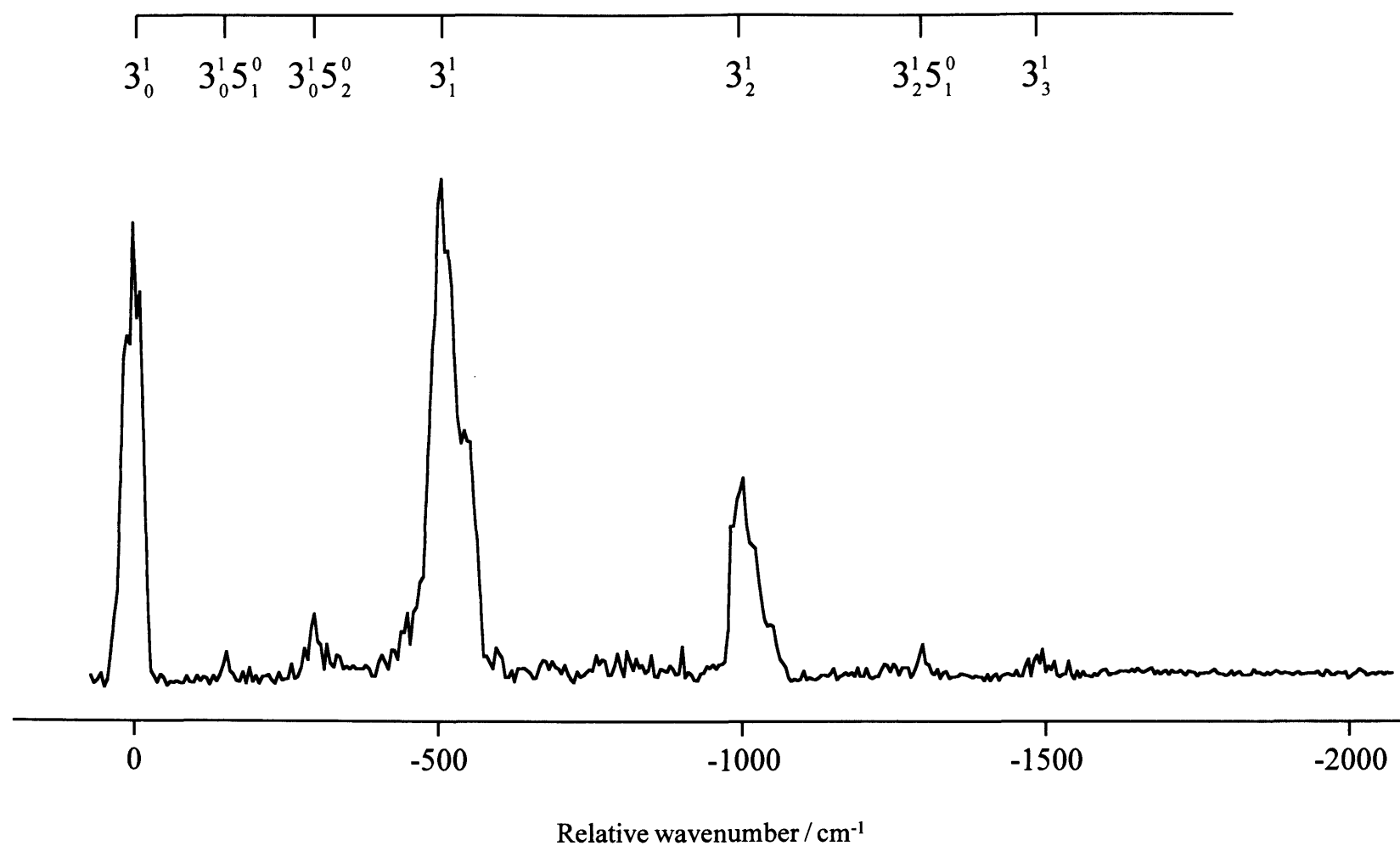


**Fig. 6.2** Dispersed fluorescence spectrum obtained by laser excitation of the  $\tilde{A}^2\Pi_{1/2} - \tilde{X}^2\Sigma^+ 3_0^1$  transition at 23359 cm<sup>-1</sup>.

quantum excitation of the C≡C stretch should be potentially observable in an electronic spectrum, since the vibration is totally symmetric. However, excitation in the  $\tilde{A} \leftarrow \tilde{X}$  electronic transition is thought to involve promotion of an electron which is localised in orbitals on the magnesium atom. The Franck-Condon factors for excitation of the C≡C stretch are therefore likely to be very unfavourable. Analogous arguments should apply to the totally symmetric C–H vibration. In the current work, repeated efforts to observe excitation of the C≡C and C–H stretching modes were unsuccessful, thereby failing to support the findings reported by Corlett.<sup>15</sup> Clearly, the dispersed fluorescence data support the conclusion that the transition is very strongly metal-localised.

#### 6.4 Conclusions

Combined matrix isolation IR and dispersed fluorescence data have now allowed four of the five normal mode vibrational frequencies of ground electronic state MgCCH to be deduced. The experimental and theoretical frequencies are collected together in Table 6.1.

**Table 6.1** Vibrational frequencies (cm<sup>-1</sup>) of MgCCH in the ground  $\tilde{X}^2\Sigma^+$  state.

Mode	Description	DF <sup>a)</sup>	IR <sup>b)</sup>	RCCSD <sup>c)</sup>	B3LYP <sup>c)</sup>
$\nu_1$	C–H stretch	-	-	3416	3433
$\nu_2$	C≡C stretch	-	1983.5 <sup>d)</sup>	1974	2055
$\nu_3$	Mg–C≡C stretch	496	491.8	489	486
$\nu_4$	C≡C–H bend	-	660.84	656	664
$\nu_5$	Mg–C≡C bend	143	-	154	136

- <sup>a)</sup> Fundamental frequencies deduced from dispersed fluorescence spectra. Estimated error is  $\pm 2$  cm<sup>-1</sup> (1 $\sigma$ ).
- <sup>b)</sup> From matrix isolation spectroscopic work of Thompson and Andrews.<sup>16</sup>
- <sup>c)</sup> Calculated frequencies are harmonic values. The RCCSD data were taken from reference 17 and the B3LYP from reference 16.
- <sup>d)</sup> Tentative value taken from the matrix IR study of Thompson and Andrews.<sup>16</sup> Two weak bands at 1982.7 and 1984.2 cm<sup>-1</sup> were attributed to matrix site splittings of the C≡C stretching fundamental.

## References

- 1 A.M.R.P. Bopegedera, C.R. Brazier and P.F. Bernath, *Chem. Phys. Lett.*, **136** (1987) 97
- 2 A.M.R.P. Bopegedera, C.R. Brazier and P.F. Bernath, *J. Mol. Spec.*, **129** (1988) 268
- 3 C.J. Whitham, B. Soep, J-P. Vesticot and A. Keller, *J. Chem. Phys.*, **93** (1990) 991
- 4 M.G. Li and J.A. Coxon, *J. Mol. Spec.*, **176** (1996) 206
- 5 M.G. Li and J.A. Coxon, *J. Mol. Spec.*, **180** (1996) 287
- 6 M.G. Li and J.A. Coxon, *J. Mol. Spec.*, **183** (1997) 250
- 7 M.G. Li and J.A. Coxon, *J. Mol. Spec.*, **184** (1997) 395
- 8 M.G. Li and J.A. Coxon, *J. Mol. Spec.*, **196** (1999) 14
- 9 A.J. Marr, J. Perry and T.C. Steimle, *J. Chem. Phys.*, **103** (1994) 3861
- 10 M.A. Anderson and L.M. Ziurys, *Astrophys. J.*, **439** (1995) L25
- 11 M.A. Anderson and L.M. Ziurys, *Astrophys. J.*, **444** (1995) L57
- 12 B.P. Nuccio, A.J. Apponi and L.M. Ziurys, *Chem. Phys. Lett.*, **247** (1995) 283
- 13 A.M. Ellis, *private communication*
- 14 G.K. Corlett, A.M. Little and A.M. Ellis, *Chem. Phys. Lett.*, **249** (1996) 53
- 15 G.K. Corlett, *Ph.D. Thesis*, Leicester University (1997)
- 16 C.A. Thompson and L. Andrews, *J. Am. Chem. Soc.*, **118** (1996) 10242
- 17 D.E. Woon, *Astrophys. J.*, **456** (1996) 602

## *Chapter Seven*

### *Testing of a new REMPI-TOF spectrometer*

## 7.1 *Introduction*

Like LIF spectroscopy, resonance-enhanced multiphoton ionisation (REMPI) spectroscopy is a form of electronic spectroscopy that relies on the detection of electronic transitions by an indirect means. LIF requires that excited states possess a significant fluorescence quantum yield following absorption of a laser photon, and this can often prove to be a considerable restriction. REMPI relies on further absorption of a photon, or photons, following excitation to the excited state, which results in ions that can be detected. The sensitivity that REMPI offers is comparable to the high sensitivity that is associated with LIF, because ions can be detected with almost 100% efficiency. In principle, excited states of any molecule can be detected using REMPI spectroscopy, even if they have zero fluorescence quantum yields.

Probably the most important advantage that REMPI spectroscopy offers, in comparison to LIF, is the ability to incorporate mass-selectivity of the ions into the design of the spectrometer. This is particularly helpful when there is some doubt about the spectral carrier, as is often the case for molecules and radicals which are prepared via laser ablation. The ablation process usually yields a number of different products and identifying the spectral carrier, by employing chemical arguments and/or analysis of the LIF spectrum, is not always definitive. Since ions are detected in REMPI spectroscopy, addition of a mass spectrometer to the apparatus allows the mass of the spectral carrier to be deduced unambiguously, generally making its identification straightforward.

The design and construction of a time-of-flight (TOF) mass spectrometer, for use in conjunction with REMPI spectroscopy, has been outlined in the Ph.D thesis of Bezant.<sup>1</sup> This apparatus was designed to complement the existing LIF instrument, described in Chapter 2, by allowing rapid interchange between an LIF experiment and a REMPI experiment. Although the majority of construction had been accomplished at the time of writing of the thesis, no experiments had been performed to test the system. In this chapter, a discussion of the fundamental principles of REMPI spectroscopy will be outlined, along with a short description of the procedure for performing a REMPI-TOF experiment using the new apparatus. Several experiments are described which have been performed to test the REMPI-TOF system. A REMPI spectrum of the well-known  $A^2\Sigma^+ - X^2\Pi$  electronic system of NO has been recorded using the new apparatus. However, obtaining a supersonically cooled REMPI spectrum of this electronic system of

NO has proved problematic. In an attempt to overcome this, and other problems, several modifications have been made to the design described by Bezant, and these are discussed. This chapter concludes with a short discussion of some laser ablation experiments that have been carried out involving the alkaline-earth metals, along with future prospects for other experiments using the new REMPI-TOF apparatus.

## 7.2 *Fundamental aspects of REMPI spectroscopy*

### 7.2.1 *The REMPI mechanism*

Compared with one-photon transitions, multiphoton transitions are inherently improbable using conventional light sources. However, if an intense laser beam is used for the light source, the probability of achieving multiphoton absorption is considerably enhanced. Provided that enough energy is absorbed, via the multiphoton process, an atom or molecule may be taken above its ionisation limit. This process is referred to as multiphoton ionisation (MPI). Under typical laser conditions the ionisation rate decreases rapidly with increasing photon order of the multiphoton process, i.e. a four-photon ionisation has a much smaller cross-section than a two-photon ionisation.<sup>2</sup>

The ionisation rate can be significantly enhanced by separating the ionisation process into distinct absorption steps. In the simplest scenario, depicted in Fig. 7.1(a), one photon is absorbed, resulting in the population of an excited electronic state of the molecule under investigation. Subsequent, absorption of a second laser photon can occur which takes the molecule above its ionisation limit and results in the formation of a molecular ion. The probability of the two-photon *resonance-enhanced* pathway to ionisation occurring is much higher than the *non-resonant* two-photon absorption. This particular type of resonance-enhanced ionisation is referred to as a one-colour (1+1) REMPI process, since it is carried out using photons of a single energy (i.e. a single laser wavelength is used to perform both the absorption and ionisation steps). Fig. 7.1(b) illustrates a more complex (2+2) ionisation mechanism. In this case, two-photon absorption results in the population of a 'resonant' state and a further subsequent two-photon absorption takes the molecule above its ionisation limit. A number of other one-colour ionisation mechanisms are possible, including (2+1), (2+2), (3+1), (1+3) etc., and many free radicals have been observed via these processes. Table 7.1, adapted from reference 3, illustrates a number of these.

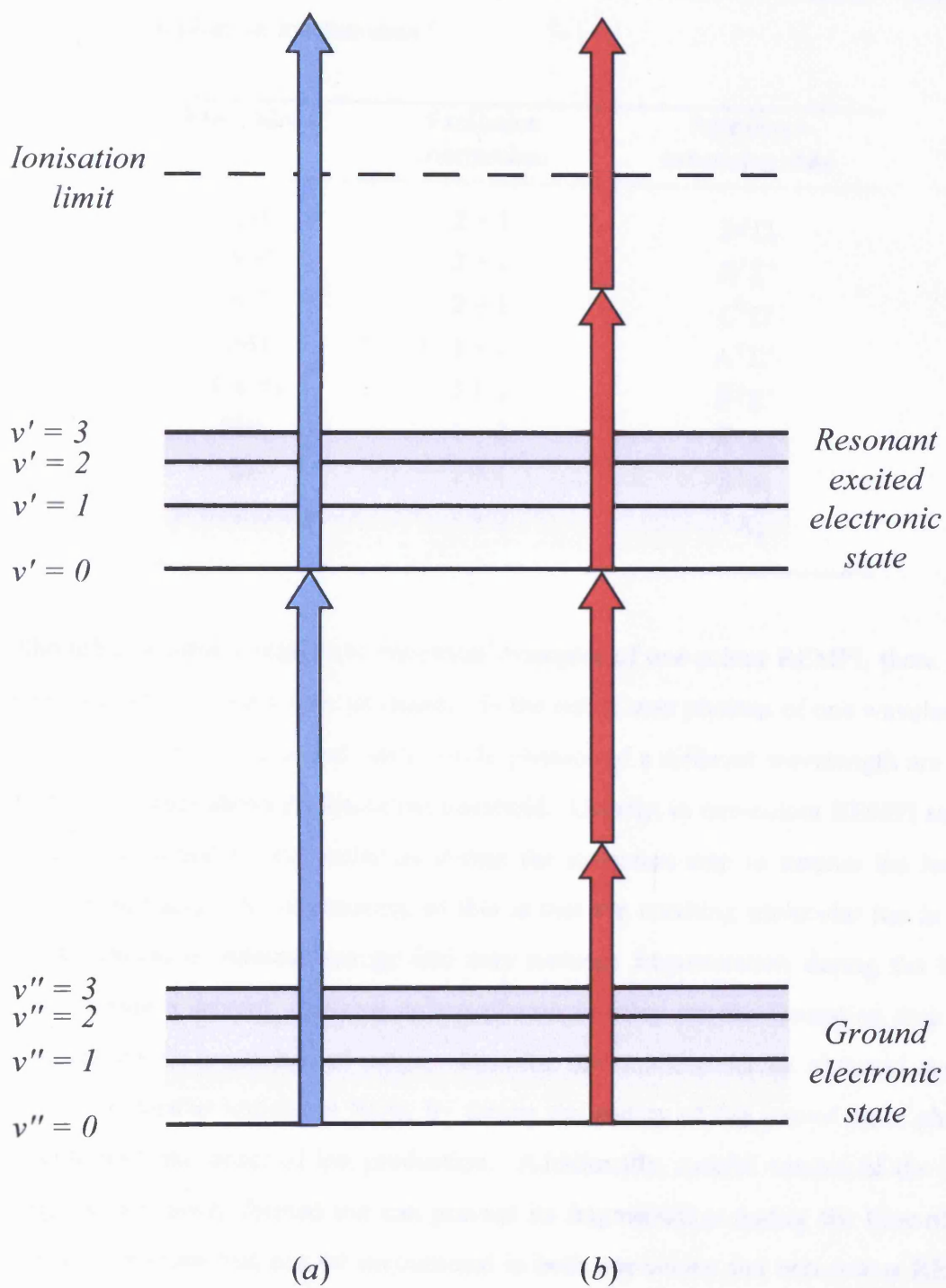


**Fig. 7.1** Schematic diagram showing *a*) one colour (1+1) and *b*) two colour (2+2) resonance-enhanced multi-photon ionisation.

**Table 7.1** Free radicals identified by various resonance-enhanced multi-photon ionisation mechanisms.<sup>3</sup>

Free radical	Excitation mechanism	Resonance enhancing state
CH	2 + 1	D <sup>2</sup> Π
AlH	2 + 1	D <sup>1</sup> Σ <sup>+</sup>
GeCl	2 + 1	C <sup>2</sup> Π
NO	1 + 1	A <sup>2</sup> Σ <sup>+</sup>
CaOH	1 + 1	$\tilde{E}^2\Sigma^+$
NH <sub>2</sub>	1 + 3	$\tilde{A}^2A_1$
SiF <sub>2</sub>	2 + 1	$\tilde{B}^1B_2$
2-methylallyl	2 + 2	<sup>2</sup> A <sub>1</sub>

Although it is more common to encounter examples of one-colour REMPI, there are also many examples of two-colour processes. In the latter, laser photons of one wavelength are used to populate the ‘resonant’ state, while photons of a different wavelength are used to take the molecule above its ionisation threshold. Usually, in one-colour REMPI sufficient energy is absorbed by the molecule during the ionisation step to surpass the ionisation limit considerably. A consequence of this is that the resulting molecular ion is formed with an excess of internal energy and may undergo fragmentation during the time-of-flight. Using a second, different colour photon to carry out the ionisation step can be advantageous in a number of ways. Detailed information can be obtained regarding absolute molecular ionisation limits by tuning the energy of the second laser photon to coincide with the onset of ion production. Additionally, careful control of the internal energy of the newly formed ion can prevent its fragmentation during the time-of-flight. Clearly, a problem that can be encountered in both one-colour and two-colour REMPI is identifying the correct photon order of the resonant process. To obtain the photon order it is advantageous to have an approximate idea of both the energy of the resonant electronic state and the ionisation limit of the molecule under investigation, although this information is often unclear or simply unknown.

As mentioned earlier, a significant limitation of LIF spectroscopy is that many excited states decay, via non-radiative pathways, on a much faster timescale than that of



fluorescence, (see section 2.3.1). Of course, the same relaxation pathways will inevitably effect the efficiency of the REMPI process. Excited state populations will be depleted to some extent by radiative processes, such as fluorescence to lower electronic states, and more importantly non-radiative processes, such as predissociation and collisional relaxation. However, such loss mechanisms are often insignificant in REMPI since in many cases they occur on a much slower timescale than resonance ionisation. Indeed, there is some evidence which shows that REMPI can overcome moderately rapid predissociation.<sup>4</sup>

### 7.2.2 *Multiphoton selection rules*

For diatomic and linear polyatomic molecules that are governed by Hund's case (a) or (b), one-photon electronic transitions are governed by the selection rule  $\Delta\Lambda = 0, \pm 1$ , where  $\Lambda$  is the quantum number representing the component of orbital angular momentum along the internuclear axis.<sup>5</sup> Consequently, for example, allowed transitions from a  $\Pi$  electronic state may only terminate in electronic states with  $\Sigma$ ,  $\Pi$  or  $\Delta$  symmetry. For multiphoton transitions the selection rule is modified to  $\Delta\Lambda = 0, \pm 1, \pm 2, \dots \pm n$ , depending on the photon order of the transition.<sup>2</sup> In essence, the modified selection rule arises from a combination of selection rules for each photon involved in the transition. Consequently, the number of allowed transitions from a particular electronic state are significantly enhanced. The allowed transitions from a  $\Pi$  electronic state are now extended to include  $\Pi \rightarrow \Phi$  (for a two-photon transition),  $\Pi \rightarrow \Gamma$  (for a three-photon transition) and so on.

Similarly, the rotational selection rule for one-photon electronic transitions,  $\Delta J = 0, \pm 1$ ,<sup>5</sup> is modified to  $\Delta J = 0, \pm 1, \pm 2, \dots \pm n$  for multiphoton transitions.<sup>2</sup> For a one-photon transition (except  $\Sigma \rightarrow \Sigma$ ) the rotational structure will involve *P*, *Q* and *R* branches. The consequence of the modified rotational selection rule is to extend the number of branches for a multiphoton transition. For example, a two-photon transition will yield rotational structure due to *O*, *P*, *Q*, *R* and *S* branches ( $\Delta J = -2, -1, 0, +1, +2$ ). A three-photon transition will yield an increasingly complex, often congested, rotational envelope due to the presence of *N*, *O*, *P*, *Q*, *R*, *S* and *T* branches.

In molecules which have high symmetry the selection rule governing inversion symmetry for one-photon transitions,  $u \leftrightarrow g$ , is modified to  $u \leftrightarrow u$ ,  $g \leftrightarrow g$  for two-photon transitions.<sup>3</sup> Clearly, transitions which are nominally forbidden in one-photon

spectroscopies become allowed by invoking two-photon REMPI processes. Similarly, the total parity selection rule for single-photon processes,  $+\leftrightarrow -$ , is modified to  $+\leftrightarrow +$ ,  $-\leftrightarrow -$  for two-photon processes and, again, transitions that are not accessible using single photon spectroscopy become allowed for multi-photon processes.<sup>3</sup>

### 7.3 *Experimental aspects of REMPI spectroscopy*

Before describing specific aspects of the REMPI apparatus, some general features of a REMPI experiment will be introduced in this section. Fig. 7.2 depicts how the key constituents link together. Items coloured *blue* in the diagram are concerned with the production of supersonically cooled free radicals, using laser ablation or other sources. This process occurs in the source chamber (LIF chamber), labelled (1) in Fig. 7.2, and has already been described in detail elsewhere in this thesis. The supersonic jet passes through a skimmer into the REMPI chamber, labelled (2), and the resulting molecular beam is directed through the central region of the ionisation source. The second part of the experiment (coloured *red*) involves directing the beam from a tunable laser through the molecular beam to initiate the REMPI process. The final part is concerned with the detection of molecular ions, resulting from laser-induced ionisation (coloured *green* in the figure). The ionisation source, flight-tube and microchannel plate detector form the basic components of a time-of-flight mass spectrometer and it is this feature which allows the detection of ions and adds mass-selectivity to the apparatus.

#### 7.3.1 *Sample preparation and radical production*

A significant consideration in the design of the REMPI-TOF system involved maintaining a sufficiently low pressure inside the REMPI chamber during routine firing of the pulsed valve.<sup>1</sup> If the pressure inside the chamber rises to above  $\sim 10^{-4}$  mbar, there is a strong possibility of damage to the microchannel plate (MCP) detector. Under normal experimental operation, a potential difference of  $\sim 2000$  V is applied across the detector and a rise in pressure may lead to severe arcing damage. Consequently, the pulsed valve is situated in the source chamber during experiments and the pulsed supersonic jet is skimmed prior to its entry into the REMPI chamber. A nickel skimmer (Beam Dynamics Inc.) is mounted onto the end flange of the source chamber for this purpose. As mentioned in Chapter 2, one end of the REMPI chamber is linked to the LIF chamber via a common coupling flange which has a 20 mm diameter channel running directly through its centre.

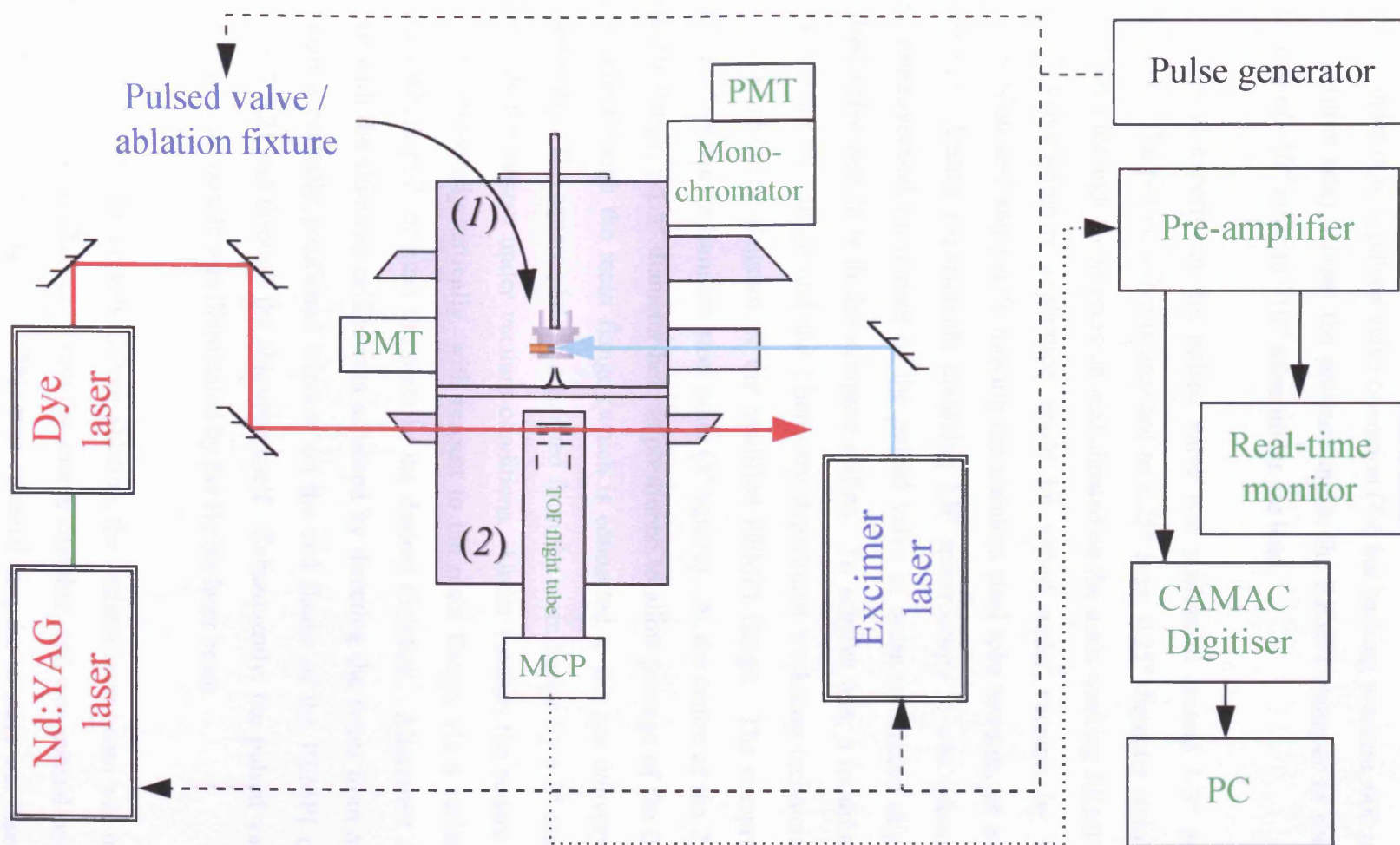


**Fig. 7.2** Schematic diagram of the experimental apparatus used in REMPI experiments.

A home-made gate-valve system,<sup>1</sup> which is incorporated into the coupling flange, is designed to allow opening and closing of the joining channel, while both chambers are under vacuum conditions. Skimming of the supersonic jet results in a molecular beam which, under typical pulsed valve operation (4-6 bar backing pressure, 600  $\mu$ s duration, 10 Hz repetition rate), causes the pressure inside the REMPI chamber to rise from a base pressure of  $\sim 10^{-7}$  mbar to  $\sim 10^{-5}$  mbar under gas load.

In a typical experiment the pulsed valve was positioned around 1-3" away from the skimmer. The pulsed valve is attached to a 25" long, 0.25" diameter stainless steel tube that passes through a compression seal situated on the main working REMPI flange. The pulsed valve/skimmer separation could be varied under vacuum by loosening the compression seal and gently moving the stainless steel tube towards, or away, from the skimmer. Unlike experiments involving LIF spectroscopy it was necessary to allow horizontal/vertical movement of the pulsed valve in order to achieve alignment of the pulsed valve nozzle with the skimmer orifice. To achieve this, a modified flange was designed by the author and the Chemistry department workshop technicians. Fig. 7.3 shows a schematic diagram of the modified REMPI flange. The compression seal is attached to a square stainless steel plate (3" square). At the centre of the 7.25" diameter circular flange, a 1.5" diameter hole is positioned to allow passage of the 0.25" stainless steel tube through the main flange (which is connected to the gas delivery system (see Chapter 2)). The square plate is separated from the main flange by a 2" diameter O-ring that seals the system under vacuum conditions. Under vacuum the square plate can be moved horizontally/vertically, with respect to the main flange, via a series of threaded screws which pull, or push the plate in the desired direction. Alignment of the pulsed valve with the skimmer orifice was achieved by directing the beam from a He:Ne laser through a centrally positioned window on the end flange of the REMPI chamber (see section 7.3.2) and through the skimmer itself. Subsequently, the pulsed valve could be moved until the nozzle was illuminated by the He:Ne laser beam.

For experiments which involved laser ablation, the excimer laser beam was diverted from its normal path (see Chapter 2) into the source chamber, and was instead passed through an adjacent port (see Fig. 7.2). This was essential in order to carry out laser ablation in close proximity to the skimmer. Instead of diverting the path of the laser beam using

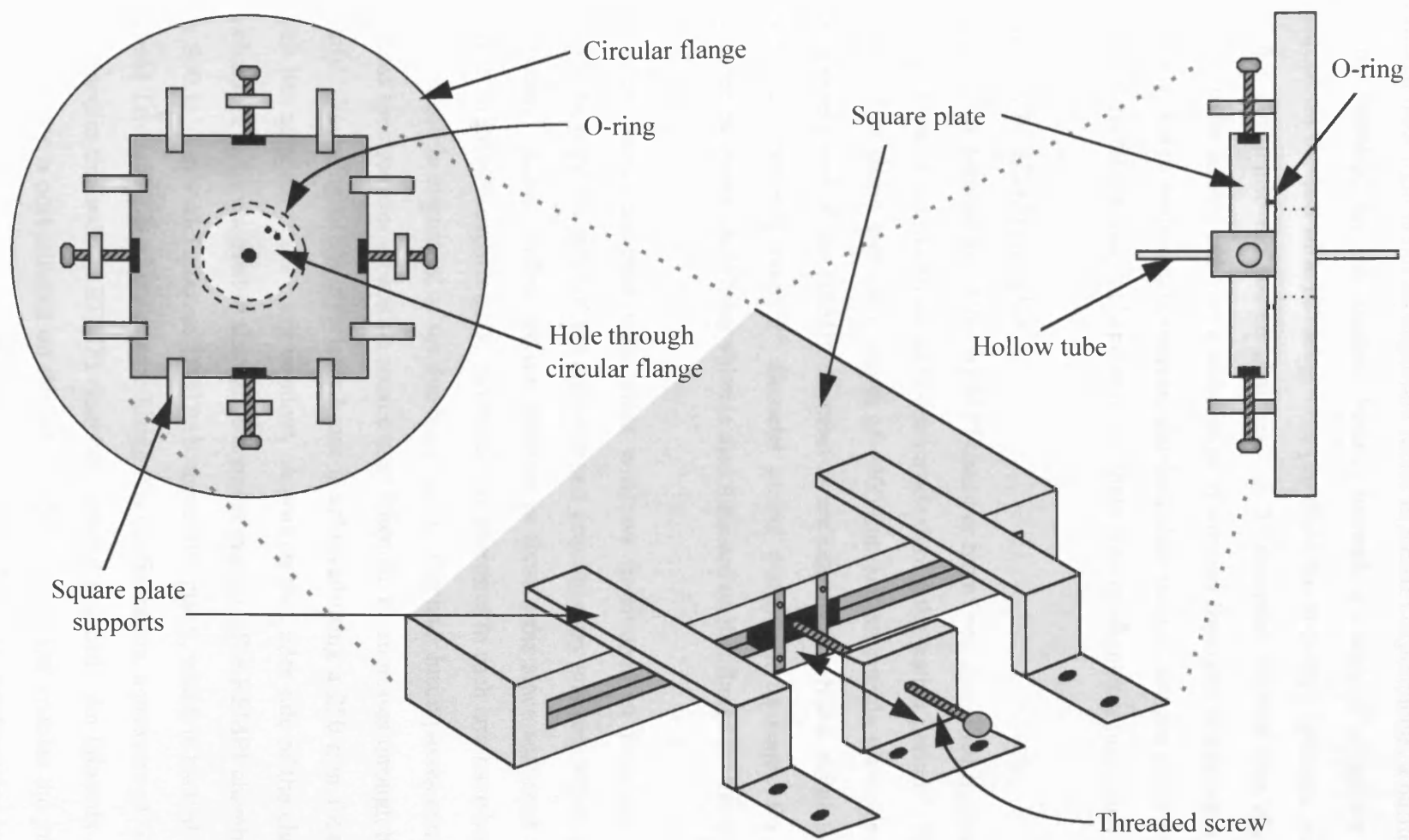


**Fig. 7.3** Schematic diagram illustrating the modified REMPI flange.

mirrors or prisms, the entire optical rail, including the 700 mm focal length excimer focusing lens, could be moved over into the necessary position to facilitate ablation. Since scattered laser light is not an important factor in REMPI experiments, a baffle arrangement was not required for the excimer beam. Instead, a simple 3" diameter quartz plate, mounted on the end of a 12" long tube, provided the necessary entrance window for the excimer beam into the source chamber. A 3" diameter window was chosen to allow ablation to be carried out over a wide range of ablation fixture/skimmer separations. As an additional aid in routine experiments, standard clear perspex flanges could be fitted to any unused ports on the source chamber to facilitate various alignment procedures.

### 7.3.2 *The REMPI chamber*

The physical dimensions of the REMPI chamber have been described in detail elsewhere, although several modifications have been made during the testing period.<sup>1</sup> The chamber is cylindrical in shape and has a length of ~360 mm and an outside diameter of ~270 mm. The opposite end of the REMPI chamber is enclosed with a blank stainless steel flange, which incorporates a small 2" diameter quartz window at its centre for viewing and alignment purposes. A Whitey valve is also mounted on this flange for venting purposes.

Two short arms, enclosed with silica windows (positioned at Brewster's angle), are attached on opposite sides of the chamber and provide entry and exit windows for the dye laser beam. Again, baffles are not required in these arms since scattered light is not a problem in REMPI experiments. However, the apertures in each arm have been reduced to ~5 mm to aid in alignment of the dye laser beam. The laser beam passes centrally through the mass spectrometer ionisation source only when the beam passes through both apertures cleanly. Focusing of the dye laser beam is achieved using a 250 mm focal length lens which lies adjacent to the entry window. A port on the under side of the chamber allows the chamber to be coupled to the vacuum pump system. The REMPI chamber is pumped by a 800 ls<sup>-1</sup> Leybold Turbovac 1000 turbomolecular pump, which is backed by a 25 m<sup>3</sup>h<sup>-1</sup> Leybold Trivac D25B rotary pump. Using this configuration, a pressure of ~10<sup>-7</sup> mbar can be attained in the isolated REMPI chamber, without gas load. An Edwards Active gauge is mounted on a port situated on the side of the chamber and enables the pressure inside the chamber to be continually monitored. Finally, the mass spectrometer is incorporated into a port on top of the chamber (see section 7.3.3).

### 7.3.3 Ion detection: Time-of-flight (TOF) mass spectrometry

The ease with which mass selectivity can be incorporated into REMPI spectroscopy is probably the most attractive feature of the technique. As mentioned earlier, the ability to unambiguously identify the mass of the spectral carrier is extremely useful. Time-of-flight (TOF) mass spectrometry is the most widely used method for obtaining mass selectivity in REMPI spectroscopy, although quadrupole mass spectrometry has also been used.<sup>6</sup> Two important advantages of TOF mass spectrometry make the technique ideally suited for use in conjunction with pulsed REMPI spectroscopy. The speed with which a mass spectrum can be acquired is on the order of a few microseconds and signal-to-noise ratios may be significantly enhanced by multiple averaging. Additionally, the entire mass spectrum can be recorded for each accelerating pulse and this may yield vital information regarding post-ionisation branching ratios.

#### 7.3.3.1 Wiley-McLaren time-of-flight mass spectrometer

The time-of-flight mass spectrometer used in the current work is based upon the Wiley-McLaren design, which was first introduced in 1955.<sup>7</sup> The advantages of using this type of mass spectrometer in conjunction with REMPI spectroscopy have been detailed in the thesis of Bezan<sup>1</sup> and in several excellent research articles.<sup>2,8</sup> Consequently, only a brief discussion is given here.

A time-of-flight mass spectrometer has three distinct regions, (i) an ionisation region, (ii) a field-free drift region and (iii) a detection region. Fig. 7.4(a) shows the most basic design of a TOF spectrometer. The ionisation region is defined by two plates, the rear plate being labelled as *repeller* (R), and the forward plate as the *accelerating plate* (AP). An appropriate potential difference is applied between these plates, with the repeller having the more positive potential. When ions are produced by the REMPI process, the newly formed ions are accelerated through the AP (which is a wire mesh electrode) into the field-free drift region and arrive at the microchannel plate detector some time later. Ideally, all of the ions receive equivalent amounts of energy from the accelerating field and upon entering the drift region their velocity, and consequently their drift time, will be dependent on the ratio of their mass,  $m$ , to their charge,  $q$ . Clearly, lighter ions will achieve a greater drift velocity than heavier ions and will arrive at the detector earlier. The time-of-flight,  $t_f$ , for an ion of mass,  $m$ , is given by,

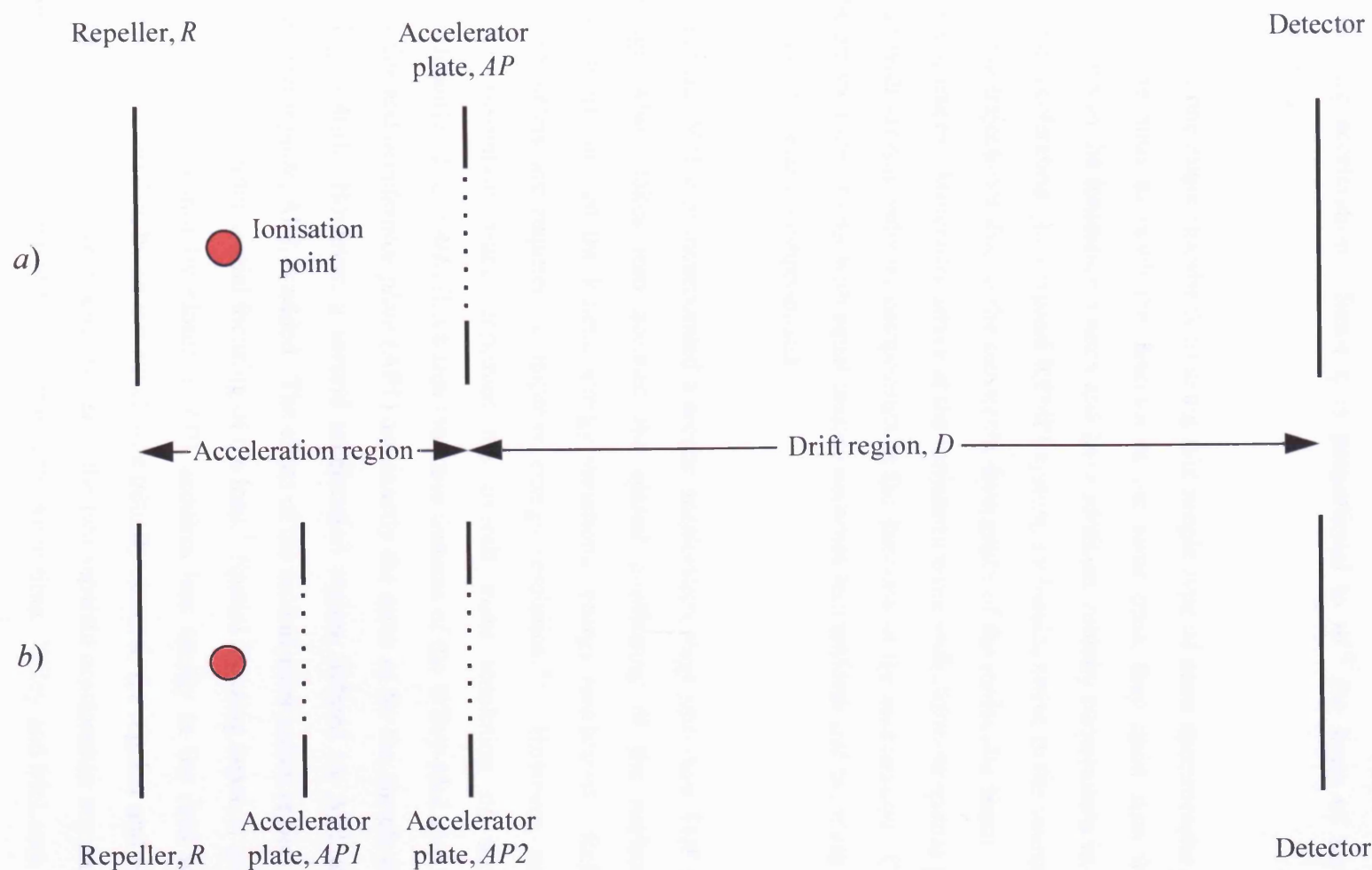


**Fig. 7.4** *a)* illustrates the most basic design of a time-of-flight mass spectrometer. *b)* illustrates the Wiley-McLaren TOF mass spectrometer which includes a second acceleration region that takes into account spatial positioning of molecules in the ionisation region (see text for further details).



$$t_f = D \left( \frac{m}{2E} \right)^{1/2} \quad (7.1)$$

where  $D$  is the length of the drift region and  $E$  is the kinetic energy attained by the ion following acceleration. Since  $t_f$  is proportional to  $m^{1/2}$  the mass of the ion can be calculated.

There is one major drawback in using this simple type of mass spectrometer. For ions of the same mass to reach the detector at the same time, they must start from identical positions in the ionisation source and have identical velocity components in the direction of the acceleration. In a typical REMPI system, molecules arrive in the source region with varying trajectories due to the inevitable divergence of the molecular beam. This has two consequences. Molecules arrive at the ionisation point with different spatial positions and also with varying velocity components in the direction of the acceleration. Consequently, the arrival time of ions with equal masses becomes less uniform and the mass resolution of the spectrometer is compromised.

Wiley and McLaren incorporated a second acceleration stage into their TOF spectrometer design which takes into account the spatial positioning of the molecules (spatial resolution), but not the kinetic energy variations (energy resolution). Reflectron TOF spectrometers are required to improve energy resolution.<sup>9-11</sup> However, improving the spatial resolution alone improves the overall mass resolution of the instrument significantly. Fig. 7.4(b) illustrates the main features of the Wiley-McLaren design. The *repeller* and *accelerator plate* (AP1) are exactly the same as for the simple design shown in Fig. 7.4(a). However, a second acceleration region, defined by AP1 and a second *accelerator plate*, AP2, is added. The effect of the second acceleration region is to achieve so-called first-order spatial focusing of the ions.<sup>7</sup> Spatial focusing depends on the fact that an ion which is initially closer to AP1 acquires less energy in the drift region and is eventually overtaken by an ion which was initially closer to the repeller and receives more energy. The respective electric fields in the two separate acceleration regions are chosen such that all ions arrive at the detector at the same time. Wiley and McLaren showed that first-order spatial focusing is achieved when,

$$D = 2s_0k_0^{3/2} \left[ 1 - \frac{d}{s_0(k_0 - k_0^{1/2})} \right] \quad (7.2)$$

where  $D$  is the length of the field-free drift region,  $s_0$  is the mid-point between the *repeller* and AP1 and  $d$  is the distance between AP1 and AP2.  $k_0$  is defined by,

$$k_0 = \frac{(s_0F_s + dF_a)}{s_0F_s} \quad (7.3)$$

where  $F_s$  is the electric field strength in the first acceleration region and  $F_a$  is the electric field strength in the second acceleration region.

Once appropriate plate separations have been specified it is a relatively simple task to determine the potentials which must be applied to each plate in order to achieve spatial focusing. The various design aspects and physical dimensions of the ionisation source used in this work have been described in reference 1. Table 7.2 summarises the dimensions and calculated working plate potentials of the time-of-flight mass spectrometer.

**Table 7.2** Time-of-flight mass spectrometer specifications.<sup>1</sup>

Drift distance / m	0.99
R - AP separation / m	0.012
AP1 - AP2 separation / m	0.016
Repeller potential / V	1060
AP1 potential / V	1000
AP2 potential / V	0
$F_a$ / kVm <sup>-1</sup>	62.5
$F_c$ / kVm <sup>-1</sup>	4.96

Detection of ions is carried out using a commercial two-stage microchannel plate (MCP) assembly (single anode MCP, Alrad Instruments). The detector is attached to a flange that

is mounted onto the end of the time-of-flight tube (see Fig. 7.2). Current generated at the anode is AC-coupled into a pre-amplifier and then fed into a transient digitiser. The ion signal is then processed in exactly the same manner as for LIF experiments (see Chapter 2).<sup>12</sup> A REMPI spectrum is obtained by plotting the ion intensity as a function of laser wavelength. Spectral resolution is governed by the linewidth of the exciting dye laser and typically spectra were recorded with resolution ranging from 0.2-0.3 cm<sup>-1</sup>. Mass spectra are observed in real-time via a Tektronix TDS 320 digital oscilloscope and can be recorded via a plotter.

## 7.4 *Results and discussion*

### 7.4.1 *REMPI spectroscopy of nitric oxide (NO)*

Initial REMPI experiments were carried out using the well-known  $A^2\Sigma^+ - X^2\Pi$  electronic transition of NO. Since a number of LIF and REMPI studies have been carried out on this electronic system in recent years,<sup>13-16</sup> it was considered an ideal system with which to test the REMPI-TOF system. One has the choice of employing either a (1+1) or (2+2) REMPI mechanism via the  $A^2\Sigma^+$  electronic state. One-photon absorption from the two spin-orbit components of the ground  $X^2\Pi$  electronic state to the  $A^2\Sigma^+$  excited electronic state occur at 44080 and 44200 cm<sup>-1</sup>, respectively. Absorption of a second UV photon takes NO above its ionisation limit of 74700 cm<sup>-1</sup>.<sup>17</sup> A laser photon of ~44000 cm<sup>-1</sup> is easily obtainable via frequency doubling of the Coumarin 460 laser dye.

#### 7.4.1.1 *Sample preparation and operational conditions*

Nitric oxide is a thermodynamically unstable gas at relatively low temperatures, and decomposes into nitrous oxide (N<sub>2</sub>O) and nitrogen dioxide (NO<sub>2</sub>).<sup>18</sup> Consequently, NO was prepared immediately prior to all experiments, using a vacuum line assembly. Initially, an evacuated gas canister (~2 litres volume) was pressurised to ~1 bar NO, using appropriate amounts of reagents in the aqueous reaction,



Preparation via this method results in NO being obtained in a reasonably pure form. Subsequently, a second evacuated gas canister was pressurised to ~30 mbar NO and back

filled with helium to  $\sim 6$  bar, resulting in a premixture concentration of  $\sim 0.5$  % NO. Finally, the canister was added to the gas delivery line (see Chapter 2) in preparation for REMPI experiments.

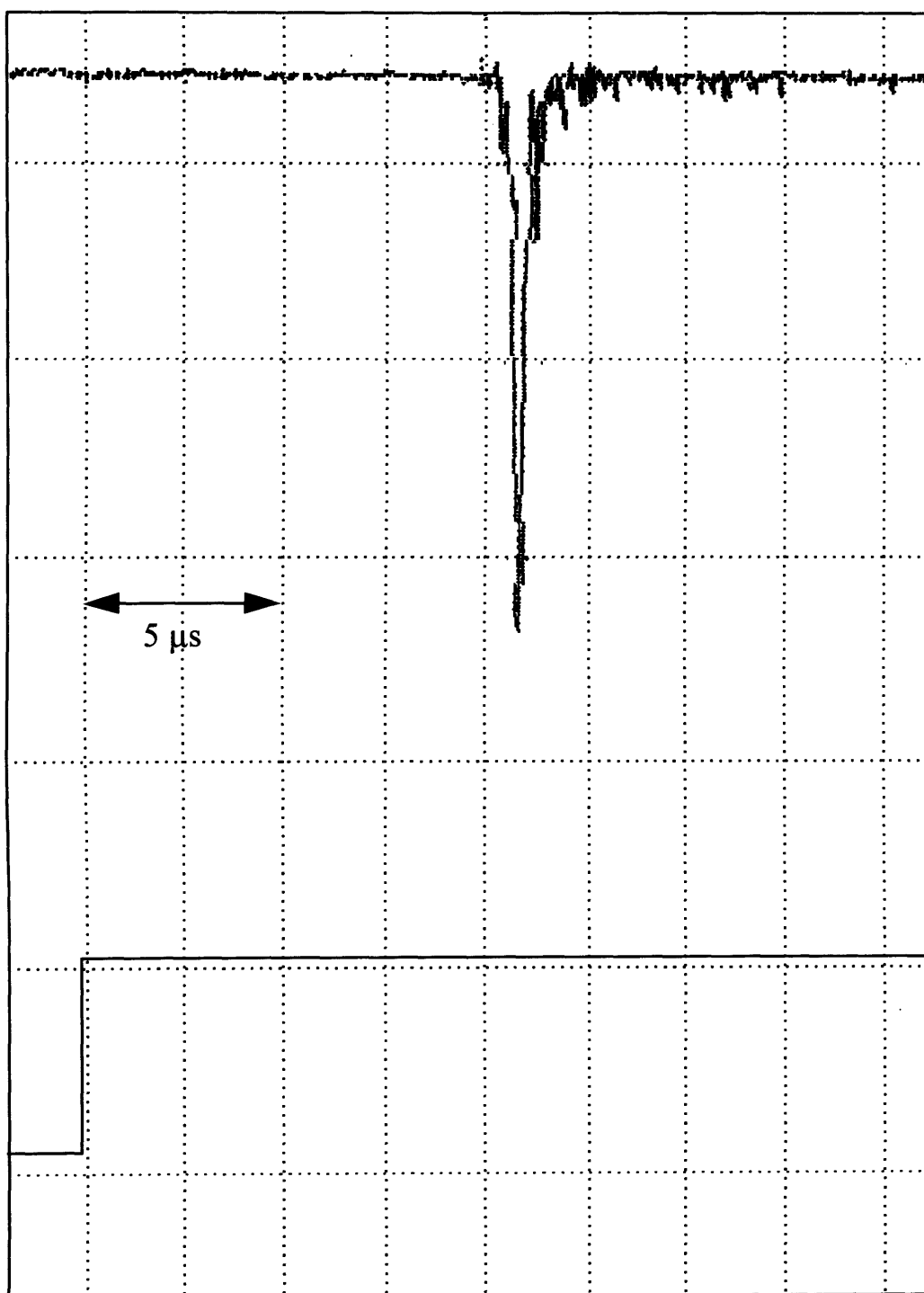
Initial experiments were carried out using a 2.0 mm diameter skimmer and a pulsed valve/skimmer separation of  $\sim 6$  cm. Under these conditions, with the gate valve open and without gas load, a pressure of  $\sim 5 \times 10^{-6}$  mbar was obtained in the REMPI chamber. Typically, the pressure would rise to  $\sim 5 \times 10^{-5}$  mbar under gas load, with the pulsed valve operating at a 10 Hz repetition rate and 600  $\mu$ s pulse duration. Firing of the dye laser was timed to occur approximately 400-800  $\mu$ s after opening of the pulsed valve. A substantial, broad (FWHM  $\sim 600$  ns) real-time ion signal could be obtained for  $\text{NO}^+$  with the plate potentials set to the values outlined in Table 7.2 and a detector voltage of  $\sim 1900$  V. However, modest adjustments to the repeller and AP1 potentials resulted in a significant improvement in the resolution of the ion signal (FWHM  $\sim 200$  ns).

Fig. 7.5 shows the real-time  $\text{NO}^+$  ion signal, or mass spectrum, as it appears on the oscilloscope display. The upper trace indicates the ion signal intensity (obtained with a photon energy of  $44200 \text{ cm}^{-1}$ , correlating to the  $A^2\Sigma^+ - X^2\Pi_{3/2} \ 0_0^0$  transition). To calculate the flight-time of the  $\text{NO}^+$  ions it was necessary to know the precise starting time ( $t = 0$  s) of the ionisation process, i.e. the firing time of the dye laser. To achieve this, a small portion of the dye laser beam was reflected, via a beamsplitter, onto a photodiode detector and the signal was displayed on the oscilloscope. A square pulse corresponding to the photodiode signal can be seen in the lower trace in Fig. 7.5.

Since the flight-time (11.2  $\mu$ s) and the relative atomic mass of NO (30 amu) are known, an estimate of the proportionality constant in equation (7.1) can be obtained, although this will change in different experiments due to small variations in the applied plate potentials. Nevertheless, a value of  $5.02 \times 10^7 \text{ s kg}^{-1/2}$  is obtained and it is useful to compare this value with other experiments which are discussed later.

#### 7.4.1.2 (1+1) REMPI spectrum of the $A^2\Sigma^+ - X^2\Pi$ electronic system of NO

Fig. 7.6(a) shows the 1+1 REMPI spectrum of the  $A^2\Sigma^+ - X^2\Pi$  electronic transition of NO in the  $44000\text{--}44500 \text{ cm}^{-1}$  region. At first glance the spectrum appears to have a relatively high rotational temperature. To determine the rotational temperature of the



**Fig. 7.5** Illustration of the real-time  $\text{NO}^+$  ion signal as it appears on the oscilloscope. The upper trace indicates the ion signal intensity. The lower trace shows the square pulse corresponding to the photodiode signal.

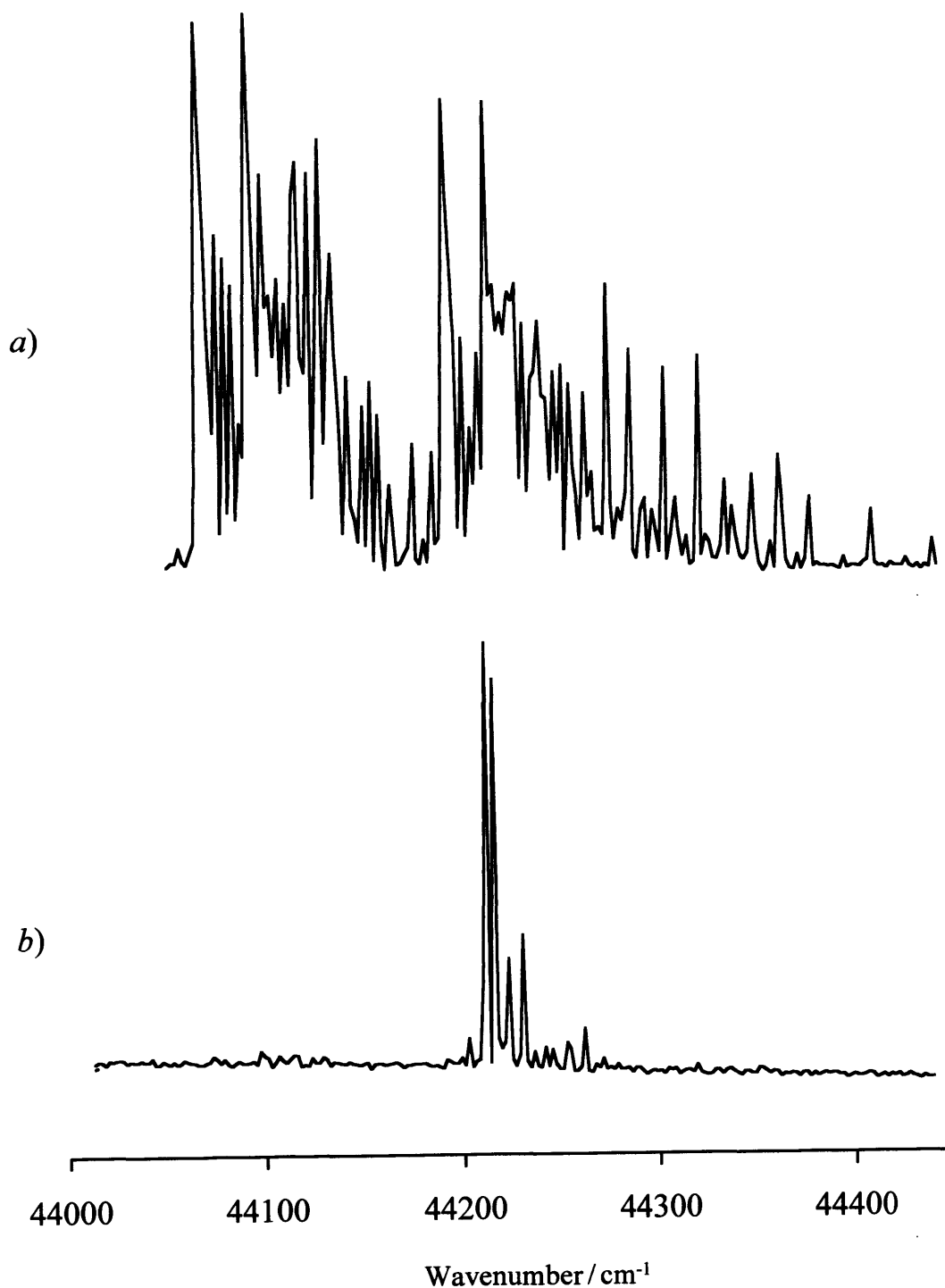


**Fig. 7.6** *a)* The (1+1) REMPI spectrum of the  $A^2\Sigma^+ - X^2\Pi$  electronic transition of NO in the 44000-44500  $\text{cm}^{-1}$ . The rotational temperature of the spectrum is  $\sim 300$  K. *b)* An LIF excitation spectrum of the same transition recorded in the source chamber. The rotational temperature of the spectrum is  $\sim 15$  K.

spectrum a simulation of the  $^2\Sigma^+ \leftarrow ^2\Pi$  transition was carried out using the SpecSim program developed by Panov and Miller.<sup>19</sup> Using rotational constants of  $B' = 1.9965 \text{ cm}^{-1}$  and  $B'' = 1.696 \text{ cm}^{-1}$ ,<sup>17</sup> along with the ground state spin-orbit coupling constant of  $119.7 \text{ cm}^{-1}$ ,<sup>17</sup> the rotational temperature was varied until a visual best fit of the simulation to experimental spectrum was obtained. This analysis showed the rotational temperature to be  $\sim 300 \text{ K}$ . Supersonic cooling should yield NO with a rotational temperature considerably lower than this value. Rotational temperatures of  $15 \text{ K}$  are routinely obtained for jet-cooled molecules in the source (LIF) chamber and lower temperatures can be achieved with some effort. Clearly, there is a problem with rotational cooling in the REMPI experiments. The most likely explanation is a breakdown in the flow conditions which causes turbulence and re-heating of the gas. This could be occurring in the source chamber or it could be a problem originating in the REMPI chamber.

In an attempt to determine the source of the breakdown in supersonic cooling a number of experiments were performed and are discussed in the next section.

#### 7.4.1.3 *Determining the source of supersonic jet/molecular beam disruption*

The first test involved investigation of the NO/He sample premixture. Efficient supersonic cooling can only occur if the ratio between sample and carrier gas is appropriately low. A high ratio can result in a loss of supersonic cooling. As mentioned above, the approximate percentage of NO in the premixture was determined to be  $\sim 0.5 \%$ . Using the experimental arrangement described in Chapter 2, a routine LIF excitation spectrum was recorded in the source chamber using exactly the same pulsed valve parameters as those used in the REMPI experiment. The resulting excitation spectrum is shown in Fig. 7.6(b). Again, a rotational simulation of the observed structure was carried out assuming a  $^2\Sigma^+ \leftarrow ^2\Pi$  transition and using the same molecular constants as in the previous simulation. A visual best fit of the simulation to the experimental spectrum was obtained using a rotational temperature of  $\sim 15 \text{ K}$ , clearly showing that the NO was supersonically cooled under the experimental conditions. Consequently it was concluded that the premixture concentration was not causing the problem with supersonic cooling.

A second possibility is that the skimmer/pulsed valve separation is critical for obtaining supersonic cooling. To investigate this a series of REMPI spectra were obtained for various skimmer/pulsed valve separations, ranging from  $2\text{-}10 \text{ cm}$  (in  $0.5 \text{ cm}$  intervals).

The rotational temperatures in all the resulting spectra were very similar, all close to  $\sim 300$  K. It is possible that severe flow disruption may occur as gas pulses travel through the skimmer and on to the REMPI chamber. There is a possibility that when excess gas, which is removed by the skimmer, strikes the end flange of the source chamber back reflections can cause severe turbulence in the incoming supersonic jet. A further possibility is that the skimmed molecular beam is disrupted as it passes through the channel linking the two chambers by gas reflecting off the inner walls.

In an attempt to eliminate these possibilities as the source of inefficient cooling, an LIF excitation spectrum was recorded inside the REMPI chamber. In order to facilitate this experiment, the time-of-flight tube and ion-optics were removed from the REMPI chamber and the collection optics used for dispersed fluorescence were attached to the vacant port. A PMT was simply positioned above the collection optics to detect fluorescence. A significant hindrance in this experiment was the presence of scattered laser light inside the REMPI chamber. This was unavoidable since no baffle arms were available to attach to the dye laser entrance and exit windows. Unfortunately, insufficient fluorescence intensity was attainable above the scattered light signal to record a convincing LIF spectrum. Consequently, it is difficult to confirm that the breakdown in supersonic cooling is due to disturbances in the gas flow as gas pulses travel through the skimmer and linking channel.

A third possibility is that the skimmed molecular beam is disrupted inside the REMPI chamber. Ideally, the molecular beam should enter the ion optics assembly exactly between the repeller and the first accelerator plate, which are normally separated by 12 mm. As shown in Fig 7.7, with a skimmer/pulsed valve separation of 6 cm and a skimmer diameter of 2.0 mm, the maximum width of the molecular beam as it enters the ionisation source is  $\sim 6.0$  mm. Clearly, if the position of the molecular beam, relative to the mid-point between the two plates, is slightly misaligned then there is a chance that the beam will strike one, or both, of the plates on its path through the ionisation source. The divergence of the beam is more pronounced as the pulsed valve is moved closer to the skimmer. At a separation of 20 mm between the skimmer and pulsed valve the maximum width of the molecular beam as it enters the ion source is  $\sim 16$  mm. Clearly, under these conditions part of the molecular beam will certainly strike the two plates, leading to potential disruption of the flow dynamics.



**Fig. 7.7** Schematic diagram illustrating the deviation of the molecular beam as it passes through the skimmer and travels through the ionisation region.

Two simple experiments were performed to investigate the extent to which supersonic cooling is compromised by contact with the ion source. In one, the skimmer was removed and the pulsed valve was pushed through the open gate valve between the two chambers such that the nozzle protruded slightly into the REMPI chamber. An LIF excitation spectrum was recorded, with the ion-optics removed, to verify the degree of supersonic cooling under the experimental conditions. In this experiment the fluorescence intensity was significantly stronger than in the fluorescence experiment described earlier and it was possible to record an LIF excitation spectrum. The rotational temperature proved to be  $\sim 20$  K. The second experiment involved recording a REMPI spectrum, using exactly the same experimental conditions. The rotational temperature of this spectrum was  $\sim 300$  K. Clearly, this experiment shows that any contact of the gas pulse with the ion optics results in severe disruption to the cooling properties of the supersonic jet/beam.

In order to reduce the potential problem of gas pulses striking the ion source accelerator plates, the separation between the plates was increased to 30 mm. As shown in Fig. 7.7 under these conditions the potential for any part of the molecular beam to strike the ion source is considerably reduced. To further reduce the possibility of gas striking the ion optics experiments were carried out in which the 2 mm aperture skimmer was replaced by a similar skimmer with a 0.5 mm aperture. However, (1+1) REMPI spectra of NO, recorded under these conditions all exhibited rotational temperatures of  $\sim 300$  K, contradicting the earlier finding and indicating that the potential source of disruption to the jet lies elsewhere in the system.

A final possibility is that, under the experimental conditions employed in the source vacuum chamber, the distance,  $x_M$ , from the supersonic nozzle to the Mach disk is considerably shorter than has previously been assumed (see Chapter 2). If this is true there is a strong chance that the supersonic jet is skimmed in the turbulent region *after* the Mach disk, resulting in ‘hot’ molecules travelling through to the REMPI chamber for subsequent detection. In a typical REMPI experiment the pressure behind the pulsed valve,  $p_0$ , is chosen to be  $\sim 2$  bar. Assuming the average pressure,  $p_c$ , per pulse is  $\sim 10^{-1}$  mbar (see Chapter 2), an approximate value for  $x_M$  can be calculated using equation (2.2). The resulting value is  $\sim 20$  cm. Even if the value for  $p_c$  is an underestimate, raising its value by one order of magnitude still results in a value of  $x_M = 8$  cm. Consequently, it would seem unlikely that the supersonic jet is skimmed after the Mach disk.

#### 7.4.1.4 *Future modifications to the REMPI-TOF apparatus.*

At the time of writing, several modifications to the existing REMPI-TOF spectrometer are planned by workers in the Ellis group. In order to improve the base pressure inside the source chamber a water-cooled Edwards turbomolecular pump (Turbovac 361, pumping speed  $300 \text{ ls}^{-1}$ ) will be incorporated onto the chamber, which should lower the pressure inside the chamber by at least one order of magnitude, from  $\sim 10^{-4}$  mbar to  $\sim 10^{-5}$ - $10^{-6}$  mbar. Perhaps more importantly, this modification will substantially increase the pumping speed in the source chamber, thereby ensuring that the Mach disk is well beyond the dimensions of the instrument. This should eliminate the possibility that the supersonic jet is skimmed *after* the Mach disk.

To reduce the possibility of back-reflected gas disrupting the supersonic jet in the source chamber, two new skimmer mount configurations will be investigated. Presently, the skimmer is mounted to the LIF/REMPI chamber joining flange via a 7 mm thick disk. In order to remove the disk completely from the source chamber, and thereby reduce the potential for back scattered gas from the disk disrupting the supersonic jet, the skimmer will be spot-welded to the joining flange. However, this does not remove the possibility that gas reflecting off the joining flange is the cause of disruption to the jet. To eliminate this possibility a number of experiments will be performed in which the skimmer is attached to the end of a hollow tube that projects from the joining flange into the source chamber. In this configuration back reflected gas pulses should be virtually eliminated.

#### 7.4.2 *REMPI spectroscopy of the CaOH and SrOH free radicals*

Although experiments involving NO have proved that supersonic cooling is not obtained in the original REMPI system, they have also shown that the time-of-flight spectrometer itself is working well. Of course, obtaining REMPI spectra of a relatively long-lived radical such as NO should be simple in comparison to obtaining spectra for short-lived metal-containing free radicals. Molecules prepared via laser ablation will inevitably exist in lower concentrations in the jet/beam environment and because of the inefficient supersonic cooling their lifetimes may be shortened even further. A second complication in experiments involving laser ablation is obtaining the optimum delays between the opening of the pulsed valve and firing of the excimer and dye lasers. In experiments involving NO the timing constraints are modest since NO molecules are entrained

throughout the whole of the gas pulse and the only requirement is that the dye laser is fired to coincide with any portion of the pulse. However, in a laser ablation experiment a narrow slug of the pulsed jet, corresponding to the maximum concentration of ablation products (probably amounting to a time spread of  $\leq 10 \mu\text{s}$ ), needs to be interrogated at the ion source by the dye laser beam.

In order to verify that REMPI spectra could be recorded for free radicals with the new system, a number of preliminary laser ablation experiments were carried out, focusing on alkaline-earth mono-ligated derivatives. In principle, many electronic states of alkaline-earth polyatomics should be observable using REMPI spectroscopy, since the ionisation limits of many of these molecules are relatively low. Indeed, recent observation of the  $\tilde{D}^2\Sigma^+$ ,  $\tilde{E}^2\Sigma^+$  and  $\tilde{F}$  electronic states of CaOH by (1+1) REMPI have proved this to be the case.<sup>20</sup>

#### 7.4.2.1 *CaOH*

An initial laser ablation experiment, involving the CaOH free radical, was carried out in an effort to obtain (1+1) REMPI spectra via resonance with the  $\tilde{E}^2\Sigma^+$  electronic state. This was one of the REMPI transitions studied by Levy.<sup>20</sup> An LIF excitation spectrum, in the range 29000-31000  $\text{cm}^{-1}$ , of the  $\tilde{E}^2\Sigma^+ - \tilde{X}^2\Sigma^+$  transition was recorded in the source chamber to verify that CaOH could be prepared efficiently under the experimental conditions chosen. Laser ablation of calcium, in the presence of a  $\sim 0.5\%$  hydrogen peroxide in helium mixture, was carried out. A strong LIF signal was observed and the resulting spectrum was almost identical to that recorded by Levy *et al.*

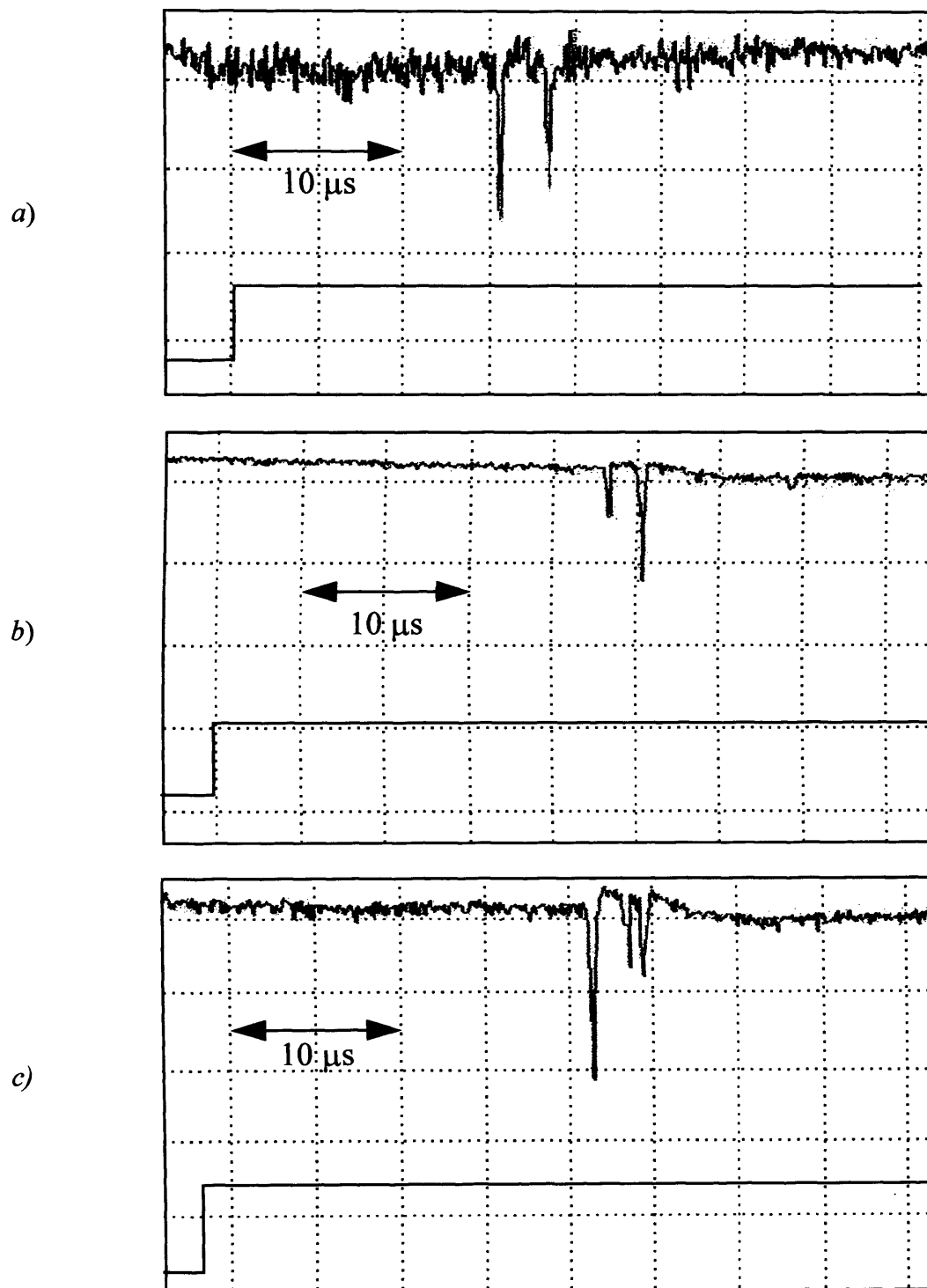
The REMPI experiment was carried out using similar conditions to those chosen for experiments involving NO, i.e. a 2.0 mm diameter skimmer aperture and a pulsed valve/skimmer separation of  $\sim 6$  cm. The apparatus was modified to facilitate laser ablation as described in section 7.3.1. With the ionisation source plate potentials set to the standard values given in Table 7.2, and a detector voltage of  $\sim 1800$  V, a substantial real-time ion signal was obtained by firing the dye laser approximately 700  $\mu\text{s}$  after opening of the pulsed valve. A significant reduction in the intensity of the ion signal occurred if the dye laser timing was outside of the 650-750  $\mu\text{s}$  range.

Fig. 7.8(a) shows the real-time mass spectrum, obtained by laser excitation at  $29879\text{ cm}^{-1}$ , corresponding to the  $\tilde{E}^2\Sigma^+ - X^2\Sigma^+ 0_0^0$  transition. Two clear mass peaks can be seen in the upper trace of Fig. 7.8(a). The flight time of the first peak is  $\sim 15.7\text{ }\mu\text{s}$ , while the second is  $\sim 18.6\text{ }\mu\text{s}$ . It is known, from LIF experiments involving laser ablation of calcium metal in our laboratory, that the major ablation products detectable by LIF spectroscopy are calcium atoms and the CaOH radical. If it is assumed that the cations of these two species are responsible for the two ion peaks in the mass spectrum, the proportionality constant of equation (7.1) can be calculated, and should be equal, for each mass/flight-time pair. The respective proportionality constants are  $6.08 \times 10^7$  and  $6.04 \times 10^7\text{ s kg}^{-1/2}$ , respectively, clearly showing that the two peaks are due to  $\text{Ca}^+$  and  $\text{CaOH}^+$ .

Real-time monitoring of the ion signal revealed that the intensity of the signal was independent of the exciting laser wavelength, indicating that significant *non-resonant* ionisation was occurring at all wavelengths. Indeed, no discernible structure of any kind could be seen in a subsequent REMPI scan of the appropriate spectral region. The obvious explanation is that the intensity of the ionising dye laser beam was too high (1 mJ per pulse), allowing *non-resonant* ionisation to dominate. This is relatively unsurprising given the low ionisation limits of alkaline-earth monoligated derivatives, and indeed, the low atomic ionisation energies. However, although experiments were carried out with lower pulse energies ( $\leq 100\text{ }\mu\text{J}$  per pulse), still no REMPI signal could be discerned.

#### 7.4.2.2 SrOH

Attempts to obtain (1 + 1) UV resonance-enhanced ionisation via the  $\tilde{E}^2\Sigma^+$  electronic state of SrOH (see Chapter 5) were also carried out. Once again, *non-resonant* ionisation dominated, making it impossible to record a REMPI spectrum. Fig. 7.8(b) shows the real-time mass spectrum, obtained by excitation with a laser photon of energy  $29990\text{ cm}^{-1}$ , corresponding to the  $\tilde{E}^2\Sigma^+ - X^2\Sigma^+ 0_0^0$  transition of SrOH. As with calcium ablation, two clear mass peaks can be seen in the upper trace of Fig. 7.8(b). The flight time of the first peak is  $\sim 22.3\text{ }\mu\text{s}$ , while the second is  $\sim 24.5\text{ }\mu\text{s}$ . If it is assumed that the  $\text{Sr}^+$  and  $\text{SrOH}^+$  cations are responsible, the proportionality constant of equation (7.1) for each mass/flight time are calculated to be  $5.85 \times 10^7$  and  $5.88 \times 10^7\text{ s kg}^{-1/2}$ . These are similar to the values obtained for  $\text{Ca}^+/\text{CaOH}^+$ , although, as stated earlier, the values are not identical because no two experiments involve exactly the same ion optic conditions.



**Fig. 7.8** Real-time mass spectra showing mass peaks due to *a)*  $\text{Ca}^+ / \text{CaOH}^+$ , *b)*  $\text{Sr}^+ / \text{SrOH}^+ / (\text{SrOH})_2^+$  and *c)*  $\text{Sr}^+ / \text{SrOH}^+ / \text{SrCCH}^+$ .

At this point it is pertinent to discuss the mass resolution of the REMPI-TOF instrument. As mentioned earlier, mass peaks with FWHM of  $\sim 200\text{-}250$  ns have been obtained for several of the ions mentioned above, with careful adjustments of the ion source potentials. With this time resolution, the corresponding mass resolution is  $\sim 1$  mass unit. Consequently, it should be possible to differentiate between molecular ions that differ in composition by one hydrogen. This is especially useful for work involving laser ablation of the alkaline-earth metals since it is known that, for example, both the metal monoxides and monohydroxides are major ablation products.

One other mass peak can be seen in Fig. 7.8(b) at  $\sim 34.2$   $\mu\text{s}$ , although it is weaker than the other two. Using the proportionality constant determined above, the mass peak is calculated to correspond to a mass of  $\sim 209$  amu. Given the experimental condition, i.e. laser ablation of strontium metal, one possible ion that corresponds to a mass of 209 amu is the strontium monohydroxide dimer ion,  $(\text{SrOH})_2^+$ , a molecule that is currently unknown in the gas-phase. The fact that a mass peak corresponding to SrOH dimer is observed in the mass spectrum has intriguing implications. For ionisation of  $(\text{SrOH})_2$  to occur via a *non-resonant* process, the molecule must have an ionisation limit that is similar to other alkaline-earth metal-containing species, such as SrOH. This implies that the spectroscopy in  $(\text{SrOH})_2$  is probably similar to that in SrOH. In other words, the low-lying electronic transitions in  $(\text{SrOH})_2$  involve promotion of an electron which resides in metal-centred orbitals. Clearly, the preliminary findings reported here require further investigation in the future and these experiments are planned.

#### 7.4.2.3 *SrCCH*

During the experiments involving laser ablation of strontium, an additional experiment was carried out in which benzene was seeded into the helium carrier gas. In similar experiments carried out in the Ellis laboratory using LIF spectroscopy it is known that SrH, SrOH, SrCCH and  $\text{SrCH}_3$  can all be detected. The real-time mass spectrum obtained in the REMPI experiment is shown in Fig. 7.8(c). The mass spectrum was obtained by excitation with the dye laser at  $29990\text{ cm}^{-1}$ . Three mass peaks can be seen in the upper trace of Fig. 7.8(c) with respective flight times of 22.3, 24.5 and 25.1  $\mu\text{s}$ . Clearly, the first two peaks have the same flight-time as the peaks in the mass spectrum of Fig. 7.8(b), and are therefore assigned to  $\text{Sr}^+$  and  $\text{SrOH}^+$ . However, the third peak, at 25.1  $\mu\text{s}$  corresponds to a mass of  $\sim 113$  amu, which corresponds to  $\text{SrCCH}^+$ .

Many possible molecules could be formed under these experimental conditions, including neutral organic fragments and small carbon clusters, such as CH and C<sub>2</sub>, in addition to unreacted benzene. However, the corresponding ions are not seen in the mass spectrum of Fig. 7.8(c). The ionisation potentials of these molecules are all relatively high and would require at least three photons to be absorbed to exceed the ionisation threshold. The fact that only ion peaks arising from strontium-containing molecules are seen in the mass spectrum (Fig. 7.8(c)) indicates that *non-resonant* ionisation is occurring under the current experimental conditions. The SrCCH radical would be expected to possess a lower ionisation energy, comparable to that of SrOH, and it is, therefore, no surprise that a mass peak for this molecule is seen in the mass spectrum. Presumably, SrCCH<sup>+</sup> is formed by *non-resonant* two-photon ionisation of SrCCH. This finding supports the idea that in all the REMPI experiments involving ablation of alkaline-earth metals, *non-resonant* ionisation of the alkaline-earth metal containing products was dominant.

## 7.5 Conclusions

Tests involving the newly constructed REMPI-TOF apparatus have shown that while the mass spectrometer is working well, supersonic cooling has proved elusive. Several arguments have been outlined that may account for the breakdown in supersonic cooling, along with details of several possible modifications to the spectrometer which may need to be carried out in the near future. Clearly, the priority of future work is to obtain jet-cooled REMPI spectra.

Ion signals due to alkaline-earth metal-containing molecules were easily detected, which is encouraging for future REMPI studies on these and other metal-containing molecules. Unfortunately, non-resonant ionisation dominated in the present work, which made it impossible to record any REMPI spectra of CaOH, SrOH, SrCCH or (SrOH)<sub>2</sub>. In the long term a wide variety of REMPI experiments are planned on new metal-containing species, most notably on transition metal-containing organometallics. Fairly complex spectra are expected for these species, and the mass-selective detection capability will be essential in confirming the identity of the spectral carrier.



## References

- 1 A.J. Bezant, *Ph.D Thesis*, University of Leicester, 1997
- 2 J.W. Hudgens, In *Advances in Multiphoton Processes and Spectroscopy*, ed. S. H. Lin (World Scientific, Singapore, 1988)
- 3 M.N.R. Ashfold, S.G. Clement, J.D. Howe and C.M. Western, *J. Chem. Soc. Faraday Trans.*, **89** (1993) 1153
- 4 J. Danon, H. Zacharias, H. Rottke and K.H. Welge, *J. Chem. Phys.*, **76** (1982) 2399
- 5 G. Herzberg, *Molecular Spectra and Molecular Structure. I. Spectra of Diatomic Molecules* (Van Nostrand Reinhold, New York, 1967).
- 6 A.M. Bush, J.M. Dyke, P. Mack, D.M. Smith and T.G. Wright, *J. Chem. Phys.*, **105** (1996) 9804
- 7 W.C. Wiley and I. H. McLaren, *Rev. Sci. Instr.*, **26** (1955) 1150
- 8 D.M. Lubman (Ed.), *Lasers and Mass Spectrometry*, (Oxford University Press, London, 1990)
- 9 B.A. Mamyrin, V.I. Karataev, D.V. Shmikk and V.A. Zagulin, *Sov. Phys. - JETP*, **37** (1973) 45
- 10 U. Boesl, H.J. Neusser, R. Weinkauff and E.W. Schlag, *J. Phys. Chem.*, **86** (1982) 4857
- 11 B.J. Pollard, *Ph.D Thesis*, University of Leicester, 1999
- 12 G.K. Corlett, *Ph.D Thesis*, University of Leicester, 1997
- 13 M. Hippler, A.J. Yates and J. Pfab, *Inst. Phys. Conf. Ser.*, **113** (1991) 303
- 14 M.D. DiRosa, K.G. Klavuhn and R.K. Hanson, *Comb. Sci. Tech.*, **118** (1996) 257
- 15 M. Hippler and J. Pfab, *Chem. Phys. Lett.*, **243** (1995) 500
- 16 M. Hippler and J. Pfab, *Mol. Phys.*, **94** (1998) 313
- 17 K.P. Huber and G. Herzberg, *Molecular Spectra and Molecular Structure. IV. Constants of Diatomic Molecules* (Van Nostrand Reinhold, New York, (1979)
- 18 E.A. Cotton, G. Wilkinson and P.L. Gaus, *Basic Inorganic Chemistry*, (Wiley, New York, 1987)
- 19 S. Panov, X.Q. Tan and T.A. Miller, 48th Ohio State University International Symposium on Molecular Spectroscopy, paper RA06 (1993)
- 20 R. Pereira and D.H. Levy, *J. Chem. Phys.*, **105** (1996) 9733